Surface Science Studies of Pd and Au on $TiO_2(110)$ Single Crystals

by Ryan Sharpe

in partial fulfilment of the requirements for the degree

Doctor of Philosophy in Chemistry

Cardiff University, May 2015

Form: PGR_Submission_2014

NOTICE OF SUBMISSION OF THESIS FORM:
POSTGRADUATE RESEARCH

APPENDIX 1:
Specimen layout for Thesis Summary and Declaration/Statements page to be included in a Thesis

DECLARATION

This work has not been submitted in substance for any other degree or award at this or any other university or place of learning, nor is being submitted concurrently in candidature for any degree or other award.

Signed ………………………………………… (candidate) Date …………………………

STATEMENT 1

This thesis is being submitted in partial fulfillment of the requirements for the degree of PhD

Signed ………………………………………… (candidate) Date …………………………

STATEMENT 2

This thesis is the result of my own independent work/investigation, except where otherwise stated. Other sources are acknowledged by explicit references. The views expressed are my own.

Signed ………………………………………… (candidate) Date …………………………

STATEMENT 3

I hereby give consent for my thesis, if accepted, to be available online in the University's Open Access repository and for inter-library loan, and for the title and summary to be made available to outside organisations.

Signed ………………………………………… (candidate) Date …………………………

STATEMENT 4: PREVIOUSLY APPROVED BAR ON ACCESS

I hereby give consent for my thesis, if accepted, to be available online in the University's Open Access repository and for inter-library loans **after expiry of a bar on access previously approved by the Academic Standards & Quality Committee.**

Signed ………………………………………… (candidate) Date …………………………

Abstract

In this thesis, the structure and reactivity of Pd, Au and Au-Pd structures on $TiO_2(110)$ single crystals has been investigated with surface science techniques, including X-ray photoelectron spectroscopy (XPS), low energy ion scattering (LEIS), Auger electron spectroscopy (AES) and temperature programmed desorption (TPD).

Sputtering a clean titania single crystal resulted in reduction of the surface. The surface was partially re-oxidised by annealing in UHV and further oxidised by annealing in O_2.

Pd growth on $TiO_2(110)$ was found to be Volmer Weber (3D island growth) regardless of the preparation and condition of the titania – whether it was heavily sputtered, sputtered then annealed or annealed in oxygen.

On annealing the $Pd/TiO_2(110)$ to temperatures above 723K, an SMSI effect was observed between the Pd nanoparticles and the TiO_2 support – the Pd is encapsulated by the reduced titania support. This was found to be affected by the oxidation state of the titania – SMSI occurred at a higher temperature for an oxidised surface than for a reduced surface. Au did not show an SMSI effect and is not encapsulated by the titania support, even when annealing to temperatures of 873K. The Au film only sinters and forms nanoparticles.

Pd and Au were deposited sequentially on to $TiO_2(110)$. They are proposed to form bimetallic Au-Pd core-shell structures on annealing. After continued annealing to higher temperatures an SMSI effect is once again seen. This appears to be diminished with a greater amount of Au present in the bimetallic structure.

The reactivity of $TiO_2(110)$ towards several small organic molecules was studied with TPD when clean and when deposited with Pd and Au, both separately and combined. Titania showed similar reactivity to that found in the literature – ethanol decomposed primarily to ethene and acetaldehyde, formic acid gave both CO and H_2O, and CO_2 and H_2, and acetic acid gave ketene, CO and

CO_2. Au was found to be unreactive. Pd was found to reduce the reactivity of the titania. Pd-Au were, in most cases, found to be more reactive than their component metals.

Acknowledgements

First of all, I would like to thank my supervisor, Professor Mike Bowker, for giving me the opportunity to carry out this PhD and for his support, encouragement and advice during these years.

A huge amount of thanks must go to Dr Robert Davies, my post-doc for the majority of my PhD, who taught me how to use the equipment and was always on hand to help fix all manner of problems encountered, whether great or small.

Dr David Morgan for his broad range of surface science knowledge and for his technical expertise, and Professor Phil Davies, who has always been willing to offer opinions and critiques and to help sort out any problems. I should especially thank Phil for always being on hand to help with baking the system, despite being extremely busy! I would also like to thank Dr Hatem Altass, who also assisted me with the equipment in my first year.

Thanks to my fellow students in the Surface Science group for welcoming me when I started, providing entertainment as I was finishing and writing up, and overall making this a much more enjoyable experience.

I also need to thank all of the technical and support staff for their help and assistance with various matters during my PhD. In particular, I'd like to thank the workshop staff, Alun and Steve, for all of their technical help and expertise.

Thanks to Cardiff Uni and the EPSRC for their financial support.

Many thanks also go to my friends outside the lab, old and new.

Special thanks go to Pratha for her friendship, support, understanding and encouragement throughout my entire PhD.

Finally, I would like to thank my family, in particular my parents, for all of their help and support, financial, emotional, and everything in between, for the duration of my time at Cardiff.

List of abbreviations

AES	Auger electron spectroscopy
DFT	Density functional theory
DRIFTS	Diffuse reflectance infrared Fourier transform spectroscopy
FTIR	Fourier transformed infrared spectroscopy
HREELS	High resolution electron energy loss spectroscopy
ISS	Ion scattering spectroscopy
LEED	Low energy electron diffraction
LEIS	Low energy ion scattering
MEIS	Medium energy ion scattering
ML	Monolayer
MS	Mass spectrometry
MVD	Metal vapour deposition
RBS	Rutherford backscattering spectroscopy
RHEED	Reflection high energy electron diffraction
STM	Scanning tunnelling microscopy
TPD	Temperature programmed desorption
UHV	Ultra high vacuum
UPS	Ultraviolet photoelectron spectrometry
VAM	Vinyl Acetate Monomer
XPS	X-ray photoelectron spectroscopy

Contents

Chapter 1 - Introduction

Chapter 2 – Experimental

Chapter 3 – Surface Science of TiO_2(110) and Pd/TiO_2(110)

Chapter 4 – Au and Pd-Au on TiO_2(110)

Chapter 5 – Reactivity of $TiO_2(110)$ and deposited metal particles

Chapter 6 – Conclusions

Appendix

Chapter 1 – Introduction

Chapter 1 Contents

1.1 Catalysis

The term "catalysis" was coined early in the 19th Century by Berzelius, to describe the property of a substance that facilitates a chemical reaction without being consumed by it[1]. A simplified definition might be "catalysis is a process whereby a reaction occurs faster than the uncatalysed reaction, the reaction being accelerated by the presence of a catalyst[2]." A catalyst is defined as "a body or a material which can induce the phenomenon of catalysis. It enhances the rate of the catalysed reaction and is regenerated at the end of it[2]."

Catalysis is a ubiquitous phenomenon. Many essential biological functions involve catalysis via enzymes, including photosynthesis and the Krebs cycle. Catalysts are also extremely prevalent in industry – approximately 90% of all our chemicals and materials are produced using catalysis at one stage or another[2].

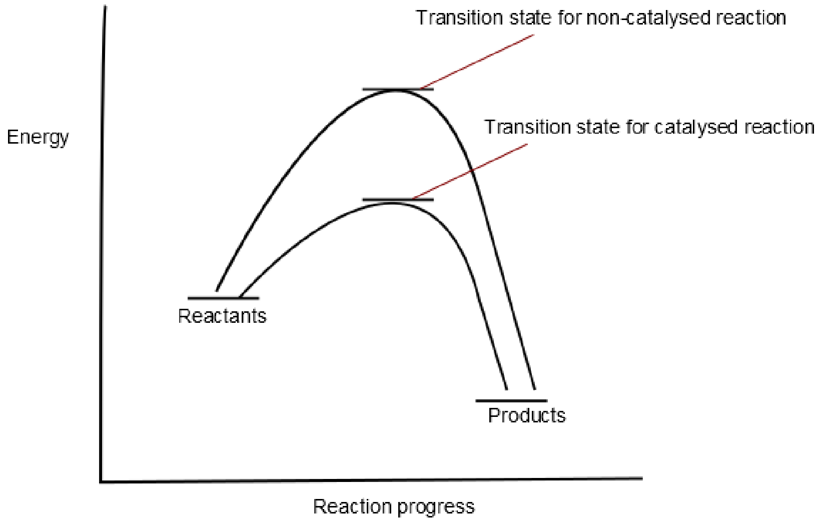

Figure 1-1 - Schematic of the activation pathways with and without the presence of a catalyst. In the presence of a catalyst, less energy is required to overcome the activation energy barrier.

The catalyst does not affect the final equilibrium of the reaction, only the speed at which the equilibrium is reached. A catalyst works by providing a reaction pathway with a lower activation energy than the usual route (see Figure 1-1).

Catalysts are defined as homogenous if they are in the same phase as the reactants and heterogeneous if they are present in a different phase (i.e. the catalyst is a solid, whereas the reactants are gaseous or liquid). An advantage of heterogeneous catalysts is that the catalyst can usually be separated with greater ease than the homogenous catalyst. A common example of the use of a heterogeneous catalyst is the catalytic converter fitted to most cars. Gaseous pollutants pass over a solid Pt/Pd/Rh catalyst and are converted to less harmful gases. In order to understand this reaction, and many other catalytic reactions, it is extremely important to understand the interaction of the reactant with the catalyst. It is at this point that surface science is extremely useful, as this interaction occurs at the surface of the catalyst.

1.2 Surface Science

Surface science is the study of physical and chemical phenomena at the interface of two different phases, e.g. a solid catalyst and gaseous reactants in a heterogeneous catalysed reaction.

The surface of a catalyst has a different structure to the bulk – surface atoms have a lower co-ordination than bulk atoms and have free bonds that can interact with other molecules.

An example of a catalysed reaction is shown in Figure 1-2:

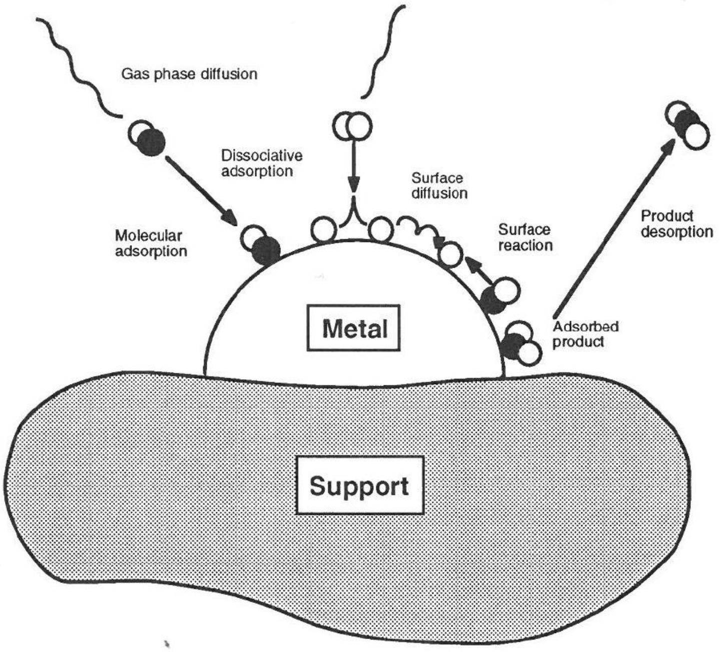

Figure 1-2 - Molecular and atomic events during a catalytic reaction[2]

The molecules diffuse through the gas phase to the metal surface where they may then adsorb molecularly. They may then dissociate to their component atoms, or diffuse across the surface. At this point, the reactive species may combine to form a new product and then desorb from the surface via cleaving of its bond to the surface. This illustrates the importance of surface science in the study of catalysis – the nature of the interface between the catalyst and the reactants is crucial for the activity of the reaction. The makeup of the top layer of atoms of a catalyst determine the speed and efficiency of a reaction, hence the ability to look at this interface is extremely useful to shed new light on catalytic reactions.

1.2.1 Single Crystals – Model Catalysts

A model catalyst is inspired by a real catalyst, and is synthesised with the purpose of understanding how it works[3]. The model catalyst has a known structure and surface topology, which can be easily characterised with surface science techniques. On the other hand, real powdered catalysts are typically pellets, powders, or coatings, i.e. very complex systems with many variables, including surface area and an ill-defined surface structure. The use of model catalysts is especially suited to investigating the nature of the metal-support interaction, including the effect of metal cluster size, cluster number density and temperature.

Single crystals make for excellent models of catalyst supports – industrial catalysts are often metal nanoparticles supported on a metal oxide substrate. Single crystals are often highly uniform and it is much easier to observe the effects of reaction on this surface than on a powdered sample

A single crystal is defined as a material in which the crystal lattice of the entire sample is continuous and unbroken to the edges of the sample, with no grain boundaries. A grain boundary is the interface between two grains, or crystal structures, in a polycrystalline material. These defects can have strong effects on the properties of a material, so removing them allows the study of the simplest forms of these crystal structures.

The most common fcc metal terminations of single crystals are the “low-index” faces, the (100), (110) and (111) planes[2]. These numbers refer to “Miller Indices,” which are explained in section 1.2.2

1.2.2 Miller Indices

The Miller index is used to denote a given plane[4]. It consists of three integers (x, y, z) for materials with a face-centred cubic (fcc) or body-centred cubic (bcc) structure (see Figure 1-3) and four integers (w, x, y, z) for materials with a hexagonal close-packed (hcp) structure.

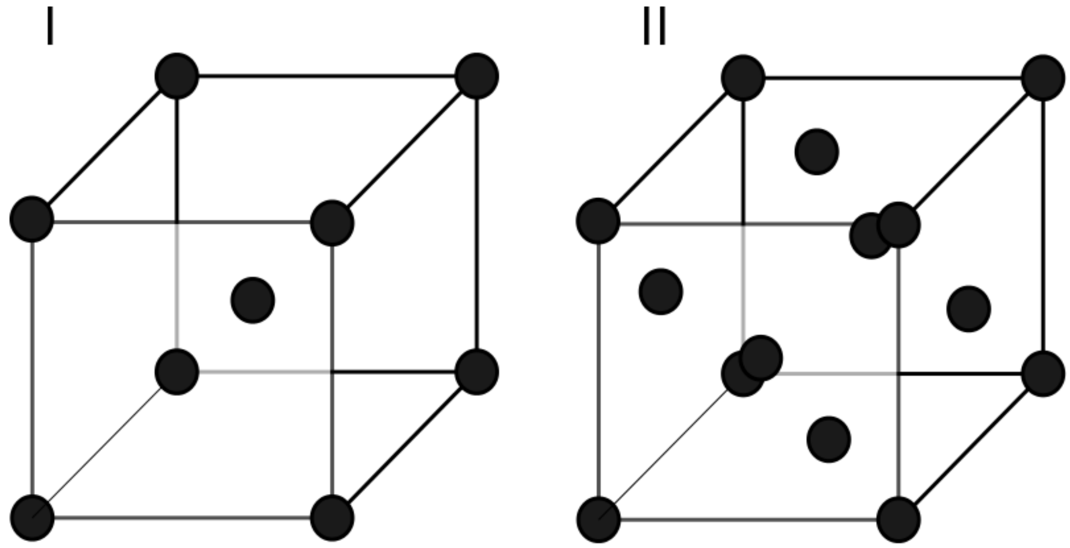

Figure 1-3 - Diagram of I) a BCC and II) a FCC structure

Using a bcc crystal structure, Miller indices can be easily understood, as shown below. The cubic structure has three mutually perpendicular Cartesian axes, labelled x, y and z (Figure 1-4), and has equal dimensions, denoted “*a*.” The shaded area is the plane of interest. To determine the Miller index of a plane, the following steps are required:

1. Decide where the plane intercepts the x, y and z axes, in multiples of the unit cell dimension, a. If the plane runs parallel to an axis, then the intercept is infinity (∞).
2. Take the reciprocal values of these intercepts
3. If step two results in fractions, reduce these indices to the equivalent ratio of whole numbers.

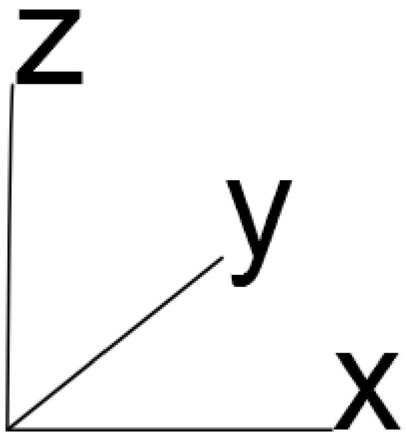

Figure 1-4 - Identification of the axes

(100) plane

This plane intersects the y axis at "*a*" and is parallel to the x and z axes, as shown in Figure 1-5. It therefore has intercepts of (∞, a, ∞), which are then expressed as fractions of "a" to give (∞, 1, ∞). The reciprocal of these fractions are then taken, giving (010) or (100).

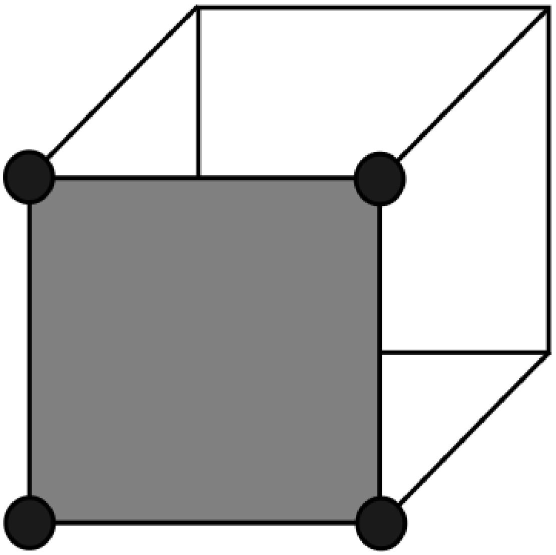

Figure 1-5 - the (100) plane on a bcc crystal

(110) plane

This plane intersects both the x and y axes at “a” and runs perpendicular to the z axes, (Figure 1-6). It therefore has intercepts of (a, a, ∞). These are expressed as fractions of “a”, giving (1, 1, ∞). Taking the reciprocal gives (110).

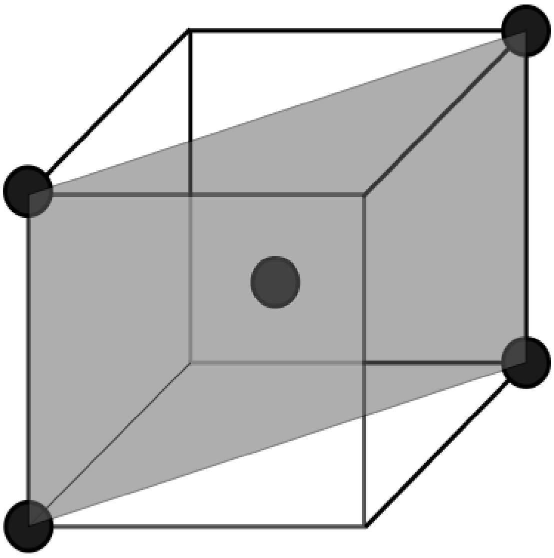

Figure 1-6 - the (110) plane on a bcc crystal

(111) plane

This plane intercepts all three axes at a value of “a,” giving intercepts of (a, a, a). It is therefore the (111) plane (Figure 1-7).

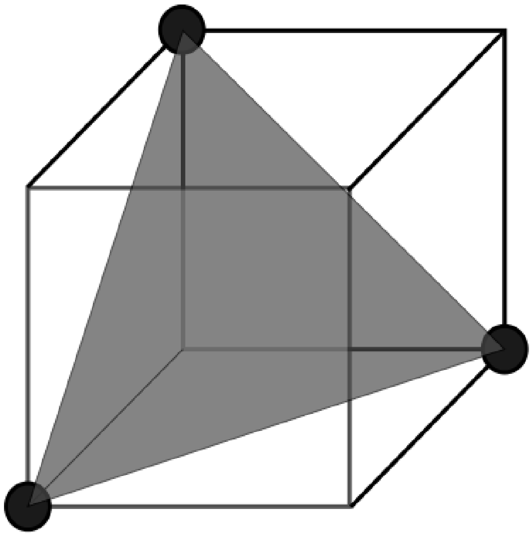

Figure 1-7 - the (111) plane on a bcc crystal

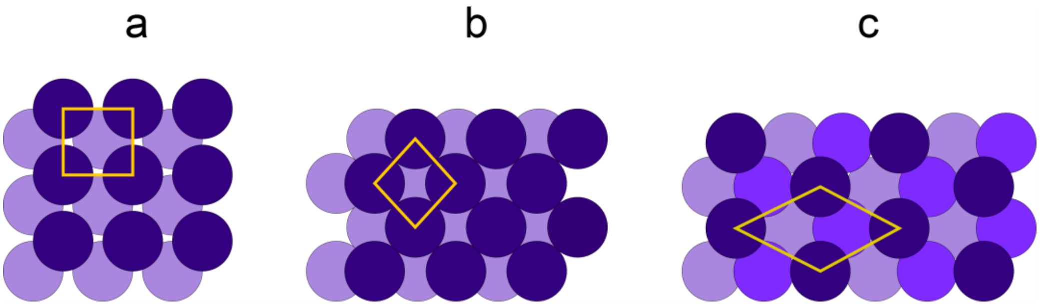

Figure 1-8 - Representation of the different planes on the surface of a bcc crystal. (a) (100); (b) (110); (c) (111). Unit cells are shown in yellow.

The corresponding surface arrangement of each crystal plane is shown in Figure 1-8. It can be seen that the atoms in each of these surface planes has a different coordination number. The atoms with the highest coordination number at the surface will have the lowest surface free energy and will therefore be the least reactive.

1.2.3 Surface restructuring

The atoms on a surface typically do not have their full co-ordination number – a surface is formed by breaking bonds, so this is not surprising. These surface atoms are therefore in a higher energy state compared to the bulk and are much more reactive. The surface may restructure itself in several different ways in order to minimise this surface energy.

In order for the surface to compensate for the "loss" of bonding, it may undergo a process known as "surface relaxation." Here, the interplanar spacing between the top layers of the material oscillate – the first layer contracts towards the second layer to increase their coordination. The third layer responds by expanding away from the second layer atoms, compensating for the over-coordination of the second layer. This oscillation permeates into the surface until it is completely dampened. This typically occurs over the top 5-6 atomic layers, in a region known as the selvedge. This process is generally greatest for surfaces with the highest surface energy, i.e. the lowest surface atom coordination.

A second process, known as “surface reconstruction,” may occur if the surface energy is large enough. Here, there will be gross restructuring of the surface plane to increase the coordination of the surface atoms and to therefore lower the surface energy.

A surface may also lower its surface energy by adsorbing a molecule or an atom.

Sintering is often observed on metal catalysts supported on metal oxide supports. The dispersed metal particles combine to form fewer, larger particles, minimising their surface energy by increasing the average coordination number of each atom.

1.2.4 Surface defects

Ideally, a single crystal will only consist of a single flat plane. However, this is extremely unrealistic; a single crystal will typically contain a mixture of flat regions (known as terraces) and defects (steps, kinks and point defects), as shown in Figure 1-9. Point defects can be an atomic vacancy or a surface adatom. These defects lead to a change in the local distribution of the surface atoms and electronic properties around them.

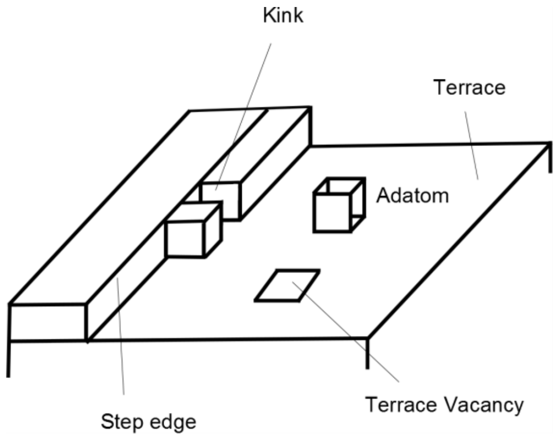

Figure 1-9 - Schematic representation of defects present on a surface, including a step, kink, terrace, adatom and a vacancy[4]

1.3 Adsorption onto the surface

"Adsorption" describes the process of a molecule (an adsorbate) forming a bond to the surface (the adsorbent)[4]. The fractional coverage (θ) of an adsorbate is given by:

$$\theta = \frac{Number\ of\ surface\ sites\ occupied\ by\ the\ adsorbate\ (N_s)}{Total\ number\ of\ substrate\ adsorption\ sites\ (N)}$$

When every available surface site is occupied, i.e. when $\theta = 1$, then the adsorbate is said to have formed a monolayer.

Associative adsorption is said to occur when a molecule adsorbs onto the surface from the gas phase and remains fully intact. When the molecule fragments instead, it is known as dissociative adsorption.

There are two broad classifications of bonding, depending on the enthalpy of adsorption of the adsorbate: physisorption and chemisorption:

In physisorption, bonding is associated with van der Waals-type interactions – long range and weak. Bonding is characterised by redistribution of electron density within the adsorbate and adsorbent respectively – there is minimal exchange of electrons. The enthalpy of adsorption (ΔH_{ad}^0) for physisorption is usually less than 35kJ mol^{-1}, which is of the order of the heat of condensation ($\Delta H^0_{condensation}$). Physisorption tends to be reversible, as the bonds are so weak.

Chemisorption involves the formation of a strong chemical bond with the surface ($\Delta H_{ad}^0 > 35$ kJ mol^{-1}) and electrons are actually exchanged between the adsorbate and the surface. The value of ΔH_{ad}^0 is very variable, and dependent on the surface coverage, the substrate and the surface face.

1.3.1 Adsorption isotherms

An adsorption isotherm is the dependence of the coverage, θ, on the pressure of the gas, P, at a constant temperature. At low pressures, all adsorption isotherms are linear:

$$P = constant \times \theta$$

One of the most basic isotherms is the Langmuir isotherm. It is based on the following assumptions:

1. All surface sites are equivalent and may only be occupied by one adsorbate
2. There is a dynamic equilibrium between the gas and the adsorbed layer at a constant temperature
3. Gas phase molecules are continually colliding with the surface – if they hit a vacant site then they form a bond with the surface. If they hit a filled site then they reflect back to the gas phase.
4. Once adsorbed, molecules are localised, i.e. they cannot move to an adjacent site, and the enthalpy of adsorption per site remains constant regardless of coverage.

The Langmuir equation can be derived by considering that the molecules in the gas phase are in dynamic equilibrium with the surface:

$$A_{(g)} + B_{(surface\ site)} \underset{\overleftarrow{k_d}}{\overset{k_a}{\rightarrow}} A - B$$

K_a and k_d are the adsorption rate constant and the desorption rate constant respectively.

Rate of adsorption is given by:

$$rate = k_a P(1 - \theta)$$

Where P is the pressure and (1-θ) is the fractional monolayer of surface sites unoccupied by an adsorbate molecule. The rate of desorption is written as:

$$rate = k_d \theta$$

At equilibrium, the two rates will be equal:

$$k_a P(1 - \theta) = k_d \theta$$

This can be rearranged to give the Langmuir adsorption isotherm:

$$\theta = \frac{N_s}{N} = \frac{KP}{1 + KP}$$

Where $K = k_a/k_d$.

The biggest problem with the Langmuir absorption isotherm is that it does not account for the formation of adsorbate film thicknesses greater than one monolayer. The heat of absorption of a molecule adsorbing onto the substrate surface will be very different from that of a molecule adsorbing onto another layer of adsorbate. The Brunauer, Emmett and Teller (BET) isotherm introduced a number of assumptions to give an improvement of the Langmuir isotherm for multilayer adsorption:

1. The first adsorbate layer will adsorb onto a surface with identical, uniform surface sites (i.e. same energy, just like the Langmuir isotherm).
2. A second layer can only adsorb on top of the first, a third layer on top of the second, etc. When $P = P_0$ (the saturated vapour pressure of the adsorbate), an infinite number of layers will form.

3. The rates of condensation and evaporation for each layer are the same at equilibrium.
4. When the number of adsorbed layers is two or more, the equilibrium constants, k^0, are equal, and the corresponding value of $\Delta H^0_{AD} = -\Delta H^0_{VAP}$. The enthalpy of adsorption for the first layer is ΔH^0_{AD}, just like the Langmuir isotherm. The amount adsorbed in all layers can be expressed in the BET equation:

$$\frac{P}{N_s(P_0 - P)} = \frac{1}{NC} + \frac{(C-1)}{NC} \times \frac{P}{P_0}$$

Where C is the BET constant:

$$C \approx e^{\frac{\left(\Delta H^0_{des} - \Delta H^0_{vap}\right)}{RT}}$$

Both isotherms, as well as several others, can give useful information on the surface area within specific values of θ. However, no isotherm can define adsorption over all ranges of θ and P.

1.3.2 Adsorption kinetics

The probability of a molecule adsorbing onto the surface is known as the “sticking probability,” S.

$$S = S_0(1 - \theta)$$

Where S_0 is the sticking probability at $\theta = 0$ and S is given by:

$$S = \frac{adsorption\ rate\ of\ molecules\ by\ the\ surface}{collision\ rate\ of\ molecules\ with\ the\ surface\ (Z)}$$

The greater the number of adsorption sites, the greater the probability of sticking. This relationship between S and θ is not linear; S may remain high as θ increases, and then suddenly decrease as θ approaches 1 (see Figure 1-10). This can be explained with a precursor state – if a molecule approaches an occupied surface site, it forms a weak interaction with the surface and then diffuses to a vacant site, rather than reflecting straight back into the gas phase, as stated by Langmuir. Whether or not the molecule will adsorb depends on the lifetime of this weak interaction, τ_0, and the enthalpy of adsorption, ΔH°_{ads}:

$$\tau = \tau_0 e^{\frac{-\Delta H^0_{ads}}{RT}}$$

The longer the molecule is at the surface, the greater the likelihood of it forming a bond with the surface.

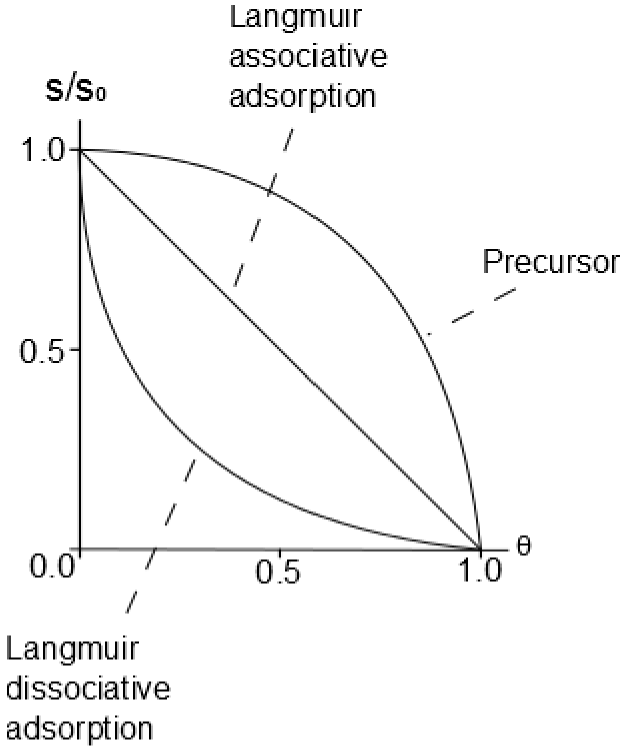

Figure 1-10 - The variation of sticking probability with surface coverage for precursor, Langmuir associative and Langmuir dissociative adsorption[4]

1.4 Overlayer structures

A three dimensional crystal can be characterised by one of 14 different "Bravais lattices." In two dimensional systems, there are only five possible Bravais lattices, shown in Figure 1-11. These are square, rectangle, centered rectangle, hexagonal and oblique.

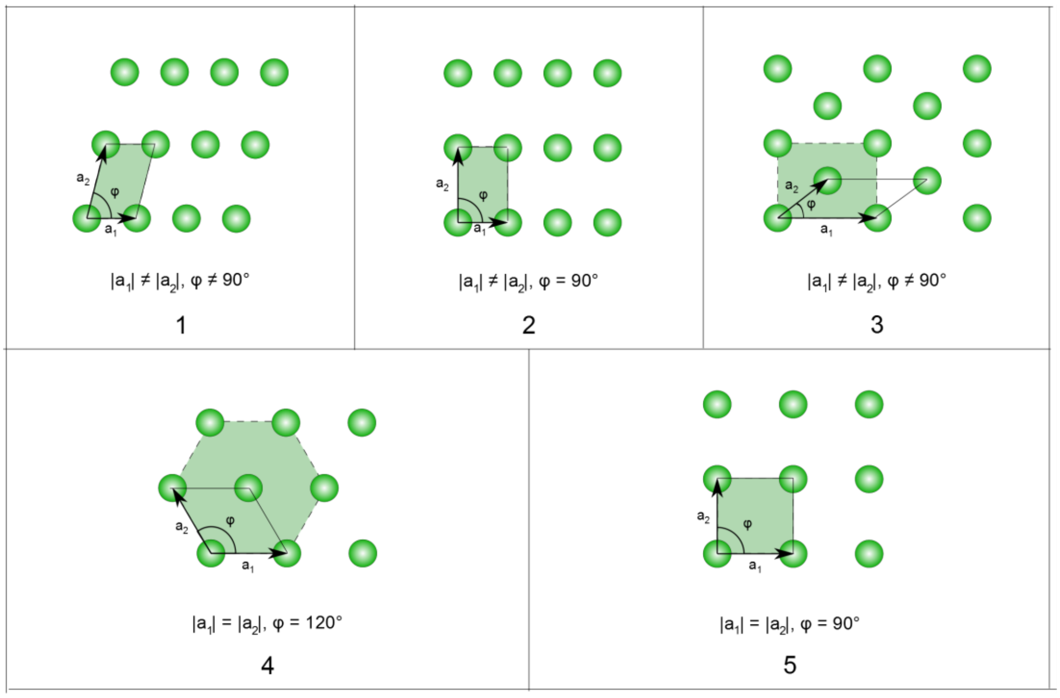

Figure 1-11 - The five Bravais surface lattices[5]

The vectors a and b in Figure 1-11 describe the unit cell in real space. Overlayer structures can be defined using Wood's notation or matrix notation, described in section 1.4.1 and 1.4.2, respectively.

1.4.1 Wood's notation

Wood's notation relates the overlayer "mesh" to the substrate mesh[4]. For example, Figure 1-12 shows an overlayer on a square substrate, with a coverage, $\theta = ½$. The unit cell describing the overlayer is centred with unit vectors (a_0 and b_0) parallel to a_s and b_s (the vectors defining the substrate primitive unit cell), respectively.

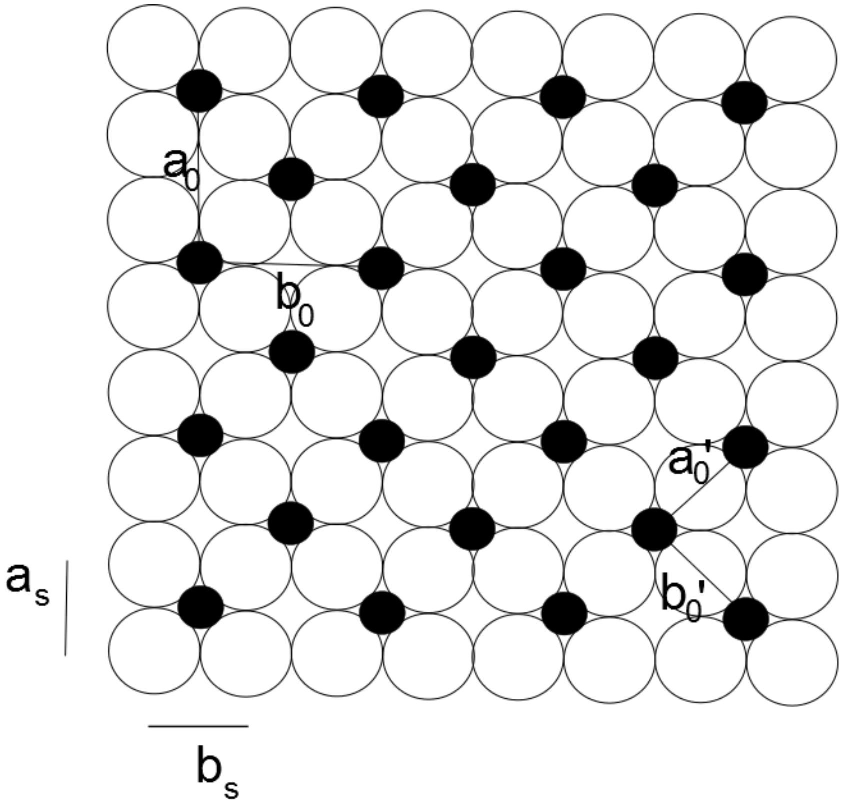

Figure 1-12 - Schematic of a surface coverage of 1/2

By looking at Figure 1-12, it can be seen that:

$$|a_0| = 2|a_s|$$

And:

$$|b_0| = 2|b_s|$$

a_0 is twice the length of a_s, and b_0 is twice the length of b_s. The overlayer structure is therefore referred to as a (2x2) overlayer. However, the overlayer mesh also contains an atom in the centre, so its full description would be a c(2x2) (centred two by two) structure.

A primitive unit cell (vectors a_0’ and b_0’) could be defined as well. The vectors a_0’ and b_0’ are rotated with respect to vectors a_s and b_s by 45°. It can also be seen that:

$$|a_0'| = \sqrt{2}|a_s|$$

And:

$$|b_0'| = \sqrt{2}|b_s|$$

Therefore, its primitive unit cell would be referred to as a (√2 x √2)R45° (root two by root two rotated 45°) structure.

Wood’s notation may be summarised as:

$$M(hkl)\left(\frac{|a_0|}{|a_s|}X\ \frac{|b_0|}{|b_s|}\right) - R\alpha° - A$$

Where M is the chemical symbol of the substrate, (*hkl*) is the Miller index of the surface plane, [a_s] and [b_s] are the substrate vectors, [a_0] and [b_0] are the surface overlayer vectors, α is the angle between the substrate and overlayer meshes (omitted if α = 0°) and A is the chemical species (omitted if A = M).

Wood’s notation is only suitable for “commensurate” structures, i.e. if the angles of the surface and substrate unit meshes match.

1.4.2 Matrix notation

Matrix notation is much more general than Wood’s notation, and can be used to describe overlayer structures that are both commensurate and incommensurate[4]. First of all the primitive overlayer mesh vectors (a_0 and b_0) must be defined in terms of a linear combination of the primitive unit mesh vectors of the substrate (a_s and b_s). For example, looking at the primitive unit cell of Figure 1-12:

$$a_0' = 1a_s + 1b_s$$

And

$$b_0' = -1a_s + 1b_s$$

In matrix notation, this may be rewritten as:

$$\begin{pmatrix} a_0 \\ b_0 \end{pmatrix} = \begin{pmatrix} 1 & 1 \\ -1 & 1 \end{pmatrix} \begin{pmatrix} a_s \\ b_s \end{pmatrix}$$

The matrix above defines the overlayer mesh in terms of the substrate. A more general representation is:

$$a_0 = G_{11} a_s + G_{12} b_s$$

And

$$b_0 = G_{21} a_s + G_{22} b_s$$

Therefore:

$$\begin{pmatrix} a_0 \\ b_0 \end{pmatrix} = \begin{pmatrix} G_{11} & G_{12} \\ G_{21} & G_{22} \end{pmatrix} \begin{pmatrix} a_s \\ b_s \end{pmatrix}$$

G_{11}, G_{12}, G_{21} and G_{22} are constants and the subscripts refer to the position of the constant in the matrix, e.g. 11 means row 1, column 1, whereas 12 means row 1, column 2.

1.5 TiO_2

TiO_2 has been the subject of several detailed reviews[6-9]. Diebold's seminal review in 2003 looked in great detail at the surface science of TiO_2[10], and Thornton et al built on this knowledge in 2013[11].

Titanium dioxide has been the object of a number of studies, mainly due to its role as a prototypical transition metal oxide surface[12]. Thanks to its wide range of applications, including as a catalyst[13], paints and optical coatings[14], antibacterial coatings, self-cleaning surfaces, a gas sensor and as a photocatalyst[15], TiO_2 is the most investigated single-crystalline system in the surface science of metal oxides[10].

Titanium dioxide is a preferred oxide system for experimentalists, as it is well suited for many techniques[10]; the fact that it is a semi-conductor means that electron-based techniques, including scanning tunnelling microscopy, may be used. Crystals with a high surface quality are easily available and can be easily reduced, which helps to prevent charging. Furthermore, new phenomena are typically much easier to observe on already well-characterised systems, such as TiO_2.

One driving force behind the huge interest in TiO_2 is the desire for an improved understanding of catalytic reactions. Heterogeneous catalysts typically consist of metal particles on an oxide support, which has led to a number of studies on the growth of metals on TiO_2[10], serving as a model for other metal/oxide systems. For example, TiO_2 is mixed with V_2O_5 to form a catalyst used for selective oxidation reactions[16], and is also used as a support for gold nanoparticles in oxidation reactions of CO[17] and in the decomposition of H_2O_2 to H_2 and O_2[18].

Another area of great interest is on the photochemical properties of TiO_2. Fujishima and Honda[19] carried out pioneering work in 1972 on the photolysis of water on TiO_2 electrodes, which has led to a vast number of studies since – the use of TiO_2 in photocatalysis will be looked at in more detail in section 1.5.1.

The photochemical properties of TiO_2 tie into its potential use for photo-assisted degradation of organic molecules, i.e. the ability of something coated in TiO_2 to clean itself. In principle, TiO_2 is a semiconductor and will generate an electron-hole pair on irradiation with light[10]. This pair may separate, and the resulting charge carriers may migrate to the surface, where they are then able to react with any adsorbed water and oxygen to create radicals. These radical species may then attack any adsorbed species, ultimately leading to the decomposition of the organic species to CO_2 and H_2O.

1.5.1 Photocatalysis

One of titania's most important and most investigated uses is as a photocatalyst for the degradation of organic molecules[10], including acetic acid, methanol[20, 21], ethanol[22], formic acid[23], and others[24-27]. The main driving force behind this line of investigation is the desire to be able to produce hydrogen cheaply and efficiently, in order to have a replacement for the dwindling supply of fossil fuels[28]. There are a number of drawbacks to using titania as a photocatalyst[29]. First of all, it has a relatively large band gap of 3.2 eV. This limits the proportion of sunlight that can be utilised to wavelengths of 388nm or shorter, which is only ~3% of sunlight, all of which is in the UV range. However, it has a very high chemical stability – it is very stable under photocatalytic conditions, including UV light. Semiconductors with smaller band gaps than TiO_2 are generally much less stable under irradiation. Secondly, TiO_2 has poor catalytic efficiency, due to the high degree of recombination between photogenerated electrons and holes[30] and recombination of the dissociated molecules at the surface. This, however, can be overcome by introducing various dopants, such as palladium or gold[31], into the TiO_2 lattice to either shift the Fermi level, decreasing the band-gap[31] or to introduce intra-band gap states, which allow activation by visible light. Furthermore, it is possible to create titanium dioxide with a very high surface area, which is not true of all oxides.

1.6 Catalysis by palladium

One of the largest uses of palladium today is in catalytic converters, where it is used for CO oxidation[32, 33] and NO reduction[34-36]. It has also been extensively studied as a catalyst for methanol dissociation and synthesis, both on single crystals[37, 38] and supported on several different substrates[39-41]. It has been found to be an important catalyst to decompose methanol to CO and H_2 via a methoxy species[42].

The use of Pd in CO oxidation was studied by Fernandez-Garcia and co-workers[43]. They studied the CO + O_2 reaction on alumina, ceria and a mixed cerium/aluminium oxide, finding that the interaction between the ceria and palladium is important. Ceria was shown to decrease the onset of the reaction by ~130 K compared to alumina, due to an enhanced activation of both reactant molecules. This was thought to be because the ceria support formed Pd^0 at temperatures of 298 K which facilitated CO oxidation and O_2 activation.

As previously mentioned, palladium has also been studied as a catalyst for the reduction of NO by both CO[35] and CH_4[34]. Again, the importance of the oxidation state of palladium was highlighted in these studies. The presence of PdO was found to strongly decrease the CO and NO binding energy on supported Pd catalysts, as indicated by the lowered temperature of the TPD peak maximum.

An important use of Pd is in the synthesis of vinyl acetate monomer (VAM)[44]. The process involves the reaction of ethene and acetic acid with oxygen[44]:

$CH_3COOH + C_2H_4 + \frac{1}{2} O_2 \rightarrow$ 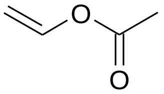 $+ H_2O$

Vinyl acetate is an important petrochemical intermediate – it can be polymerised to polyvinyl acetate or other polymers, which are used in the manufacture of adhesives, paints and coatings[44, 45]. The catalyst is typically either a supported palladium or palladium-gold bimetallic system[46]. The synthetic process was originally based on a homogenous catalyst, but now has been almost completely substituted by a heterogeneous process[47-49]. There is debate about whether the Pd in the active site for VA synthesis is present as Pd^0 or Pd^{2+} [45]. VAM has been synthesised on a Pd(111) single crystal from acetic acid, oxygen and ethylene[50]. There have been two mechanisms for this reaction on the Pd(111) surface. Moiseev suggested that the first step is dehydrogenation of ethene forming an intermediate on the surface, which then binds with surface bound acetate to form VAM[51], whereas Samanos suggested that ethene couples directly with adsorbed acetate, which then undergoes β-hydride elimination to give vinyl acetate[49]. Gao recently used reflection-absorption infrared spectroscopy to show that the Samanos pathway seems the more likely of the two[52].

Palladium is also widely used as a catalyst in pharmaceuticals. There are a variety of reactions, but three of the most popular reaction types are the Heck reaction[53], the Suzuki[54], Negishi[55] and Kumada coupling reactions, and the Sonogashira reaction[56].

1.7 Catalysis by gold

Up until as recently as the 1980s, gold catalysis was considered unremarkable, and gold itself was thought to be too stable and too unreactive, and therefore completely unsuitable as a catalyst.

This all changed, however, with two seminal findings by Haruta[57] and Hutchings[58] in the 1980s. Hutchings found that gold was the best catalyst for acetylene hydrogenation[58], which is an important industrial process to produce vinyl chloride, a hugely important petrochemical. This chemical is used in the production of polyvinyl chloride (PVC)[59] and is produced on a huge scale – 31.1 million tonnes were produced in 2000[60]. At the time, mercuric chloride was used as the catalyst, which has since been superseded due to its environmental problems. Hutchings identified a trend between standard electrode potential and catalytic activity and predicted that Au^{3+} would be the best catalyst for acetylene hydrogenation[61].

At almost the same time, Haruta discovered that supported gold nanoparticles had an extremely high catalytic activity for the oxidation of carbon monoxide at temperatures below 0°C[57]. CO oxidation has important environmental applications, and is also useful for CO gas sensors.

Since then, there has been an explosion of interest in gold catalysis. In 2008 alone there were over 1200 papers and patents published[62] and the number of reactions that gold is a viable catalyst for has increased. It has since been shown to be an excellent catalyst in the epoxidation of propylene to propylene oxide[63], the oxidation of alcohols to acids[64] and the direct synthesis of hydrogen peroxide from oxygen and hydrogen[65].

1.8 Catalysis by supported bimetallic Au-Pd nanoparticles

Alloys often show unique properties compared to the corresponding component metals[66, 67]. The activity of bimetallic catalysts can typically be related to one (or both) of two effects – ligand (or electronic)[68] and ensemble (or geometric)[69]. “Ligand effects” is the name given to the electronic interactions between the two metals, such as changes to the electrons in the d-band or charge redistribution which arise from metal-metal bonding, which may affect the reactivity of the catalyst. “Ensemble” refers to the number of active sites on the surface required for a particular reaction[69]. Metal alloys may have different available active sites from their component parts, affecting their catalytic activity. Geometric effects may also manifest themselves in changes to the geometry of the metals themselves, for example in changes to the interatomic distances in the bimetallic particles.

Bimetallic catalysts may be categorised into the following types[70]:

- Core-shell structure – where one metal overlayer completely covers the other metal, covering all active sites. Reactivity can be strongly affected by the electronic interaction between the two metals and the geometric effect caused by a mismatch in the lattice.

- Alloyed structure – when the two metal atoms have a homogenous distribution in the surface on one particle. Both metals may be active in the surface. The two metals may interact with each other in such a way that leads to intermediate reactivity characteristics.
- Supported cluster structure – where clusters of one metal are supported on another. An example is the “crown-jewel” structure, where one precious metal is supported on other, cheaper metal atoms. This can give rise to strong electronic interactions, modifying the electronic state of the primary catalytic component and improving its catalytic properties.

Au-Pd catalysts are used in a number of applications. There has recently been a large amount of interest in their use in the synthesis of hydrogen peroxide from H_2 and O_2. Hutchings investigated the synthesis of hydrogen peroxide by the oxidation of hydrogen[71]. Supported Au was found to be very selective; however, adding Pd lead to a huge improvement in catalytic activity.

Au-Pd bimetallic catalysts are also used for the industrial production of vinyl acetate monomer via the acetoxylation of ethylene. The addition of Au to Pd significantly enhances its selectivity, activity and stability[45]. However, the details of this promotional effect are not completely understood. It’s thought that the role of the gold is to isolate single Pd sites that facilitate the coupling of the necessary surface species to give the desired reaction, whilst inhibiting the formation of undesirable by-products (CO, CO_2 and surface carbon)[70].

Au-Pd alloys have also been shown to have good activity for the hydrodesulphurisation of thiophene[72]. Adding gold to the palladium catalyst increased hydrodesulphurisation activity. This was thought to be due to the formation of Au_xPd_y clusters which inhibited the formation of palladium sulphide.

1.9 Aims of this work

The main aims of this work were to investigate the growth of palladium thin films on a titanium dioxide single crystal, the interaction between palladium thin films and palladium nanoparticles with $TiO_2(110)$ (especially with a view to finding out more about the "SMSI" effect), the formation of gold-palladium core-shell structures on $TiO_2(110)$ and the reactivity of these Au-Pd structures on $TiO_2(110)$ with small organic molecules.

1.10 Outline of the Thesis

Chapter 1 provides a background to this work, especially with regards to surface science and catalysis. It also provides details of the reactions catalysed by gold, palladium or gold/palladium bimetallics.

Chapter 2 gives detailed descriptions and theoretical background of the techniques used in this work, as well as details of the methods used during the practical work and of any formula used for data analysis.

Chapter 3 concerns the surface of the $TiO_2(110)$ single crystal and it's interaction with palladium. The growth of palladium on differently prepared TiO_2 surfaces is investigated, as well as the SMSI effect between palladium and $TiO_2(110)$ on annealing.

Chapter 4 is about Au on $TiO_2(110)$ and considers whether there is an SMSI effect between gold and $TiO_2(110)$. It also looks at the interaction between gold and palladium and the SMSI effect between these bimetallics and the $TiO_2(110)$ surface.

Chapter 5 covers the reactivity of $TiO_2(110)$, Pd/$TiO_2(110)$, Au/$TiO_2(110)$ and Au-Pd/$TiO_2(110)$ with several small organic molecules, including ethanol, formic acid and acetic acid.

Chapter 6 concludes and summarises the main findings of this work, together with recommendations for further work following on from that reported here.

1.11 References

1. J. Berzelius, *Edinburgh New Philosophical Journal*, 1836, **21**.
2. M. Bowker, *The Basis and Applications of Heterogeneous Catalysis*, Oxford University Press, 1998.
3. M. Boudart, *Topics in Catalysis*, 2000, **13**, 147.
4. G. Attard and C. Barnes, *Surfaces*, OUP Oxford, Oxford, 1998.
5. "Bravais lattice," taken from http://en.wikipedia.org/wiki/Bravais_lattice.
6. C. L. Pang, R. Lindsay and G. Thornton, *Chemical Society Reviews*, 2008, **37**, 2328.
7. M. A. Henderson, *Surface Science Reports*, 2011, **66**, 185.
8. Z. Dohnalek, I. Lyubinetsky and R. Rousseau, *Progress in Surface Science*, 2010, **85**, 161.
9. A. G. Thomas and K. L. Syres, *Chemical Society Reviews*, 2012, **41**, 4207.
10. U. Diebold, *Surface Science Reports*, 2003, **48**, 53.
11. C. L. Pang, R. Lindsay and G. Thornton, *Chemical Reviews*, 2013, **113**, 3887.
12. D. Brinkley, M. Dietrich, T. Engel, P. Farrall, G. Gantner, A. Schafer and A. Szuchmacher, *Surface Science*, 1998, **395**, 292.
13. S. C. N, *Heterogeneous Catalysis in Industrial Practice*, (New York: McGraw-Hill), 2nd edn., 1991.
14. H. Selhofer and R. Muller, *Thin Solid Films*, 1999, **351**, 180.
15. Y. V. Pleskov, *Russian Journal of Electrochemistry*, 1999, **35**, 1137.
16. X. L. Lu, Z. F. Qin, M. Dong, H. Q. Zhu, G. F. Wang, Y. B. Zhao, W. B. Fan and J. G. Wang, *Fuel*, 2011, **90**, 1335.
17. G. C. Bond, *Catalysis Today*, 2002, **72**, 5.
18. A. Thetford, G. J. Hutchings, S. H. Taylor and D. J. Willock, *Proceedings of the Royal Society a-Mathematical Physical and Engineering Sciences*, 2011, **467**, 1885.
19. A. Fujishima and K. Honda, *Nature*, 1972, **238**, 37.
20. M. Bowker, D. James, P. Stone, R. Bennett, N. Perkins, L. Millard, J. Greaves and A. Dickinson, *Journal of Catalysis*, 2003, **217**, 427.
21. M. M. Shen and M. A. Henderson, *Journal of Physical Chemistry Letters*, 2011, **2**, 2707.

22. J. Arana, J. M. Dona-Rodriguez, O. Gonzalez-Diaz, E. T. Rendon, J. A. H. Melian, G. Colon, J. A. Navio and J. P. Pena, *Journal of Molecular Catalysis a-Chemical*, 2004, **215**, 153.
23. M. Bowker, P. Stone, R. Bennett and N. Perkins, *Surface Science*, 2002, **511**, 435.
24. Y. K. Kim and C. C. Hwang, *Surface Science*, 2011, **605**, 2082.
25. P. Sawunyama, A. Fujishima and K. Hashimoto, *Langmuir*, 1999, **15**, 3551.
26. J. Arana, A. P. Alonso, J. M. D. Rodriguez, G. Colon, J. A. Navio and J. P. Pena, *Applied Catalysis B-Environmental*, 2009, **89**, 204.
27. J. Arana, J. L. M. Nieto, J. A. H. Melian, J. M. D. Rodriguez, O. G. Diaz, J. P. Pena, O. Bergasa, C. Alvarez and J. Mendez, *Chemosphere*, 2004, **55**, 893.
28. H. Bahruji, M. Bowker, P. R. Davies, L. S. Al-Mazroai, A. Dickinson, J. Greaves, D. James, L. Millard and F. Pedrono, *Journal of Photochemistry and Photobiology a-Chemistry*, 2010, **216**, 115.
29. M. Bowker, *Green Chemistry*, 2011, **13**, 2235.
30. B. P. Xie, Y. Xiong, R. M. Chen, J. Chen and P. X. Cai, *Catalysis Communications*, 2005, **6**, 699.
31. G. R. Bamwenda, S. Tsubota, T. Nakamura and M. Haruta, *Journal of Photochemistry and Photobiology a-Chemistry*, 1995, **89**, 177.
32. M. Bowker, I. Z. Jones, R. A. Bennett and S. Poulston, *Catalysis and Automotive Pollution Control Iv*, 1998, **116**, 431.
33. I. Z. Jones, R. A. Bennett and M. Bowker, *Surface Science*, 1999, **439**, 235.
34. R. Burch and A. Ramli, *Applied Catalysis B-Environmental*, 1998, **15**, 49.
35. M. Valden, R. L. Keiski, N. Xiang, J. Pere, J. Aaltonen, M. Pessa, T. Maunula, A. Savimaki, A. Lahti and M. Harkonen, *Journal of Catalysis*, 1996, **161**, 614.
36. I. V. Yentekakis, R. M. Lambert, M. Konsolakis and V. Kiousis, *Applied Catalysis B-Environmental*, 1998, **18**, 293.
37. S. M. Francis, J. Corneille, D. W. Goodman and M. Bowker, *Surface Science*, 1996, **364**, 30.
38. J. L. Davis and M. A. Barteau, *Surface Science*, 1988, **197**, 123.
39. D. T. Wickham, B. W. Logsdon, S. W. Cowley and C. D. Butler, *Journal of Catalysis*, 1991, **128**, 198.
40. A. Berko, J. Rasko, F. Solymosi, G. A. Somorjai, J. H. Block and D. Chadwick, *New Frontiers in Catalysis, Pts a-C*, 1993, **75**, 359.

41. M. L. Poutsma, L. F. Elek, P. A. Ibarbia, A. P. Risch and J. A. Rabo, *Journal of Catalysis*, 1978, **52**, 157.
42. E. Demirci and A. Winkler, *Journal of Vacuum Science & Technology A*, 2008, **26**, 78.
43. M. Fernandez-Garcia, A. Martinez-Arias, L. N. Salamanca, J. M. Coronado, J. A. Anderson, J. C. Conesa and J. Soria, *Journal of Catalysis*, 1999, **187**, 474.
44. M. Bowker, C. Morgan and J. Couves, *Surface Science*, 2004, **555**, 145.
45. D. Kumar, M. S. Chen and D. W. Goodman, *Catalysis Today*, 2007, **123**, 77.
46. M. Bowker, C. Morgan and V. P. Zhdanov, *Physical Chemistry Chemical Physics*, 2007, **9**, 5700.
47. S. Nakamura and T. Yasui, *Journal of Catalysis*, 1970, **17**, 366.
48. S. Nakamura and T. Yasui, *Journal of Catalysis*, 1971, **23**, 315.
49. B. Samanos, P. Boutry and Montarna.R, *Journal of Catalysis*, 1971, **23**, 19.
50. Y. F. Han, D. Kumar, C. Sivadinarayana and D. W. Goodman, *Journal of Catalysis*, 2004, **224**, 60.
51. Moiseev, II, M. N. Vargaftik and J. K. Syrkin, *Doklady Akademii Nauk Sssr*, 1960, **133**, 377.
52. W. T. Tysoe, F. Gao, Y. L. Wang, F. C. Calaza and D. Stacchiola, *Abstracts of Papers of the American Chemical Society*, 2007, **233**.
53. I. P. Beletskaya and A. V. Cheprakov, *Chemical Reviews*, 2000, **100**, 3009.
54. N. Miyaura, K. Yamada and A. Suzuki, *Tetrahedron Letters*, 1979, **20**, 3437.
55. A. O. King, N. Okukado and E. I. Negishi, *Journal of the Chemical Society-Chemical Communications*, 1977, 683.
56. K. Sonogashira, *Journal of Organometallic Chemistry*, 2002, **653**, 46.
57. M. Haruta, T. Kobayashi, H. Sano and N. Yamada, *Chemistry Letters*, 1987, 405.
58. G. J. Hutchings, *Journal of Catalysis*, 1985, **96**, 292.
59. E. Dreher, T. Torkelson and K. Beutel, *Chloroethanes and Chloroethylenes; Ullman's Encyclopedia of Industrial Chemistry*, Wiley-VCH, Weinheim, 2011.
60. K. Weissermel and H.-J. Arpe, *Industrial Organic Chemistry*, Wiley VCH, 2003.
61. B. Nkosi, N. J. Coville and G. J. Hutchings, *Journal of the Chemical Society-Chemical Communications*, 1988, 71.
62. G. J. Hutchings, M. Brust and H. Schmidbaur, *Chemical Society Reviews*, 2008, **37**, 1759.

63. T. Hayashi, K. Tanaka and M. Haruta, *Journal of Catalysis*, 1998, **178**, 566.
64. S. M. Tembe, G. Patrick and M. S. Scurrell, *Gold Bulletin*, 2009, **42**, 321.
65. P. Landon, P. J. Collier, A. J. Papworth, C. J. Kiely and G. J. Hutchings, *Chemical Communications*, 2002, 2058.
66. J. H. Sinfelt, *Bimetallic Catalysts: Discoveries, Concepts and Applications.*, Wiley, New York, 1983.
67. M. Sankar, N. Dimitratos, P. J. Miedziak, P. P. Wells, C. J. Kiely and G. J. Hutchings, *Chemical Society Reviews*, 2012, **41**, 8099.
68. T. Bligaard and J. K. Norskov, *Electrochimica Acta*, 2007, **52**, 5512.
69. J. A. Rodriguez, *"Bimetallic Model Catalysts" in the "Handbook of Heterogeneous Catalysis"*, Wiley-VCH, 2008.
70. X. W. Liu, D. S. Wang and Y. D. Li, *Nano Today*, 2012, **7**, 448.
71. P. Landon, P. J. Collier, A. F. Carley, D. Chadwick, A. J. Papworth, A. Burrows, C. J. Kiely and G. J. Hutchings, *Physical Chemistry Chemical Physics*, 2003, **5**, 1917.
72. A. M. Venezia, V. La Parola, V. Nicoli and G. Deganello, *Journal of Catalysis*, 2002, **212**, 56.

Chapter 2 – Experimental

Chapter 2 Contents

2.1 Introduction

This chapter describes the materials and methods used throughout this research. The single crystal catalysts were characterised by ion scattering spectroscopy (ISS), low energy electron diffraction (LEED), X-ray photoelectron spectroscopy (XPS), Auger electron spectroscopy (AES) and temperature programmed desorption (TPD).

2.2 Equipment

The experiments were carried out in one of two systems, designated UHV1 and UHV2.

2.2.1 UHV1

UHV1 consists of a custom designed Multiprobe UHV system, made by Omicron. The system consists of four chambers; preparation (P), central (C), analysis (A) and STM. The STM chamber contains the STM equipment and is equipped with a vibration damping tool to minimise noise. The P chamber is equipped with an ion gun to clean the sample, and a resistive heating filament. The C chamber is used for metal deposition and, if required, sample heating. The A chamber is equipped with ISS, XPS and LEED. The sample can be transferred between each of the chambers using manipulators and a magnetic probe and each of the chambers can be isolated using gate valves. Labelled photographs of UHV1 are shown in Figure 2-1 and Figure 2-2 and a schematic is shown in Figure 2-3.

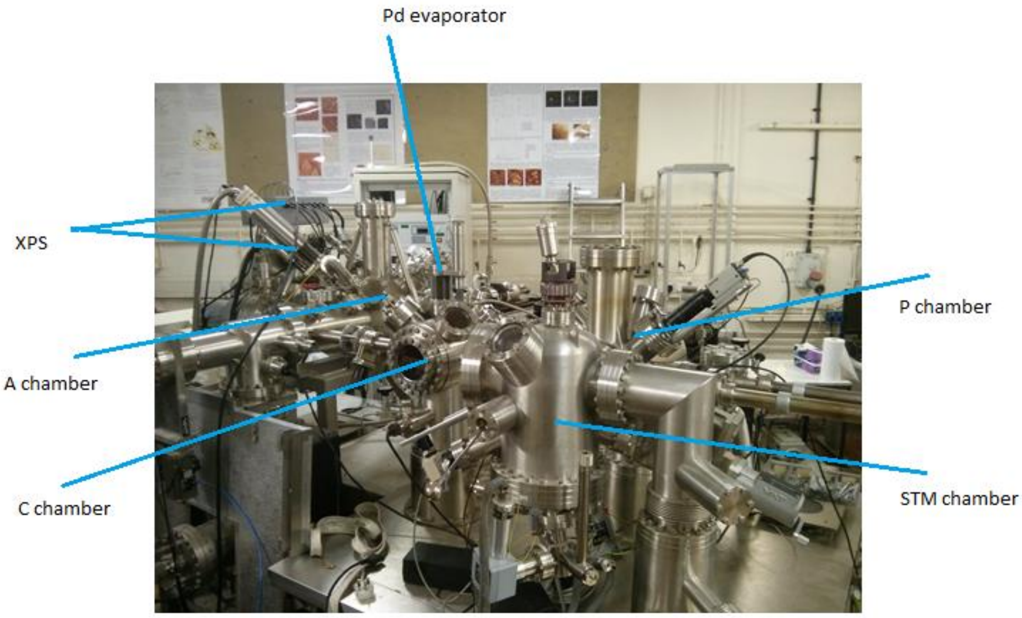

Figure 2-1 - Photo of the front of UHV1

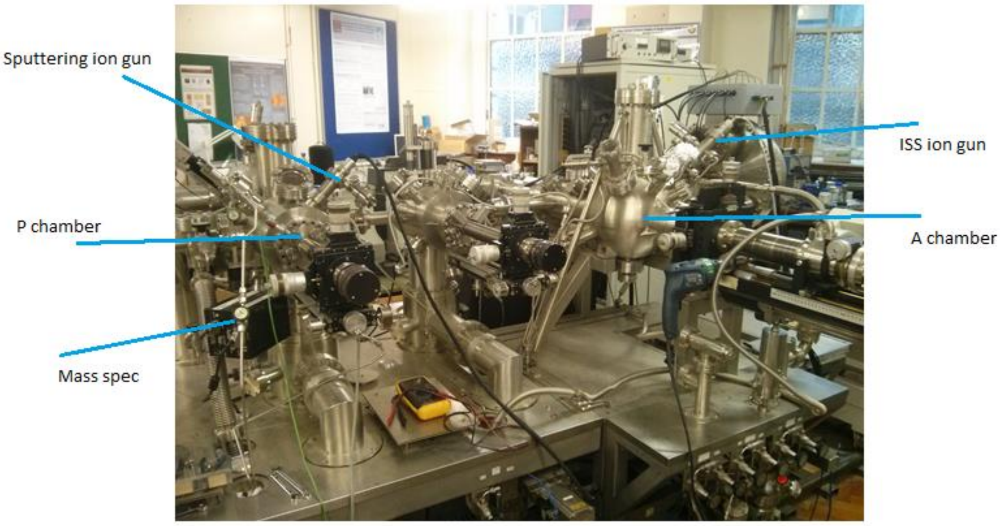

Figure 2-2 - Photo of the back of UHV1

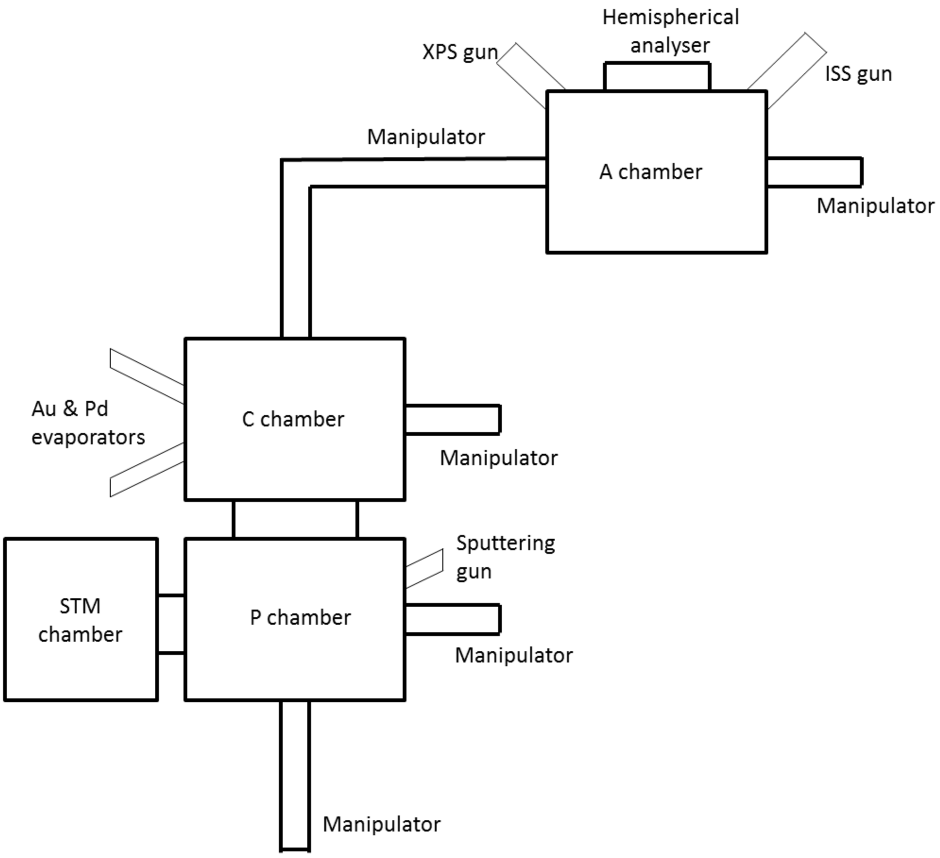

Figure 2-3 - Schematic of UHV1

2.2.2 UHV2

UHV2 consists of a small ultra-high vacuum (UHV) system for TPD measurements. Labelled photographs of the machine are shown in Figure 2-4 to Figure 2-6. The main stainless steel chamber can maintain a base pressure of ~5x10^{-10} mbar. An OCI system was used for LEED and AES. AES were recorded at a beam current of at least 10mA at 2 keV, and LEED measurements were conducted with an electron energy of 80 eV, 100 eV, 110 eV or 120 eV after taking an auger. A Hiden quadrupole mass spectrometer was used for TPD measurements.

The sample was mounted on a tantalum basket which was then supported directly on the W filaments. This had three controllable axes of translation and one of rotation. The temperature was monitored by a thermocouple which was spot welded onto the Ta basket, next to the surface of the sample. For TPD experiments and annealing, organic reactants and gases (e.g. oxygen) were dosed via a leak valve through a stainless steel dosing tube, directed at the sample. The organic reactants were all purified by repeated pump-thaw cycles.

The sample was heated by passing a current through tungsten wire underneath the sample holder.

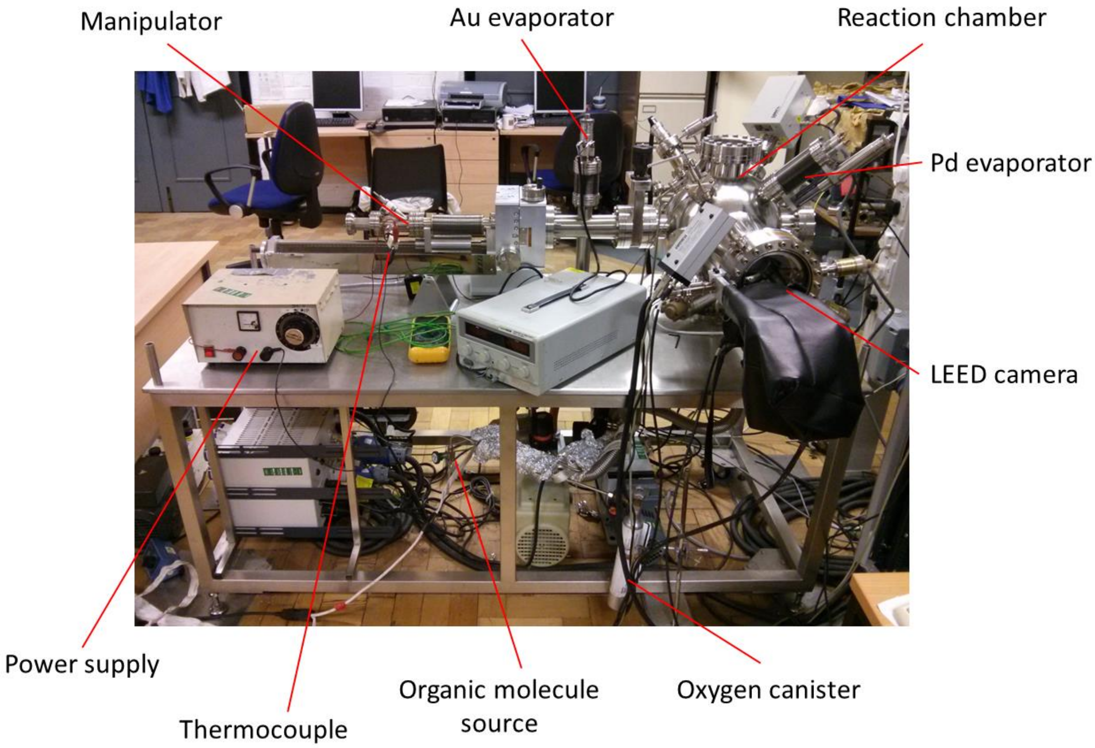

Figure 2-4 - Photograph of the UHV2 machine set up

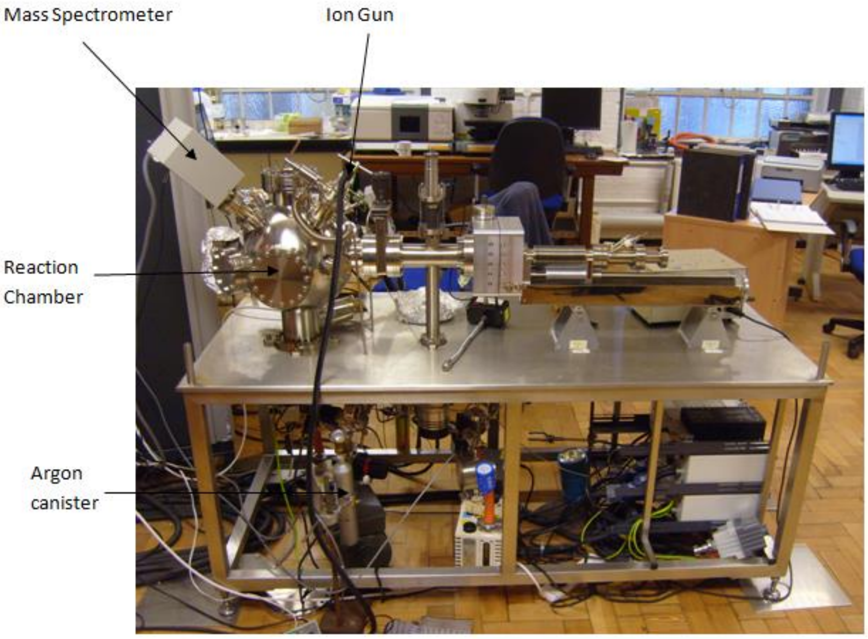

Figure 2-5 - Photograph of the UHV2 machine set up from the opposite side

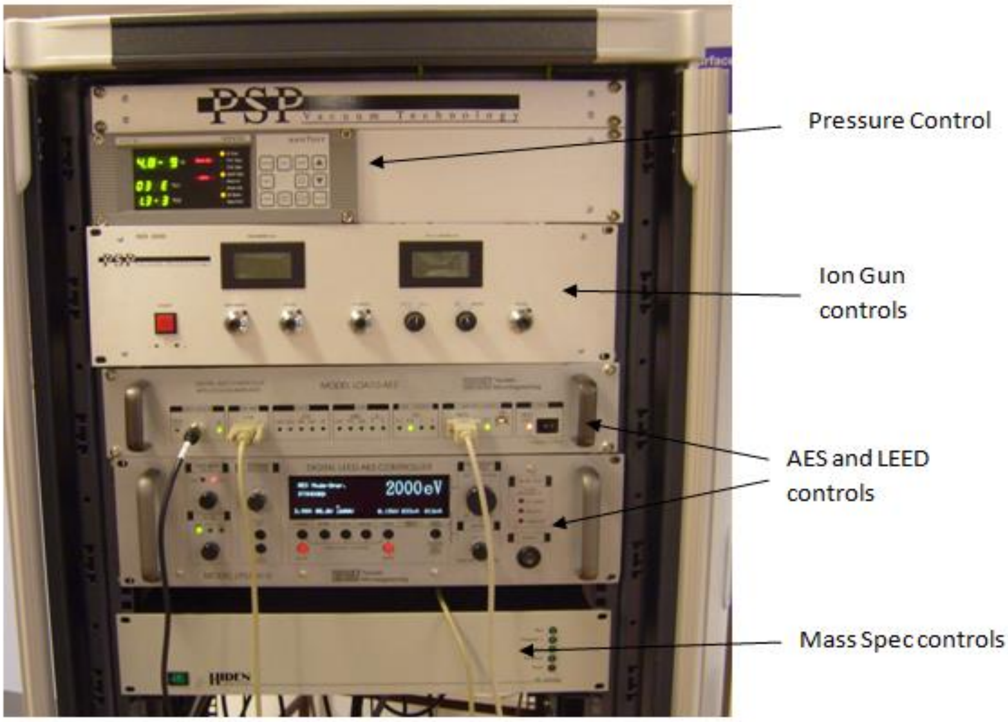

Figure 2-6 - Photograph of the UHV2 machine controls

2.3 Ultra High Vacuum (UHV)

UHV conditions are required so that the electron spectrometers (LEED and XPS) maintain their effectiveness. The electrons emitted from a sample should collide with as few gas molecules as possible on the way to the analyser so that they are not scattered and therefore lost from the analysis[1] i.e. their mean free paths should be much greater than the dimensions of the spectrometer (Table 2-1). A vacuum in the range of 10^{-5}-10^{-6} Torr would be suitable for this. However, there is a second, much more stringent requirement for the vacuum – the techniques used are very sensitive to surface contamination. Since even small amounts of contamination can severely affect the results of an experiment, it is obviously necessary to work under conditions where the rate of contamination is negligible[1]. The rate of contamination of a surface depends upon the rate at which gaseous molecules collide with the surface[2] and the sticking probability, S(θ), of the molecule. The rate of surface bombardment by molecules (Z) is given by the kinetic theory of gases[2]:

$$Z = \frac{P}{(2\pi mkT)^{\frac{1}{2}}}\ \mathrm{cm^{-2}\ s^{-1}} \qquad [2.1]$$

Where P = ambient pressure, in $\mathrm{Ncm^{-2}}$; m = molecular mass, in kg $\mathrm{molecules^{-1}}$; T = absolute temperature, in K; and k = Boltzmann constant, in $\mathrm{JK^{-1}}$.

Assuming S(θ) = 1 (i.e. if a gas molecule hits the surface of the sample, it will always stick), an estimate can be given of the coverage of a gas (for example, CO is a common contaminant) produced at a temperature of 300 K and at pressures of 10^{-6} Torr and 10^{-10} Torr respectively using equation 2.1 (1 Torr = 1.333×10^{-2} $\mathrm{Ncm^{-2}}$).

At 10^{-6} Torr:

$$Z = \frac{1.333 \times 10^{-2} \times 10^{-6}}{\left[2\times\pi\times\left(\frac{28}{1000\times6.02\times10^{23}}\right)\times(1.38\times10^{-23})\times300\right]^{\frac{1}{2}}} \text{ cm}^{-2}\,\text{s}^{-1} \qquad [2.2]$$

$$= 3.83\text{x}10^{14} \text{ cm}^{-2}\text{s}^{-1}$$

Assuming an atomic density of 10^{15}cm^{-2}, the rate of surface contamination by a gas would be:

$$\frac{3.83 \times 10^{14}\ cm^{-2}s^{-1}}{10^{15} cm^{-2}\ per\ monolayer} = 0.383\ monolayers\ s^{-1} \qquad [2.3]$$

Therefore, the time taken to adsorb one monolayer of gas (assuming that the sticking probability is 1) at 10^{-6} Torr = 1/0.382 = 2.6 seconds.

The same calculations performed at 10^{-10} Torr give a rate of surface contamination of 3.83 x10^{-5} monolayers s^{-1}. So in this case, the time taken to adsorb one monolayer of gas at 10^{-10} Torr = 1/3.83x10^{-5} = 26094 seconds, or 7.2 hours. These calculations show that, in order to prevent surface contamination, the ambient pressure needs to be reduced as much as possible. The use of UHV allows the surface to be kept in its clean or otherwise well-characterised condition once produced, for the duration of an experiment[3]. “Ultra High Vacuum” indicates that the pressure has been reduced to below 10^{-9} Torr[2].

Level of vacuum	**Pressure (mbar)**	**Mean free path of electron (m)**
Rough	~1	~5×10^{-5}
Medium	~10^{-3}	~5×10^{-2}
High	~10^{-7}	~50
Ultra-high	~10^{-10}	~5×10^{5}

Table 2-1 - classification of vacuum conditions in relation to pressure and the mean free path of the travelling electrons

2.3.1 Achieving UHV conditions

The UHV machines are made from stainless steel and have viewing ports made from glass. A variety of pumps are used to reduce the pressure to an appropriate level[1]:

- rotary pump – can achieve pressures of 10^{-3}mbar and are used to back the turbomolecular pumps;
- turbomolecular pump – can achieve pressures up to 10^{-9}mbar. Pumping efficiency decreases directly with the molecular weight of the gas, so that the efficiency for hydrogen and helium is not good. The residual gas at UHV is therefore mainly hydrogen.
- ion pump – pump that ionises chemically active gases and removes them from the system, attaining pressures of 10^{-10}mbar.
- titanium sublimation pump – coats the walls of the chamber with a thin reactive film of Ti. Gas molecules then collide with this and adsorb onto the sides of the wall, forming stable products.

All junctions are sealed with copper gaskets in order to keep the vacuum. If a machine is let up to atmospheric pressure (e.g. for maintenance work), it needs to be baked (typically 393 K) with all pumps running in order to remove any atmospheric gases adsorbed on to the chamber walls before use.

2.3.2 Measuring UHV

The system goes through a range of pressures (from atmospheric to UHV) and as such, no one gauge is able to accurately measure pressure over the entire range.

Pirani gauges are used to measure the pressure in the range of $1\text{-}1\text{x}10^{-3}$ mbar and work by measuring the resistance of a heated wire placed within the vacuum system. A current is passed through the filament, generating heat, which is transferred to the surrounding gas molecules. At atmospheric pressure, a lot of gas molecules collide with the wire and so a lot of heat energy is removed. In a vacuum there are fewer molecules – fewer molecules therefore hit the wire, and so less heat is transferred from the wire. As the temperature of the wire increases, the resistance increases. A simple circuit is then used to give a reading of the pressure.

Ionisation gauges are used to measure pressures in the range of $10^{-3}\text{-}10^{-11}$ mbar. A heated filament will produce electrons by thermionic emission. These electrons are then accelerated to an anode grid (the grid has a positive charge, which attracts the electrons away from the filament). They circle the grid, passing through the fine structure several times, before eventually colliding with the grid. These electrons will possess enough energy to ionise gas particles within the anode on contact. These (now positively-charged) ions are attracted to the negatively charged collector and simultaneously repelled by the negatively charged grid. The number of ions to collide with the detector is directly proportional to the number of molecules within the vacuum system, so that measuring the ion current can give a direct reading of the pressure.

2.4 Sample preparation

2.4.1 Cleaning the sample

"'Clean' is defined as the state of a surface in which the techniques of XPS, ISS and AES cannot detect characteristic spectral features from any elements, except those constituting the bulk composition of the sample, above the limits of detection[1].”

The catalyst surface is cleaned by sputtering with argon (Ar^+) from an ISIS ion gun at a pressure of $5x10^{-6}$ mbar and 1 KeV (ion source, PSP vacuum, ISIS 3000), with a beam current of 40mA. When the beam of argon ions hits the crystal surface, it “knocks off” surface atoms, that are then either deposited on to the walls of the chamber, or are pumped out of the chamber. This method removes both impurities and atoms of the crystal itself from the surface, so care should be taken to not sputter for extended periods of time.

Sputtering usually leaves behind a very rough, disordered surface, so the surface is then annealed to high temperatures to smooth the surface and restore order.

The titania crystal was cleaned using a series of sputtering and annealing cycles. Sputtering was typically from 20-60 minutes at room temperature, and annealing was typically at temperatures up to 873 K for periods of 10-20 minutes. This process was repeated several times, until ISS and XPS no longer detected any impurities.

2.4.2 Metal Vapour Deposition

Metal atoms are deposited onto the sample using metal vapour deposition (MVD) under UHV. A filament coated in the desired metal is heated to its melting point, releasing its vapour that then travels in a straight line towards the sample.

For Au deposition a piece of Au foil was wrapped around a 0.2mm diameter W wire which was coiled then heated under UHV to form a Au bead. For Pd deposition a length (~40mm) of 0.125mm diameter Pd wire was coiled tightly around a length (~100mm) of 0.25mm diameter W wire which was then adjusted to a coil of ~3mm in diameter. In both instances, a current of 2.9-3.1A was passed through the tungsten wire.

2.4.3 Dosing reactants

Both machines are equipped with facilities to introduce reactants into the system. In the cases where these reactants are liquids (e.g. formic acid, methanol) at room temperature, they were purified by repeated cycles of freeze-pump-thaw prior to use.

2.5 Ion Scattering Spectroscopy (ISS)

ISS is a surface sensitive technique, also referred to as Low Energy Ion Scattering (LEIS), which gives information on the elements present on the surface of a sample. The technique does not have the wide range of applications of AES/XPS, but it does have the unique advantage of giving information on the outermost atom layer only[1]. It can also give information on the adatom site position by varying the polar and azimuthal angles of the interrogating ion beam with respect to a single crystal target[1].

LEIS has been used by various groups to study growth, mainly by exploiting the surface sensitivity to obtain first layer information[4] and using shadowing features of this technique to isolate backscattered yield from specific surface layers[5].

2.5.1 Scattering and collision theory

A monoenergetic beam of noble gas ions (He^+ , Ne^+, Ar^+), in the range of 0.5-3.0 keV is directed at the surface in a well-defined direction. The incident ion beam hits the surface of the sample at an angle α to the surface normal (Figure 2-7)[6]. The particles are then backscattered; the energy of the primary scattered ions is measured at a well-defined scattering direction[3] – the only ones analysed are those that are backscattered into a certain solid angle element $d\Omega$. Projectiles are scattered from surface atoms, almost exclusively by binary collisions (a single collision of the He^+ ion with the surface).

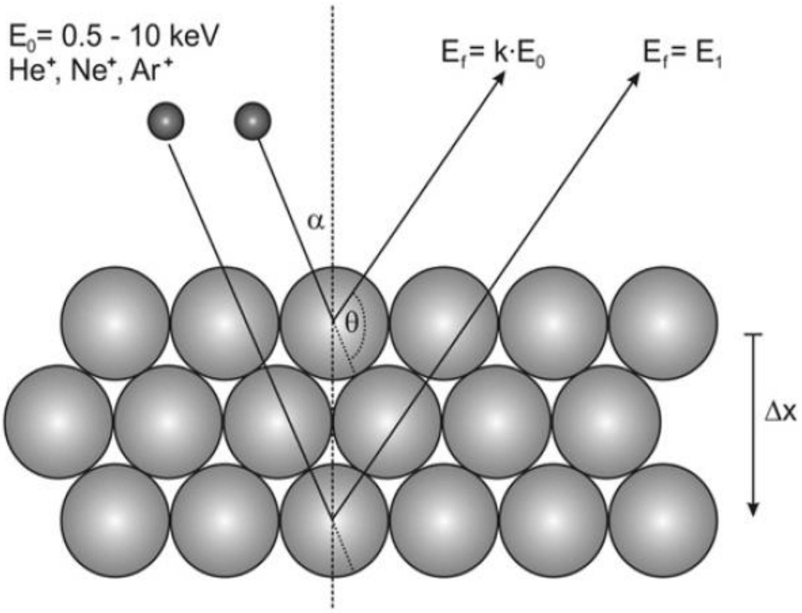

Figure 2-7 - illustration of an ISS experiment[6]

Using equations 2.6 and 2.7, the composition of the surface can be determined.

$$\frac{E_1}{E_0} = \frac{1}{(1+A)^2}\left[\cos\theta_1 \pm (A^2 - \sin^2\theta_1)^{\frac{1}{2}}\right]^2 \qquad [2.6]$$

$$A = \frac{M_2}{M_1} \qquad [2.7]$$

The incident ion of energy E_0 and mass M_1 strikes a surface atom of mass M_2 and is therefore scattered through an angle of θ_1. E_0, M_1 and θ_1 are fixed so that the energy of the scattered particle, E_1, gives the mass of the surface atoms, M_2. The positive sign in equation 2 is for $A > 1$, and both signs apply for $A < 1$. The equation can also be represented as a graph, as seen in Figure 2-8.

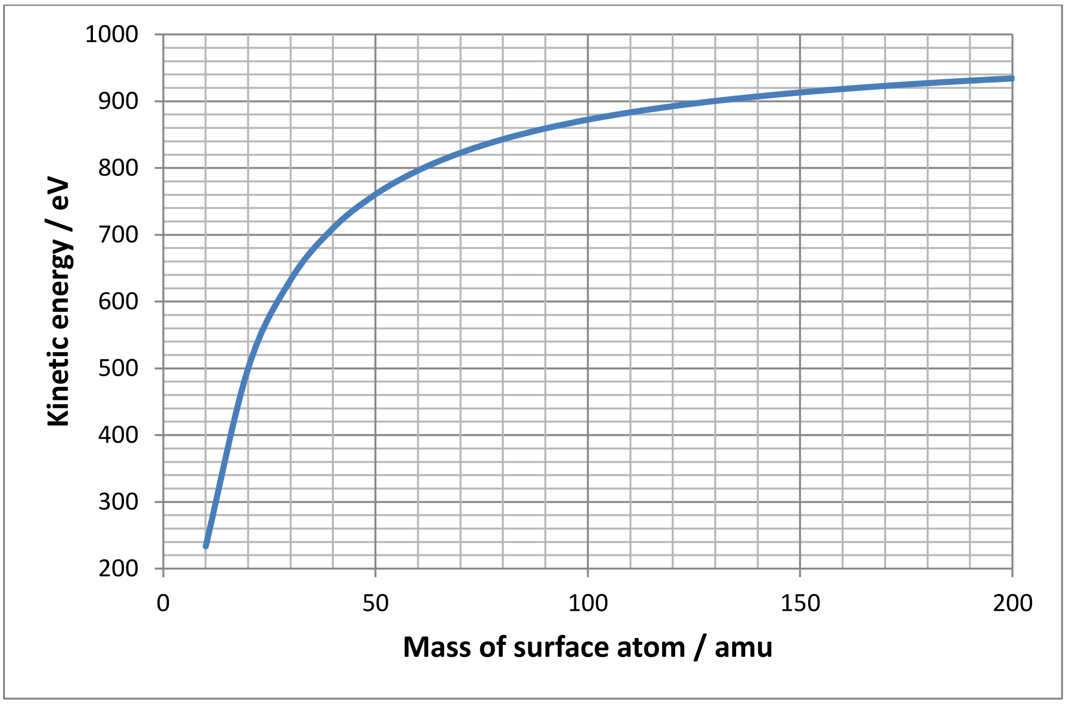

Figure 2-8 - Plot of energy of the scattered particles (E_1) against mass of scattering atoms (M_2). Calculated using equation 2.6 with θ = 135° as in UHV1

The atom on the surface which is struck simultaneously gains energy, recoiling with energy E_2 at an angle θ_2:

$$\frac{E_2}{E_0} = \frac{4A}{(1+A)^2} \cos^2\theta_2 \qquad [2.8]$$

Energy conservation requires that $E_0 = E_1 + E_2$.

The only elements that ISS are unable to directly detect in backscattering are hydrogen and helium. This is because, as can be seen in equation 2.6, backscattering (θ > 90°) for a mass ratio, $q = M_2/M_1 < 1$ is not possible[6].

2.5.2 Instrumentation

The instrumental requirements for ISS are an ion source, an energy analyser, a detector and a sample manipulator, to control the scattering angle. The monoenergetic ion beam is produced by the ion gun; thermal electrons are emitted from a Th-Ir filament. These travel through a volume of a noble gas (in this case He), ionising the neutral particles, to an anode where they are accelerated to the filament (cathode). The ions are subsequently extracted from the source volume and accelerated to the pre-selected kinetic energy. An ion-optic lens focuses the ions into a beam with a diameter of 100-800µm FWHM, which is then focused onto the target.

2.5.3 ISS Spectra

A typical ISS spectrum is shown in Figure 2-9. Only single collisions contribute to the peak. Multiple scattering events are minimised by the neutralisation process – when an inert gas ion approaches a surface, charge transfer from the valence electrons of the surface can occur leading to neutralisation of the ion and its subsequent loss from the scattered ion signal[3]. Ions that penetrate below the top layer of atoms suffer a very high neutralisation probability. Although neutralisation has its benefits, it also has a pronounced effect on the single scattering yield, which makes determining the absolute composition difficult. Another effect that makes ISS extremely surface specific is elastic shadowing. The surface atoms of a given sample cast a "shadow cone" over the atoms beneath it. The width of this shadow cone is approximately 1.5Å, which is comparable to interatomic spacings. This means that the top atomic layer will usually shadow most of the second atomic layer and all of the deeper atomic layers.

The varying energies of the ion beam and the scattering angle both have an effect on the width of the ISS peak. At low scattering angles the resolution is poor, as the energy loss is low so that all scattered peaks are bunched up at the high energy end of the spectrum close to E_0.

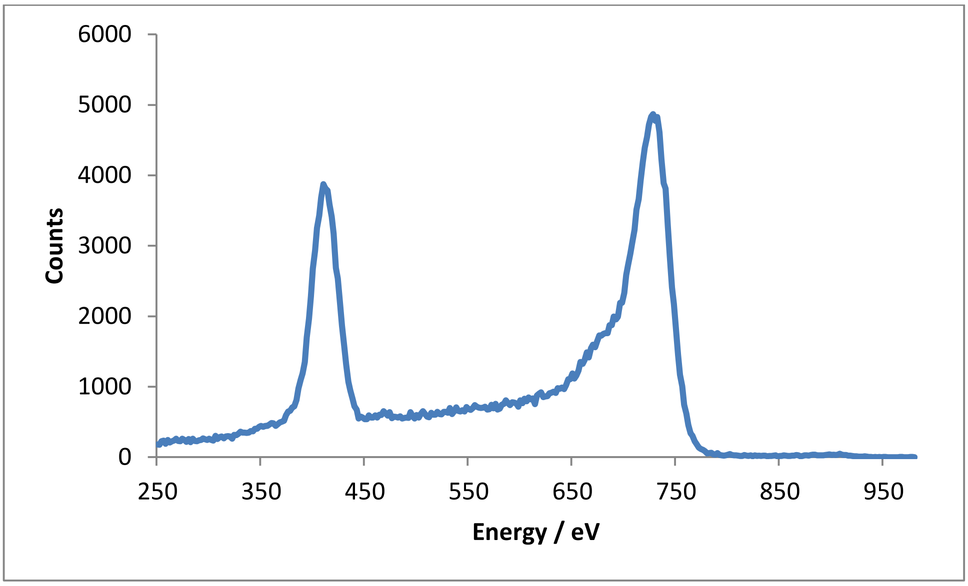

Figure 2-9 - An ISS spectra of clean TiO_2; O peak at 400 eV, Ti peak at 740 eV

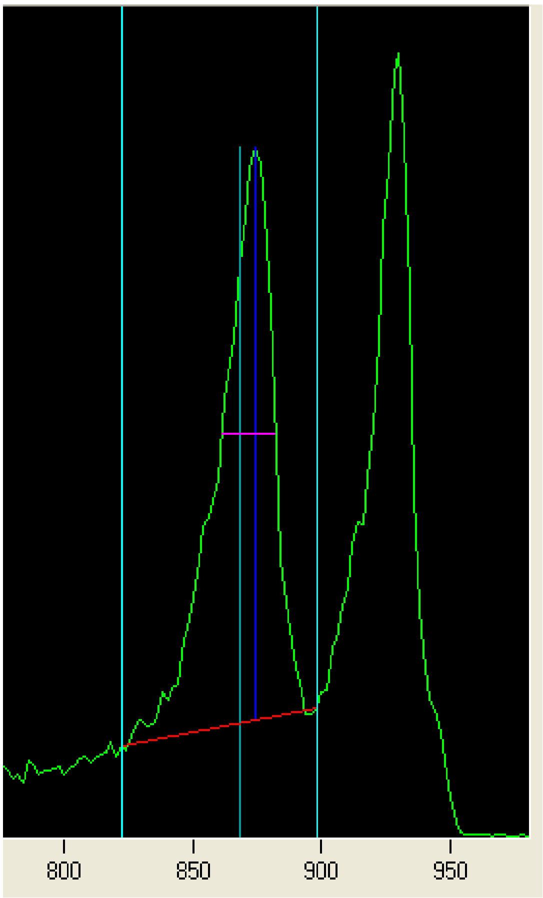

Figure 2-10 - ISS spectrum showing how peak area was measured in order to calculate peak to peak ratios

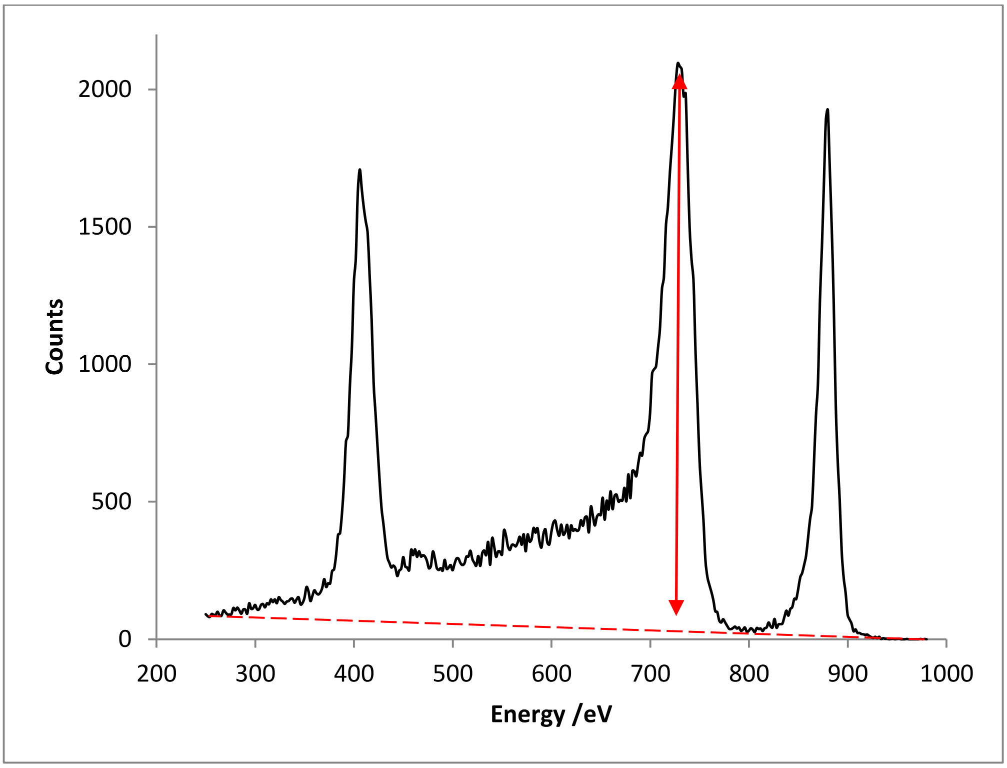

Figure 2-11 - ISS spectrum showing how peak heights were measured

Measurement of peak-to-peak ratios in ISS is a simple way to quantify the relative surface concentrations of any species present on the surface. In order to measure peak area, the "perpendicular drop" method is used – two vertical lines are drawn from the left and right bounds of the peak down to the x-axis. The total area bound by the signal curve, the x axis (y=0) and the two vertical lines is measured, as shown in Figure 2-10. Measurement of peak heights was slightly more complicated. The background level in ISS spectra tend to decrease from low to high kinetic energy, complicating the measurement of peak heights to a small extent. To ensure consistency in the measurement of peak heights, an approximate linear background was applied, as shown in Figure 2-11. Peak heights were then measured from the peak to this line.

2.6 X-ray Photoelectron Spectroscopy (XPS)

2.6.1 Basic principles

XPS is a surface sensitive technique, used to establish the composition of the outer few atom layers for all elements except hydrogen and helium[7]. Spectra are obtained by irradiating the sample with a monochromatic beam of X-rays – typically Al or Mg Kα is used[1]. This causes photoemission from both core and valence levels of surface atoms into the vacuum[2]. “Core levels” are the inner quantum shells. They do not participate in chemical bonding, whereas “valence levels,” those electrons in the more weakly bound, partially-filled outer quantum shells, do. The core electrons are largely insensitive to their surroundings when condensed into the solid phase and retain binding energies, E_B, that are signatures of that atom, i.e. the number of protons in the nucleus. The photoelectron kinetic energy, E_K, is given by Einstein’s law[8]:

$$E_K = h\nu - (E_B + \phi), \qquad [2.9]$$

where $h\nu$ is the energy of the incident radiation and ϕ is the work function of the solid. In order for electron emission to occur from the solid, the photon energy must be greater than the work function of the solid (i.e. $h\nu > \phi$)[2]. The work function is defined as the energy required to remove an electron from the highest occupied energy level in the solid, to the “vacuum level.” The vacuum level is the energy of an electron at rest (zero kinetic energy) in a vacuum, such that it has no interaction with neighbouring particles (zero potential energy).

XPS is able to measure the elemental composition, empirical formula, chemical state and electronic state of the elements of the material. It is sensitive to oxidation state[8] – atoms in a high formal positive oxidation state will give XPS peaks at a higher binding energy than the same atom in a low oxidation state.

2.6.2 Koopmans' theorem

If the energy and spatial distribution of the electrons remaining after photoemission are assumed to be exactly the same as in the initial state, the binding energy, E_B, can be equated to the negative orbital energy, ε, of the emitted electron[2]:

$$E_B = -\varepsilon \qquad [2.10]$$

However, in reality, the remaining electrons relax to different energy states after photoemission due to initial and final state effects.

2.6.3 Initial state effects

Initial state effects refer to any change in the atom's "initial state (i.e. it's "ground state") which will then result in a change in the binding energies of the electrons in the atom. This is commonly called the "chemical shift." The charge of the atom involved has a great effect on the binding energy. As the formal oxidation state of the element increases, so will the binding energy of the emitted photoelectrons, i.e. a peak will be seen at a higher binding energy for Ti^{4+} than Ti^{2+}.

2.6.4 Final state effects

This refers to effects that occur after an electron is removed from its shell. When the core hole is created by ionisation, other electrons relax in energy to a lower energy state to partially screen this hole and to make more energy available to the outgoing photoelectrons[3]. This can cause a shift towards lower binding energy in the XPS spectrum. This type of relaxation varies depending on the sample. In metals/conducting samples, the electrons are free to move between atoms to screen the hole created by photo-ionisation, whereas this is not the case in insulators.

There are other processes, known as “shake up” and “shake off” events, which can also occur. In a shake-up event, the outgoing photo-electron is excited to a bound state of the atom. In a shake-off event, the photo-electron is excited to the continuum, i.e. leaving the core and valence levels of the atom, resulting in a doubly ionised state. The shake-up event can give satellite peaks at higher binding energy than the parent peak, whereas shake-off events are not usually observed in the XPS, as the energy is not discrete.

2.6.5 Features of an XPS spectrum

Figure 2-12 shows a wide scan XPS of the clean TiO_2 (110) single crystal surface. Collecting an XPS spectrum usually involves a wide scan over a range of 1100 eV, followed by narrow scans (typically around 25 eV) on any areas of interest. A spectrum has intensity on the y-axis and binding energy on the x-axis.

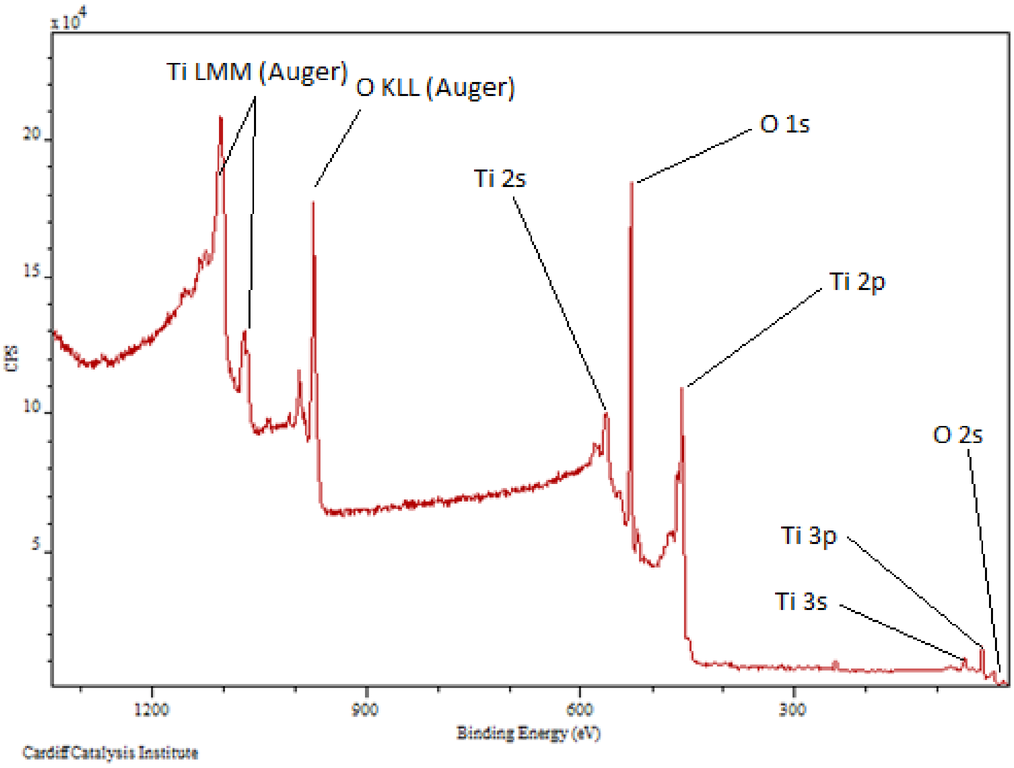

Figure 2-12 - XPS wide scan of a clean TiO_2 (110) single crystal surface

The background of the spectrum is caused by inelastic scattering[1]. This is where the photo-electron suffers an energy loss between photo-emission from an atom in the solid and detection in the spectrometer.

There are two types of peaks present in the XPS – those caused by core-level photoemission and those caused by x-ray excited Auger emission[1] (see the labelled wide scan in Figure 2-12).

As mentioned above, areas of interest are then investigated further with a narrow scan (See Figure 2-13 of a labelled Ti 2p region). This narrow scan usually has a range of 10-50 eV. It will also have a longer dwell time than the wide scan, a larger number of “sweeps” to eliminate noise and the pass energy (energy at which the photo-electrons pass through the analyser) will be decreased.

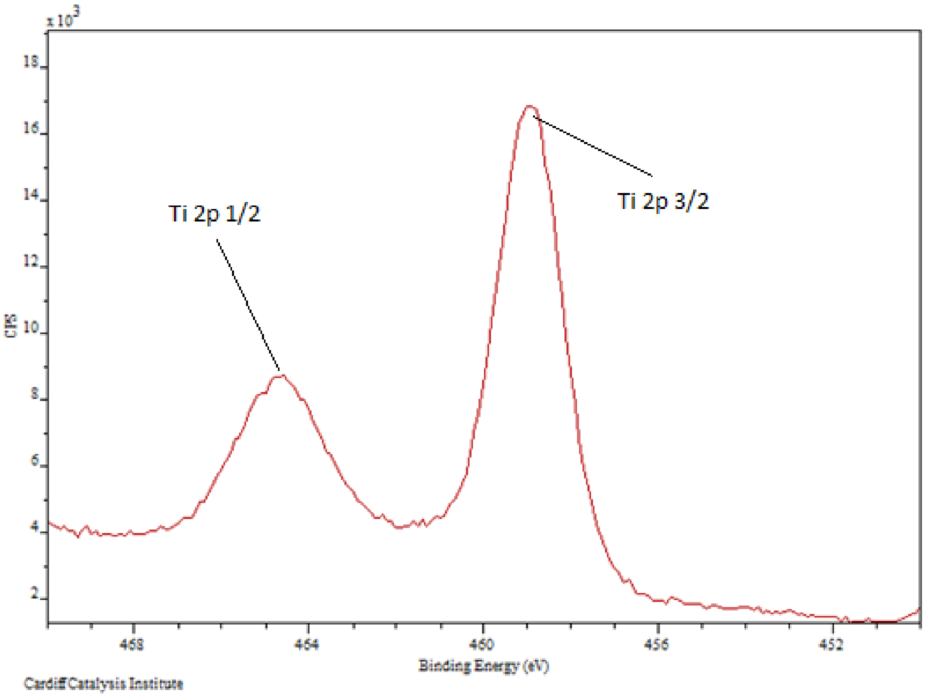

Figure 2-13 - narrow scan of the Ti 2p region

The peaks in Figure 2-12 and Figure 2-13 are labelled according to the shell (the principal quantum number, n. n=1, 2, 3, …) and the orbital (the orbital quantum number, l. l = s, p, d, f, g, h, …) that the electron is emitted from. The subscript (total angular quantum number) is given by the following equation:

$$j = (|l \pm s|), \tag{2.11}$$

where s is the electron spin.

Auger notation is described in detail in section 2.8.2. In summary, Auger notation is as follows; the first letter is the level that is ionised by the electron beam. The second letter indicates the level where the electron is lost from in order to fill the vacancy in the core level. The third letter shows where the Auger electron was emitted from. K, L and M are used for shells with principal quantum number 1, 2 and 3 respectively.

It can be seen that all of the peaks caused by electrons with an orbital angular momentum greater than 1 (i.e. l > 0, for example p, d, f, etc) are split into doublets[2]. This is due to spin-orbit coupling. Before ionisation, the electrons exist in pairs with opposing spin, resulting in a zero net magnetic moment. However, upon photo-ionisation the atom loses an electron and is left with one remaining unpaired electron. This electron's spin angular momentum interacts with its orbital angular momentum. It can either reinforce or oppose this angular momentum, depending on whether it is "spin up" or "spin down." This causes two distinct states to be formed, with two distinct values of j. These two states give rise to a splitting of the primary peak with intensities equal to "2j + 1." For the Ti 2p peak, j can be 1/2 or 3/2. The relative intensities are therefore 1 (2 x ½ +1 = 2) vs 2 (2 x 3/2 +1 = 4), i.e. there is a 2:1 ratio in the intensities of the Ti 2p peaks.

2.6.6 Instrumentation

XPS needs to be carried out in UHV conditions for three reasons. Firstly, the x-ray source can only operate under vacuum. Secondly, photoemitted electrons must be able to travel from the sample to the analyser without encountering gas molecules. Thirdly, the surface being analysed during XPS must avoid being contaminated with other gaseous molecules.

2.6.6.1 X-ray Source[9]

The X-ray gun is a twin anode Dar400 X-ray Source with two separate sources; Mg Kα (1253.6 eV) or Al Kα (1486.6 eV). Electrons are extracted from a heated filament to bombard the selected surface of an anode at high positive potential. The focus electrode and the shape of the nose cone ensure that the electrons hit the anode in the right area. The anode is water-cooled, preventing evaporation of the surface Mg or Al.

2.6.6.2 Analyser assembly[10]

The EA 125 has an electrostatic hemispherical deflection analyser, a multi element universal lens and seven Channeltron electron multipliers, as shown in Figure 2-14.

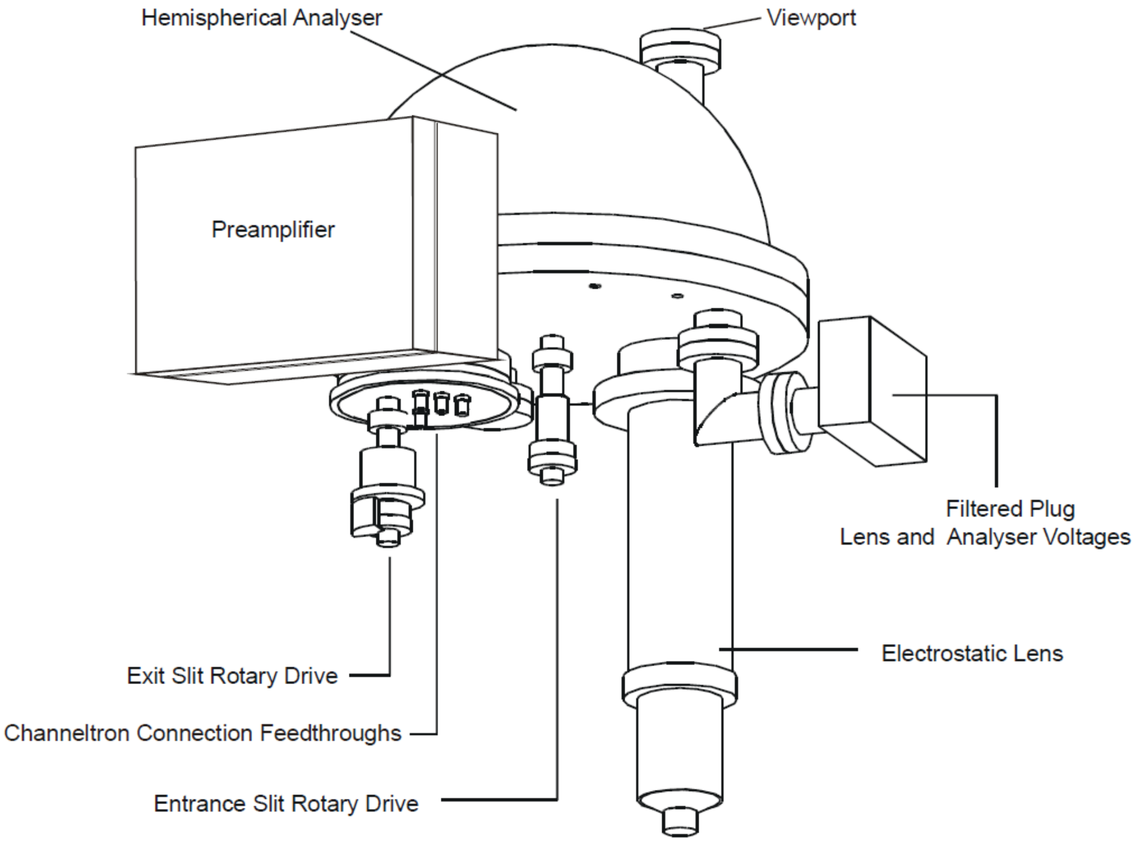

Figure 2-14 - The EA 125 analyser components (cables not shown)[10].

2.6.6.3 Electrostatic input lens

The lens consists of a double lens design, where two lenses are stacked one above the other.

The first lens selects the analysis area (spot size) and angular acceptance of electrons which pass through the analyser. The second lens retards or accelerates the electrons to match the pass energy of the analyser and focuses the electrons on the analyser entrance aperture.

2.6.6.4 Hemispherical Analyser

The hemispherical analyser consists of two concentric hemispheres. A potential, V, is applied between the surfaces, so that the outer is negative and the inner is positive with respect to V_0. This electrostatic field separates electrons by only allowing electrons of a specific kinetic energy (the "pass energy") through to the detector. Electrons with kinetic energies less than the chosen pass energy are attracted to the inner positive hemisphere and neutralised, whilst electrons with a higher energy hit the outer hemisphere and are also lost. Reducing the pass energy will improve the resolution of the spectrum but also lower the intensity.

2.6.6.5 Channeltron Detector

There are seven channel electron multipliers, known as "Channeltrons," which are placed across the exit plane of the analyser. Their function is to amplify the current of a single electron by a factor of 10^8 (see Figure 2-15).

Electrons/ions which arrive at the input of the Channeltron detector generate secondary electrons which are then accelerated down the Channeltron by a positive voltage bias (2-3 kV at the output). These electrons strike the Channeltron wall and progressively produce additional electrons down the Channeltron to output where between 10^7-10^8 electrons arrive. The statistical nature of the multiplication process results in a Gaussian distribution of pulse heights at the output from the Channeltron.

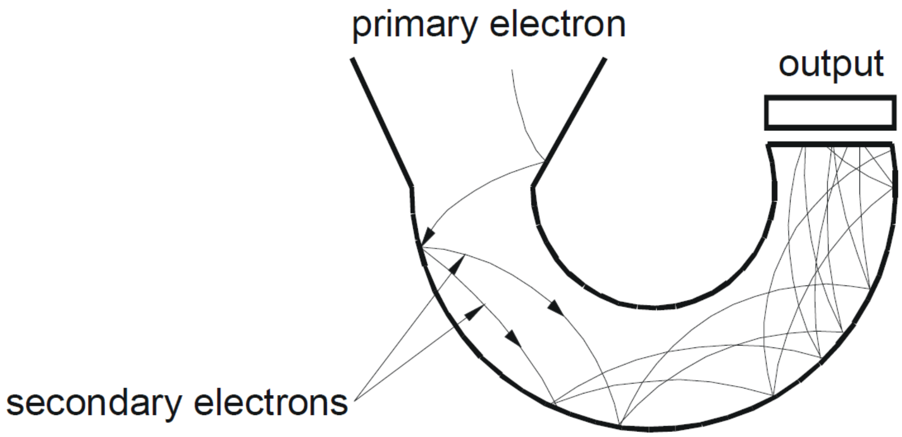

Figure 2-15 - Schematic of electron amplification in the Channeltron[10]

The electron pulse is then routed to the preamplifier which filters out the system noise. The signal is converted to an electronic pulse which is then counted by the computer, where the spectrum is produced.

2.6.7 Quantitative analysis

2.6.7.1 Determining concentration of surface species

The relative intensities of the XPS peaks can be related to the concentration of species on the surface. The measured peak area is dependent on the following variables:

- The photo emission cross section (the probability of photo emission occurring from a particular core level).
- The inelastic mean free path of the photo-emitted electron
- The instrument itself, and how efficient the spectrometer is at detecting electrons as a function of kinetic energy

To determine the peak area, a point either side of the peak is selected, and the software measures the peak area[11]. A small difference in position of these points can lead to a large variation in peak area. Curve fitting may be done when two or more peaks overlap.

A background in the spectra is caused by electrons that have lost energy during emission at binding energies higher than the peak energy. This background is removed before peak measurement. A Shirley background subtraction was used, calculated by the CasaXPS software[11].

Equation 2.12, developed by Carley and Roberts[12], was used to determine the concentration of the surface species.

$$\sigma_a = \frac{A_a}{A_s} \times \frac{KE_a}{KE_s} \times \frac{\mu_s}{\mu_a} \times \frac{(N\lambda_s\rho_s)}{M_s} \cos\varnothing \qquad [2.12]$$

σ_a - Surface concentration of the adsorbate

A - Peak areas of the adsorbate and surface material respectively

KE - Photoelectron Kinetic Energy of the adsorbate and surface material respectively

μ - Photo-ionic cross section of the adsorbate and substrate respectively. There are tabulated values for each element[13].

N - Avogadro's constant

λ_s - Inelastic mean free path of the surface substrate. There are tabulated values[14].

ρ_s - Density of the surface substrate

M_s - Relative molecular mass of the surface

$\emptyset$ - Angle at which photo-electrons are collected with respect to the sample normal

The photoionisation cross section (μ') of C or Ti is determined with equation 2.13 to account for the angle between the analyser and the source. Equation 2.13 takes into account the angular distribution asymmetry parameter, β, to account for the influence of the specific Hartree-Slater wavefunction. There are tabulated values for each sub-shell[15], i.e. s, p, d etc.

$$\mu' = \mu\left(1 - \frac{\beta}{2}\left(\frac{3\cos^2\theta - 1}{2}\right)\right) \qquad [2.13]$$

μ - Photoionisation cross section at a source-analyser angle of 90°.

β - Angular distribution asymmetry parameter

θ - Angle between the source and the analyser

For example, the coverage of C on $TiO_2(110)$, is worked out:

Carbon:

A_a = 1444.1

KE_{C1s} = Al source energy – Binding Energy of C_{1s} = 1486.6 – 284.5 = 1201.1 eV

$\mu_{1s\,½} = 1$

$\beta_c = 2$

$$\mu_{1s\frac{1}{2}}{}' = \mathbf{1}\left(1-\frac{2}{2}\left(\frac{3cos^{2}45-1}{2}\right)\right) = 1-0.25 = 0.75$$

Titanium:

A_s = 144263

$KE_{Ti\,2p}$ = Al source energy – (($BE_{Ti2p\,3/2}$ + $BE_{Ti2p\,½}$) / 2) = 1486.6 – ((464.4 + 459.0) /2)

= 1024.9 eV

$\mu_{Ti2p} = (2p_{3/2} + 2p_{1/2}) = 2.68 + 5.22 = 7.90$

$\beta_{Ti} = 1.39$

$$\mu_{2p}{}' = 7.90\left(1-\frac{1.39}{2}\left(\frac{3cos^{2}45-1}{2}\right)\right) = 6.53$$

$N_A = 6.023\text{x}10^{23}$ atoms mol^{-1}

$M_{TiO2} = 79.898$g mol^{-1}

λ_{TiO2} = 21.21Å = 21.21x10^{-8} cm

ρ_{TiO2} = 4.26g cm^{-3}

ϕ = 0. Analyser points directly at the sample

θ = 45°

The coverage of C on TiO_2 is:

$$\sigma_C = \frac{1444.1}{144263} \times \frac{1202.1}{1024.9} \times \frac{6.53}{0.75} \times \frac{(6.023\times10^{23})(21.21\times10^{-8})(4.26)}{79.898}$$

$$\sigma_c = \frac{1444.1}{144263} \times 1.17 \times\ 6.811 \times 10^{15}$$

7.98 x10^{13} atoms cm^{-2}

The unit cell of the $TiO_2(110)$ surface has dimensions of 2.96Å x 6.49Å, giving 5.2×10^{14} unit cells per cm^2 of surface area[16, 17]. The carbon concentration is therefore 0.15 monolayers.

2.6.7.2 Determining film thickness

The thickness of an overlayer on top of a substrate can be calculated using the following equation:

$$I = I_0 exp\left(\frac{-t}{\lambda\ sin\theta}\right) \qquad [2.14]$$

I_0 – the substrate signal with no adsorbate

I – the substrate signal with adsorbate

t – film thickness

λ – the inelastic mean free path for the substrate electrons escaping through the adsorbate film

θ – the angle between the analyser entrance lens and the sample. In this case, the angle was always 90°. Sin90 is equal to 1.

2.7 Low Energy Electron Diffraction (LEED)

LEED is a technique used to give information about the surface structure of a solid crystalline material by bombardment with a beam of low energy electrons (20-200 eV)[18]. The diffraction pattern from the surface is measured giving information on the atomic arrangement at solid surfaces - the diffracted electrons are observed as spots on a fluorescent screen. The diffraction pattern then gives information of the unit cell, which gives an indication of the arrangement of the adsorbate on the single crystal surface.

The technique is surface sensitive due to the two effects[3]. Firstly, the mean free path for inelastic scattering is very short – about 5 Å. This is because the electrons used have a very low energy, and so are unable to penetrate more than a few atomic layers into the solid. Those that do, have a high probability of losing energy and becoming incoherent. The second effect arises due to elastic scattering – backscattering is extremely strong, so that each successive layer in the solid receives a much smaller incident electron beam and so contributes much less to the scattering.

LEED requires that the surface is periodic. It can only operate under ultra-high vacuum conditions in order to ensure that the mean free path of the incident electrons is sufficient for the beam to reach the sample

2.7.1 Theory

The wavelength of electrons may be estimated from the de Broglie equation:

$$\lambda = \frac{h}{mv} \qquad [2.14]$$

The equation may be modified specifically for electrons[2]:

$$\lambda = \frac{h}{\sqrt{2mE}} \qquad [2.15]$$

$$\lambda(\text{Å}) = \left(\frac{150.6}{E(eV)}\right)^{\frac{1}{2}} \qquad [2.16]$$

which gives de Broglie wavelengths of 2.74 - 0.388Å for kinetic energies between 20-1000 eV.

Figure 2-16[2] illustrates the scattering of electrons from a one dimensional periodic array. The electrons are scattering at an angle θa from atoms in a one-dimensional chain (the lattice constant is “a”). For constructive interference between scattered electron waves, the path length must be equal to an integral number of wavelengths:

$$\Delta a = n\lambda$$

Where λ is the de Broglie wavelength of the electron and is constant at a fixed incident electron kinetic energy.

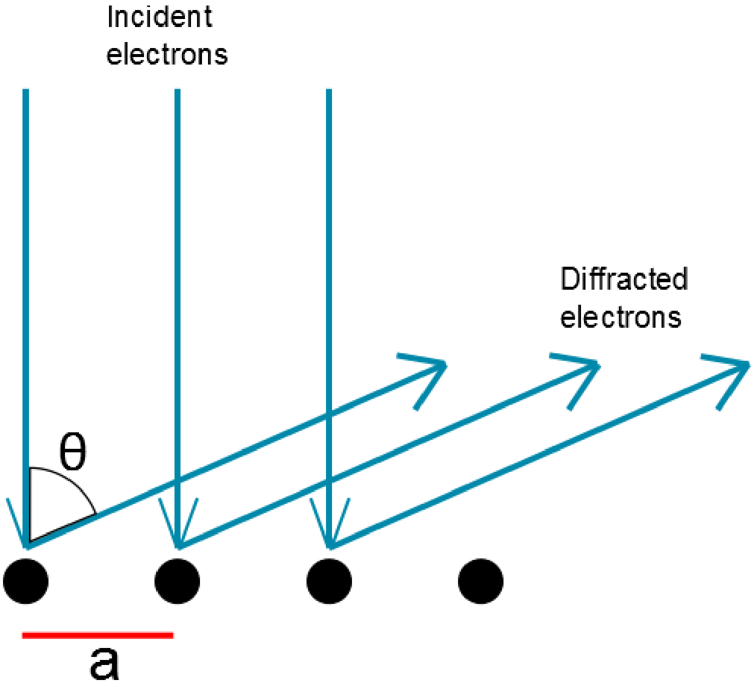

Figure 2-16 - Diffraction from a one-dimensional array

The path length difference is:

$$\Delta a = a \sin \theta a \qquad [2.17]$$

These two can be combined to give:

$$n\lambda = a \sin \theta a \qquad [2.18]$$

Or

$$\sin\theta a = \frac{n\lambda}{a} \qquad [2.19]$$

This means that, for a fixed wavelength and a fixed lattice spacing, only well defined values of θa are allowed. Constructive interference will then be observed at values corresponding to integer values of n, meaning that discrete diffracted beams will be seen at particular angles[2].

Equation 2.18 is a form of the Bragg equation, nλ = 2d sin θ. For a one-dimensional array, the diffraction pattern consists of a set of parallel lines, perpendicular to the one-dimensional lattice where the atom spacing is inversely related to the periodic spacing in the diffraction pattern. For fixed values of λ, as “a” increases, sinθa decreases, leading to the diffracted beams moving closer together.

The wave vector of an electron is defined as:

$$|k_0| = \frac{2\pi}{\lambda} = \frac{2\pi}{h}\,mv \qquad [2.20]$$

Where mv is the momentum of the electron. Equation 2.18 and 2.20 can be combined to give:

$$|k_0|\sin\theta_0 = \frac{2\pi}{a}(n) \qquad [2.21]$$

This is the component of momentum parallel to the surface of the incident electron, ($k_{||}$). This equation shows that parallel momentum is only exchanged with the surface in quantised units of 2π/a, which is the magnitude of the one-dimensional reciprocal lattice vector. For the diffracted beams to arise (i.e. for the electrons to undergo a change in direction) the electron must exchange parallel momentum with the one dimensional lattice, conserving momentum.

The surfaces studied with LEED are typically two-dimensional. Introducing periodicity in a second, orthogonal direction in which the lattice constant is b leads to an equation similar to 2.21:

$$|k_0| \sin\theta_a = \frac{2\pi}{b}\,(m) \qquad (m = 0, \mp 1, \mp 2, \mp 3, \ldots). \qquad [2.22]$$

Both equations 2.21 and 2.22 have to be satisfied simultaneously for diffraction to be observed, i.e. two-dimensional diffraction is only allowed at the intersection of the one-dimensional reciprocal lattice rods generated in directions a and b, respectively, and the LEED pattern consists of a series of diffraction spots corresponding to these points of intersection. The exchange of parallel momentum is restricted to a two-dimensional reciprocal lattice vector (G):

$$G = \Delta K_{\downarrow}(||) = n\ 2\pi/a + m\ 2\pi/b\ . \qquad [2.23]$$

Every real space lattice will generate an associated “reciprocal lattice” upon diffraction, obeying these rules:

$$G = n\boldsymbol{a}^{*} + m\boldsymbol{b}^{*}, \qquad [2.24]$$

$$|a^{*}| = {}^{2\pi}/_{|a|}\ ;\ |b^{*}| = {}^{2\pi}/_{|b^{*}|}\ ; a.b^{*} = a^{*}.b = \mathbf{0}\ , \qquad [2.25]$$

where G is the reciprocal lattice vector, n and m are integers, **a** and **b** are the elementary vectors of the surface two-dimensional unit cell, and **a*** and **b*** are the elementary vectors of the corresponding reciprocal lattice. This means that a large distance in real space becomes a small distance in reciprocal space (and vice versa), and that **a** and **b** are perpendicular to **a*** and **b***, respectively.

2.7.2 Experimental set-up

The apparatus required for LEED is shown in Figure 2-17[2]. The sample is grounded in order to prevent charging.

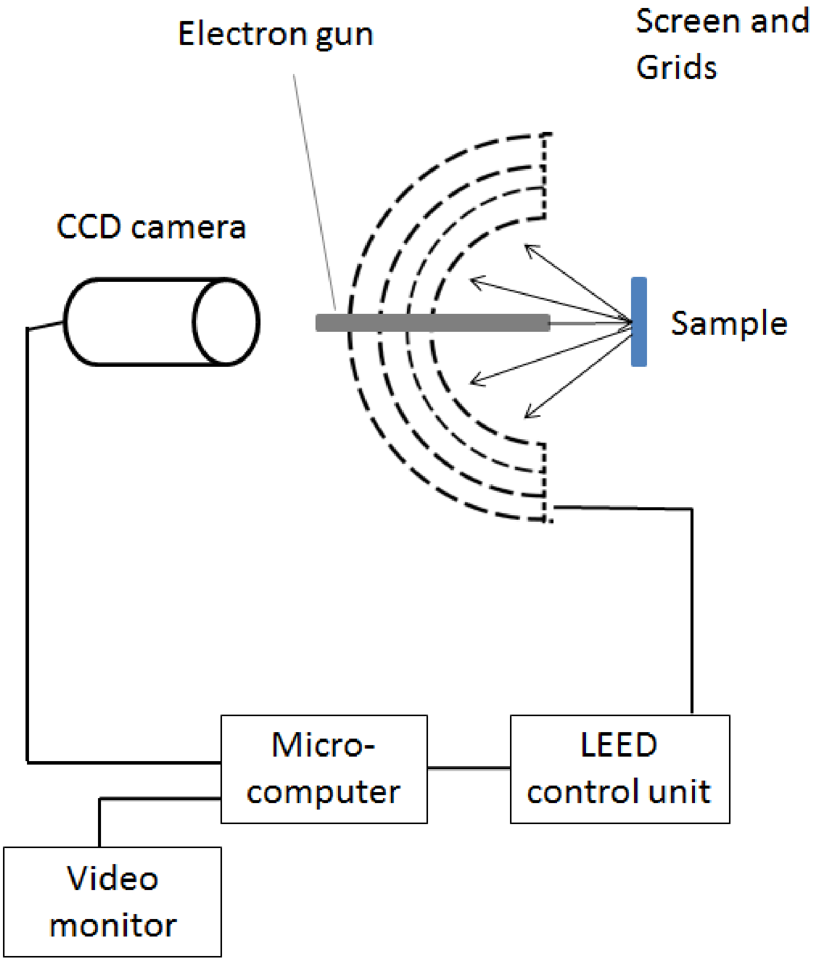

Figure 2-17 - experimental set up for LEED[2]

The equipment consists of an electron gun, a grid system and a fluorescent screen. The gun produces an electron beam (E = 0 – 1000 eV) which incidents on the sample, resulting in the diffraction of the electrons. The back-scattered electrons travel towards the series of four concentric grids. The first grid is at ground potential. The second and third grid are held at a negative potential to reject inelastically scattered electrons with $E_{kin} < E_p$ which would otherwise contribute to make a very bright background on the screen. After passing this grid, the electrons are accelerated towards the screen, which is held at a high positive voltage (~4 keV) to provide the diffracted electrons with enough energy to cause fluorescence on the screen and create a pattern of bright spots on a dark background. The LEED pattern is captured by a camera positioned directly opposite the LEED screen.

2.8 Auger Electron Spectroscopy (AES)

2.8.1 General

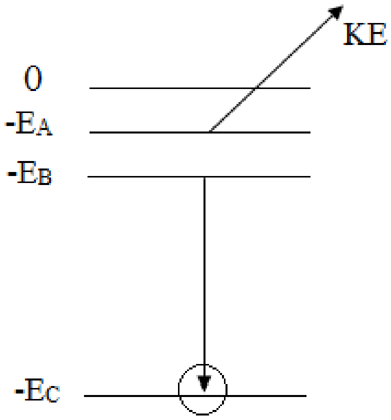

Figure 2-18 - Energy level diagram showing the filling of a core hole in energy level A, giving rise to Auger electron

Auger electron spectroscopy is a technique used to study surfaces using the Auger effect; electrons are emitted from an excited state atom after a series of internal relaxation events[1]. It is named after Pierre Auger, who had studied electron emission from a gas after irradiation with X-rays[19]. These electrons are then analysed, providing some indication of chemical composition and characterising the cleanliness of the surface[3].

In Auger electron spectroscopy, an atom is hit by an electron beam (between 2 – 20 keV). This removes a core state electron, leaving behind a hole. The core hole is filled by an outer shell electron, due to the instability of this state[20]. The electron moving to the lower energy level loses an amount of energy equal to the difference in orbital energies. These transitions give rise to characteristic peaks, specific to each element[21]. Comparison of the ratios of different peaks within the same Auger spectra gives an indication of the composition of the surface. Figure 2-18[3] shows a schematic of the process. For Auger emission[3]:

$$KE = E_A - E_B - E_C \qquad [2.26]$$

Where "KE" is the kinetic energy of the Auger electron.

As shown in Figure 2-19, Auger is a three electron process, hence it cannot be used to detect hydrogen and helium.

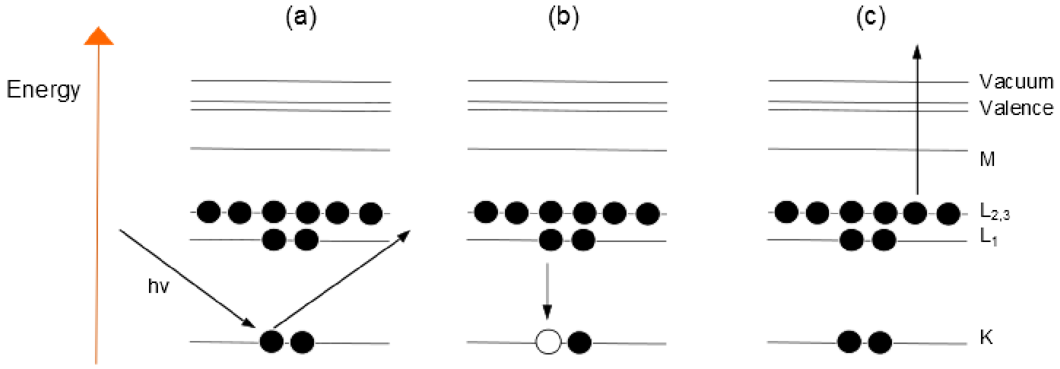

Figure 2-19 - Schematic diagram of the Auger process. (a) ionisation, (b) relaxation, (c) emission

The technique requires ultra-high vacuum (UHV) conditions. This prevents scattering of electrons off of gas atoms.

2.8.2 Auger notation

Equation 2.26 gives an approximate formula for the kinetic energy of an Auger electron based on the one-electron binding energies of the core levels involved. The transition shown in Figure 2-18 is an ABC transition, where A, B and C are the X-ray levels K, L_1 and L_2.

Figure 2-20 shows a typical spectra. The peak at 510 eV is an oxygen KLL peak, and the peaks at 380 and 420 eV are titanium LMM peaks.

Auger notation is as follows; the first letter is the level that is ionised by the electron beam. The 2nd letter indicates the level where the electron is lost from in order to fill the vacancy in the core level. The 3rd letter shows where the Auger electron was emitted from. K, L and M are used for shells with principal quantum number 1, 2 and 3 respectively.

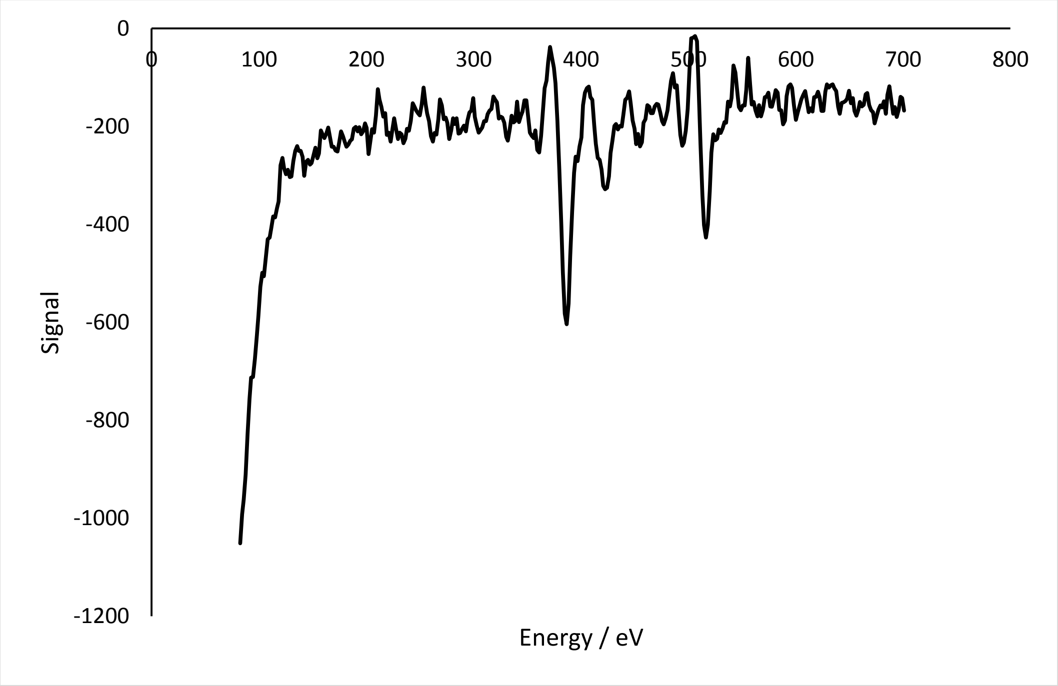

Figure 2-20 - clean TiO_2 Auger spectra

2.8.3 Fluorescence vs Auger Emission

The ionised atom is in a highly excited state, and has two available relaxation pathways; Auger emission and x-ray fluorescence. The probability that one or the other will occur depends on the atomic number of the element in question (see Figure 2-21). Auger emissions are favoured for lighter elements as electrons are less tightly bound to the nucleus, whereas fluorescence is favoured for heavier elements, as the ionisation probability for electrons is reduced. Measurement of Auger peaks of heavy elements (i..e. atomic number > 50) is therefore difficult. Auger spectroscopy is, however, very sensitive to lighter elements.

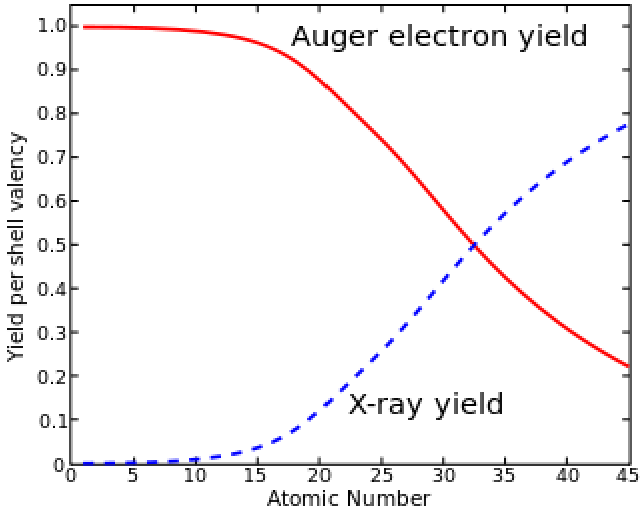

Figure 2-21 - Comparison of Auger yield vs fluorescence yield as a function of atomic number[22]

2.8.4 Surface sensitivity

The energy of Auger electrons is usually up to 2000 eV, which is equivalent to an inelastic mean free path of approximately 0.5 to 5 nm[1], making Auger electron spectroscopy a very surface sensitive technique. The electrons are only able to escape from the top layers of the surface due to their short attenuation length.

2.8.5 Instrumentation

AES requires UHV to minimise interference (preventing electrons from hitting gas molecules) and minimise contamination. The spectrometer consists of an electron gun and an energy analyser.

The electron source is a tungsten-rhenium filament. A current is passed through the filament, emitting an electron beam. The beam is focused onto the sample, usually with an energy of 2 keV. There are typically two types of analyser for AES, a hemispherical analyser and a cylindrical mirror analyser. In this case, a hemispherical retarding field analyser is used.

2.8.6 Acquiring data

Emitted electrons are mostly “secondaries” i.e. they have undergone multiple energy losses due to inelastic scattering processes (excitation of plasmons or interband transitions)[2]. Because of this, Auger peaks are generally small and are against a large background of secondary electrons (see Figure 2-22). This is overcome by differentiating the peak to give a dN(E)/dE curve. In this format the signals appear as double peaks that are much easier to identify (see Figure 2-23). The peaks observed on the Auger spectra can then be compared to reference data[23] in order to be sure that the corresponding elements are present.

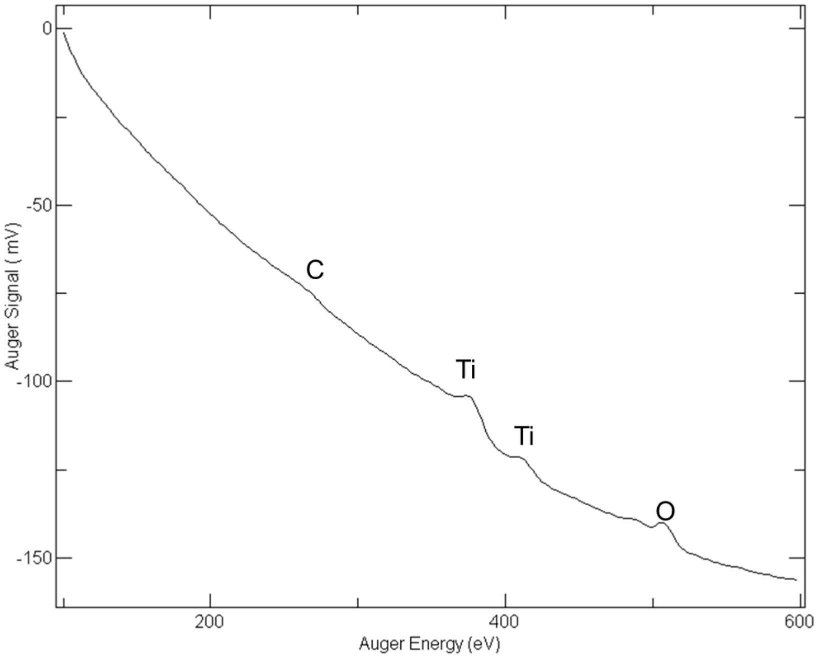

Figure 2-22 - Example of an N(E)/E Auger spectrum

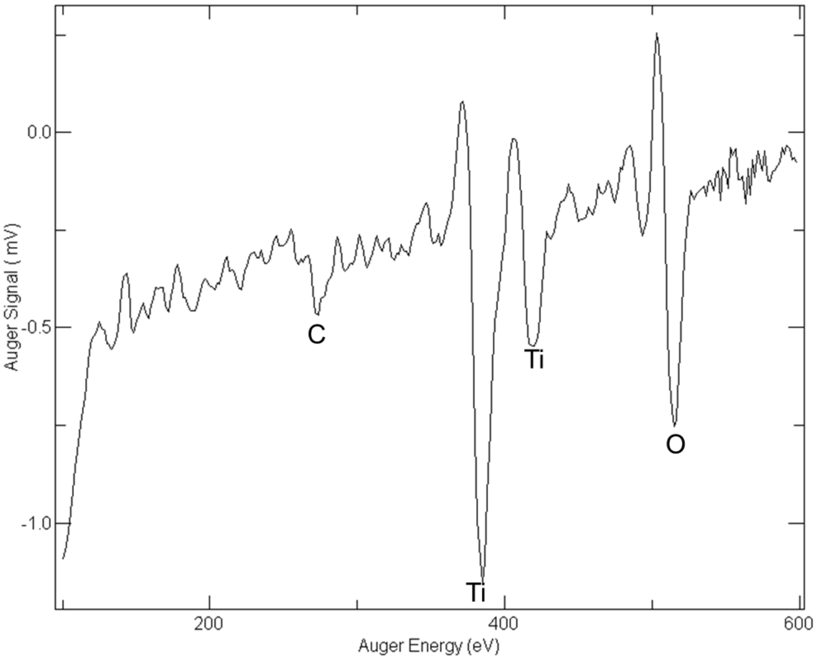

Figure 2-23 - Differentiated Auger spectrum

2.8.7 Sensitivity factors

Auger spectroscopy has varying sensitivity to different elements, as shown in Table 2-2[23]:

Table 2-2 - PHI sensitivity factors for designated Auger electron transitions

Element	Peak (eV)	Sensitivity	Transition	Material
C	275	0.282	KLL	Graphite
O	510	0.788	KLL	SiO_2
Ti	390	0.702	LMM	Not stated
Ti	421	1.10	LMM	Not stated
Pd	283	0.352	MNN	Not stated
Pd	333	2.04	MNN	Not stated
Au	74	1.420	NVV	Not stated

2.8.8 Quantification

Measurement of peak-to-peak height ratios in Auger is a simple way to quantify the relative concentrations of any species present on the surface. For most elements, it was simply a case of measuring the height of the top of the peak to the bottom (as shown in Figure 2-24, with Pd). However, measurement of the Au peak height (at ~70 eV in Figure 2-24) was complicated by it being in the background of the Auger spectrum, making it appear smaller than it really is. To overcome this, a background was applied, to try to get a better estimation of the Au peak height.

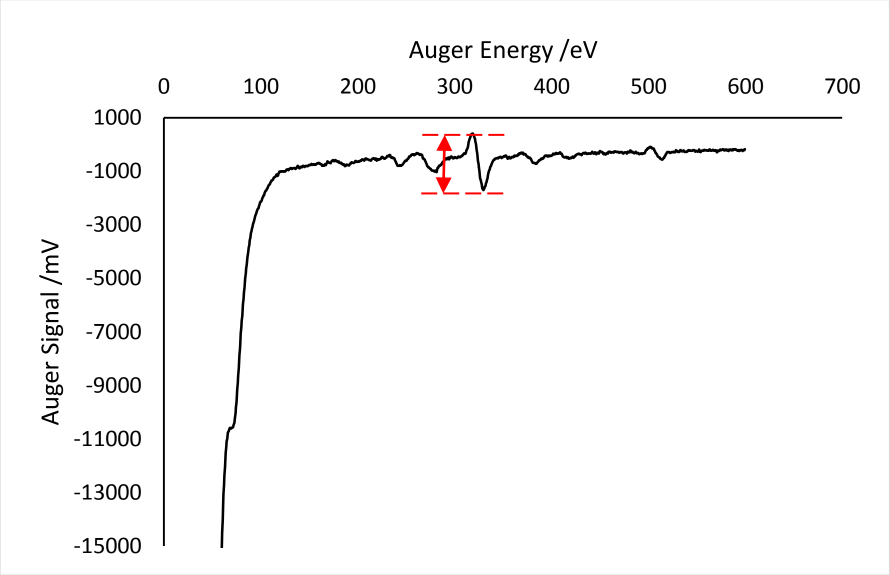

Figure 2-24 - Example of how Auger peak heights were measured

2.9 Temperature Programmed Desorption (TPD)

2.9.1 Theory

Temperature programmed desorption can provide information on the reaction kinetics and reaction steps.

In a TPD experiment, the catalyst is dosed with a chemical species, (which could be any organic molecule, e.g. ethanol, formic acid, or any gas, e.g. oxygen) at room temperature. The temperature is then increased linearly (typically 3 to 7 K s^{-1}). As the temperature increases, and the thermal energy becomes sufficient to break surface bonds, the adsorbate and any reaction products desorb from the surface and move into the gas phase, where they are then detected by a mass spectrometer.

A graph showing the variation of desorption of the different species as a function of temperature can then be produced.

For a first order process, the rate of desorption can be described as[2]:

$$Rate = k_d\theta, \qquad [2.26]$$

where k_d is the rate constant for desorption and θ is the surface coverage. The rate constant is given by the Arrhenius equation:

$$k_d = A\, exp\left(\frac{-E_d}{RT}\right), \qquad [2.27]$$

where A is the pre-exponential factor, E_d is the activation energy for desorption, R is the gas constant and T is the temperature.

The rate of desorption can be more generally written as:

$$\frac{-dN}{dT} = k_d N^m \qquad [2.28]$$

Where *N* is the number of adsorbed molecules and *m* is the reaction order. A substitution can then be made:

$$\frac{-dN}{dT} = \frac{dN}{dT} \times \frac{dT}{dt}\,\frac{dN}{dt}\beta \qquad [2.29]$$

Where β is the heating rate (dT/dt). Using equation 2.29, equation 2.28 can be rewritten as:

$$\frac{-dN}{dT} = \frac{k_d}{\beta} N^m \qquad [2.30]$$

Equation 2.27 can then be substituted in for k_d:

$$\frac{-dN}{dT} = N^m \frac{A}{\beta} exp\left(-\frac{E_d}{RT}\right) \qquad [2.31]$$

Where A is assumed to equal 10^{13} s^{-1}.

The temperature at which maximum desorption occurs (T_p) corresponds to the maximum desorption rate[2] i.e. when $T=T_p$,

$$\frac{d^2N}{dT^2} = 0 \qquad [2.32]$$

A general equation relating T_p and E_d can be obtained by differentiating equation 2.31 with respect to T and equating to zero:

$$\frac{E_d}{RT_p^2} = \frac{A}{\beta} mN^{-1} exp\left(-\frac{E_d}{RT_p}\right) \qquad [2.33]$$

If m = 1, i.e. desorption is first order:

$$\frac{E_d}{RT_p^2} = \frac{A}{\beta} exp\left(-\frac{E_d}{RT_p}\right) \qquad [2.34]$$

β and T_p are experimentally measurable parameters. As mentioned before, the pre-exponential factor, A, is assumed to equal 10^{13} s^{-1}. The desorption energy can therefore be evaluated by guessing the value of E_d and refining the guess, until equation 2.34 is satisfied.

It can be seen from equation 2.34 that, when the process is first order, the desorption peak maximum is independent of coverage, as there are no N terms in the equation. As the adsorbate coverage increases, Tp remains the same whilst the intensity increases.

If m = 2, i.e. desorption is second order:

$$\frac{E_d}{RT_p^2} = \frac{2AN}{\beta}\, exp\left(-\frac{E_d}{RT_p}\right) \qquad [2.35]$$

Equation 2.35 shows that, for a second order process, T_p is now dependent on the coverage, N.

2.9.2 TPD Spectra

TPD data are presented as the change in signal intensity of the mass fragment of interest versus temperature.

A spectrum can be analysed by examining the shape, size and the position of the peak. The position of the peak is related to the strength of the binding between the molecule and the surface it is adsorbed on to. The area underneath a peak is proportional to the surface coverage.

Typically, two or more products will desorb in the same temperature range. This indicates that these products all originated from the same surface intermediate. An example TPD is shown in Figure 2-25, where coincident mass 28 and mass 44 peaks can be observed.

Often, a particular mass in a TPD will produce several peaks at different temperatures. This indicates that the same species is bound in different states. The higher the temperature when each state desorbs, the more stable the state.

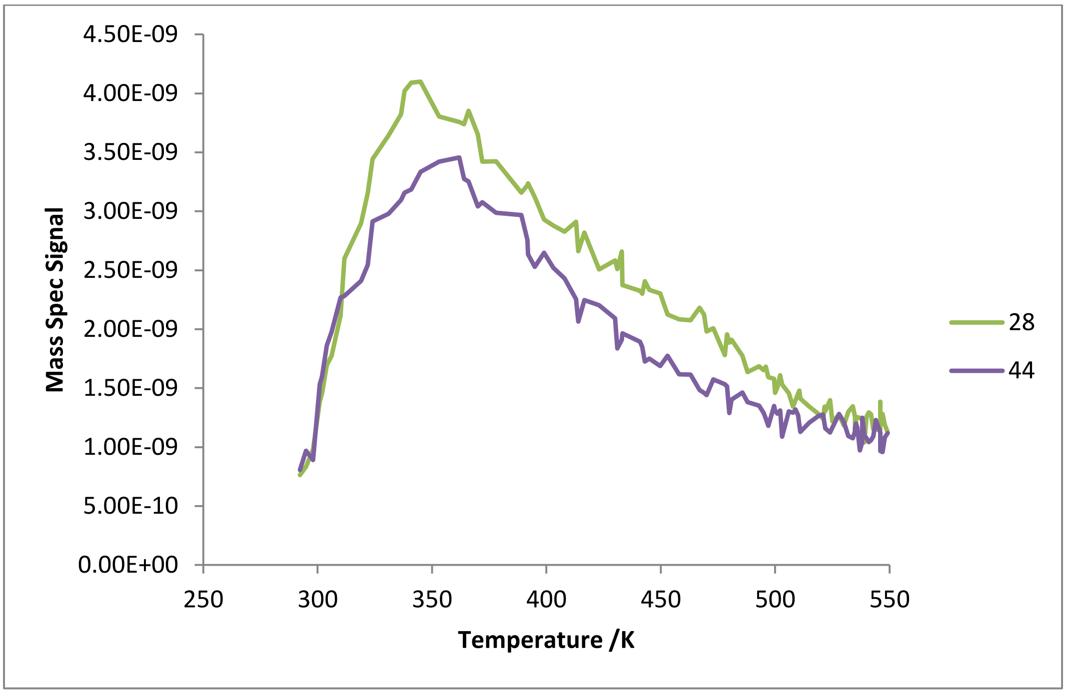

Figure 2-25 - Raw TPD of formic acid on TiO_2, showing two coincident peaks

Compound	Relative Peak Intensity
Hydrogen	2 (100), 1 (2)
Ketene	14 (100), 42 (95), 41 (30), 28 (12)
Water	18 (100), 17 (21), 16 (1)
Ethene	28 (100), 27 (65), 26 (55)
Carbon Monoxide	28 (100), 12 (5), 16 (2), 29 (1), 14 (1)
Formic Acid	29 (100), 46 (65), 45 (50), 28 (18)
Acetaldehyde	29 (100), 44 (85), 43 (45), 15 (37), 14 (10), 42 (10)
Ethanol	31 (100), 45 (50), 29 (30), 27 (22)
Oxygen	32 (100), 16 (22)
Acetic Acid	43 (100), 45 (90), 60 (75), 15 (20), 42 (15)
Ethyl Acetate	43 (100), 45 (15), 61 (15), 29 (13)
Carbon Dioxide	44 (100), 16 (10), 28 (10)

Table 2-3 – Relative intensities of major molecules from the mass spectrometer

Table 2-3 shows the relative peak intensities observed in mass spec of the major molecules monitored in this study, taken from the National Institute of Standards and Technology reference database[24]. This table was used as a guide as to which masses to monitor during TPD.

2.9.3 Instrumentation

The essential components of a TPD are a quadrupole mass spectrometer, a multiplier control unit and a power supply. The mass spectrometer is placed close to the sample (~5cm) with no obstructions, preventing the desorbed species from interacting with anything on the way to the mass spectrometer and affecting the results. The multiplier is used to magnify the signal from the detector. Any masses of interest are selected before the experiment begins and are detected exclusively by the equipment.

2.10 Quadrupole Mass Spectrometry

A quadrupole mass spectrometer separates ions according to their mass to charge (m/z) ratios[25]. In a typical mass spectrometer, molecules (gas, liquid or solid) enter the spectrometer and are bombarded by electrons. This ionises the molecules, which are then accelerated into a magnetic or an electric field. Here, they are deflected; the extent of which depends on their mass. These deflected ions are then detected, generating a mass spectrum which plots the relative abundance of the ions against the m/z ratio.

The quadrupole analyser is made of four, perfectly parallel rods of either circular or (preferably) hyperbolic section (Figure 2-26 and Figure 2-27). An oscillating voltage is applied to one pair of rods, and a direct voltage is applied to the other. Ions travel down the quadrupole, between the rods. The field is rapidly alternated, causing some ions to destabilise and lose their trajectory. Ions with a particular m/z ratio will continue to follow a stable trajectory and therefore reach the detector[25]

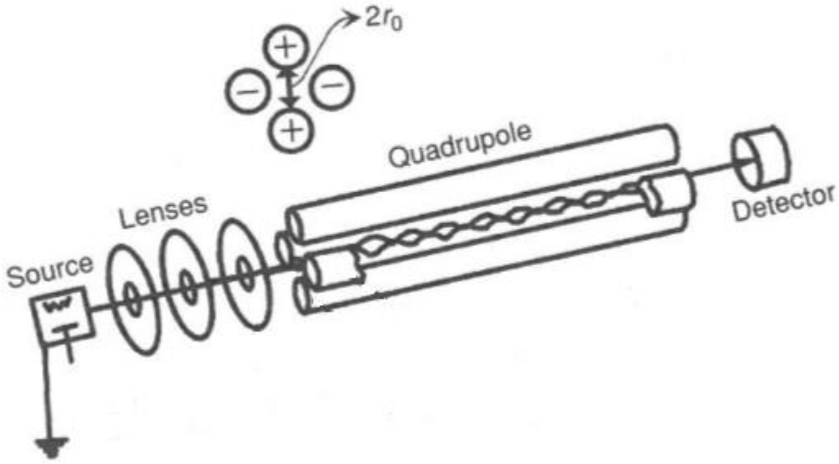

Figure 2-26 - Quadrupole instrument. Made up of the source, focusing lens, quadrupole cylindrical rods and the detector[25].

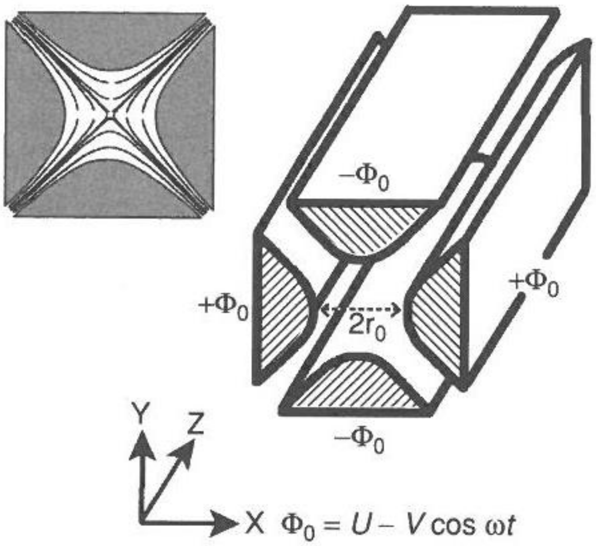

Figure 2-27 - Quadrupole with hyperbolic rods and applied potentials[25].

2.11 References

1. D. Briggs and M. Seah, *Practical Surface Analysis by Auger and X-ray Photoelectron Spectroscopy*, John Wiley & Sons, Chichester, 1983.
2. G. Attard and C. Barnes, *Surfaces*, OUP Oxford, Oxford, 1998.
3. D. Woodruff and T. Delchar, *Modern Techniques of Surface Science*, Cambridge University Press, 2nd edition edn., 1999.
4. H. H. Brongersma and J. P. Jacobs, *Applied Surface Science*, 1994, **75**, 133.
5. Y. Tanaka, H. Morishita, J. T. Ryu, I. Katayama and K. Oura, *Surface Science*, 1996, **363**, 161.
6. H. H. Brongersma, M. Draxler, M. de Ridder and P. Bauer, *Surface Science Reports*, 2007, **62**, 63.
7. M. P. Seah, *Vacuum*, 1984, **34**, 463.
8. A. M. Venezia, *Catalysis Today*, 2003, **77**, 359.
9. *Dar400 X ray Source and Power Supply User's Guide, Version 1.0, Omicron Vakuumphysik GmbH, Germany, 15 January 1998*.
10. *EA 125 Energy Analyser User's Guide, Version 2.1, Omicron Vakuumphysik GmbH, Germany, 11 July 2002, Omicron*.
11. *CasaXPS, Version 2.3.15, Casa Software Ltd, 1999-2011*.
12. A. F. Carley and M. W. Roberts, *Proceedings of the Royal Society of London Series a-Mathematical Physical and Engineering Sciences*, 1978, **363**, 403.
13. J. H. Scofield, *Journal of Electron Spectroscopy and Related Phenomena*, 1976, **8**, 129.
14. D. R. Penn, *Journal of Electron Spectroscopy and Related Phenomena*, 1976, **9**, 29.
15. R. F. Reilman, A. Msezane and S. T. Manson, *Journal of Electron Spectroscopy and Related Phenomena*, 1976, **8**, 389.
16. A. W. Grant and C. T. Campbell, *Physical Review B*, 1997, **55**, 1844.
17. C. L. Pang, R. Lindsay and G. Thornton, *Chemical Reviews*, 2013, **113**, 3887.
18. K. Oura, V. Lifshits, A. Saranin, A. Zotov and M. Katayama, *Surface Science: An Introduction*, Springer, 2003.
19. P. Auger, *Journal De Physique Et Le Radium*, 1925, **6**, 205.

20. T. Carlson, *Photoelectron and Auger Spectroscopy*, Plenum Press, New York, 1975.
21. M. Thompson, M. Baker, A. Christie and J. Tyson, *Auger Electron Spectroscopy*, John Wiley & Sons, Chichester, 1985.
22. http://en.wikipedia.org/wiki/File:Auger_Yield.svg.
23. K. Childs, B. Carlson, L. LaVanier, J. Moulder, D. Paul, W. Stickle and D. Watson, *Handbook of Auger Electron Spectroscopy*, Physical Electronics, Inc., 3rd edn., 1995.
24. NIST Chemistry WebBook, http://webbook.nist.gov.chemistry.
25. E. de Hoffman and V. Stroobant, *Mass Spectrometry: Principles and Applications*, Wiley & Sons, 3 edn., 2007.

Chapter 3 – Surface Science of TiO_2(110) and Pd/TiO_2(110)

Chapter 3 Contents

3.1 Introduction

In this chapter the surface of titania single crystals and palladium doped titania single crystals is explored using surface science techniques including XPS, ISS and LEED.

The effect of heating and sputtering TiO_2 is initially examined. Then the growth of Pd on several differently prepared TiO_2(110) surfaces is studied. Finally, the effect of heating on the Pd thin films on the TiO_2 substrate is looked at, specifically investigating the SMSI (Strong Metal Support Interaction) effect. The aim of these experiments is to bring about an increased understanding of the interaction of small metal particles and thin metal films with reducible metal oxides, particularly Pd on TiO_2.

A model catalyst is inspired by a real catalyst, and is synthesised with the purpose of understanding how it works[1]. The model catalyst has a known structure and surface topology, which can be easily characterised with surface science techniques. On the other hand, real powdered catalysts are very complex systems with many variables, including surface area and an ill-defined surface structure. The use of model catalysts is especially suited to investigating the nature of the metal-support interaction, including the effect of metal cluster size, cluster number density and temperature.

Titanium dioxide has been the object of a number of studies, mainly due to its role as a prototypical transition metal oxide surface[2]. Thanks to its wide range of applications, including as a catalyst[3], paints and optical coatings[4], antibacterial coatings, self-cleaning surfaces and as a photocatalyst[5], TiO_2 is the most investigated single-crystalline system in the surface science of metal oxides[6]. Titanium dioxide is a preferred system for experimentalists, as it is well suited for many techniques[6]. Crystals with a high surface quality are easily available and can be easily reduced, which helps to prevent charging. Furthermore, new phenomena are typically much easier to observe on already well-characterised systems, such as TiO_2.

3.1.1 Structure of TiO_2

TiO_2 has three naturally occurring main crystal structures: anatase, brookite and rutile[7]. Anatase and rutile are tetragonal structures; anatase has a unit cell consisting of 12 atoms, whereas rutile's consists of 6 atoms[8], as shown in Figure 3-1 and Figure 3-2. Brookite has an orthorhombic structure[9].

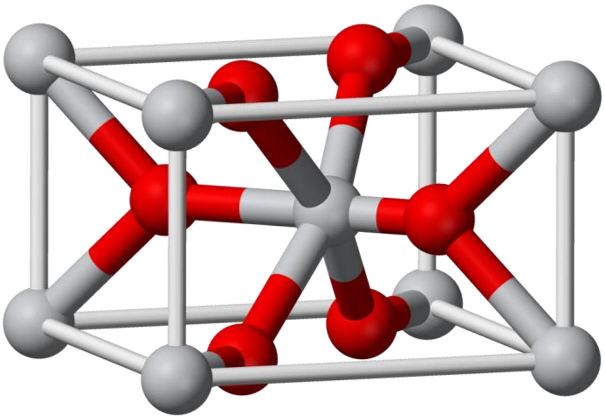

Figure 3-1 - Unit cell of Rutile TiO_2. Red atoms are Ti, grey atoms are O.

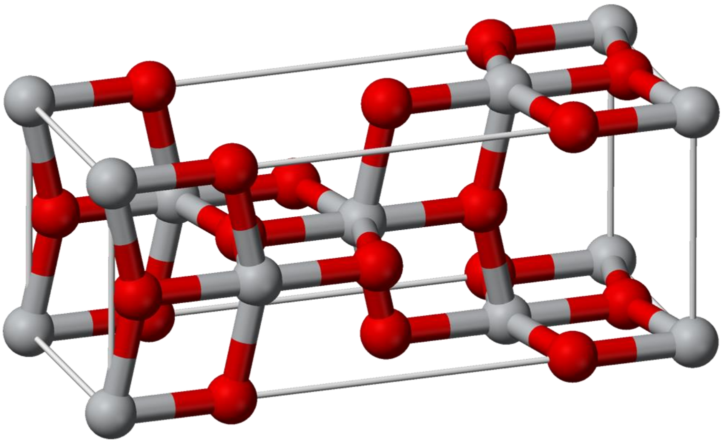

Figure 3-2 - Unit cell of Anatase TiO_2. Red atoms are Ti, grey atoms are O.

Anatase tends to be more stable at low temperature, whereas rutile is more stable at high temperature.

TiO_2 is a transition metal oxide with poor conductivity. However, when reduced or when defects are introduced to the crystal, it becomes an n-type semi-conductor with a band gap of approximately 3.1 eV[10]. The colour of the crystal gives an indication of how reduced it is – it is initially transparent, and becomes light blue, then dark blue, before finally turning black, on reduction and as more and more defects are introduced into the crystal[10].

3.1.2 TiO_2 surfaces

A number of stable rutile TiO_2 surfaces can be formed, and the (110) face is the most stable. It was found to have the lowest surface energy and the fewest number of dangling covalent bonds[11].

Two concepts have been proposed to predict the stability of oxide surfaces. In the first, proposed by Tasker[12], the stability is based on electrostatic considerations only. Tasker proposed that the dipole moment of a repeat unit perpendicular to the surface must be zero in order for the surface energy to go to a minimum. From this, he defined three categories for ionic structures:

- Type 1 – consists of an equal number of cations and anions on each plane parallel to the surface, and is therefore neutral. These structures are stable.
- Type 2 – consists of charged planes but, due to a symmetrical stacking sequence, has no dipole moments. These structures are also stable.
- Type 3 – consists of charged planes with a dipole moment in the repeat unit, perpendicular to the surface. These structures are unstable.

The second proposal, by Lafemina[13], introduced the idea of autocompensation, i.e. the most stable surfaces are those where the excess charge from cationic dangling bonds compensate anionic dangling bonds. The end result of this is that cationic dangling bonds are empty, whilst the anionic dangling bonds are full, giving a stable surface.

Both of these concepts are used together and have both been shown to be necessary for a stable surface[6]. In fact, both of these proposals are illustrated in the structure of TiO_2(110)(1x1), shown in Figure 3-3. The surface layer consists of an equal number of Ti and O atoms, with a charge of 4+ and 2- respectively, leaving an overall positive net charge, whilst the second layer consists of only O atoms and therefore has a net negative charge. This structure is then repeated, so that there is no dipole and the crystal is neutral. Cleaving this sample to expose the (110) plane along line A or B (Figure 3-3) will leave behind a layer of O atoms, corresponding to the bulk termination. This same structure is also predicted using autocompensation – in Figure 3-3b, the same number of Ti-to-O bonds are broken as O-to-Ti. The electrons from the Ti dangling bonds can be transferred to the O dangling bonds, compensating for the missing charge.

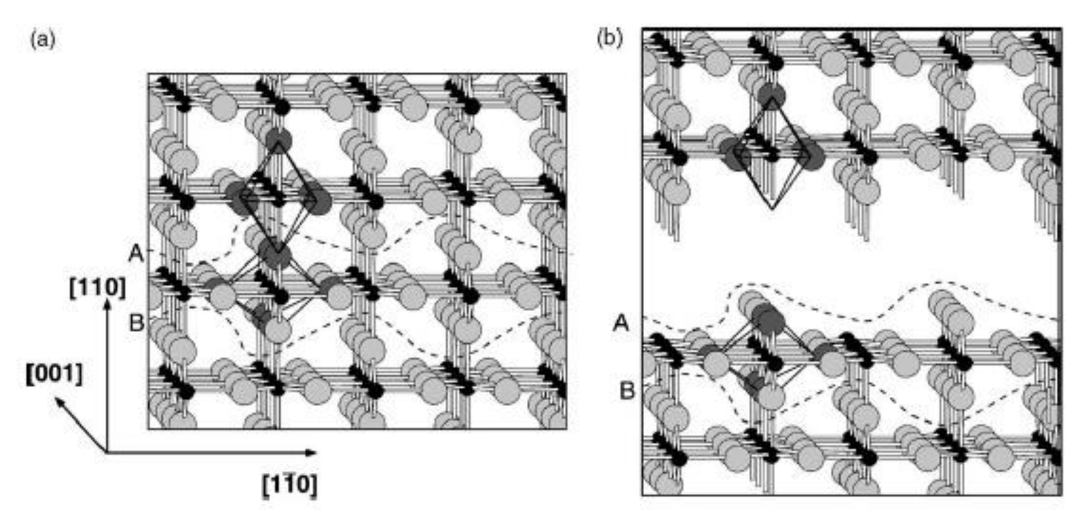

Figure 3-3 - Ball and stick diagram of the rutile TiO_2 crystal in the (110) plane[6]. (a) Two octahedral units are indicated. The dashed lines A and B indicate a charge neutral repeat unit without a dipole moment, perpendicular to the (110) direction. (b) Shows the crystal cut along line A.

The TiO_2(110)-(1 x 1) surface consists of alternating rows of fivefold-coordinated Ti (5f-Ti) atoms and protruding, twofold-coordinated bridging oxygen (O_{br}) atoms[14]. The Ti atoms underneath the O_{br} atoms are sixfold-coordinated.

This structure has been observed in STM and SPM by many groups. STM typically shows rows of ordered dark and bright lines running along the (001) direction[15]. The bright rows were deduced to be 5-fold Ti^{4+} cations by Onishi and Iwasawa[16], who observed that formate ions deposited on to the surface were sat on the bright rows and knew that formates adsorb on Ti sites. This was later confirmed by Diebold[17], who observed similar results with other adsorbates. In contrast to STM, non-contact atomic force microscopy (NC-AFM) images the O_{br} rows as protrusions[18].

On TiO_2(110)(1x1), the most commonly observed defect is a bridging oxygen vacancy ($O_{b\text{-}vac}$)[15]. These usually appear in STM images as a bright spot in the dark O_b row. Standard sputter-anneal cycles in UHV can lead to surface coverages of these defects up to 0.1 monolayers. The reactivity of TiO_2 is thought to be due to intrinsic defects on TiO_2 such as these oxygen vacancies[19, 20], as well as Ti^{3+} interstitials[14, 21]. These are important in catalytic reactions on TiO_2 surfaces.

There is some debate into what gives rise to the Ti 3d band gap state. Using ultraviolet photoemission spectroscopy and STM, Yim suggested that the band gap state in TiO_2(110) originated primarily from the bridging oxygen vacancies (O_{br} vac), and that the population of the band gap state increased with the increasing density of O_{br} vac[20]. They noted however that the population of the band gap state was not solely dependent on the density of bridging oxygen vacancies, but also that a minority contribution came from some other defect unrelated to O_{br} vacancies. Whether this was interstitial Ti or a subsurface oxygen species, they could not say. This was in direct contrast to an earlier study by Wendt, which proposed that the dominant contribution to the band gap state was from interstitial Ti[14]. He suggested that the Ti interstitial defect sites provide the electronic charge enabling dissociative and molecular adsorption for important reactions. Using high resolution STM, photoelectron spectroscopy and DFT, they observed that the gap state remains largely unchanged on surfaces where the O_{br} vacancies have been removed. Henderson used isotopically labelled ^{18}O and ^{46}Ti in static secondary ions mass spectrometry to show that bulk assisted re-oxidation of reduced surfaces was carried out by titanium cation diffusion rather than oxygen anions or vacancies[22]. Onishi and Iwasawa used STM to follow a surface/gas-phase reaction in-situ[23]. They exposed a reduced surface to temperatures of 800 K and a pressure of oxygen, and observed the growth of new surface layers. They proposed that reduced Ti^{3+} ions had accumulated in interstitial positions and had been oxidised to form hill like structures which became new terraces and new rows of Ti atoms. Walle[24] and Mitsuhara[25] both concluded that both O_{br}-vacancies and Ti^{3+} interstitials in the subsurface region both contribute to the band gap state. Mitsuhara[25] showed that non-O_{br}-vacancy contribution decreased as the TiO_2 surface became more and more reduced. Shibata[26] used advanced-TEM to actually observe Ti^{3+} interstitials – it is hoped that this may allow more insight into the $O_{b\text{-}vac}$ vs Ti^{3+} interstitials argument in the future.

Mao et al[27] used a combined theoretical and experimental to further investigate the origin of the band gap state on TiO_2(110). UPS was used to establish a linear dependence of the band gap states on the bridging hydroxyl ($O_{br}H$) concentration, which agreed with DFT calculations. Further experimental results showed that the contribution of subsurface defects to the band gap states was equal to ~2% monolayer of $O_{br}H$, demonstrating the importance of surface defects in changing the electronic structure of TiO_2.

Surface oxygen vacancies have been shown to play a role in certain reactions. Wendt used STM and DFT to study the interaction of water with reduced TiO_2(110)-(1 x 1) surface, showing that water dissociatively adsorbed to the oxygen vacancies, forming stable pairs of bridging hydroxyl groups[28] .

Zhang et al found that vacancies in the rows of bridge-bonded oxygens are mobile and migrate along the rows of bridge-bonded oxygens[19] using STM and DFT calculations.

It was also found that the nature of the support influences catalytic activity – Au/TiO_2(110) catalysts with a stoichiometric TiO_2(110) support exhibit a much lower catalytic activity compared to those with a reduced crystal[29]. AFM and STM were used to image the nanoparticles on different surfaces – Au nanoparticles were typically smaller on a fully oxidised surface. It was proposed that the reduced surface has a higher density of states and therefore a higher binding strength, which agreed with model calculations by Wendt[14].

A review by Bowker describes several other surface phases of TiO_2(110) that appear when the substrate is further reduced[30]. One such phase is the (1x2) reconstruction, obtained by heating in vacuum to over 1000 K. This is an added row reconstruction, and has been the cause of much debate in the literature, partly because there are two types of (1x2) reconstruction[30], the "simple" and "complex" reconstruction. There were originally suggestions of a "missing row" model by Moller[31], based on LEED and AES observations, and further confirmed by others using STM[32-34]. However, further STM studies by Novak[35] and Onishi[36] led to this model being rejected, in favour of two other possibilities for the simple reconstruction. The first, by Onishi and Iwasawa[36], was based on their STM work, and is known as the Ti_2O_3 added row termination. It consists of double rows of Ti cations along the (001) direction. Ab initio calculations by Elliot[37] and further experiments by Guo[38] and Asari[39], also provided further evidence in favour of an interface with added Ti_2O_3 rows. The second model was proposed by Pang[40] and is known as the Ti_3O_5 model. In this model, there is an added layer of Ti_3O_5 to the bulk termination. The second, complex (1x2) structure is a cross-linked reconstruction and has been observed in STM[41]. Bennett et al suggested that these added rows had a Ti_3O_6 stoichiometry[41], which was later confirmed by NC-AFM studies[42].

Another interesting feature of bulk rutile TiO_2 is the formation of crystallographic shear planes when it becomes even further reduced[43]. These often appear as linear features extending across large distances of the crystal, typically without regard for any other features on the crystal. These tend to increase in number as the crystal becomes more reduced. Eventually, the crystal becomes black and is too rough to be imaged by STM[30].

3.1.3 Strong Metal-Support Interaction effects

A topic of great interest in the last several years, an SMSI effect is typically observed on heating a metal on a reducible support (such as Pd on $TiO_2(110)$) to elevated temperatures in a reducing environment[44]. This typically leads to loss of reactivity (but not always) and so, as a real catalyst is often made of a metal oxide support with metal nanoparticles dispersed on its surface, it is necessary to use simpler model systems to understand the processes involved.

SMSI (Strong Metal-Support Interaction) of oxide supported metal catalysts was discovered by Tauster et al[45]. They coined the term “SMSI” to explain the suppression of the H_2 and CO_2 chemisorption capacity of metal clusters at high temperatures. The term was then later used to account for changes in activity and selectivity in group 8 metals when supported on reducible oxides and treated by high temperature reduction processes[46, 47]. It has also been found to have a negative effect on the reaction rate of other reactions, including alkane hydrolysis[48]. However, the effect is not always negative – it appears to have a positive effect on the CO-H_2 reaction[49].

Two factors contribute to the SMSI states; electronic and geometric factors[50]:

The electronic factor is determined by a perturbation of the electronic structure of the metal catalyst. This typically originates from an interaction between the cluster and the oxide support, for example charge transfer between the metal and oxide[51, 52].

The geometric factor is due to the physical covering of the metal particles by a thin layer of the reduced oxide support. This is referred to as the “encapsulation” or the “decoration” model. The support then blocks active sites on the catalyst surface[50], acting as a poison[53-55].

A number of experiments have shown encapsulation for different metal/oxide systems. Bernal and co-workers[56, 57] used HRTEM (high resolution transmission electron microscopy) to show that oxide layers form on top of the metal clusters in Rh/TiO_2 and Rh/CeO_2 systems. Diebold et al[58] recorded images of encapsulated Pt clusters on $TiO_2(110)$ with atomic resolution and proposed an oxygen terminated $TiO_{1.1}$ (111) double layer to be the covering layer. Bowker et al[59, 60] reported a similar well-ordered TiO or $TiO_{1.4}$ overlayer decorating Pd clusters after high temperature treatment. The presence of partially reduced oxides has been considered to be proof of encapsulation in a number of systems, including Pd/TiO_2[59], Pt/TiO_2[61-63] and Rh/TiO_2[64]. The partial reduction of metal ions (e.g. Ti^{n+} in TiO_m, where $n<4$ and $m<2$) was attributed to the formation of a reduced oxide layer on top of the metal clusters. DFT calculations of $TiO_x/Pt(111)$ systems revealed a preference for the initial Pt interface layer to consist of Ti with an O overlayer[65], which agreed with experimental STM and ISS observations observed by Dulub et al[58]. This also agrees with conclusions drawn by Bugyi et al after observing a large increase in the work function after annealing Rh/TiO_2 to ~1000 K. They suggested that the Rh had been encapsulated by a TiO_x layer, with a thickness of a few atomic layers, consisting of positively charged metal ions at the metal-oxide interface and negative oxygen ions in the topmost layer.

SMSI usually arises when metal/reducible metal oxide systems are heated under reducing conditions[59]. However, Bowker et al[60, 66] demonstrated novel SMSI phenomena on $Pd/TiO_2(110)$ which occurs by heating in an oxidising environment of low pressure O_2. O_2 preferentially adsorbs onto Pd nanoparticles then migrates/spills over onto the surrounding titania, accelerating the re-oxidation of $TiO_2(110)$[41, 67, 68]. This spillover process leads to burial of the Pd particles forming a new type of SMSI.

More recently, O'Shea[69] obtained TEM images of Co nanoparticles covered by a few atomic layers of TiO_x ($x<2$) after a reduction treatment (TPR). XPS showed that this might be Ti^{3+}.

Majzik[70] used AES and STM to show SMSI on Rh nanoparticles on $TiO_2(110)$. STM showed ordered decoration of TiO_x on Rh, exhibiting a “wheel structure.” This decoration was removed with a short sputtering (0.5 eV).

Linsmeier[71] used ISS, XPS and thermal desorption experiments to view SMSI after high-temperature reduction treatment. Thermal desorption spectra showed lots of CO adsorption on a normal, clean Rh/TiO_2 sample, and very little adsorption after SMSI had been induced. XPS showed Ti^{3+} present in the SMSI state.

Reactivity measurements by Bonanni[72] suggest that high temperature annealing of Pt on reduced TiO_2 results in the encapsulation of Pt by a reduced titania layer, agreeing with a mechanism proposed by Fu[50, 73]. Fu proposed that encapsulation depended on the amplified outward diffusion of Ti^{n+} toward the TiO_2 surface and the migration of TiO_x onto the surface of the metal[50]. Bowker and co-workers used a molecular beam reactor to study the sticking probability of CO on $Pd/TiO_2(110)$[44]. They found a substantial decrease in the sticking probability with increasing anneal temperature, suggesting that an SMSI effect deactivated the particle surface to CO adsorption.

SMSI of Pd on $TiO_2(110)$ formed by annealing in UHV has also been looked at with coaxial impact collision ISS (CAICISS) and reflection high energy electron diffraction (RHEED), suggesting that the Pd is encapsulated by TiO_x (x is ~2)[74]. In-situ STM studies of a Pd film in the SMSI state annealed to higher temperatures in O_2 showed that the film became thicker[75]. It was surmised that either the layer had become TiO_2, or that mass transport of Ti to the surface had occurred.

SMSI of Pd/TiO_2 catalysts has also been found to be influenced by the titania polymorph[76]. Anatase TiO_2 supported palladium exhibited SMSI at lower temperatures than a rutile supported catalyst, which is related to the fact that rutile is more stable.

Encapsulation mechanism:

It is accepted that encapsulation involves mass transport from the oxide support on to the surface of the metal particle[50]. Several different mechanisms have been proposed to explain encapsulation.

Taglauer and Knozinger[77] correlated the SMSI state with the surface energy (γ) of the oxide supports, noting that oxides with low surface energy e.g.

TiO_2, V_2O_5, undergo SMSI more easily than oxides with relatively high surface energy, eg SiO_2 and Al_2O_3.

Gao[62] et al suggested that metals with high surface energy (e.g. Pt and Pd, but not Au and Cu) favour encapsulation. Minimisation of surface energy seems to be one of the main driving forces for encapsulation[62, 77].

The effect of subsurface non-stoichiometry of TiO_2 on encapsulation of Pt and Rh was studied in great detail[62, 64], concluding that the decoration of clusters mainly depends on the existence of oxygen vacancies in the TiO_2 which were introduced by sputtering or reduction.

Fu and Wagner[50] used XPS, AES and RBS (Rutherford backscattering spectrometry) to try to work out the influence of the oxides electronic structure on the encapsulation process on $Pd/TiO_2(110)$. They came to the conclusion that encapsulation depends on the electronic structure of TiO_2, and decided on the following pre-requisites for the encapsulation of metal clusters on oxide supports:

1) $E_{f\,(oxide)} > E_{f\,(metal)}$ (E_f is the fermi energy level - in the case of SMSI with TiO_2, the reaction process depends on the amplified outward diffusion of Ti^{n+} toward the TiO_2 surface and the migration of TiO_x onto the surface of the metal clusters)

2) Reduced or n-type doped oxides with small surface energies e.g. TiO_2, CeO_2

3) Metals with large work functions and large surface energies eg Pd, Pt, Rh, Ni, Ir

4) Sufficiently high temperature to activate the transport processes

3.1.4 Growth mode of nanoparticles and thin films

A metal interacts with an oxide surface in a variety of ways. Typically, the structure of the metal surface when deposited depends on charge transfer between the metal and the support, as well as the electronic configuration. XPS can be used to look at binding energies and obtain information on the chemical bonding and interactions at the surface. ISS can be used to see what chemical species are present on the surface. LEED and STM can sometimes be used to show reconstruction and to see structures at the surface.

By constantly depositing the metal at the surface, a metal film can be formed. The change in peak intensities in XPS and ISS can give information on how the film grows on the surface.

It has been recognised for several decades that vapour-deposited thin films can grow in a number of distinct modes[78]. In a landmark paper, Bauer[79, 80] proposed that there were three principal growth modes, named after the authors who originally discovered/considered them: Volmer and Weber[81]; Stranski and Krastanov[82]; Frank and van der Merwe[83, 84]. These can be distinguished based on their surface free energy criteria[78]. The growth mode is governed by thermodynamic and kinetic factors dependent on the substrate/adsorbate combination[78]. If the adsorbate has a surface energy, γ_A, the substrate a surface energy, γ_S, and the interface between the two an energy, γ_I, then:

$$\Delta\gamma = \gamma_A + \gamma_I - \gamma_S \leq 0$$

will favour FM growth, whilst:

$$\Delta\gamma = \gamma_A + \gamma_I - \gamma_S > 0$$

will favour SK or VW growth[85].

1. Volmer-Weber

Figure 3-4 – Volmer-Weber growth mode

Shown in Figure 3-4, Volmer-Weber (VW) growth is also known as “3D island” growth. Adatom-adatom interactions are stronger than adatom-surface interactions. This leads to the formation of 3D islands or clusters, which eventually grow enough to become a multi-layer film.

2. Frank-Van der Merwe

Figure 3-5 – Frank-Van der Merwe growth

Figure 3-5 shows Frank-Van der Merwe (FdM) growth, also referred to as layer-by-layer growth, as a complete film is formed before the next layer of film begins to grow. In this case, adatoms attach preferentially to the surface.

3. Stranski Krastanov

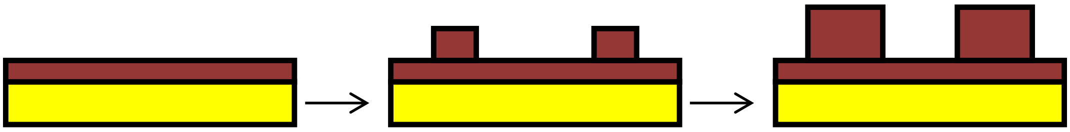

Figure 3-6 – Stranski Krastanov growth

Stranski Krastanov (SK - Figure 3-6) is a combination of the previous two growth modes, showing both 2D layer and 3D island growth. There is a transition from layer-by-layer to island-based growth at a critical layer thickness, which varies depending on the surface and the film.

3.1.4.1 Distinguishing growth mode using ISS and XPS

The analysis of the growth mechanisms of thin films has usually been studied with AES or XPS, by plotting the intensity of a peak of the deposited material against the deposition time[78]. When using AES, this is called an Auger signal – deposition time (AS-t) plot. This method assumes that the flux of the deposit (the rate of flow of a property per unit area, with dimensions $[quantity].[time]^{-1}.[area]^{-1}$)[86] and the sticking probability remain constant with time.

Figure 3-7 shows how the variations in the Auger signal vs time can be used to help determine growth modes, as described by Argile[78]. In the case of the Volmer-Weber mechanism (Figure 3-7a), the S-t plot consists of a smooth decay of the substrate signal and a simultaneous smooth increase of the adsorbate peak intensity. The exact rate of decay of the substrate peak (and increase of the adsorbate signal) will depend on the shape of the clusters formed on the surface, but will always be slower than the FdM mechanism[87]. In Frank-van der Merwe growth, growth of a new atomic layer does not start until the preceding layer is complete. This leads to break points in the graph (as shown in Figure 3-7b), where the gradient of the curve changes abruptly. These break points correspond to the completion of each monolayer. Stranski-Krastanov growth leads to an intermediate of the two plots, with a linear segment as the initial layer adsorbs, followed by a more gradual change similar to VW growth (Figure 3-7c).

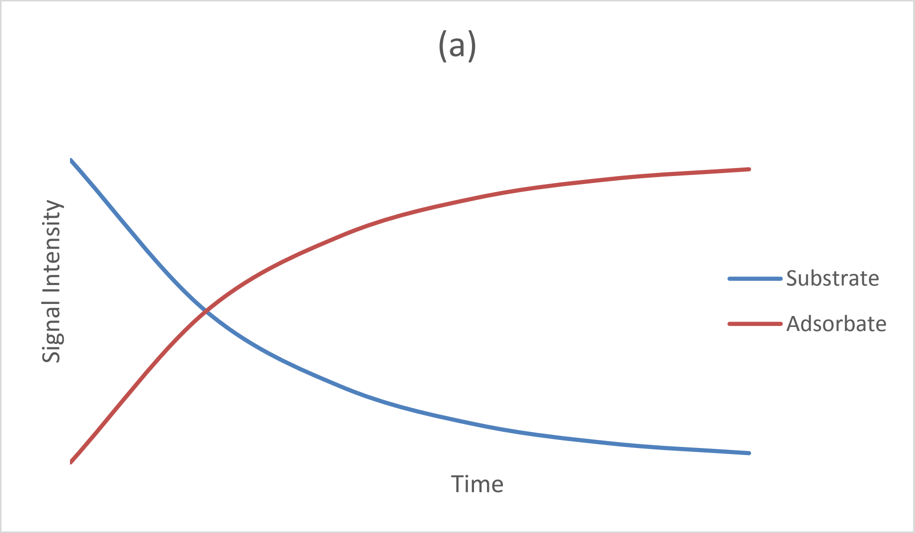

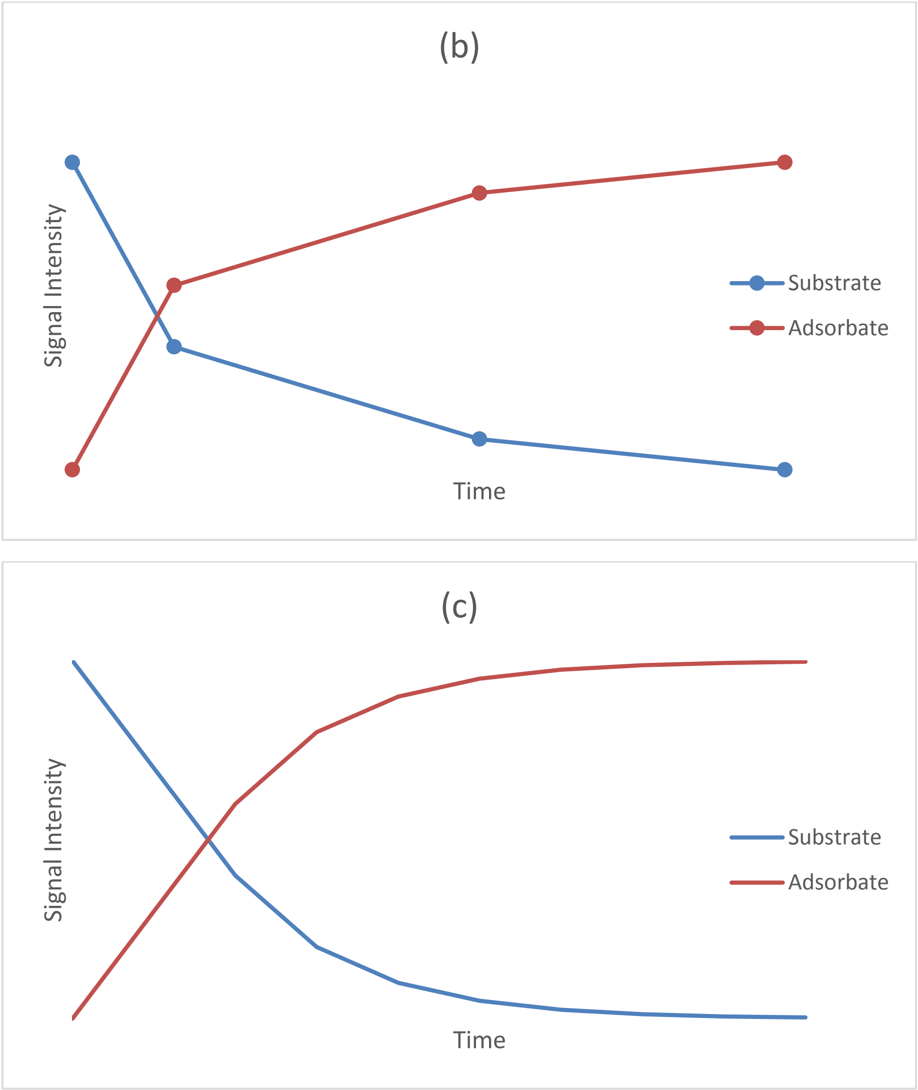

Figure 3-7 – Theoretical Auger signal-time plot for the variation of the adsorbate and the substrate signal during (a) VW, (b) FvdM and (c) SK growth modes

However, a problem with these S-t plots is that they struggle to differentiate between Volmer-Weber and Stranski-Krastanov growth, as the two plots can look very similar. Diebold and Madey[88] proposed a method to use LEIS measurements to distinguish between growth modes. In the case of VW growth, the substrate is expected to continue to give a signal even at high coverages of adsorbate, whereas this would not be the case in FM or SK growth modes. LEIS, however, cannot distinguish between SK and FM growth. In both cases, the adsorbate signal should increase linearly with coverage whilst the substrate signal should decrease linearly. Once the first monolayer is completed, the substrate signal should drop to zero and the adsorbate signal should remain constant, making it impossible to distinguish between the different mechanisms of FM and SK growth. For VW growth, both the substrate and adsorbate signals should be smooth functions of adsorbate coverage[88].

3.1.4.2 Growth of Pd on $TiO_2(110)$

There have been a variety of studies on the growth of Pd on $TiO_2(110)$, as summarised by Diebold[6], Fu[73] and Thornton[15]. Growth of Pd and the other group 10 metals on $TiO_2(110)$ is thought to be one of two mechanisms. SPM, ISS and RHEED studies have shown that Pd grows as either 3D islands or via a 2D islanding mechanism[89]. 2D islanding growth is a kinetically limited 3D growth, where 2D growth occurs up to a critical; submonolayer coverage, after which 3D growth takes over, as described by Ernst et al[90]. For Pd, the transition to 3D islanding is thought to occur at a coverage of ~0.0012 monolayers[89]. However, it has been found that the coverage range of 2D particle growth can be extended by enhancing the kinetic hindrance for particle growth[91]. This can be achieved by reducing and roughening the TiO_2 surface by prolonged sputtering before metal deposition. It has been found that Pd grows preferentially on step edges rather than terraces[15].

3.2 Experimental

The experiments were carried out as described in Chapter 2, in the system referred to as “UHV1.”

A $TiO_2(110)$ single crystal was placed into the machine via the fast-entry lock and subject to cleaning cycles until the ISS and XPS showed no contaminations. The cycles consisted of sputtering (1 keV, 20-40 minutes) at room temperature, followed by annealing to 873 K for 15 minutes.

When trying to achieve a well-oxidised TiO_2 surface, the sample was heated in oxygen (10^{-6} mbar) at temperatures up to 873 K for 10 minutes.

Palladium was deposited on to the crystal by MVD (metal vapour deposition). A current was passed through the metal filament and allowed to degas for 20 seconds. The crystal was then moved below the filament, approximately 1-2 cm below.

Three surfaces were prepared – a sputtered surface, a sputter-annealed surface, and an oxidised surface. All three surfaces were initially cleaned via sputter-anneal cycles, as described above. The sputtered surface was then prepared by sputtering the sample for 60 minutes. The sputter-annealed surface was sputtered and then annealed in UHV for 15 minutes. The oxidised surface was prepared by sputtering, then annealing in oxygen for 60 minutes and then cooling in oxygen.

XPS peak fitting was carried out using CasaXPS[92]. Fitting of the Ti2p peak was carried out according to the observations of Carley et al[93]. The $2p_{3/2}$ peaks were confined to 459, 457.5 and 455.5 eV for the $Ti^{4+,\ 3+\ \&\ 2+}$ components respectively. The $Ti^{4+,\ 3+\ \&\ 2+}$ $2p_{1/2}$ components were constrained to a distance of ~6, 5 and 5.5 eV respectively from their respective $Ti2p_{3/2}$ components. There is very little information on the peak shapes of the Ti^{2+} and $^{3+}$ components of Ti, so a best approximation was used, using the shape of Ti^{4+} in stoichiometric TiO_2 Ti2p spectra as a guidance, keeping the peak widths constant. The XPS were referenced to the O1s peak at 530.4 eV[94].

3.3 Results and Discussion

3.3.1 Characterising the $TiO_2(110)$ surface

The observed structure of the $TiO_2(110)$ single crystal depends on how it was prepared, and can vary depending on whether it was sputtered (length of time and voltage of argon ions) or annealed (both the temperature and anneal time are important), as well as its previous history. The effect of sputtering and annealing is examined in sections 3.3.2 and 3.3.3 respectively.

After several cleaning cycles (see chapter 2) a 1 x 1 LEED pattern was obtained, as shown in Figure 3-8. An ISS of this clean TiO_2 sample is shown in

Figure 3-9. The ISS shows very little surface contamination; the peak at 410 eV is oxygen, and the peak at 722 eV is titanium. The XPS of this TiO_2 sample is shown in Figure 3-10 and Figure 3-11. Figure 3-10 shows the Ti2p spectra. The surface is highly oxidised with peaks occurring at a binding energy of 459 eV (Ti $2p_{3/2}$) and 465 eV (Ti $2p_{1/2}$), characteristic of the Ti^{4+} oxidation state. Figure 3-11 shows the O1s spectra, with the 1s peak occurring at 530.4 eV.

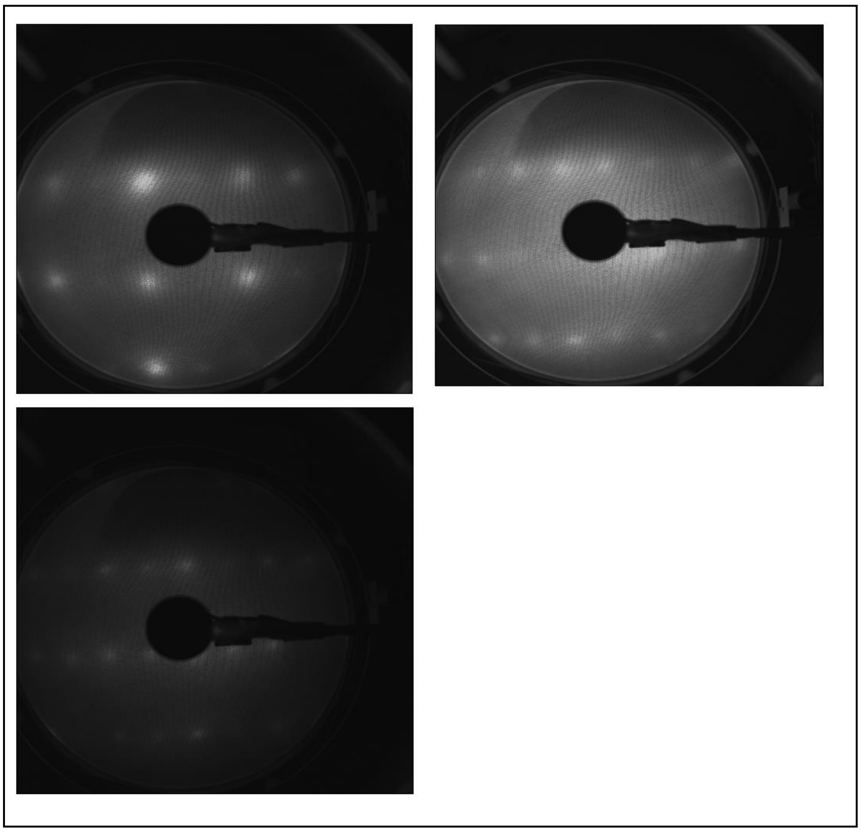

Figure 3-8 - LEED of clean TiO_2 surface at (a) 80 eV, (b) 100 eV & (c) 120 eV

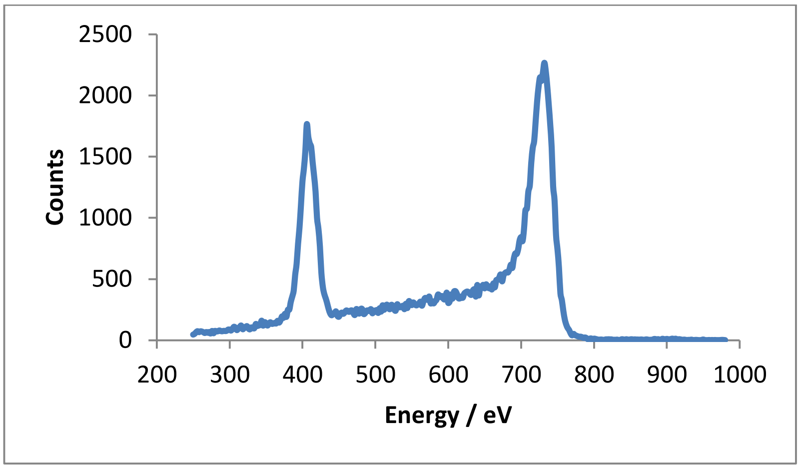

Figure 3-9 - ISS of clean TiO_2 (110)

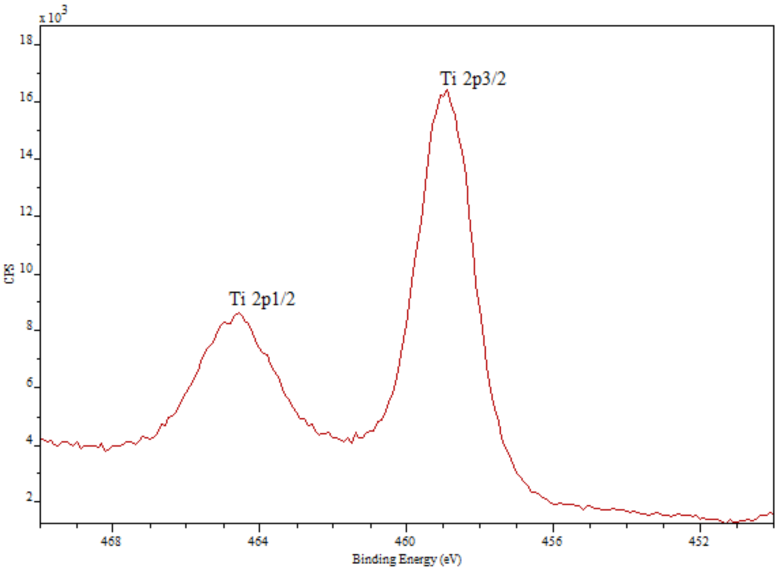

Figure 3-10 - Ti2p XPS region of clean TiO_2

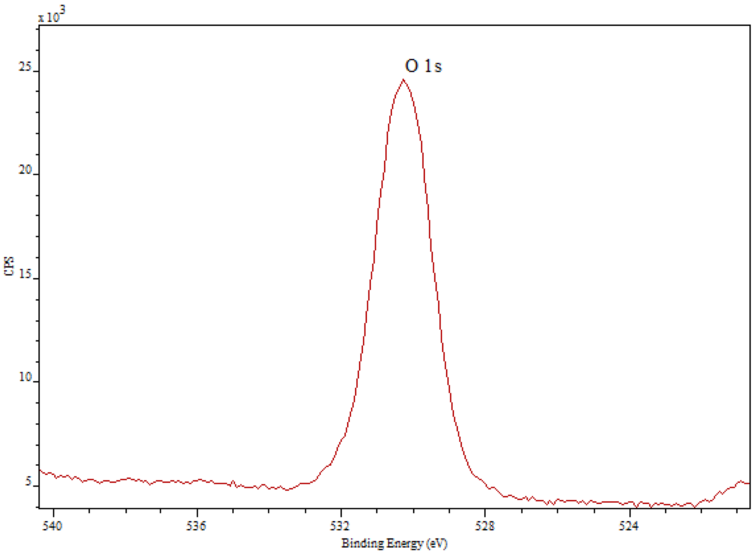

Figure 3-11 - O1s XPS region of clean TiO_2

3.3.2 Effect of sputtering TiO_2 (110) on ISS & XPS

When the sample is sputtered, not only are contaminants removed, but the surface is damaged and becomes rough and disordered. Sputtering preferentially depletes surface oxygen from TiO_2[22] until a steady state level of surface reduction has been established. After sputtering LEED only shows a uniform background, indicating that there is an absence of crystallographic order. XPS and ISS are both also strongly affected by sputtering.

Figure 3-12 shows how sputtering over an extended period of time affects the TiO_2 surface. Figure 3-13 and Figure 3-14 highlight that the Ti/O area ratio in the ISS and the Ti2p/O1s XPS area ratio respectively both increase on sputtering. This agrees with previous research by Kelly and Lam on titania surfaces. They found that TiO_2 shows preferential oxygen sputtering[95], such that the single crystal will first amorphise, then lose oxygen, and eventually crystallise as Ti_2O_3.

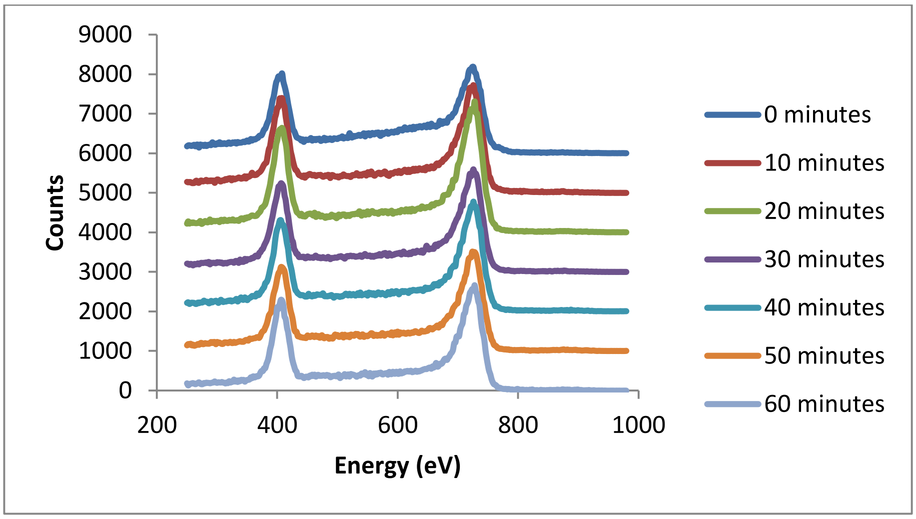

Figure 3-12 - The effect of sputtering on the TiO_2 ISS, from 0 to 60 minutes of sputtering

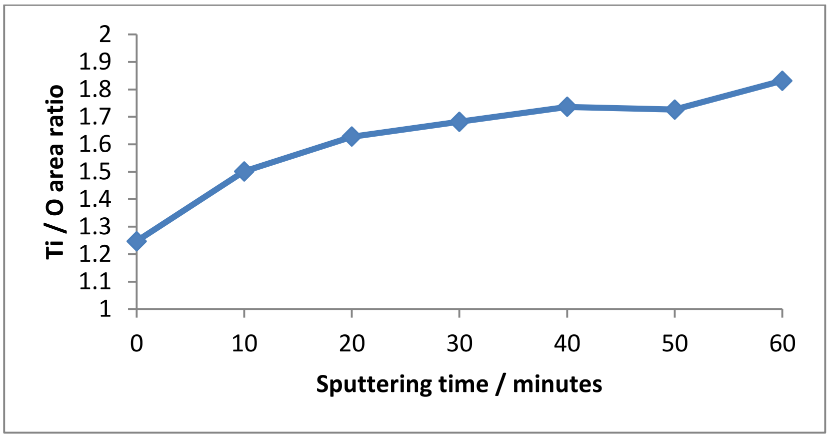

Figure 3-13 - How the Ti/O area ratio in the ISS is affected by sputtering

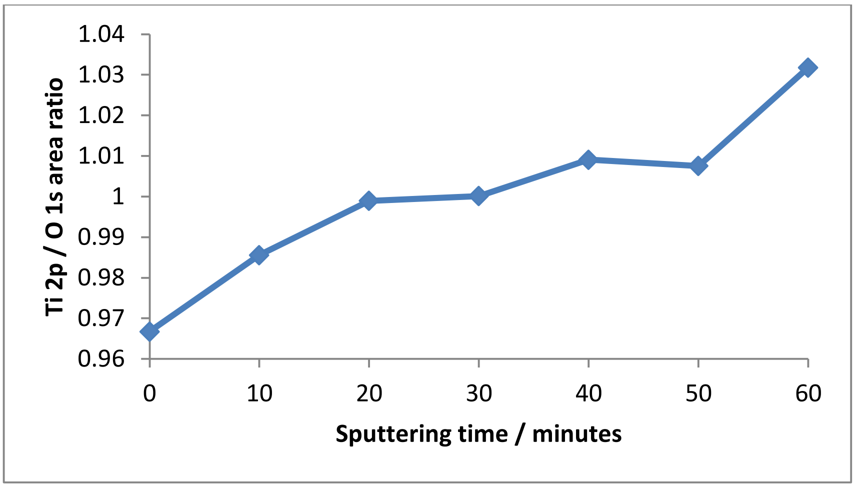

Figure 3-14 - How the ratio of the area of the Ti 2p peak vs the O 1s peak is affected by sputtering

Figure 3-15 shows how the shape of the Ti2p XPS spectra changes on sputtering. Curve (I) shows a highly oxidised surface with peaks at a binding energy of 459 eV and 465 eV for the $2p_{3/2}$ and $2p_{1/2}$ states respectively, characteristic of the Ti^{4+} oxidation state. Curve (II) shows the TiO_2 surface after it has been heavily sputtered at ambient temperature. The peaks have become very poorly defined and broadened, typical of a reduced titania surface. Ti^{3+} and Ti^{2+} components have appeared in the spectra, as observed by Tanaka[96], indicating a decrease in the cation charge at the surface. Figure 3-16 shows the O1s XPS before and after heavy sputtering, showing a decrease in the O1s signal after sputtering.

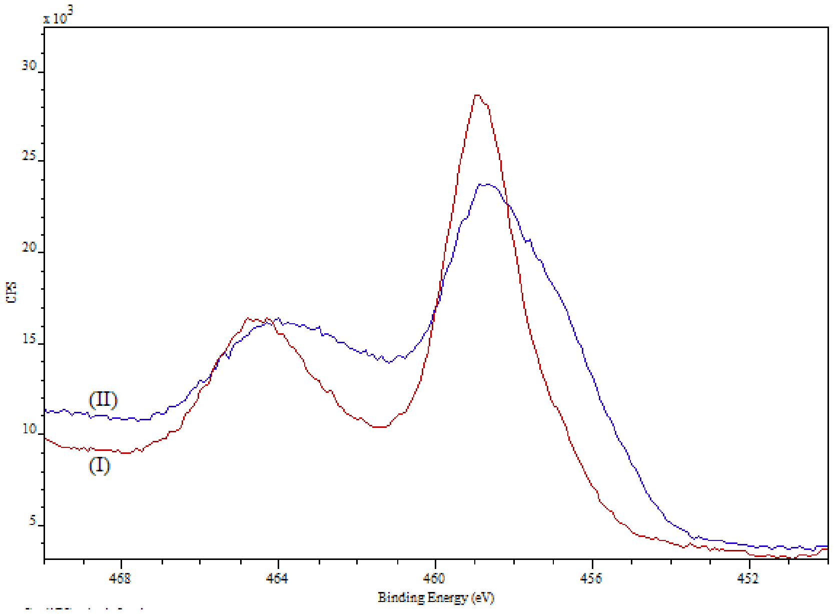

Figure 3-15 - Ti2p XPS of TiO_2 (I) before sputtering and (II) after 300 minutes of sputtering

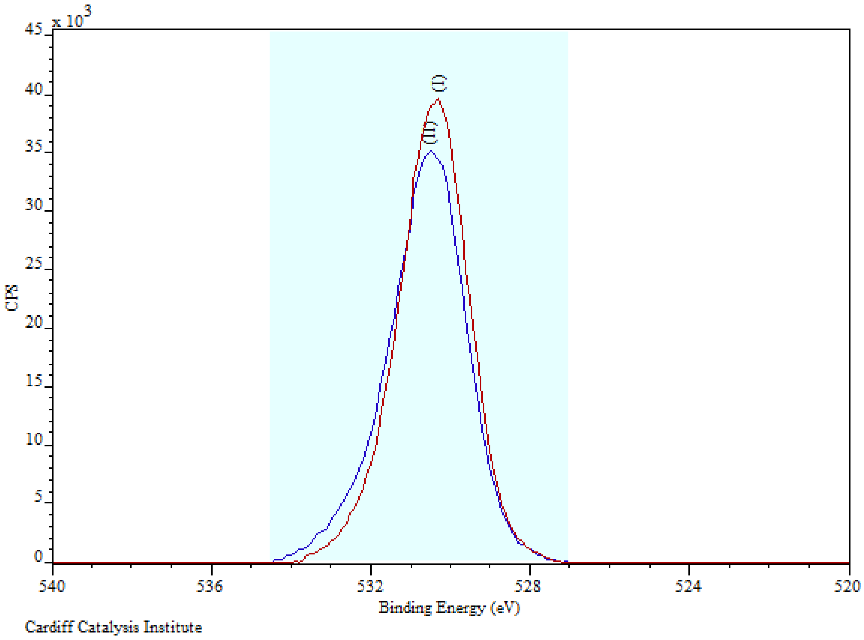

Figure 3-16 - O1s XPS of TiO_2 (I) before sputtering and (II) after 300 minutes of sputtering

3.3.3 Compare heating in UHV and in O_2

The effect of heating the TiO_2 sample in different environments was investigated, in order to examine the reoxidation of the TiO_2 surface. As mentioned above, sputtering preferentially removes oxygen from the TiO_2 surface, creating defects. In order to create a well ordered surface again, this surface oxygen needs to be replaced.

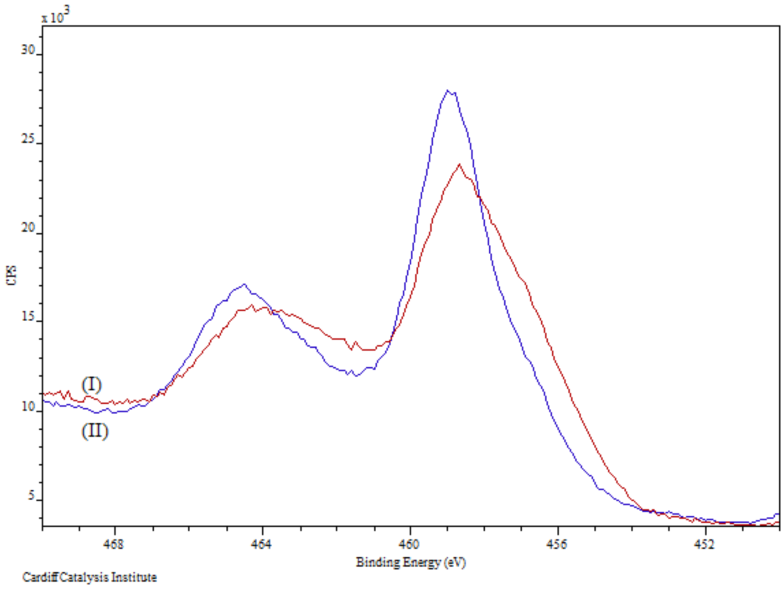

Figure 3-17 - Ti2p XPS of the TiO_2 sample (I) before (red) and (II) after (blue) annealing to 873 K in UHV

Figure 3-17 shows the Ti2p region before and after heating in UHV. The surface was heavily sputtered, giving the broad signal shown in curve (I). This was peak fitted (Figure 3-18), giving 47% Ti^{4+}, 35% Ti^{3+} and 18% Ti^{2+}. This was then heated in UHV up to 873 K and characterised at stepwise increments (every 50 K), as shown in Figure 3-19. There is not much change in the oxidation of the TiO_2 surface until approximately 773 K. At this point, the peaks begin to change, and by 873 K the composition of the surface has changed to approximately 66% Ti^{4+}, 25% Ti^{3+} and 9% Ti^{2+}, as shown in Figure 3-20. This observation agrees with Henderson et al[22, 97], who used SSIMS (static secondary ion mass spectrometry) to show that TiO_2 is able to replenish its surface oxygen on heating, transporting surface defects into the bulk and restoring surface stoichiometry. This can be further illustrated by looking at the O1s XPS (Figure 3-21) – there is a slight increase in the O1s peak after annealing to 873 K. The O1s peak is also wider prior to annealing – this is due to the presence of H_2O in the system, present as hydroxyl groups on the surface of the titania, which is then desorbed on annealing.

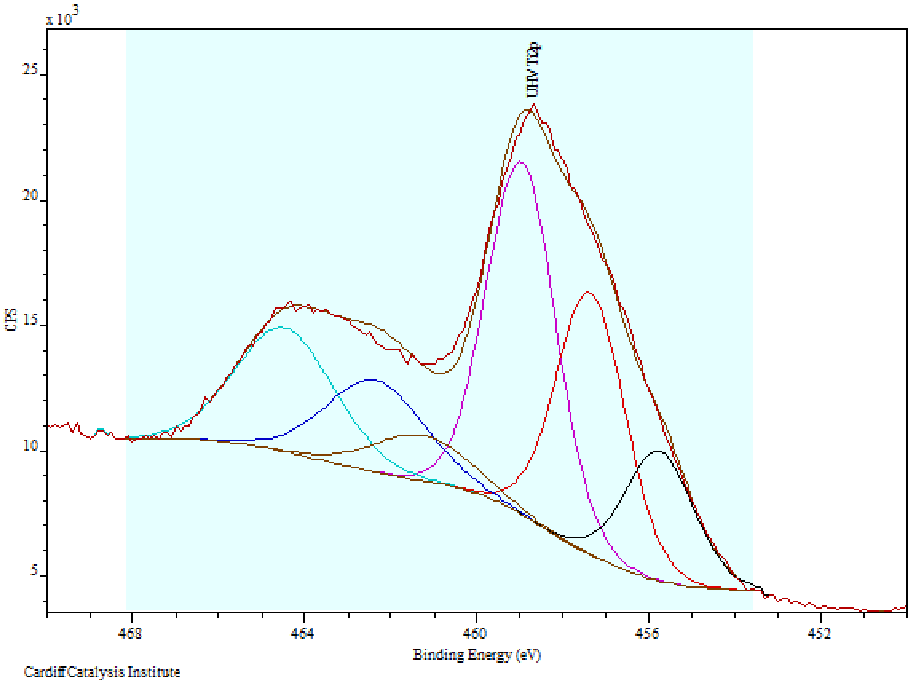

Figure 3-18 - Peak fitting of Figure 3-17, curve I

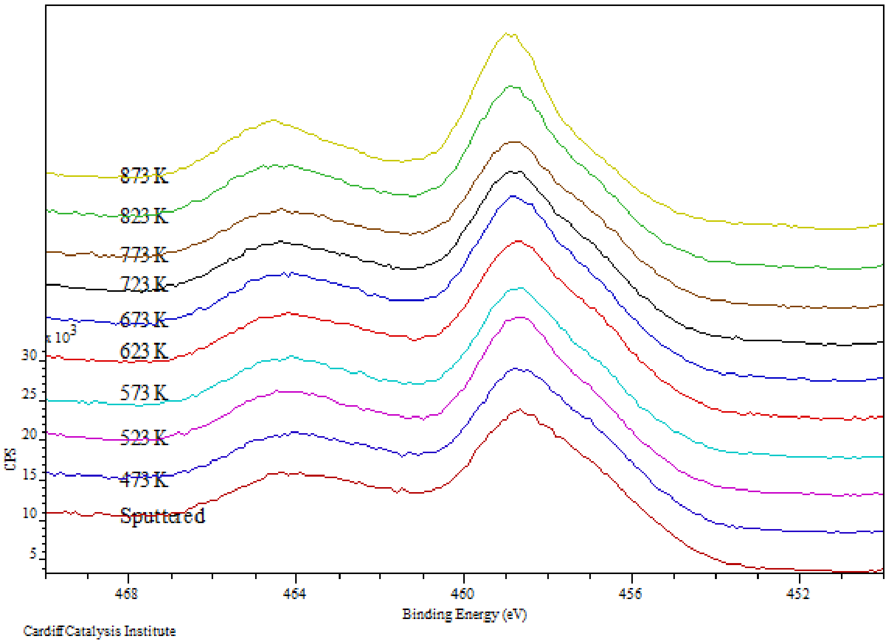

Figure 3-19 - Change in the Ti2p XPS as it is annealed at increasing temperature in UHV

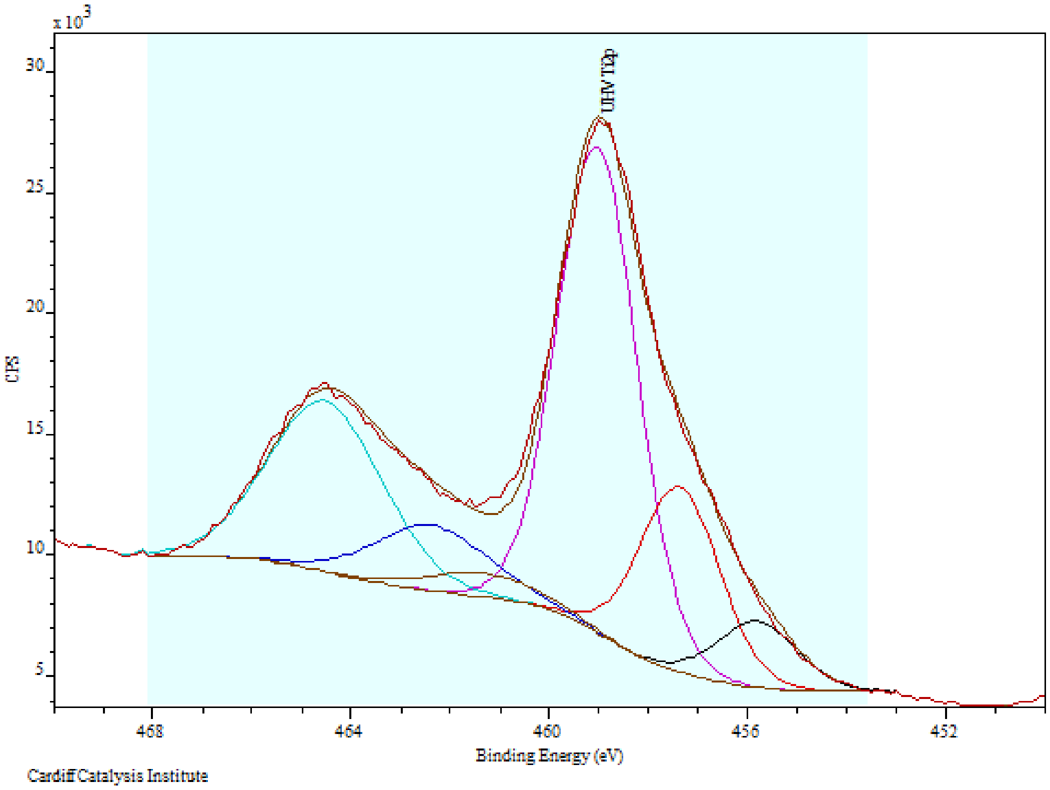

Figure 3-20 - Peak fitting of Figure 3-17, curve II

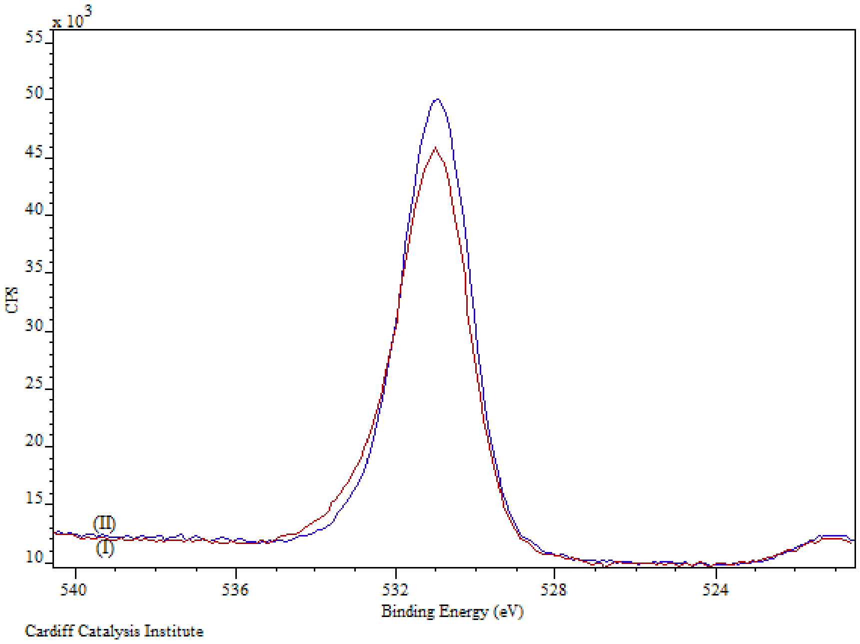

Figure 3-21 – O1s XPS of the TiO_2 sample before (I – red) and after (II – blue) annealing to 873 K in UHV

Figure 3-22, on the other hand, shows the Ti 2p region before and after heating in O_2 ($2x10^{-6}$ mbar). Again, the TiO_2 sample was heavily sputtered, giving 39% Ti^{4+}, 36% Ti^{3+} and 25% Ti^{2+}, as shown in Figure 3-23. The sample was then heated up to 873 K and characterised at stepwise increments (Figure 3-24). Changes in the Ti2p spectra begin to occur at temperatures as low as 523 K, and by 873 K the surface appears almost fully oxidised, with 93% Ti^{4+} and 7% Ti^{3+} (Figure 3-25). Figure 3-26 shows a plot of the effect of annealing on the Ti2p signals. It is clear that, although annealing in UHV has an oxidative effect, annealing in oxygen, even at lower temperatures, is much more effective. Figure 3-27 shows that the ratio of the Ti2p peak to the O1s peak doesn't change very much when annealing in UHV. However, when annealing in O_2, it changes drastically. This is further illustrated by comparing the O1s spectra - Figure 3-28 shows the O1s spectra after annealing in oxygen. There is a much greater increase in the O1s signal after annealing in oxygen than there is after annealing in UHV (Figure 3-21). This shows that TiO_2 can oxidise itself much easier by pulling in O_2 from the atmosphere rather than using oxygen from the bulk. Table 3-1 also backs this up – the Ti/O area ratio in the ISS changes by a very small amount between sputtering and annealing in UHV. After annealing in oxygen however, the Ti/O ISS area ratio decreases by 30%, from 2.82 to 1.97. This is because it has previously been shown that oxygen is taken up by the surface by reaction with interstitial ions, resulting in the growth of new TiO_2 layers[68] -Ti^{3+} migrates from subsurface sites back to the surface and reacts with the gaseous oxygen. Bennett et al also found that, the greater the oxygen pressure, the greater the rate of growth[98].

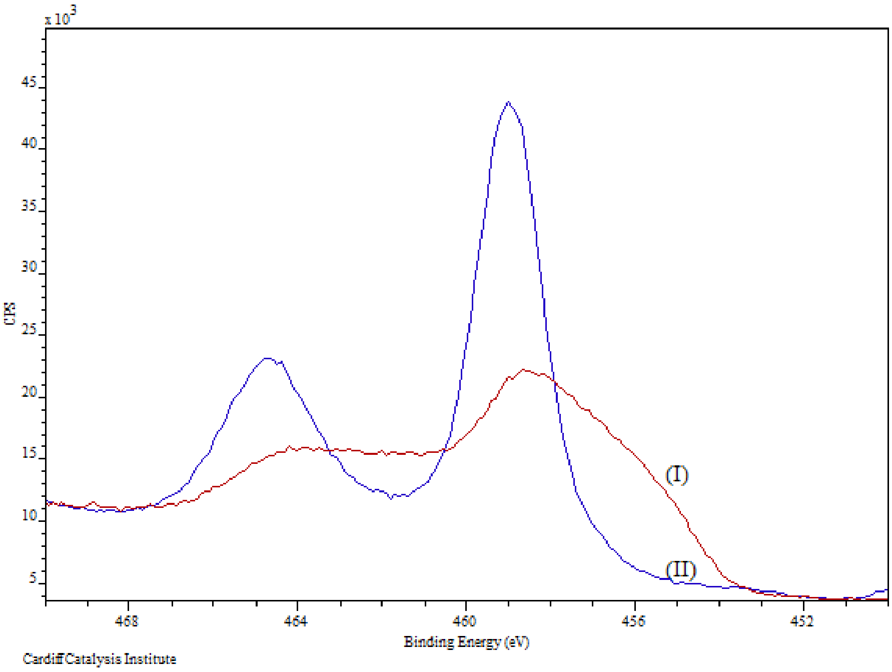

Figure 3-22 - Ti2p XPS of the TiO$_2$ sample before and after annealing to 873 K in O$_2$ (2x10^{-6} mbar)

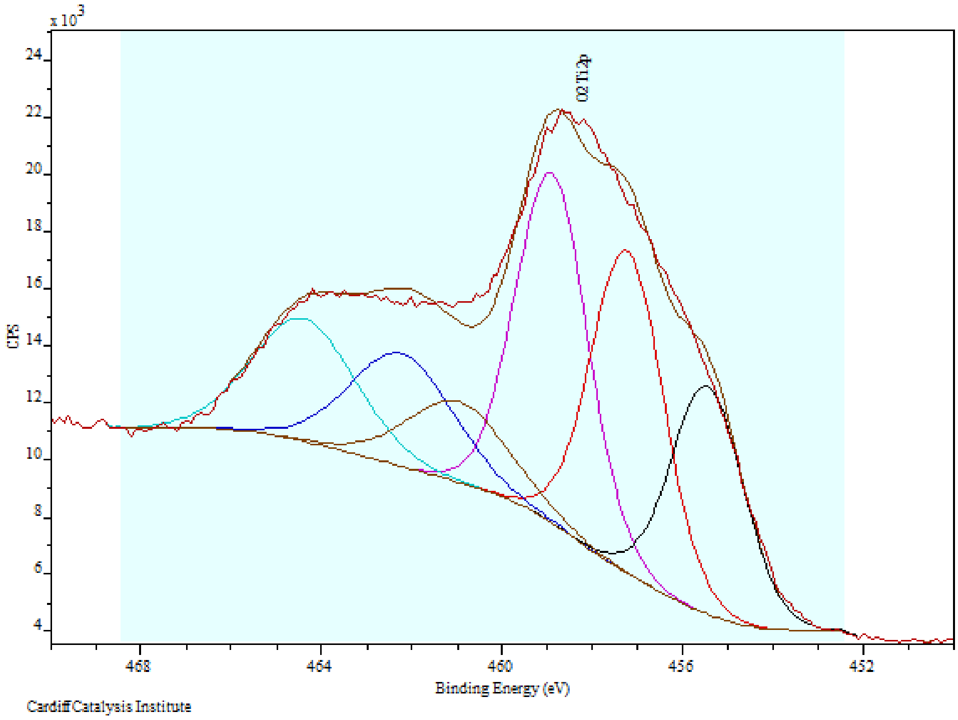

Figure 3-23 - Peak fitting of Figure 3-22, curve I

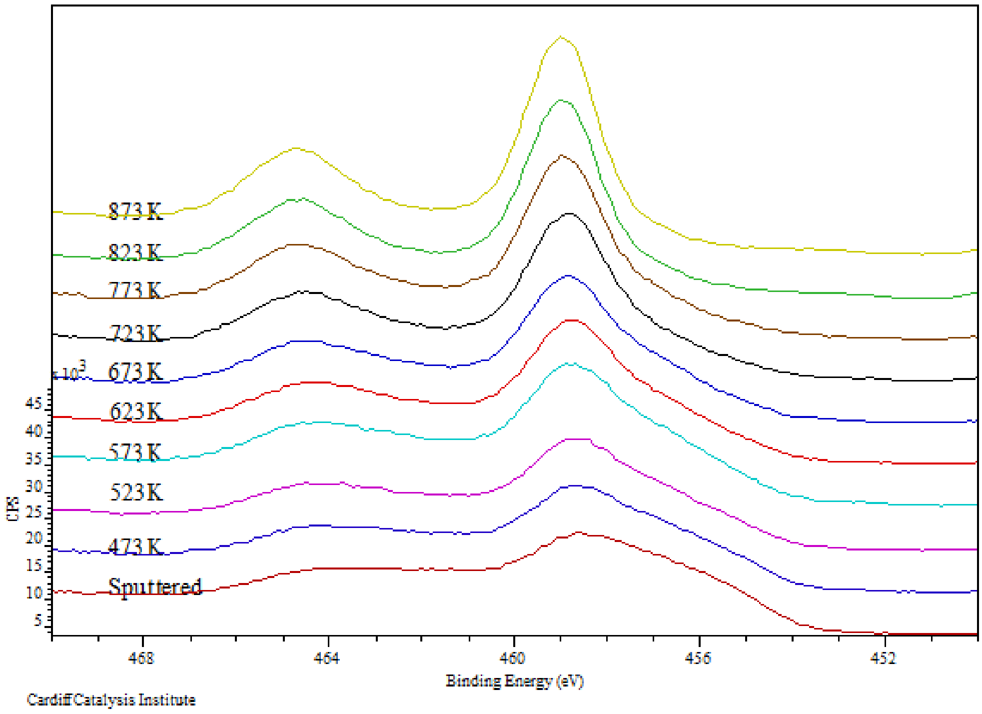

Figure 3-24 - Change in the Ti2p XPS as it is annealed at increasing temperature in O_2 ($2x10^{-6}$ mbar)

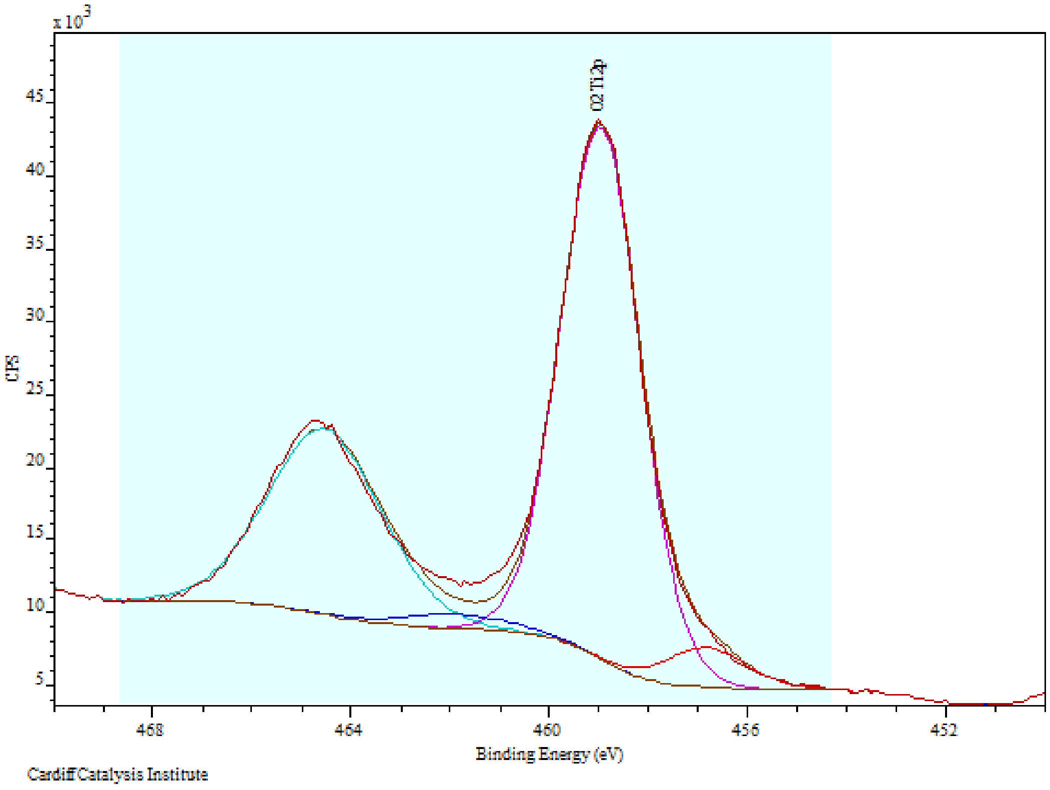

Figure 3-25 - Peak fitting of Figure 3-22, curve II

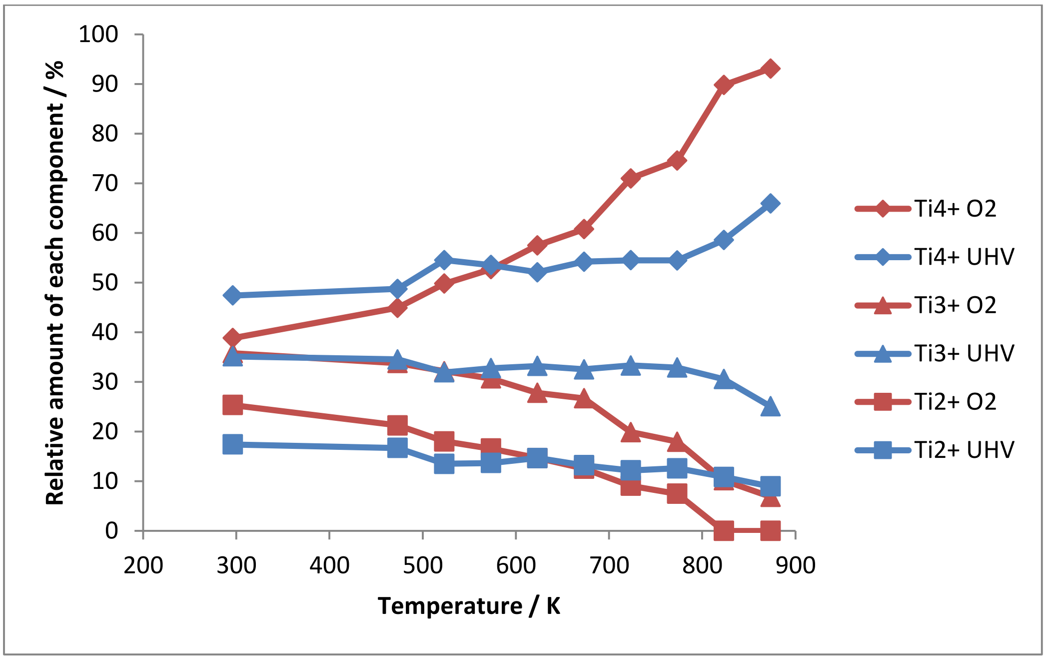

Figure 3-26 - Variation of the various Ti states as a function of anneal time for a sputtered surface being annealed in O_2 and in UHV

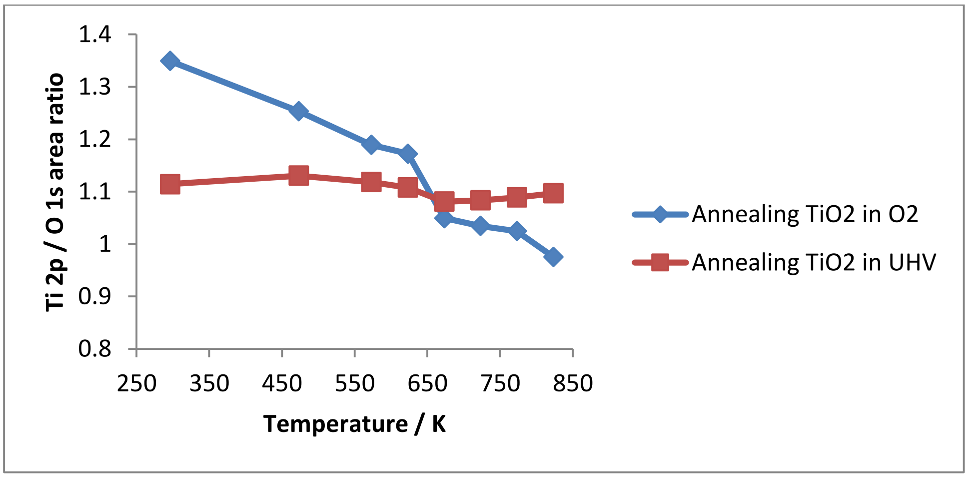

Figure 3-27 - Comparison of the change in Ti2p/O1s ratio when annealing in oxygen and in UHV

Surface	Ti/O ISS ratio
Sputtered	2.82
Sputtered-annealed	2.72
Oxidised	1.97

Table 3-1 - Ti/O ISS area ratios for the TiO_2 surface after sputtering, annealing in UHV and annealing in O_2

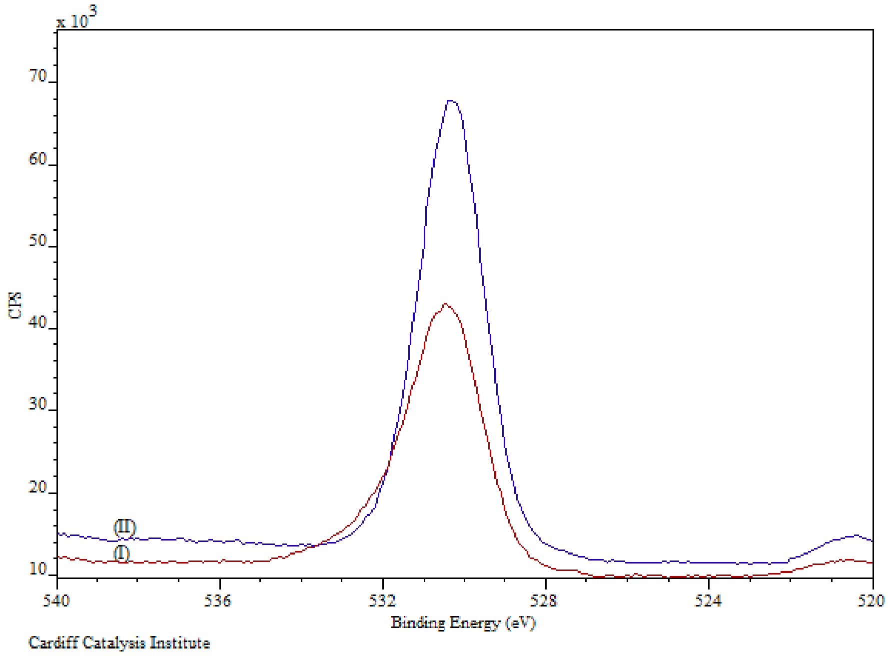

Figure 3-28 – O1s XPS of the TiO_2 (I) before and (II) after heating to 873 K in O_2

3.3.4 Preparation of Pd/TiO_2

Palladium was deposited on to each of these surfaces with metal vapour deposition. The length of time and current applied to the palladium evaporator vary with the state of the filament. A new filament will have more palladium than an old one, and so a low current and short time will be sufficient to deposit the metal. Over the lifetime of the filament, higher current and longer deposition times will be required to achieve an equal coverage. The current used was typically ~3A.

The ISS (Figure 3-29) shows a large palladium peak at 876 eV. It appears that there is a thick film of palladium on the surface, as the titanium and oxygen peaks are much, much smaller. The Pd 3d XPS peak is shown in Figure 3-30. It has a doublet structure, with the peak at 335 eV corresponding to $Pd3d_{5/2}$ and the peak the 340 eV corresponding to $Pd3d_{3/2}$. The $3d_{5/2}$ peak is 1.5 times bigger than the $3d_{3/2}$ peak, due to the spin orbit splitting. A more in-depth look at the deposition of palladium on to $TiO_2(110)$ follows in section 3.3.5.

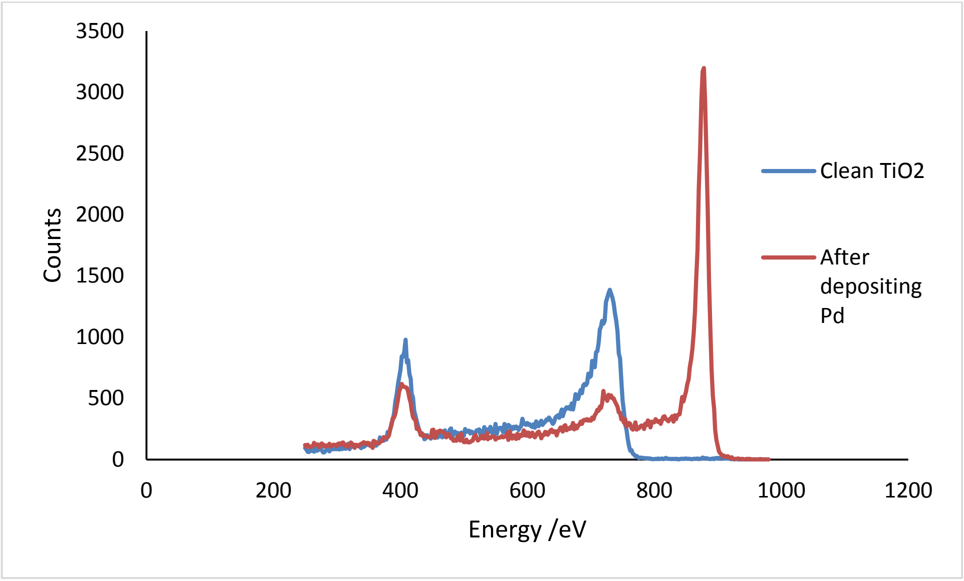

Figure 3-29 - Example ISS spectra of the TiO_2 sample after dosing with Pd

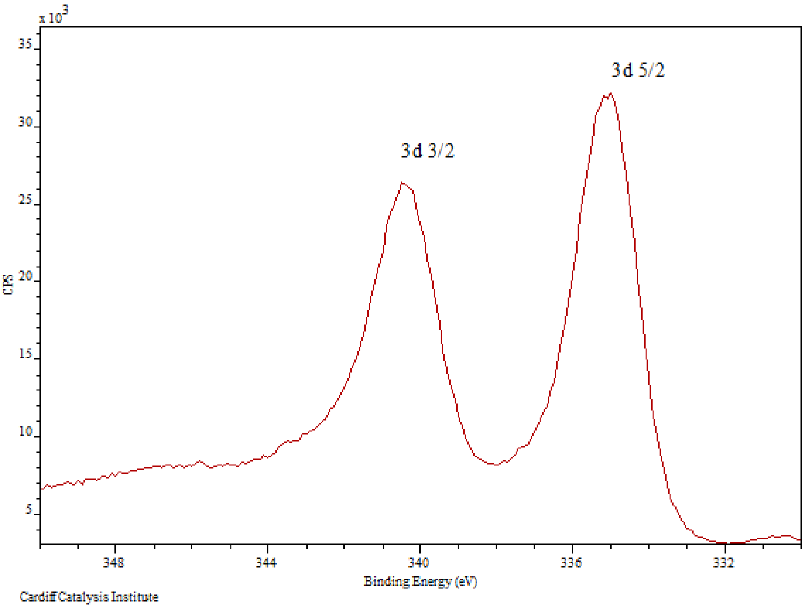

Figure 3-30 - Example XPS spectra of the Pd 3d region, after dosing TiO_2 with Pd

Immediately after depositing the Pd, an attempt was made to obtain a LEED pattern. This was unsuccessful, suggesting that the Pd had deposited in a random, unordered manner. Annealing to 873 K failed to give a good LEED pattern. The effect of heating Pd/TiO_2(110) is investigated further in this chapter, in section 3.3.6.

Palladium was removed from the surface with alternate cycles of ion bombardment at room temperature (1 keV) and annealing to 873 K for 10 minutes, and monitored using ISS and XPS.

3.3.5 Depositing Pd on differently prepared TiO_2 surfaces

The $TiO_2(110)$ surface was prepared in several different ways before the deposition of Pd, as follows:

a) sputtered at ambient temperature
b) sputtered then annealed to 873 K, and
c) sputtered then annealed to 873 K in the presence of $2x10^{-6}$ mbar of O_2 for 60 minutes.

The Ti2p spectra of each surface before Pd deposition is shown in Figure 3-31. Figure 3-31c shows a highly oxidised surface, as described in section 3.3.1. Figure 3-31a shows the surface after sputtering at ambient temperature, and Figure 3-31b shows the surface after sputtering and then annealing in UHV. The growth of Pd on each of these three different surfaces has been investigated using ISS and XPS.

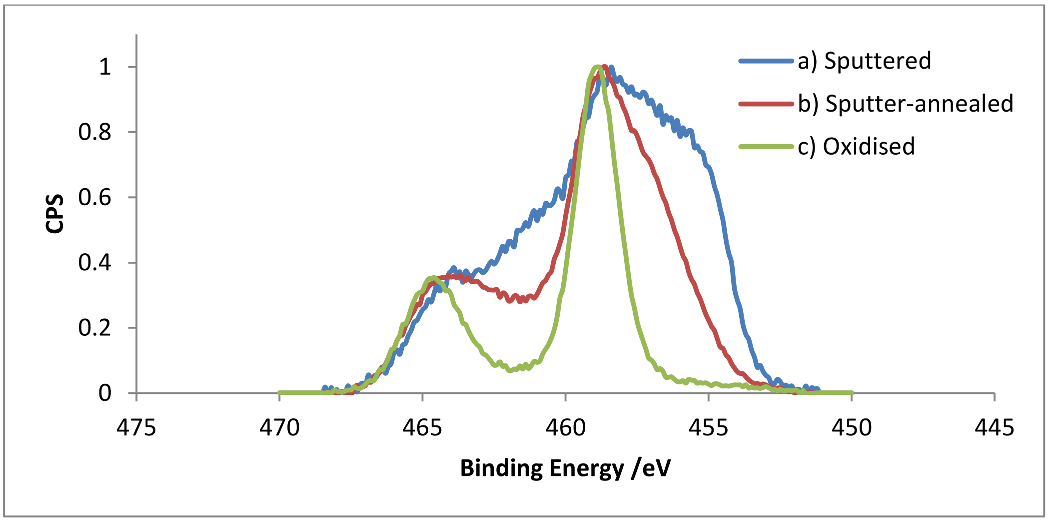

Figure 3-31 - Ti 2p spectra from the $TiO_2(110)$ surface after a) sputtering, b) sputtering and annealing to 873 K for 10 minutes and c) sputtering and then annealing at 873 K in oxygen ($2x10^{-6}$ mbar) for 60 minutes

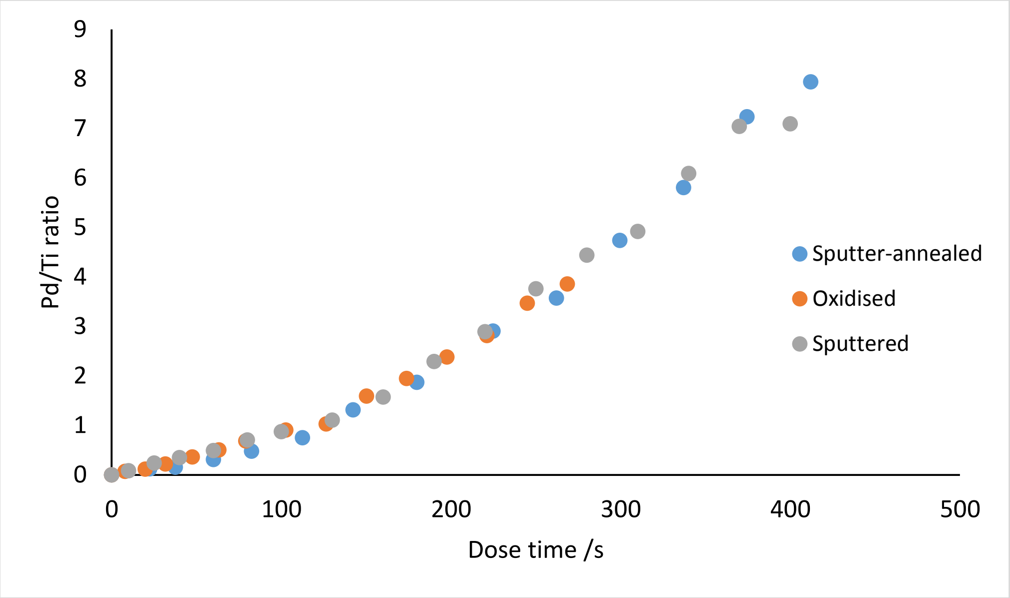

Figure 3-32 - Normalised Pd3d:Ti2p XPS area ratios for each surface during deposition

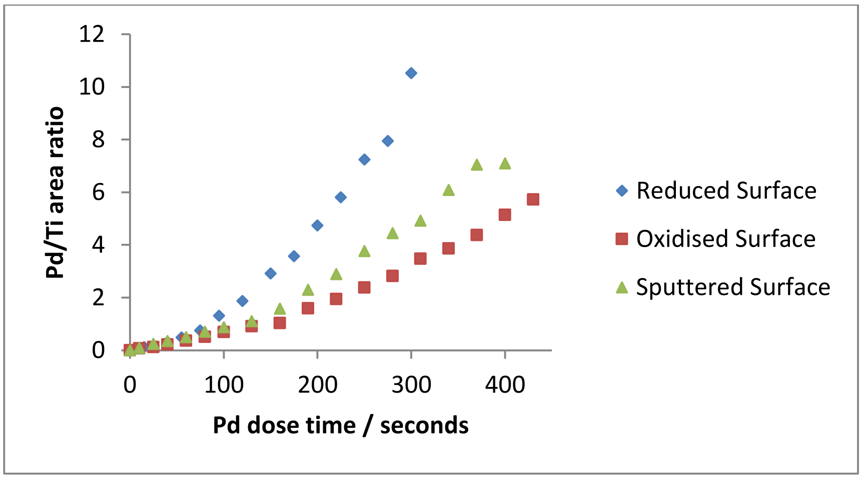

Figure 3-33 – Pd 3d:Ti 2p area ratio, showing a Pd growth curve as a function of Pd deposition time – not normalised

There are a number of ways to manipulate the ISS and XPS data to gain information about the growth mode of an adsorbate on a substrate, as discussed in section 3.1.5.1.

Figure 3-32 shows how the ratio of Pd3d:Ti2p area in the XPS changes as more Pd is dosed on all three TiO$_2$(110) surfaces. The dose time has been normalised to that of the sputtered surface to correct for flux variations between experiments (Figure 3-33 shows the uncorrected ratios). The curves indicate an initial period of linearity, up to 150 seconds of dosing, followed by an increased slope. This could indicate that the Pd islands initially grow as a monolayer, as previously proposed by Kaden[99], before forming 3D islands via multilayer island growth. The absence of any line breaks in the plot confirms that the growth is not layer by layer. The shape of the graph is identical for all three surfaces, which suggests that the number of defects on the surface doesn't affect the growth of the palladium. This result is similar to that found by Diebold et al[88], who studied the growth of Cu on TiO_2(110) and found that defects created by sputtering the substrate before Cu deposition do not influence the subsequent growth of Cu thin films.

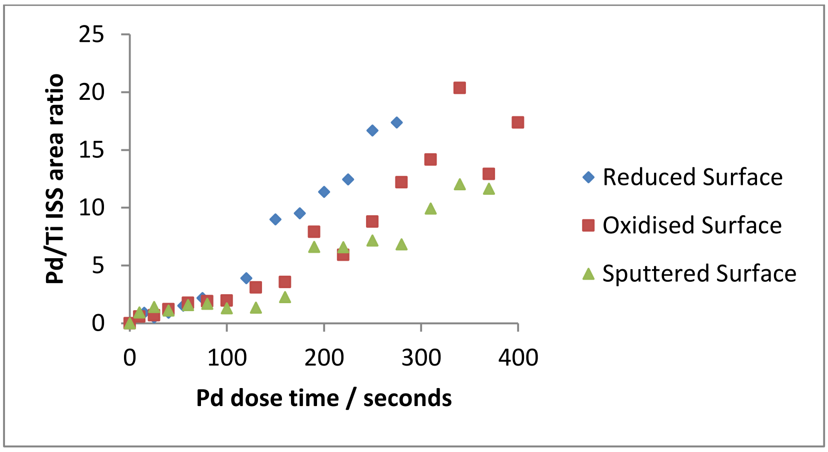

Figure 3-34 – Pd/Ti ISS area ratio as a function of Pd dose time

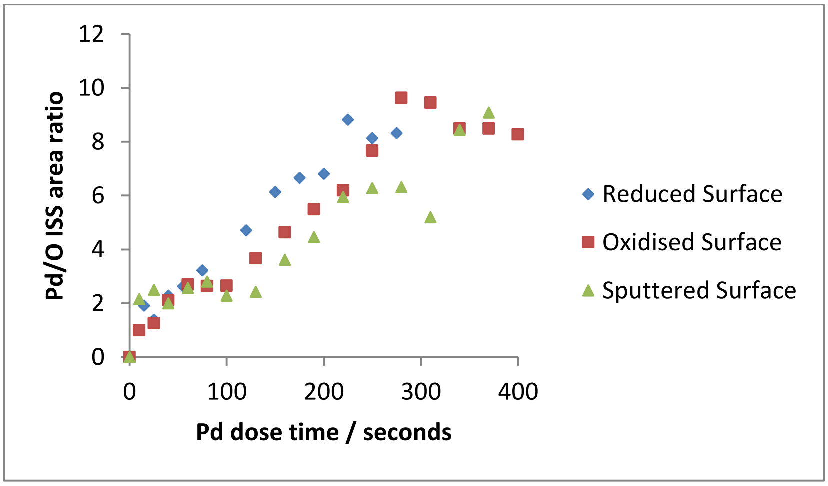

Figure 3-35 – Pd/O ISS area ratio as a function of Pd dose time

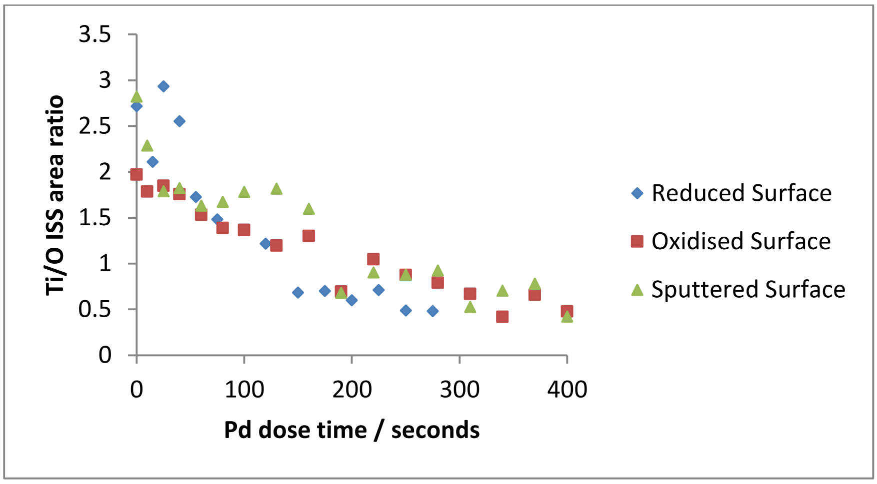

Figure 3-36 – Ti/O IS area ratio as a function of Pd dose time

Figure 3-34, Figure 3-35 and Figure 3-36 show the relationships between Pd, Ti and O from the ISS as a function of Pd dose time. Each of the Pd growth curves (ISS and XPS) increase with dose time, indicating that Pd grows in a Volmer-Weber mode. This agrees with previous findings, as summarised by Diebold[6]. Figure 3-36 shows that the Ti/O ratio decreases as more Pd is deposited on to the surface. This also coincides with the Ti2p XPS raw data, shown in Figure 3-37 - Figure 3-39. With the sputtered (Figure 3-38) and sputter-annealed (Figure 3-37) surfaces, the Ti2p signal becomes more oxidised, i.e. more Ti^{4+} and less Ti^{3+} and Ti^{2+} is present in the spectra after dosing palladium. However, the Ti2p spectra of the already-oxidised TiO_2 sample (Figure 3-39) is unchanged after dosing palladium. These figures have been normalised to 1, in order to better see the difference in oxidation. As a result, it does not take into account the decrease in Ti2p signal as more Pd is dosed on to the TiO_2 surface (Figure 3-40).

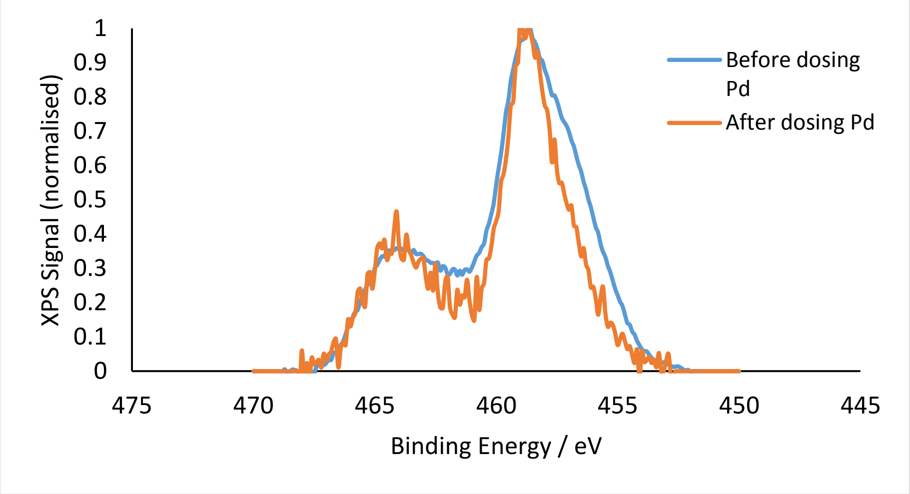

Figure 3-37 - Ti2p spectra (with normalised intensity) before and after dosing Pd onto a sputter-annealed TiO_2(110) surface

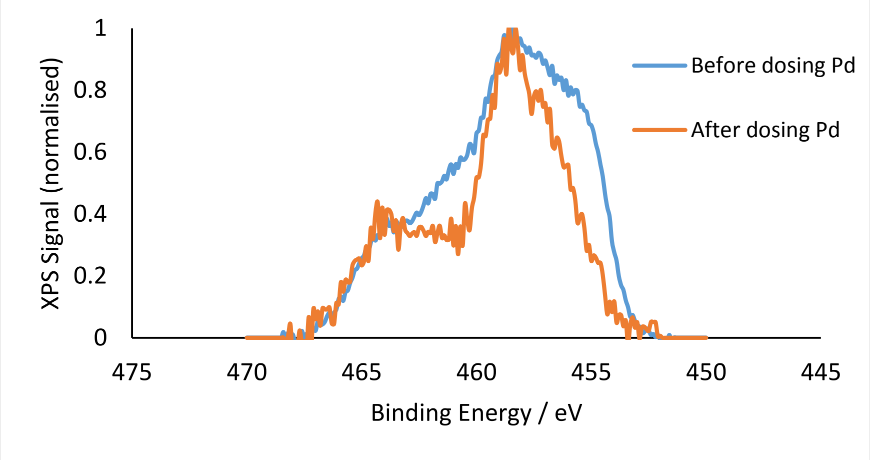

Figure 3-38 - Ti2p spectra (normalised) before and after dosing Pd onto a sputtered TiO_2(110) surface

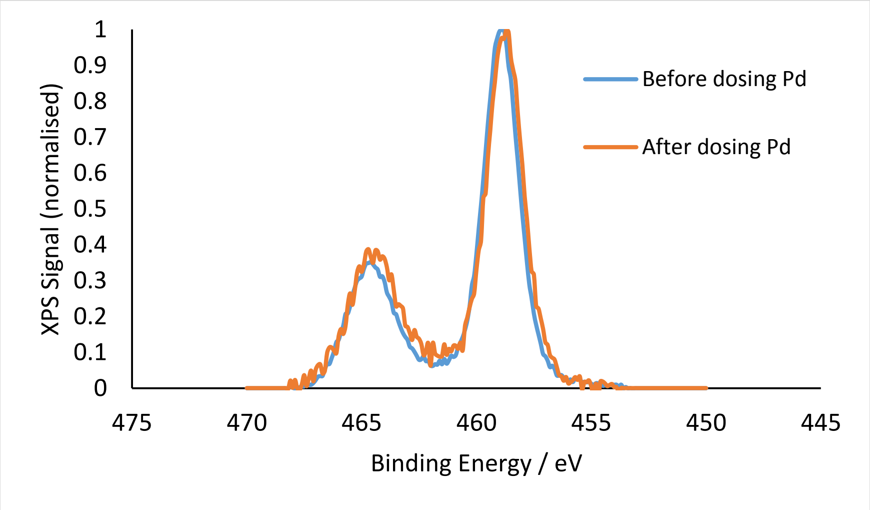

Figure 3-39 - Ti2p spectra (normalised) before and after dosing Pd onto an oxidised TiO_2(110) surface

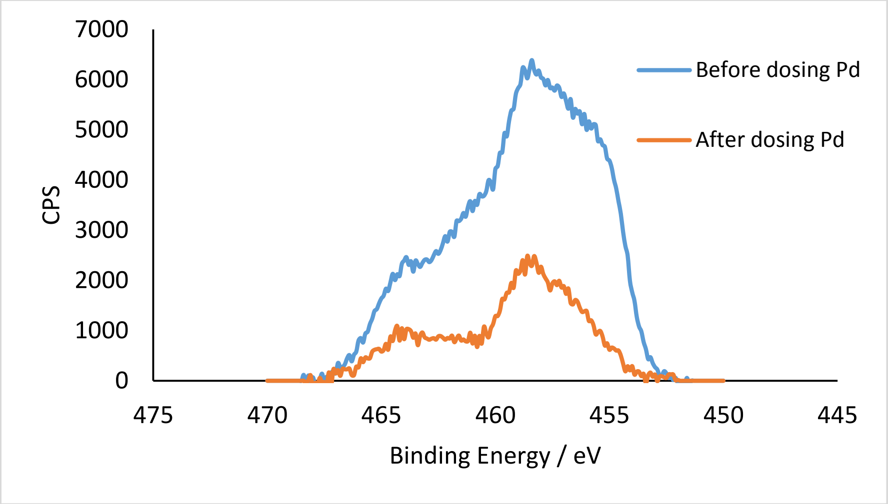

Figure 3-40 - Ti2p raw data - spectra before and after dosing Pd onto the sputtered $TiO_2(110)$ surface

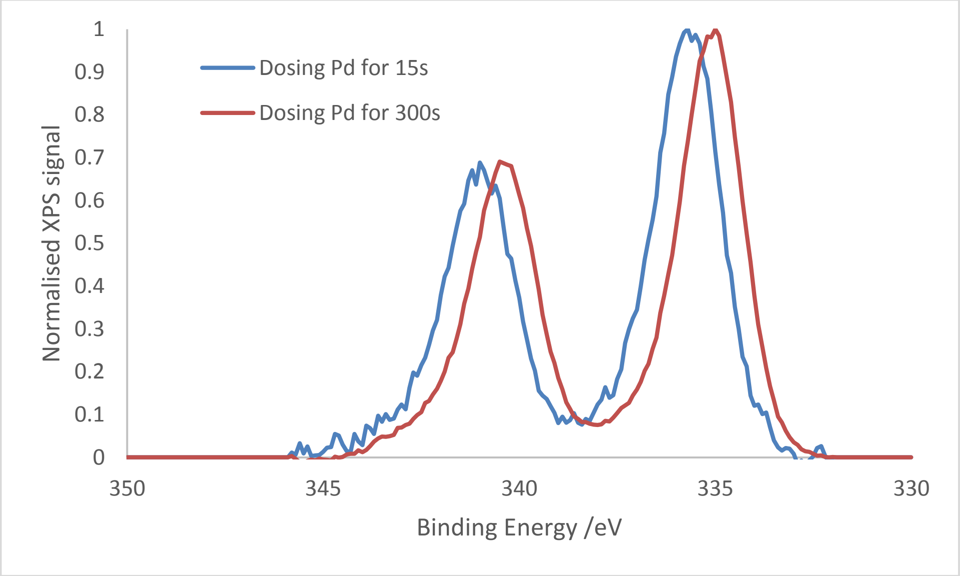

Figure 3-41 - Pd 3d XPS spectra after dosing 15s and 300s of Pd onto sputter-annealed $TiO_2(110)$

At the same time, as Pd is dosed onto TiO_2, there is a shift in the binding energy of the Pd, as shown in Figure 3-41. There is a shift towards lower binding energy as more Pd is dosed on to the surface. The total shift in value after dosing 300s of Pd is ~0.6 eV. This also occurred when dosing Pd onto oxidised and sputtered TiO_2, shown in the appendix (section A.1). There is, however, no change in the peak position of the Ti2p signal. This agrees with Negra et al[100], who used photoelectron spectroscopy to look at the early growth of Pd on oxidised TiO_2 and monitor the Ti2p and Pd3d peaks. $Pd3d_{5/2}$ showed a shift to lower binding energy with increasing Pd coverage, whereas the Ti2p peak did not change. This binding energy shift was therefore attributed to a size effect of the Pd only, rather than the occurrence of charge transfer. However, Bugyi et al[101], using work function data for the deposition of Rh on $TiO_2(110)$, came to a different conclusion – they found that Rh deposition below 0.1 monolayer coverage lead to electron transfer from metal to the TiO_2 surface, forming positively charged Rh atoms and clusters on the surface.

The film thickness was calculated from the XPS data (see Chapter 2, section 2.6.7.2) and plotted vs Pd, Ti and O XPS signals, as described by Madey et al[88] in order to further confirm the growth mode of Pd on each of the titania surfaces. The graphs are shown in Figure 3-42-Figure 3-44. Again, the lack of clear breaks suggest that the growth is not FdM. These same thickness values were plotted against the Pd, Ti and O ISS signals, as shown in Figure 3-45.

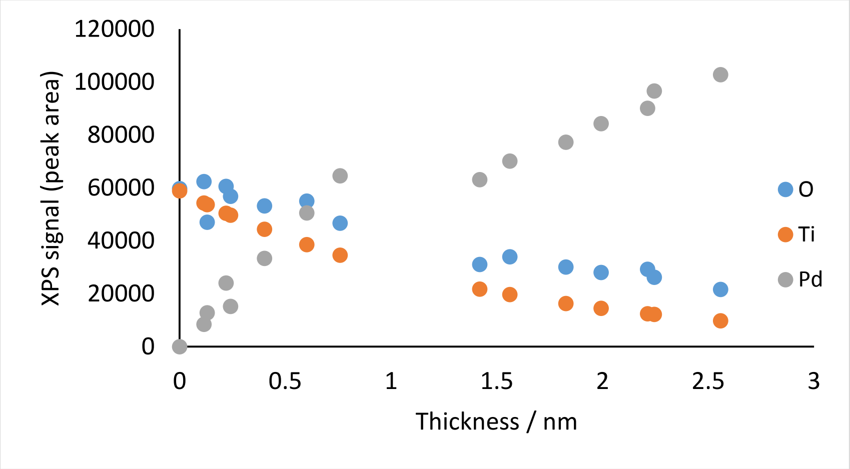

Figure 3-42 - XPS signal vs Pd film thickness for dosing Pd onto sputter-annealed TiO_2

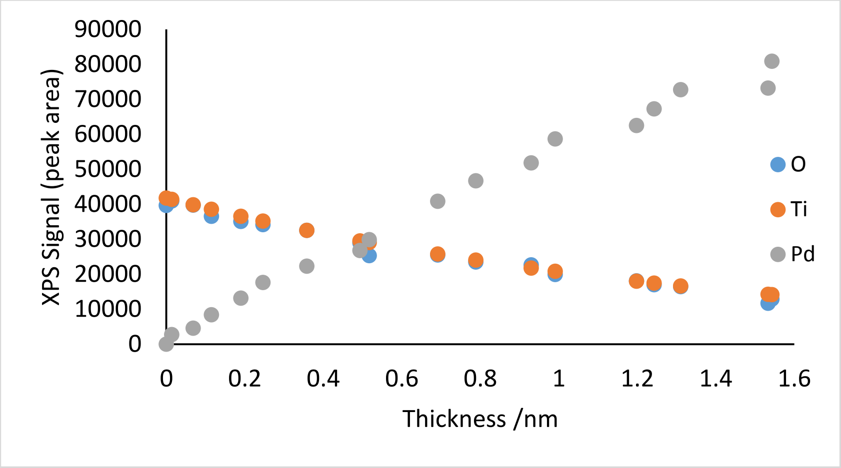

Figure 3-43 - XPS signal vs Pd film thickness for dosing Pd onto oxidised TiO_2

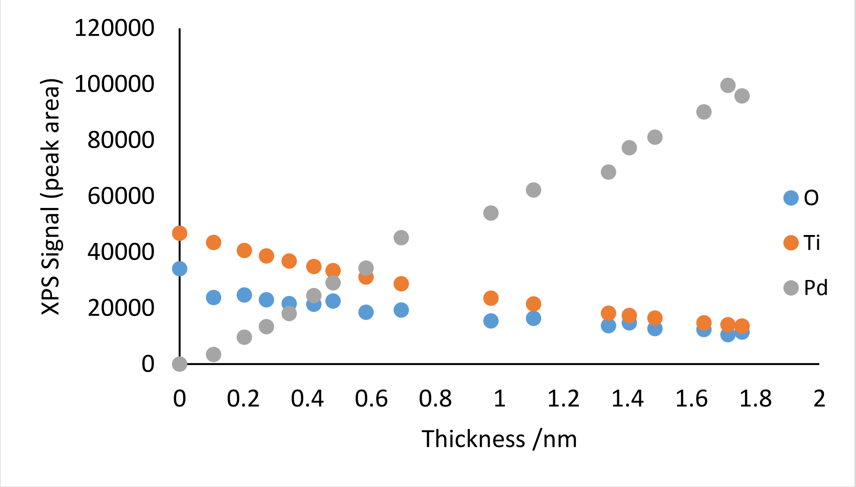

Figure 3-44 - XPS signal vs Pd film thickness for dosing Pd onto sputtered TiO_2

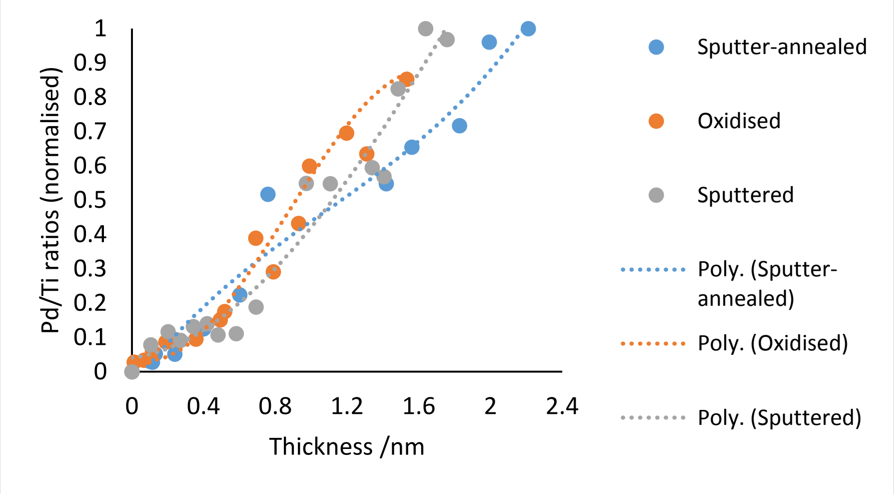

Figure 3-45 - Pd:Ti ISS area ratio vs the Pd film thickness for dosing Pd onto each of the three differently prepared TiO_2 surfaces

3.3.6 Annealing Pd on differently prepared TiO_2 surfaces

The effect of heating Pd on each of the three $TiO_2(110)$ surfaces (sputtered, sputtered-annealed and oxidised) over a range of temperatures (473-873 K) was examined with XPS and ISS. Figure 3-46 summarises the effect of heating on the Pd and Ti XPS. All three curves show a decrease at low temperature (up to 573 K), probably due to sintering and de-wetting of the film[60]. Bowker et al used Auger and STM to show that particle formation occurs when annealing Pd films at temperatures as low as 473 K[102, 103]. They observed a change from a "spongy" film to a particulate array with a narrow size distribution (42±1Å in diameter). It is also known that 473 K corresponds to the Huttig temperature for Pd – this is where we expect the onset of metal adatom mobility[104].

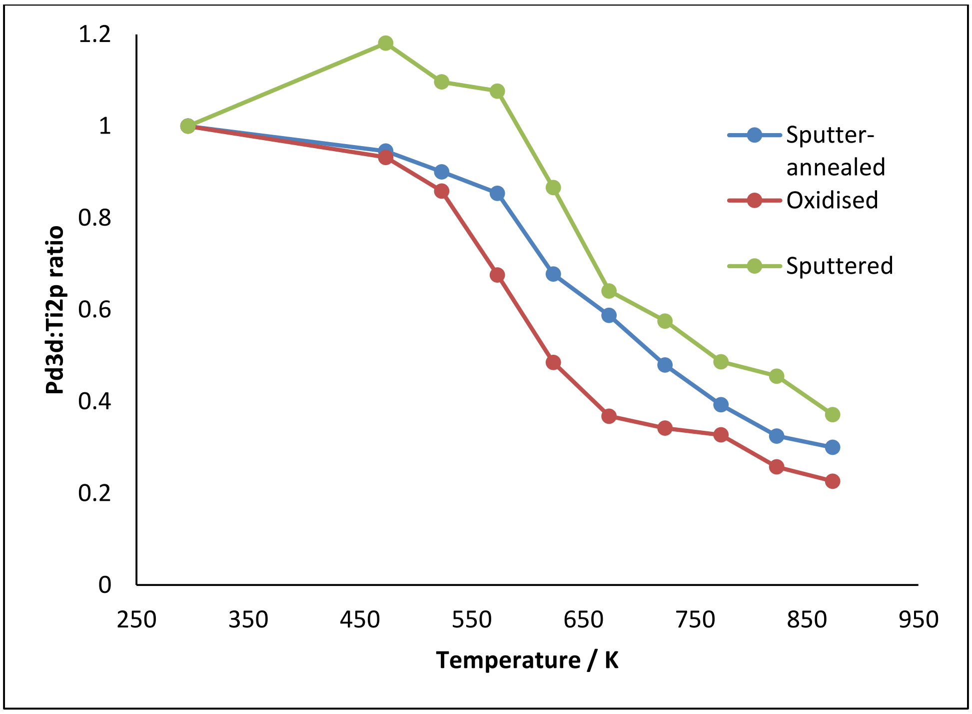

Figure 3-46 – The change in Pd3d:Ti2p area ratio against annealing temperature of the three prepared surfaces

This decrease in low temperature in Figure 3-46 is then followed by a much larger decrease in the ratio at higher temperatures. The XPS raw data for the sputtered surface is shown in Figure 3-47 and Figure 3-48, which show the Ti2p and Pd3d spectra respectively. There isn't much change in the Ti2p spectra shown in Figure 3-47 when annealing up to 673 K. However, on annealing to higher temperatures, a shoulder peak begins to emerge at 455.5 eV, becoming extremely prominent at 823 K. Figure 3-48 shows that the Pd signal decreases on annealing, with a 33% decrease in the Pd signal by 873 K. The same graphs for the sputter-annealed and the oxidised surface are shown in the appendix (section A.2).

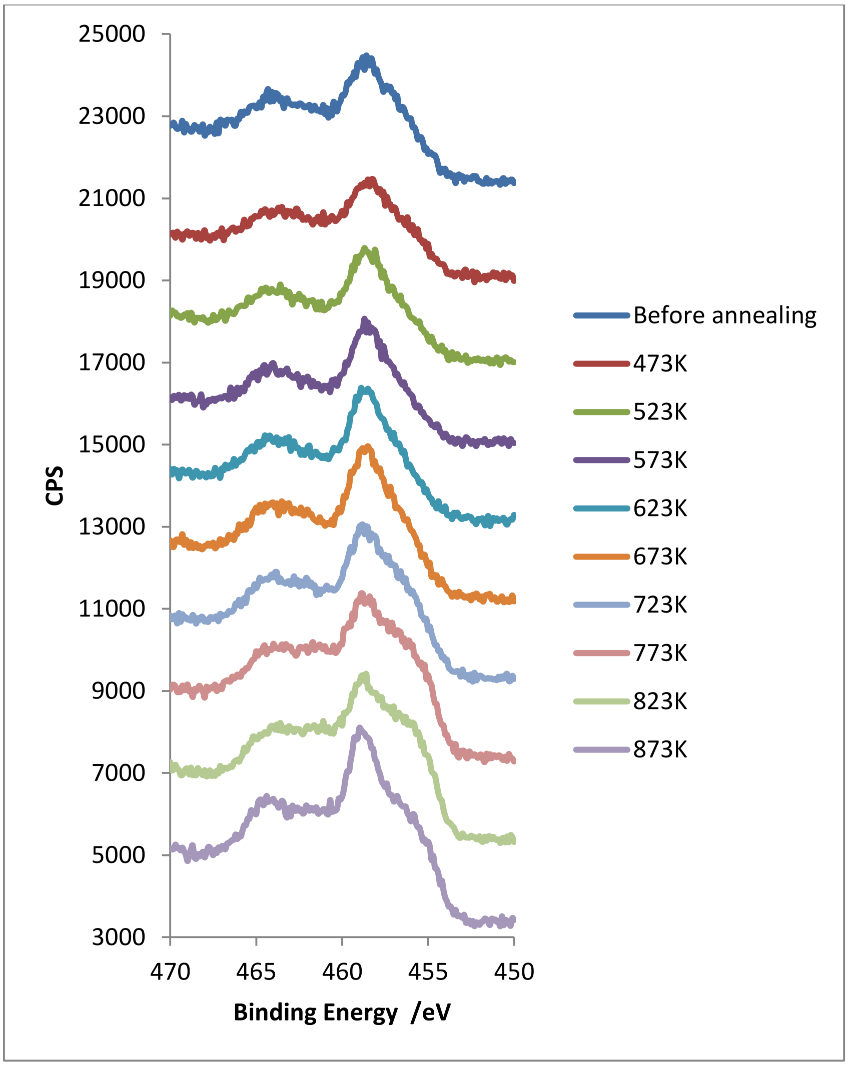

Figure 3-47 - The variation in the Ti 2p XPS signal with increasing temperature for the sputtered surface dosed with Pd

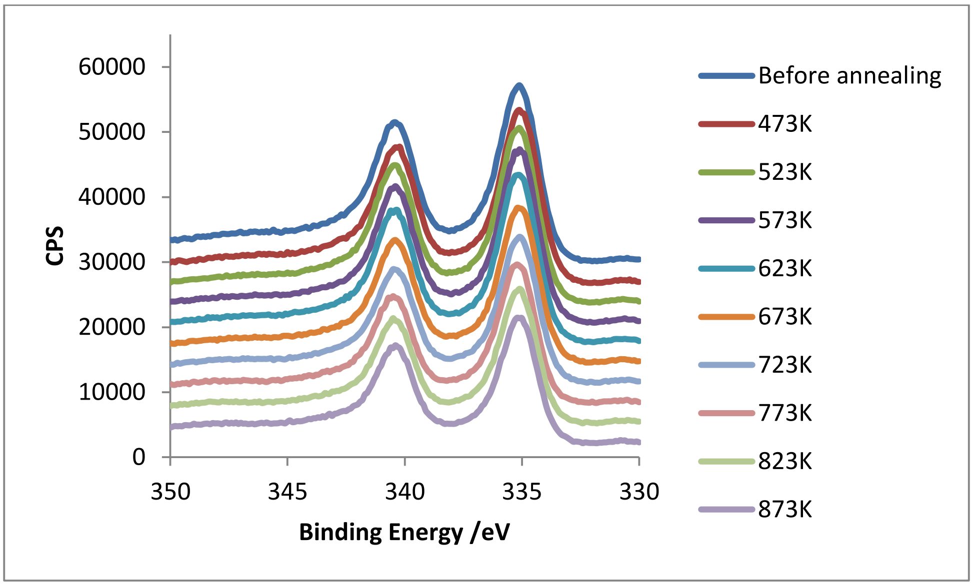

Figure 3-48 - The variation in the Pd 3d XPS spectra with increasing temperature for the sputtered surface dosed with Pd

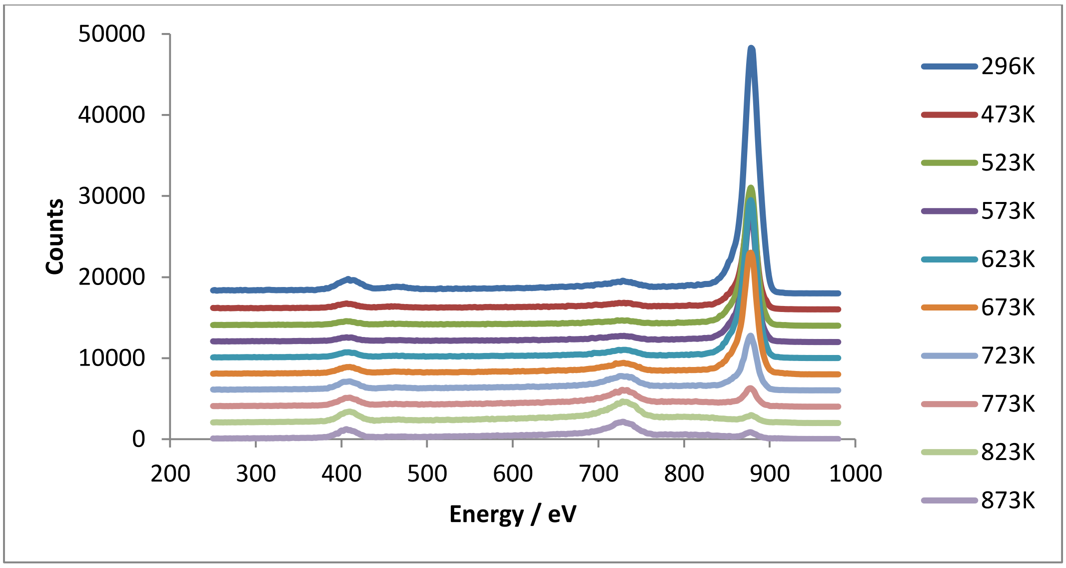

Figure 3-49 - ISS Raw Data of Pd on the sputtered TiO_2(110) surface taken after annealing to increasing temperatures

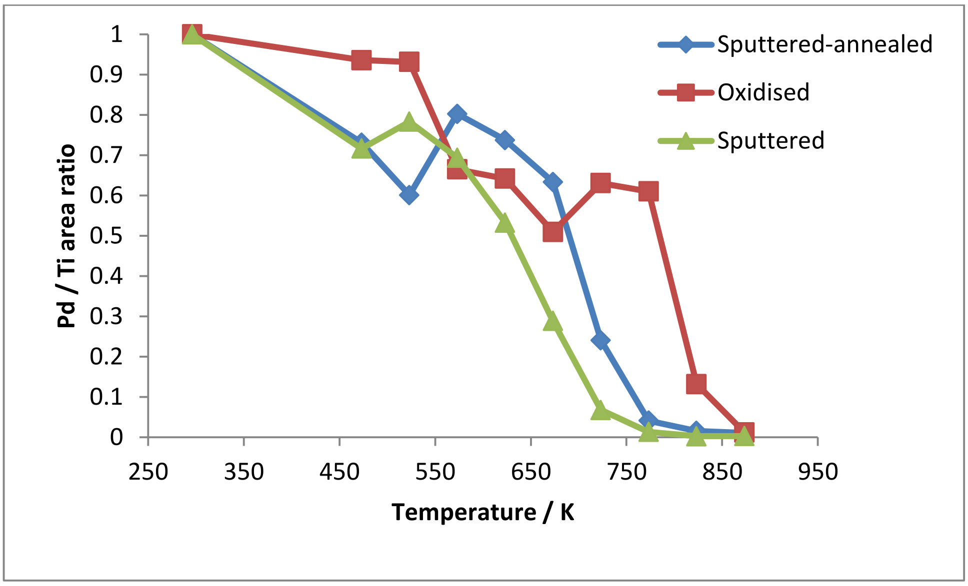

Figure 3-50 - How the Pd/Ti area ratio in the ISS is affected by temperature on each of the three investigated surfaces

It is interesting to compare the XPS raw data with the ISS raw data. Figure 3-49 shows the raw data obtained from the ISS after heating the sputtered TiO_2(110) sample to increasing temperatures (the ISS raw data for the other two surfaces is in the Appendix – section A.3). In the temperatures up to 673 K, there is very little change in the spectra. Then, at 773 K there is a drastic reduction in the Pd signal and by 873 K there is minimal Pd remaining. This can be further visualised in Figure 3-50 and Figure 3-51 which show how the ratio of Pd area to Ti and O area is affected by increasing temperature on each of the three surfaces that were looked at. The ratio of Pd/Ti and Pd/O areas stay broadly consistent up to 673 K. After this there is a drastic drop in the ratios. There is an increase in the Pd/O ratio on the sputtered and oxidised surface. It is possible that CO has adsorbed onto the Pd on deposition, and this is being removed after annealing to ~523 K (CO is known to desorb from Pd at 543 K[58]) , leading to the increase in Pd/O ratio. Figure 3-52 demonstrates how the ratio of Ti area to O area in the ISS is altered by temperature. On the sputter-annealed surface, the ratio varies from 0.5:1 to 1:1 up to ~623 K. Following this, the ratio of Ti/O begins to increase up to 3:1 at 873 K. The oxidised surface shows a similar trend, increasing slightly at 523 K, and then decreasing again at 573 K, before steadily increasing again afterwards. The sputtered surface is slightly different, as it shows a steady increase, up to a ratio similar to the other two surfaces.

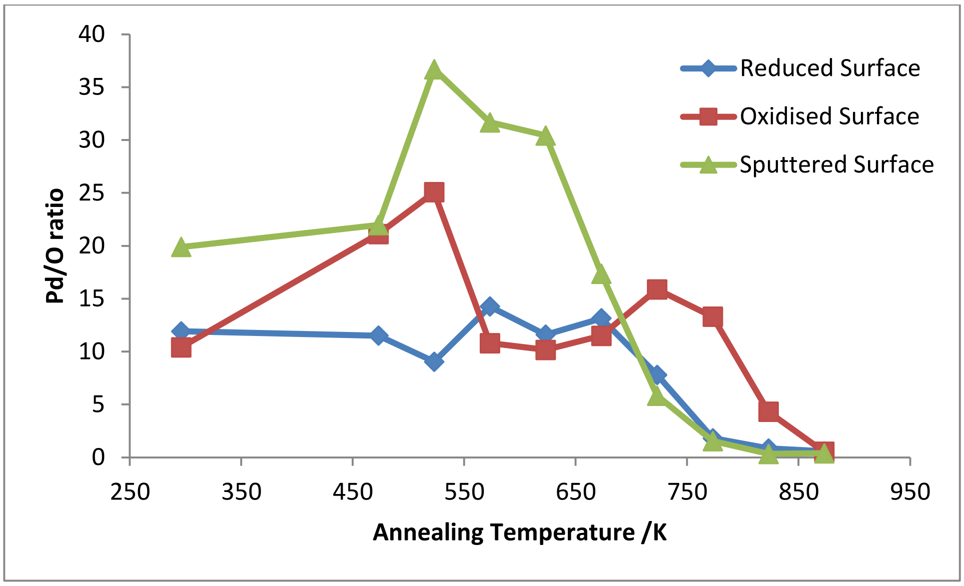

Figure 3-51 – How the Pd/O area ratio in the ISS is affected by temperature on each of the three investigated surfaces

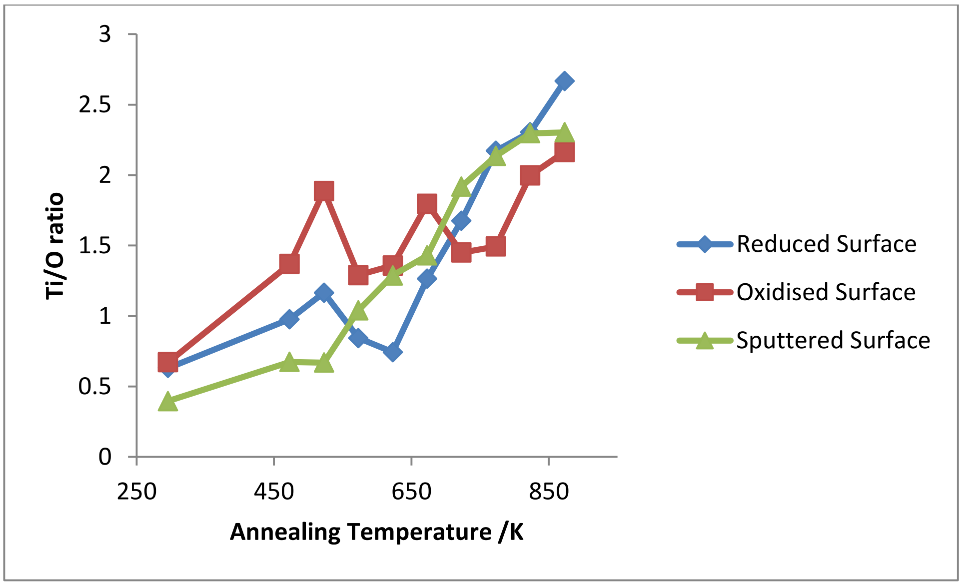

Figure 3-52 – How the Ti/O area ratio in the ISS is affected by temperature on each of the three investigated surfaces

Figure 3-53 and Figure 3-54 shows clearly the change in the Pd3d and Ti2p signal before and after annealing the Pd-dosed sputtered TiO_2 surface to 873 K – although the Pd does decrease, it is much less drastic than the decrease in the ISS spectra. Likewise, the Ti2p signal does increase, but not as much as in the ISS. As previously mentioned, there is also a shoulder peak emerging at 455.5 eV. Figure 3-55 looks at this in greater detail, and attempts to peak fit the Ti2p XPS spectra taken after annealing to 873 K, finding that the contribution to the overall peak is 39% Ti^{4+}, 36% Ti^{3+} and 25% Ti^{2+}.

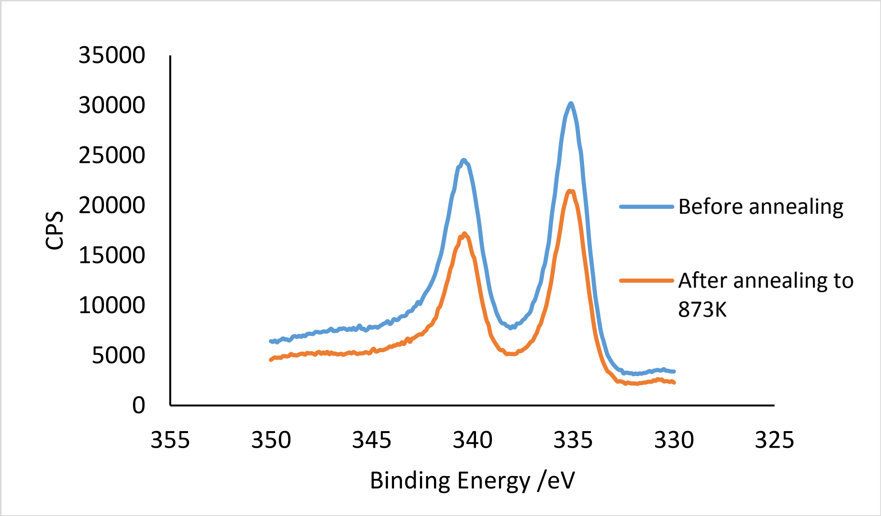

Figure 3-53 – Pd 3d signal before any heating and after heating to 873 K on the sputtered surface

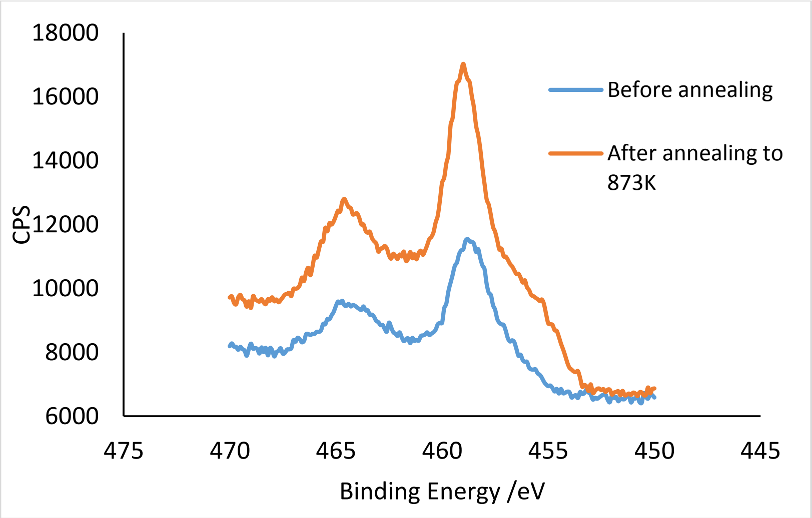

Figure 3-54 - Ti2p signal before and after heating to 873 K on the sputtered surface

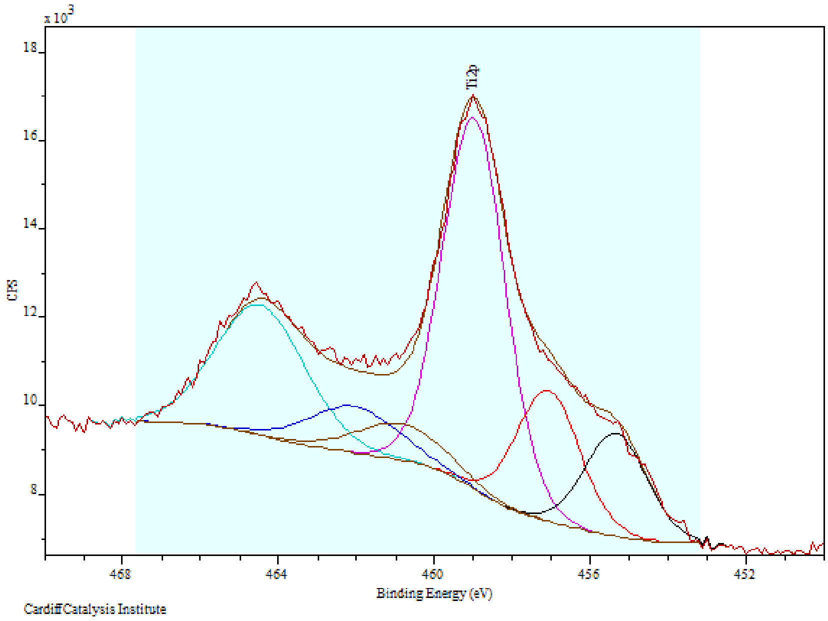

Figure 3-55 - Peak fit of the Ti 2p peak after annealing the reduced $TiO_2(110)$ surface to 600°C

The differing XPS and ISS results seem strange at first, until we consider that ISS is much more surface sensitive than XPS; ISS sees only the top layer of a surface whereas XPS has a penetration of 1-10 nm.

It seems that, on heating above ~773 K, an SMSI (strong metal support interaction) effect is occurring between the TiO_2 support and the Pd nanoparticles. In this case, the extremely surface sensitive ISS would only be able to see the Ti, whereas the XPS is able to penetrate past the TiO_2 overlayer and still see the Pd underneath. The fact that the Ti^{2+} shoulder in the Ti2p region of the XPS appears at the same temperature as the Pd peak in the ISS drastically decreases suggests that the overlayer is actually Ti^{2+}, rather than the stoichiometric Ti^{4+}. This may also explain why the Ti/O ratio in the ISS gets very high at temperatures above 673 K. This encapsulation effect is seen for all three surfaces in the ISS, Figure 3-50. However, it clearly occurs at a lower temperature (between 80-100 K) for the sputtered and sputter-annealed surfaces compared to the oxidised surface. This implies that the oxidised surface contains reduced states, but that they take longer to reach the surface, and therefore to reach the palladium, than with the sputtered and sputter-annealed surface, which already has reduced states of Ti at the surface. Dulub and Diebold[58] carried out a similar experiment with Pt on TiO_2 and also observed SMSI. They dosed approximately 25 monolayers of Pt onto the TiO_2, enough to eliminate the Ti signal in the ISS, and then annealed to 973 K for 5 minutes and 773 K for 30 minutes. The Pt signal disappeared from the ISS and the Ti signal reappeared. However, these results differ slightly from previously published results by Fu et al[50], who found a strong dependence of the encapsulation process on the electron density in the conduction band of TiO_2. Encapsulation of Pd clusters was observed in TiO_2 crystals that were either heavily sputtered or reduced, but not on unreduced or slightly sputtered crystals. In some instances, they also found a mix of Ti^{2+} and Ti^{3+} in the XPS after annealing Pd/TiO_2 to 823 K.

It is likely that this encapsulation effect is strongly related to the state of reduction of the crystal used in these cases. It is possible that there were enough reduced states in the bulk of the oxidised crystal studied in this thesis to still enable the SMSI effect to occur, even if only at higher temperatures than the other two prepared surfaces, which was presumably not the case for Fu et al[50]. It is possible that my crystal was only oxidised in the near-surface region. This does correlate with Bennett et al[59], who showed a 4th order dependence of the oxidation of reduced titania crystals upon the amount of Ti^{3+} in the bulk.

The effect of heating was also looked at on a smaller coverage of Pd – a coverage of 6.5×10^{14} atoms cm^{-2} (using Carley's equation – see chapter 2) were deposited onto clean TiO_2. The ISS is shown in Figure 3-56. Much like with higher coverages of Pd, there are small changes in temperatures up to 673 K, and then larger changes up to 873 K. The ISS ratios are shown in Figure 3-57 – at 773 K and above the Pd:Ti and Pd:O ratio sharply decrease, just as with greater amounts of Pd. The Pd XPS shown in Figure 3-58 shows a decrease on annealing to 873 K, but not as much as in the ISS. The big difference, however, between annealing this smaller coverage on TiO_2 and annealing the much greater coverages is the Ti2p spectra, shown in Figure 3-59. The Ti2p signal increases on annealing, but there is no sign of the emergence of a Ti^{2+} shoulder.

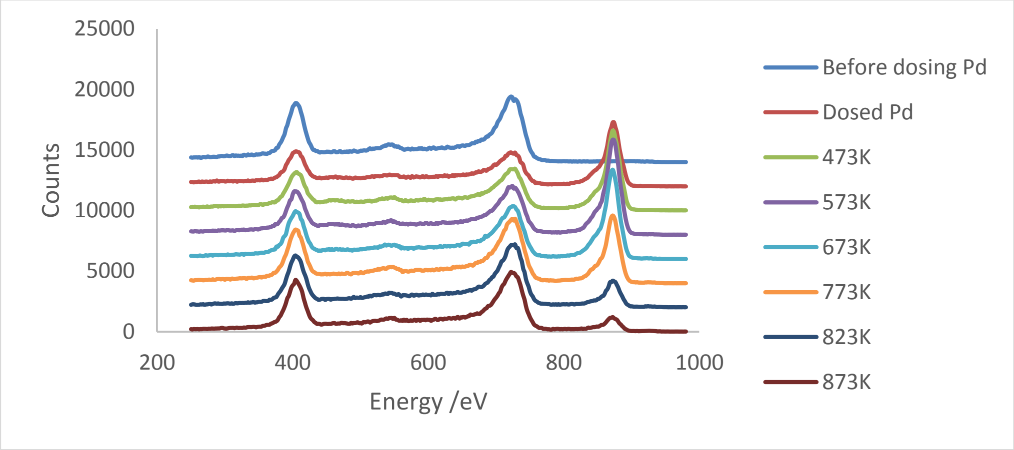

Figure 3-56 – ISS raw data of heating 6.5×10^{14} atoms cm^{-2} of Pd on TiO_2

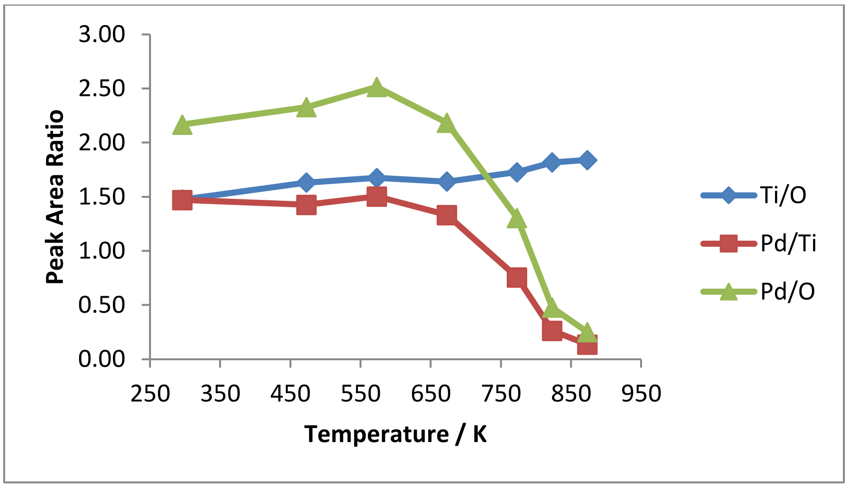

Figure 3-57 - ISS area ratios with heating

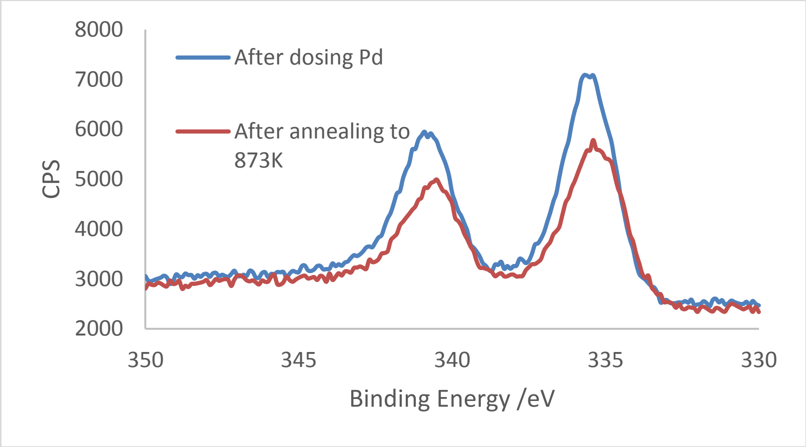

Figure 3-58 - Pd3d raw data for heating a smaller coverage of Pd on TiO_2

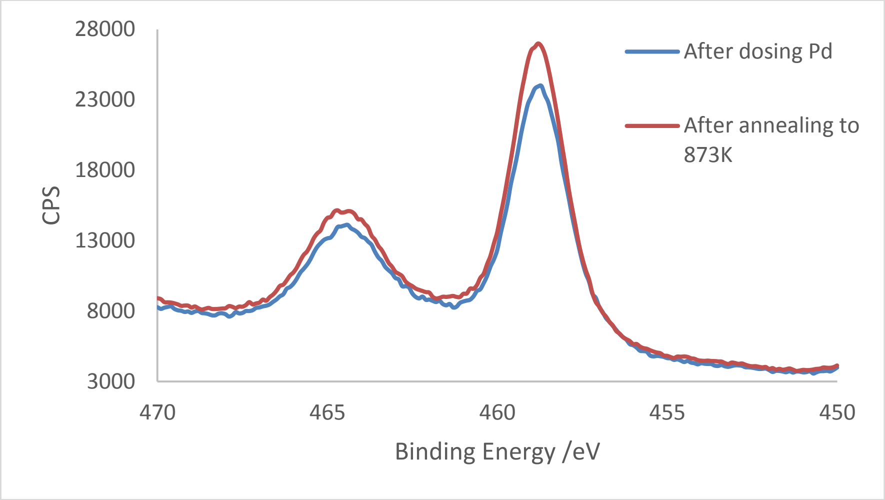

Figure 3-59 - Ti2p raw data for heating a smaller coverage of Pd on TiO_2

The fact that the Pd signal still decreases by so much in the ISS suggests that an SMSI effect is still occurring at higher temperatures and that the Pd is still being encapsulated. However, it is possible that there was such a small amount of Pd on the surface to begin with, that the XPS is unable to identify the even smaller amount of Ti^{2+} that may be present.

The Ti signal and Pd signal increase and decrease respectively, even at low temperatures. Pd clusters on TiO_2(110) have previously been shown to increase in size when annealed after being monitored in-situ by high-temperature STM[105, 106]. It was suggested that the mechanism was probably Ostwald ripening, as the Pd particles were static on the TiO_2(110)(1x1) surface. It was also suggested however that coalescence may be a factor at lower coverages of Pd[107]. It's interesting to note that the Pd/Ti ratio doesn't change as much at low coverages as at high coverages, something that was also observed by Bowker et al using Auger and STM[102].

3.4 Conclusions

In this chapter, the TiO_2(110) surface has been characterised with ISS, XPS and LEED. The growth of Pd on TiO_2(110) and the effect of annealing Pd/TiO_2(110) has been studied. The aim of this was to further investigate SMSI.

It was found that sputtering clean TiO_2(110) can result in reduction of the surface, with an increase in Ti^{2+} and Ti^{3+} in the Ti2p XPS. Annealing this in UHV allows some re-oxidation of the surface layers, especially converting Ti^{2+} to Ti^{3+}, but annealing in oxygen is much more effective.

The growth mode of Pd on TiO_2(110) is surprisingly unaffected by the reduction of the crystal. Pd appears to grow in a Volmer-Weber fashion, which agrees with previous findings.

On annealing Pd/TiO_2 to temperatures above 723 K, an SMSI effect occurs between the Pd nanoparticles and the TiO_2 support. A layer of TiO_x begins to cover the Pd nanoparticles, as determined from XPS and ISS. This is strongly affected by the oxidation state of the titania surface – SMSI occurs at a higher temperature for an oxidised surface than for a reduced surface.

3.5 References

1. M. Boudart, *Topics in Catalysis*, 2000, **13**, 147.
2. D. Brinkley, M. Dietrich, T. Engel, P. Farrall, G. Gantner, A. Schafer and A. Szuchmacher, *Surface Science*, 1998, **395**, 292.
3. S. C. N, *Heterogeneous Catalysis in Industrial Practice*, (New York: McGraw-Hill), 2nd edn., 1991.
4. H. Selhofer and R. Muller, *Thin Solid Films*, 1999, **351**, 180.
5. Y. V. Pleskov, *Russian Journal of Electrochemistry*, 1999, **35**, 1137.
6. U. Diebold, *Surface Science Reports*, 2003, **48**, 53.
7. J. Panpranot, K. Kontapakdee and P. Praserthdam, *Journal of Physical Chemistry B*, 2006, **110**, 8019.
8. A. Stashans, S. Lunell and R. W. Grimes, *Journal of Physics and Chemistry of Solids*, 1996, **57**, 1293.
9. C. N. Rao, S. R. Yoganarasimhan and P. A. Faeth, *Transactions of the Faraday Society*, 1961, **57**, 504.
10. V. E. Henrich and P. A. Cox, *The Surface Science of Metal Oxides*, Cambridge University Press, Cambridge, 1994.
11. M. Ramamoorthy, D. Vanderbilt and R. D. Kingsmith, *Physical Review B*, 1994, **49**, 16721.
12. P. W. Tasker, *Journal of Physics C-Solid State Physics*, 1979, **12**, 4977.
13. J. P. Lafemina, *Crit. Rev. Surf. Chem.*, 1994, **3**, 297.
14. S. Wendt, P. T. Sprunger, E. Lira, G. K. H. Madsen, Z. S. Li, J. O. Hansen, J. Matthiesen, A. Blekinge-Rasmussen, E. Laegsgaard, B. Hammer and F. Besenbacher, *Science*, 2008, **320**, 1755.
15. .
16. H. Onishi and Y. Iwasawa, *Chemical Physics Letters*, 1994, **226**, 111.
17. U. Diebold, W. Hebenstreit, G. Leonardelli, M. Schmid and P. Varga, *Physical Review Letters*, 1998, **81**, 405.
18. J. V. Lauritsen, A. S. Foster, G. H. Olesen, M. C. Christensen, A. Kuhnle, S. Helveg, J. R. Rostrup-Nielsen, B. S. Clausen, M. Reichling and F. Besenbacher, *Nanotechnology*, 2006, **17**, 3436.

19. Z. Zhang, Q. Ge, S. C. Li, B. D. Kay, J. M. White and Z. Dohnalek, *Physical Review Letters*, 2007, **99**, 4.
20. C. M. Yim, C. L. Pang and G. Thornton, *Physical Review Letters*, 2010, **104**.
21. M. Bowker and R. A. Bennett, *Journal of Physics-Condensed Matter*, 2009, **21**, 9.
22. M. A. Henderson, *Surface Science*, 1999, **419**, 174.
23. H. Onishi and Y. Iwasawa, *Physical Review Letters*, 1996, **76**, 791.
24. L. E. Walle, A. Borg, P. Uvdal and A. Sandell, *Physical Review B*, 2012, **86**.
25. K. Mitsuhara, H. Okumura, A. Visikovskiy, M. Takizawa and Y. Kido, *Journal of Chemical Physics*, 2012, **136**.
26. N. Shibata, A. Goto, S. Y. Choi, T. Mizoguchi, S. D. Findlay, T. Yamamoto and Y. Ikuhara, *Science*, 2008, **322**, 570.
27. X. C. Mao, X. F. Lang, Z. Q. Wang, Q. Q. Hao, B. Wen, Z. F. Ren, D. X. Dai, C. Y. Zhou, L. M. Liu and X. M. Yang, *Journal of Physical Chemistry Letters*, 2013, **4**, 3839.
28. S. Wendt, J. Matthiesen, R. Schaub, E. K. Vestergaard, E. Laegsgaard, F. Besenbacher and B. Hammer, *Physical Review Letters*, 2006, **96**, 4.
29. M. Eyrich, S. Kielbassa, T. Diemant, J. Biskupek, U. Kaiser, U. Wiedwald, P. Ziemann and J. Bansmann, *Chemphyschem*, 2010, **11**, 1430.
30. M. Bowker, *Current Opinion in Solid State & Materials Science*, 2006, **10**, 153.
31. P. J. Moller and M. C. Wu, *Surface Science*, 1989, **224**, 265.
32. A. Szabo and T. Engel, *Surface Science*, 1995, **329**, 241.
33. P. W. Murray, N. G. Condon and G. Thornton, *Physical Review B*, 1995, **51**, 10989.
34. M. Sander and T. Engel, *Surface Science*, 1994, **302**, L263.
35. D. Novak, E. Garfunkel and T. Gustafsson, *Physical Review B*, 1994, **50**, 5000.
36. H. Onishi and Y. Iwasawa, *Surface Science*, 1994, **313**, L783.
37. S. D. Elliott and S. P. Bates, *Physical Review B*, 2002, **65**.
38. Q. Guo, I. Cocks and E. M. Williams, *Physical Review Letters*, 1996, **77**, 3851.
39. E. Asari and R. Souda, *Physical Review B*, 1999, **60**, 10719.
40. C. L. Pang, S. A. Haycock, H. Raza, P. W. Murray, G. Thornton, O. Gulseren, R. James and D. W. Bullett, *Physical Review B*, 1998, **58**, 1586.
41. R. A. Bennett, P. Stone, N. J. Price and M. Bowker, *Physical Review Letters*, 1999, **82**, 3831.

42. H. H. Pieper, K. Venkataramani, S. Torbrugge, S. Bahr, J. V. Lauritsen, F. Besenbacher, A. Kuhnle and M. Reichling, *Physical Chemistry Chemical Physics*, 2010, **12**, 12436.

43. R. A. Bennett, S. Poulston, P. Stone and M. Bowker, *Physical Review B*, 1999, **59**, 10341.

44. M. Bowker, P. Stone, P. Morrall, R. Smith, R. Bennett, N. Perkins, R. Kvon, C. Pang, E. Fourre and M. Hall, *Journal of Catalysis*, 2005, **234**, 172.

45. S. J. Tauster, S. C. Fung and R. L. Garten, *Journal of the American Chemical Society*, 1978, **100**, 170.

46. S. J. Tauster, S. C. Fung, R. T. K. Baker and J. A. Horsley, *Science*, 1981, **211**, 1121.

47. G. L. Haller and D. E. Resasco, *Advances in Catalysis*, 1989, **36**, 173.

48. E. I. Ko and R. L. Garten, *Journal of Catalysis*, 1981, **68**, 233.

49. M. A. Vannice and R. L. Garten, *Journal of Catalysis*, 1979, **56**, 236.

50. Q. Fu, T. Wagner, S. Olliges and H. D. Carstanjen, *Journal of Physical Chemistry B*, 2005, **109**, 944.

51. C. G. Vayenas, S. Brosda and C. Pliangos, *Journal of Catalysis*, 2003, **216**, 487.

52. T. Ioannides and X. E. Verykios, *Journal of Catalysis*, 1996, **161**, 560.

53. P. Meriaudeau, O. H. Ellestad, M. Dufaux and C. Naccache, *Journal of Catalysis*, 1982, **75**, 243.

54. J. Santos, J. Phillips and J. A. Dumesic, *Journal of Catalysis*, 1983, **81**, 147.

55. G. B. Raupp and J. A. Dumesic, *Journal of Physical Chemistry*, 1984, **88**, 660.

56. S. Bernal, F. J. Botana, J. J. Calvino, C. Lopez, J. A. PerezOmil and J. M. RodriguezIzquierdo, *Journal of the Chemical Society-Faraday Transactions*, 1996, **92**, 2799.

57. S. Bernal, J. J. Calvino, M. A. Cauqui, J. M. Gatica, C. L. Cartes, J. A. P. Omil and J. M. Pintado, *Catalysis Today*, 2003, **77**, 385.

58. O. Dulub, W. Hebenstreit and U. Diebold, *Physical Review Letters*, 2000, **84**, 3646.

59. R. A. Bennett, C. L. Pang, N. Perkins, R. D. Smith, P. Morrall, R. I. Kvon and M. Bowker, *Journal of Physical Chemistry B*, 2002, **106**, 4688.

60. R. A. Bennett, P. Stone and M. Bowker, *Catalysis Letters*, 1999, **59**, 99.

61. F. Pesty, H. P. Steinruck and T. E. Madey, *Surface Science*, 1995, **339**, 83.

62. Y. Gao, Y. Liang and S. A. Chambers, *Surface Science*, 1996, **365**, 638.

63. H. P. Steinruck, F. Pesty, L. Zhang and T. E. Madey, *Physical Review B*, 1995, **51**, 2427.
64. A. Berko, I. Ulrych and K. C. Prince, *Journal of Physical Chemistry B*, 1998, **102**, 3379.
65. D. R. Jennison, O. Dulub, W. Hebenstreit and U. Diebold, *Surface Science*, 2001, **492**, L677.
66. M. Bowker, R. D. Smith and R. A. Bennett, *Surface Science*, 2001, **478**, L309.
67. R. A. Bennett, *Physchemcomm*, 2000, 6.
68. P. Stone, R. Bennett and M. Bowker, *New Journal of Physics*, 1999, **1**, 1.1.
69. V. A. D. O'Shea, M. C. A. Galvan, A. E. P. Prats, J. M. Campos-Martin and J. L. G. Fierro, *Chemical Communications*, 2011, **47**, 7131.
70. Z. Majzik, N. Balazs and A. Berko, *Journal of Physical Chemistry C*, 2011, **115**, 9535.
71. C. Linsmeier and E. Taglauer, *Applied Catalysis a-General*, 2011, **391**, 175.
72. S. Bonanni, K. Ait-Mansour, H. Brune and W. Harbich, *Acs Catalysis*, 2011, **1**, 385.
73. Q. Fu and T. Wagner, *Surface Science Reports*, 2007, **62**, 431.
74. T. Suzuki and R. Souda, *Surface Science*, 2000, **448**, 33.
75. M. Bowker and E. Fourre, *Applied Surface Science*, 2008, **254**, 4225.
76. Y. Z. Li, B. L. Xu, Y. N. Fan, N. Y. Feng, A. D. Qiu, J. M. J. He, H. P. Yan and Y. Chen, *Journal of Molecular Catalysis a-Chemical*, 2004, **216**, 107.
77. S. Labich, E. Taglauer and H. Knozinger, *Topics in Catalysis*, 2001, **14**, 153.
78. C. Argile and G. E. Rhead, *Surface Science Reports*, 1989, **10**, 277.
79. E. Bauer and Z. Krist, *Zeitschrift für Kristallographie*, 1958, **110**, 372.
80. E. Bauer, *Applications of Surface Science*, 1982, **11-2**, 479.
81. M. Volmer and A. Weber, *Zeitschrift Fur Physikalische Chemie--Stochiometrie Und Verwandtschaftslehre*, 1926, **119**, 277.
82. I. N. Stranski and L. Krastanow, *Sitzungs-berichte-Akademie Der Wissenschaften in Wien, Mathematisch-Naturwissenschaftliche Klasse Abteilung IIb*, 1938, **146**, 797.
83. F. C. Frank and J. H. Vandermerwe, *Proceedings of the Royal Society of London Series a-Mathematical and Physical Sciences*, 1949, **198**, 205.
84. F. C. Frank and J. H. Vandermerwe, *Proceedings of the Royal Society of London Series a-Mathematical and Physical Sciences*, 1949, **200**, 125.

85. C. P. Oliver, B. V. King and D. J. O'Connor, *Surface Science*, 2004, **557**, 101.

86. R. B. Bird and W. E. Stewart, *Transport phenomena*, Wiley, 1960.

87. G. Attard and C. Barnes, *Surfaces*, OUP Oxford, Oxford, 1998.

88. U. Diebold, J. M. Pan and T. E. Madey, *Physical Review B*, 1993, **47**, 3868.

89. C. Xu, X. Lai, G. W. Zajac and D. W. Goodman, *Physical Review B*, 1997, **56**, 13464.

90. K. H. Ernst, A. Ludviksson, R. Zhang, J. Yoshihara and C. T. Campbell, *Physical Review B*, 1993, **47**, 13782.

91. C. T. Campbell, *Surface Science Reports*, 1997, **27**, 1.

92. N. Fairley, *CasaXPS, Version 2.3.15, Casa Software Ltd, 1999-2011*.

93. A. F. Carley, P. R. Chalker, J. C. Riviere and M. W. Roberts, *Journal of the Chemical Society-Faraday Transactions I*, 1987, **83**, 351.

94. U. Diebold and T. Madey, *Surface Science Spectra*, 1997, **4**, 227.

95. R. Kelly and N. Lam, *Radiation Effects*, 1973, **19**, 39.

96. S. Hashimoto and A. Tanaka, *Surface and Interface Analysis*, 2002, **34**, 262.

97. M. A. Henderson, *Surface Science*, 1995, **343**, L1156.

98. R. D. Smith, R. A. Bennett and M. Bowker, *Physical Review B*, 2002, **66**.

99. W. E. Kaden, T. P. Wu, W. A. Kunkel and S. L. Anderson, *Science*, 2009, **326**, 826.

100. M. Della Negra, N. M. Nicolaisen, Z. S. Li and P. J. Moller, *Surface Science*, 2003, **540**, 117.

101. L. Bugyi, L. Ovari and Z. Konya, *Applied Surface Science*, 2013, **280**, 60.

102. P. Stone, R. A. Bennett, S. Poulston and M. Bowker, *Surface Science*, 1999, **433**, 501.

103. P. Stone, S. Poulston, R. A. Bennett and M. Bowker, *Chemical Communications*, 1998, 1369.

104. E. G., J. Knozinger and (Eds). *Handbook of Heterogeneous Catalysis*, Wiley-VCH, New York, 1997.

105. A. Howard, C. E. J. Mitchell and R. G. Egdell, *Surface Science*, 2002, **515**, L504.

106. R. A. Bennett, D. M. Tarr and P. A. Mulheran, *Journal of Physics-Condensed Matter*, 2003, **15**, S3139.

107. M. J. J. Jak, C. Konstapel, A. van Kreuningen, J. Verhoeven and J. W. M. Frenken, *Surface Science*, 2000, **457**, 295.

Chapter 4 – Au and Pd-Au on $TiO_2(110)$

Chapter 4 Contents

4.1 Introduction

In this chapter the effect of adding Au to TiO_2(110) and Pd/TiO_2(110) is examined with XPS, ISS and Auger electron spectroscopy.

The effect of heating Au/TiO_2(110) is initially examined. Then the deposition of Au on Pd/TiO_2(110) is looked at, followed by the effect of annealing Au-Pd/TiO_2(110).

4.1.1 Au supported on TiO_2

Au catalysts on TiO_2 have been found to be a good chemical sensors[1], and can act as catalysts for the room temperature oxidation of CO[2, 3]. Fine Au particles on TiO_2 have been found to show high activity as a catalyst for the water-gas shift reaction, comparable to a conventional copper catalyst[4].

There has been a lot of work on Au/TiO_2(110) and on other oxides, as summarised by an especially excellent review of Au based model catalysts by Gong[5]. Au has a high electronegativity (2.3eV) and ionisation potential (9.2 eV) making it a poor electron donor[5]. As a result of this, Au interacts weakly with many oxides.

4.1.2 Growth of Au on TiO_2(110)

Au particle growth at low coverage (<0.1 ML) follows a 2D growth mode and then transitions to a 3D growth mode upon increasing coverage[6-8]. In the early stages of growth, they are elongated in the direction of bridge bonded oxygen rows.

The mode of nucleation and growth of the Au on TiO_2(110) is dependent on the density of oxygen vacancies[9]. Besenbacher et al carried out combined DFT and STM studies. DFT calculations showed that Au particles bind more strongly to a defect-rich surface, and STM confirmed that bridging oxygen vacancies are the active nucleation centres for the growth of Au[9]. Au particles nucleate preferentially at the sites of oxygen vacancies. As the number of oxygen vacancies increases, the number of Au particles increases whilst the average particle size decreases. If there are few oxygen vacancies, the Au nanoparticles preferentially nucleate and grow on the extended defects such as step edges[10]. UPS studies showed that, on deposition of Au, the Ti^{3+} signal intensity decreases, again suggesting that Au atoms adsorb at oxygen vacancy sites[11]. The coverage at which the growth mode of Au changes from 2D to 3D is dependent on the density of defects on the TiO_2 surface. On a surface with few or no defects, the critical coverage is ~0.09 ML, whereas the critical coverage is ~0.22 ML on a sputtered surface[12]. The nature of surface defects strongly affects particle shape, adsorption energy and electronic structure of deposited Au nanoparticles and their catalytic properties. Au nanoparticles on very defective TiO_2 were found to be more chemically active than on less-defective TiO_2[13, 14].

Madey et al looked at the growth of gold films (thickness of 0.2-12 nm)[6, 15]. Using LEIS and XPS, they determined that Au grows via a Volmer-Weber mode. They observed that, even at 40 angstroms Au average coverage, the Ti intensity in LEIS had only been reduced by ~50%. This meant that ~50% of the substrate was still uncovered, a clear indication that Au grows in 3D clusters on TiO_2[6]. They also used LEIS signal intensity vs Au thickness graphs, observing a smooth, non-linear curve, characteristic of VW growth. Madey et al observed this growth using high resolution SEM (HRSEM)[15]. They describe the growth in detail, growing initially as 3D hemispherical islands (average film thickness, *h,* <1.0 nm), to partially coalesced worm-like island structures (*h* >1.5 nm), to percolation (*h*~8nm) and finally to a continuous and rough film (*h*~12 nm). STM studies by Goodman[16, 17] and LEIS studies by Campbell[12] further confirmed this growth method.

4.1.3 Annealing Au/TiO_2(110)

Au nanoparticles with a diameter of 2 nm or less have a low melting point (600 K) and tend to sinter, forming larger Au particles upon calcination. This causes poor dispersion and therefore poor catalytic activity[5]. As a result, there have been numerous studies looking at sintering of Au nanoparticles on TiO_2(110).

Zhang et al annealed Au/TiO_2 up to temperatures of 775 K and, using ISS and XPS, observed that less substrate area was covered by Au, due to island growth or thickening[6]. There was, however, no observation of the encapsulation of Au by TiO_x, suggesting that Au doesn't diffuse into the oxide on annealing[5]. Using HRSEM, they observed results consistent with their XPS/ISS results[15] – upon annealing to 775 K, the island size had increased whilst the island density had decreased. The Au islands were observed to be highly faceted with hexagonal shapes[15]. STM studies by Barteau et al showed that the gold nanoparticles (with a diameter of 1-3 nm) were not stable to even short durations of annealing to 700 K, resulting in significant growth of the particles and a reduction in their density[18]. Average particle size increased from 2.7 to 5.5 nm and the particle height increased from 0.45 to 0.75 nm. Molybdenum on TiO_2 was found to have much greater resistance to sintering – this was attributed to a stronger particle-surface interaction for Mo than for Au, due to partial oxidation of the Mo at the interface. STM movies were used to show that the sintering of Au nanoparticles on TiO_2 occurs via Ostwald ripening[19]. Larger clusters (above 50Å diameter) were found to be fairly static on the surface, whereas smaller clusters (<30Å diameter) were very mobile. They also clearly observed that the smaller clusters shrunk in size whilst larger clusters grew, as expected with the Ostwald ripening mechanism. Subsequent in-situ STM whilst annealing to 950 K by Goodman et al[16] suggested that the Au clusters grow by cluster migration and coalescence, as the annealed clusters were seen to move up to 5 nm from their original positions, which would not happen with Ostwald ripening.

4.1.4 Growth of Au on Pd(110)

Several studies have been carried out looking at the growth of Au on Pd(110), each with differing conclusions. Schmilz investigated the growth of Au films on Pd(110) in 1991 using Auger spectroscopy and CO thermal desorption[20].

They concluded that the films grew via a Stranski-Krastanov mode, with a critical thickness of two monolayers. A year later, Vos used MEIS to conclude that Au films grow in a layer-by-layer fashion on Pd(110), rather than Stranski-Krastanov, agreeing with findings by Kuk et al, who found that Au grows layer-by-layer on Pd(111)[21]. However, several years later, Kralj used STM and surface x-ray diffraction and concluded that the growth mode was actually a multi-layer/Volmer-Weber type growth[22]. Below one monolayer, strained gold islands were formed.

4.1.5 Palladium-gold bimetallic model catalysts

Alloyed / bi-metallic catalysts have applications in a wide range of processes, due to their increased activity, stability and selectivity compared to their component metals[23]. The activity of a bimetallic catalyst depends on several factors, including the distribution of electron density over the particle, the positions of the component species on the catalyst and changes in geometry caused by the interactions of the two metals[24]. A detailed review of catalysis by supported Au-Pd catalysts is presented in chapter 1 of this thesis.

4.2 Experimental

Most of these experiments were carried out as described in chapter 2, in the system referred to as “UHV1.” The only exception is that the Auger experiments in section 4.3.2.2 were carried out in “UHV2.”

A TiO_2(110) single crystal was placed into the machine via the fast-entry lock and subject to cleaning cycles until the ISS and XPS showed no contaminations. The cycles consisted of sputtering (1 keV, 20-40 minutes) at room temperature, followed by annealing to 873 K for 15 minutes.

When trying to achieve a well-oxidised TiO_2 surface, the sample was heated in oxygen (10^{-6} mbar) at temperatures up to 873 K for 10 minutes.

Gold was deposited on to the crystal by MVD (metal vapour deposition). A current was passed through the metal filament and allowed to degas for 20 seconds. The crystal was then moved below the filament, approximately 1-2 cm below. Palladium was deposited on to the crystal by MVD, as described in chapter 3.

4.3 Results

4.3.1 Au on TiO_2(110)

4.3.1.1 Preparation of Au/TiO_2

Gold was deposited on to TiO_2 via metal vapour deposition at room temperature. The ISS (Figure 4-1) shows a large gold peak at 928 eV. The Au4f XPS peak is shown in Figure 4-2. It has a doublet structure, with the peak at 84 eV corresponding to the $4f_{7/2}$, and the peak at 87 eV corresponding to $4f_{5/2}$. The ratio of the $4f_{7/2}$ peak to the $4f_{5/2}$ peak is 4:3, due to spin orbit splitting.

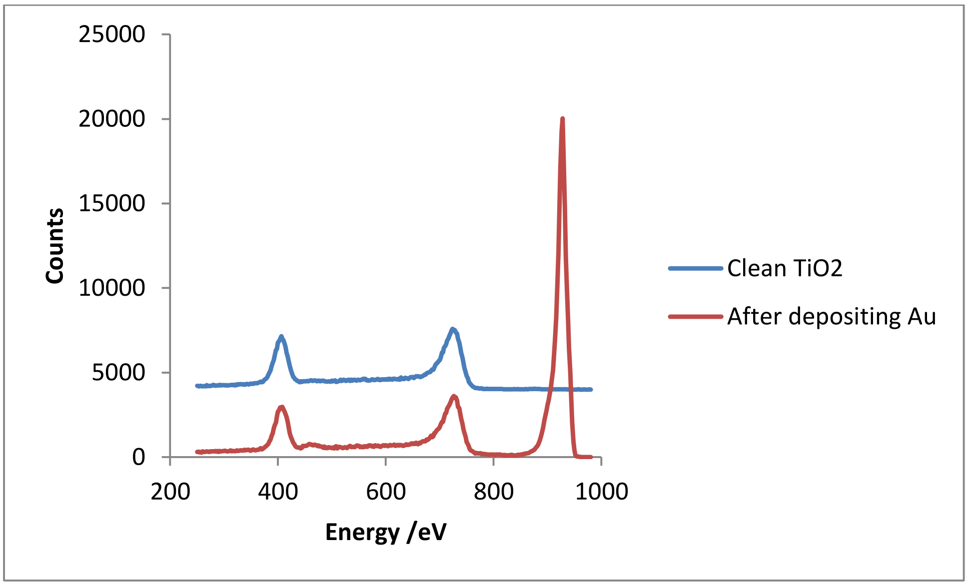

Figure 4-1 - Example ISS spectra of the TiO_2 sample after dosing with Au

There appears to be no change in the XPS binding energies of Au and Ti during Au deposition, as shown in Figure 4-2 and Figure 4-3. This agrees with work by Madey et al[6], who observed only a small change in XPS binding energy for Au and Ti during early stages of Au deposition. The Au binding energy was shifted by 0.4 eV to high binding energy. This slight shift was due to low coverages resulting in reduced coordination and electron screening effects. The Ti binding energy shifted by 0.1-0.2 eV to high binding energy, due to band bending. However, looking at the Ti2p XPS spectra in Figure 4-3, it does look as though a very small amount of Ti^{3+} has been converted to Ti^{4+} on deposition of Au; there is a slight shoulder at ~457 eV that is not present after depositing Au. Au is more electronegative than Ti, so it is possible that the small amount of gold present on the surface is taking some of the Ti electron density.

Gold was removed from the surface with alternate cycles of ion bombardment at room temperature (1 keV) and annealing to 873 K for 10 minutes, and monitored using ISS and XPS.

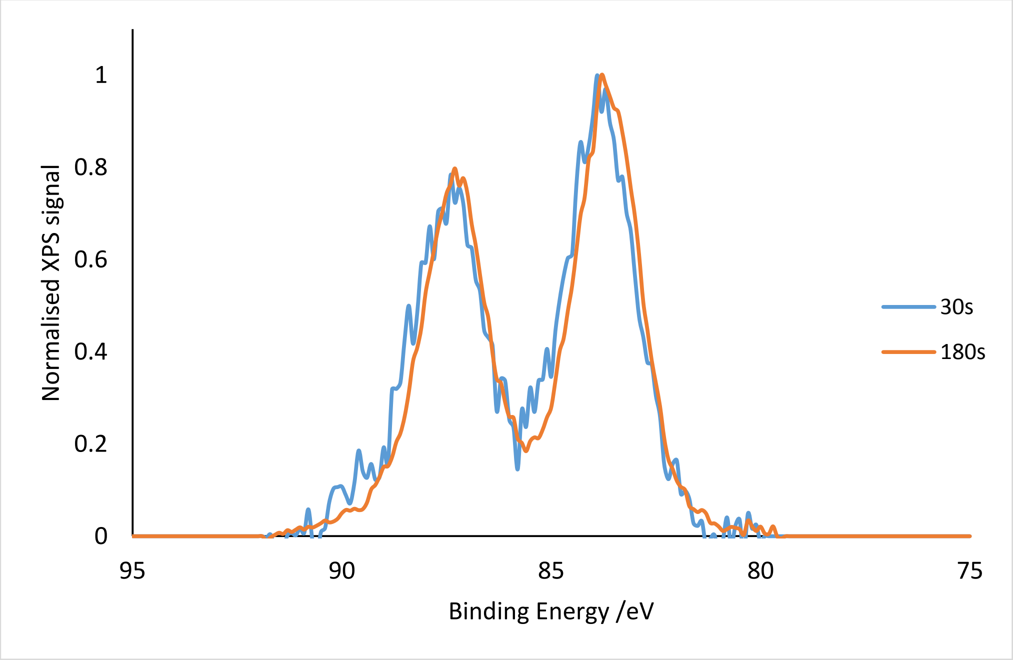

Figure 4-2 - Au4f XPS spectra after dosing Au onto $TiO_2(110)$ for (i) 30s and (ii) 180s

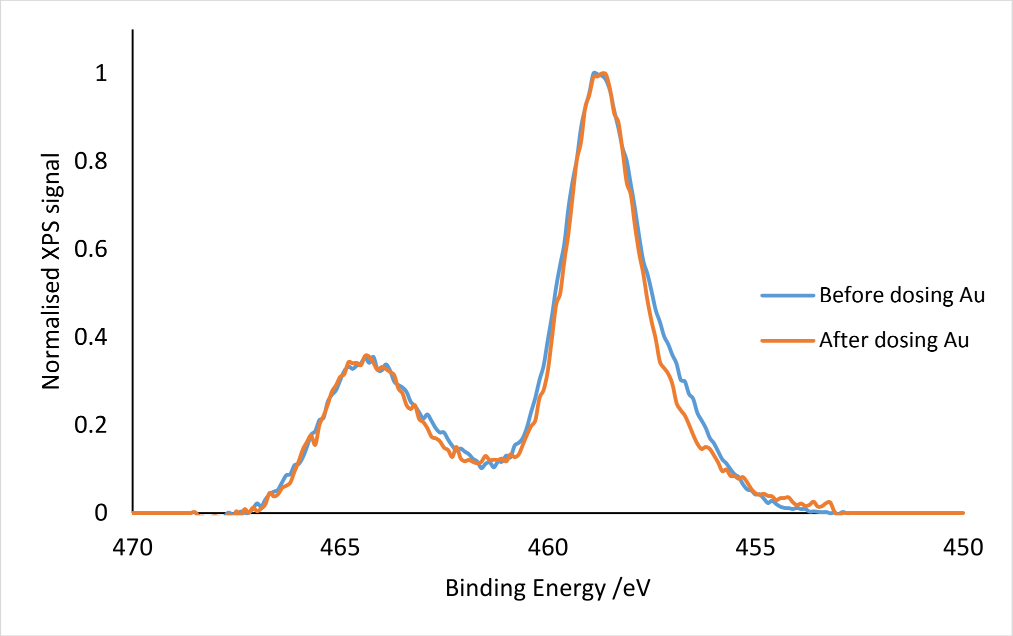

Figure 4-3 - Ti2p XPS spectra (i) before dosing Au and (ii) after dosing Au for 180s onto TiO$_2$(110)

4.3.1.2 Annealing Au on TiO$_2$(110)

The effect of heating varying coverages of Au on TiO$_2$(110) over a range of temperatures (473-873 K) was investigated using XPS and ISS.

Figure 4-4 and Figure 4-5 show the Ti2p and Au4f XPS respectively after annealing a coverage of 1.40x10^{15} atoms cm^{-2} of Au on TiO$_2$(110) (calculated using Carley's equation, described in chapter 2 of this thesis). There is no visible change in the shape of the Ti2p spectra on annealing to 873 K. The intensity does increase, however, by 23%. Likewise, the Au4f peak doesn't change shape but decreases by 9%.

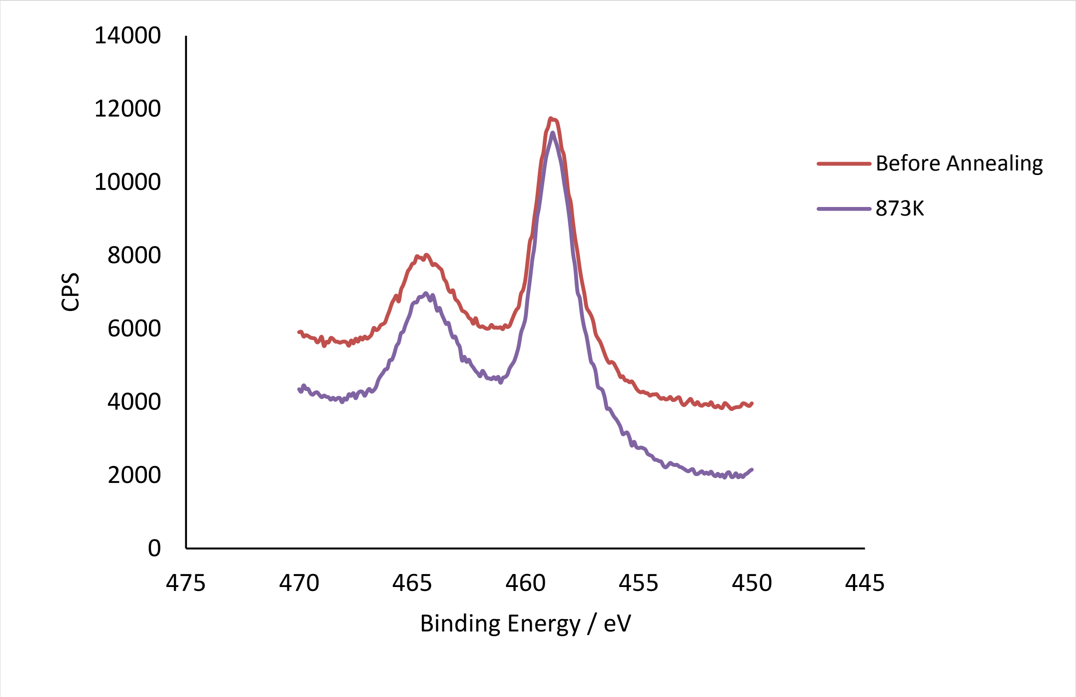

Figure 4-4 - Ti2p XPS data before and after annealing Au/TiO_2 to 873 K

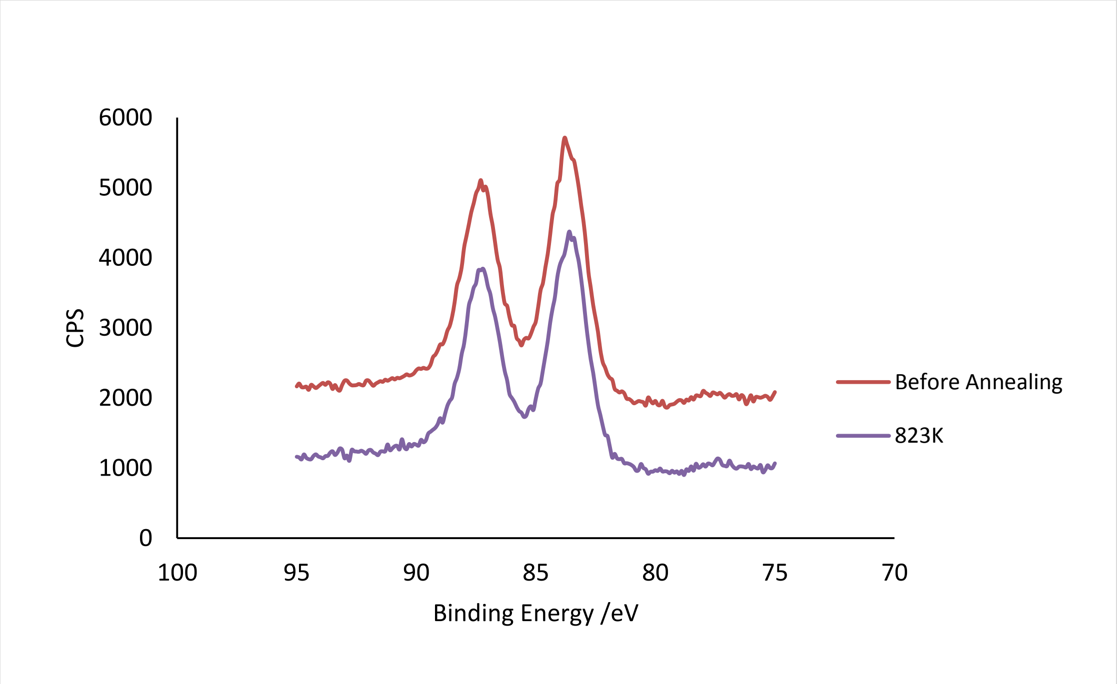

Figure 4-5 - Au4f XPS data before and after annealing Au/TiO_2 to 873 K

Figure 4-6 shows the ISS data taken from annealing the same coverage of Au. Before annealing, the Au peak dominates the spectra. On annealing to 473 K the Ti and O peaks become more prominent. The Ti and O peaks increase in size on annealing to higher temperatures, as does the Au peak up to 773 K, before decreasing at 873 K. Figure 4-7 shows in detail how the ISS area ratios are affected. The gold signal drops dramatically at low temperatures, from 60:1 for Au:Ti and 40:1 for Au/O to ~10:1 for both at 573 K. After this, the Au:Ti and Au:O ratios decrease very slightly on increasing anneal temperature, reaching ~5:1 by 873 K. Figure 4-8 shows the Au:Ti and Au:O height ratios taken from ISS, and they follow a similar trend – a sharp decrease in the Au:Ti and Au:O ratios at 573 K, and then a more gradual decrease at higher temperatures. This suggests that at low temperatures the Au film de-wets and forms nanoparticles. The continuing decrease in Au:Ti and Au:O ISS signals at higher temperatures suggests that the Au nanoparticles continue to coalesce and form fewer, larger particles. This is known as mass conservation[6] – an increase in island size is accompanied by a reduction in the area of the substrate that is covered in islands. Zhang et al surmised that, at low temperatures, kinetic factors favour a high density of small islands. At high temperatures, thermal effects dominate and the kinetic barriers are overcome. There are two theories about how these Au clusters grow in size upon annealing[6] – the first is that the clusters grow in size by a combination of sintering and coalescence. The second is an “island thickening model,” proposed by Campbell[25]. This suggested that the 2D islands nucleate and grow in diameter until they reach a certain critical size, after which they thicken. Zhang et al also studied this system with high resolution scanning electron microscopy (HRSEM)[15], observing that annealing leads to increased area of exposed substrate, agreeing with the ISS and XPS data presented in this chapter. There is no evidence in the Ti2p XPS of the encapsulation of the Au by the support, as there is no Ti^{2+} present in the spectra at any point. Zhang et al suggested that the metal has to be reactive enough to cause the decomposition of TiO_2 to TiO_x($x<2$). A schematic is shown in Figure 4-9, illustrating what is thought to occur on annealing Au/TiO_2(110), depicting what has been described above.

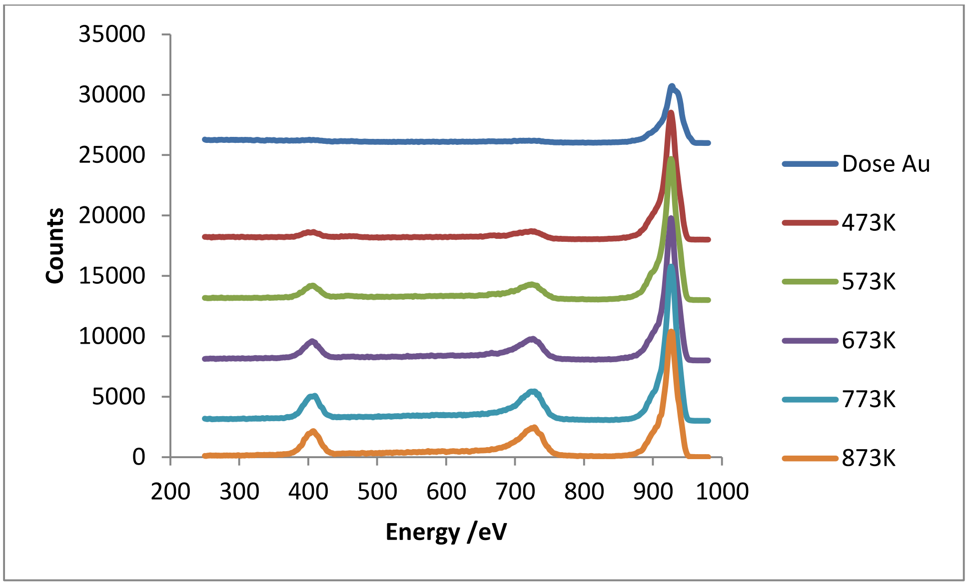

Figure 4-6 – ISS raw data of Au on TiO_2(110) taken after annealing to increasing temperatures

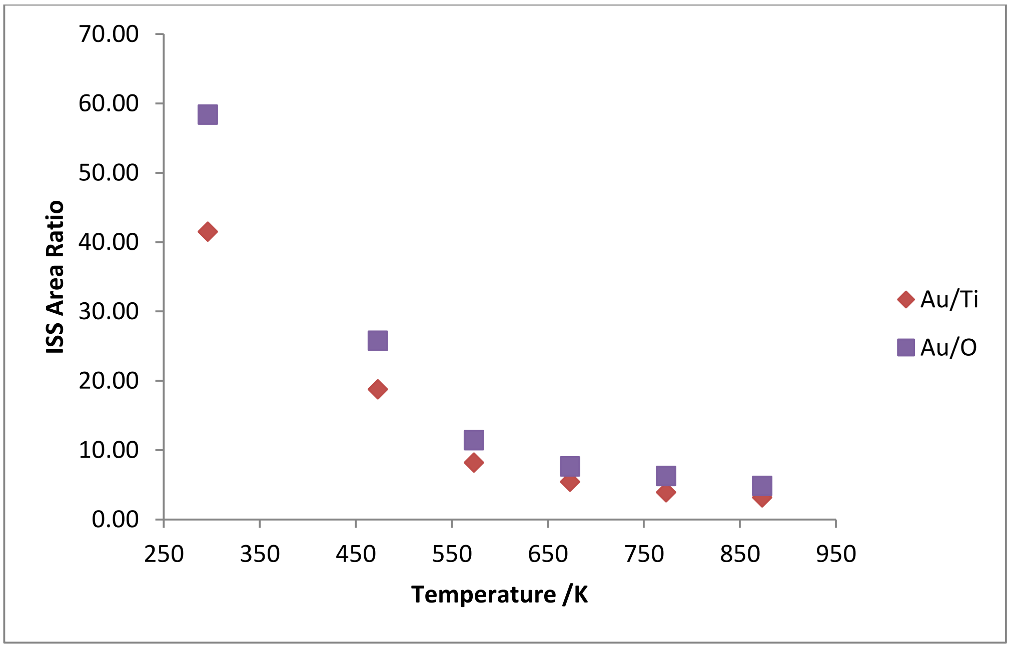

Figure 4-7 – How the Au/Ti and Au/O area ratios in the ISS are affected by temperature

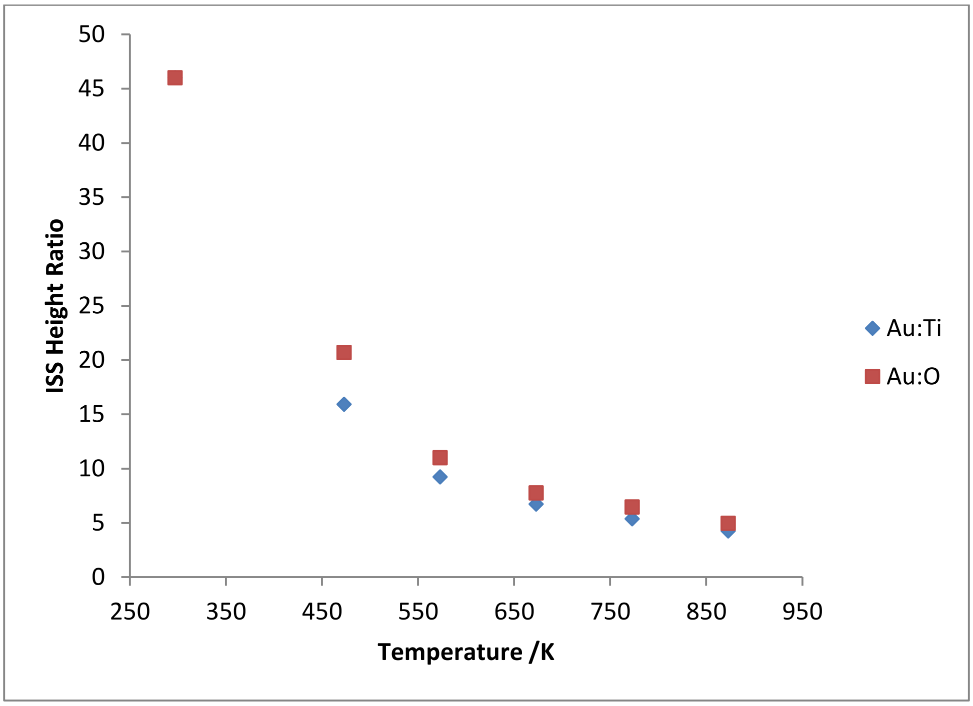

Figure 4-8 - How the Au:Ti and Au:O height ratios are affected by temperature

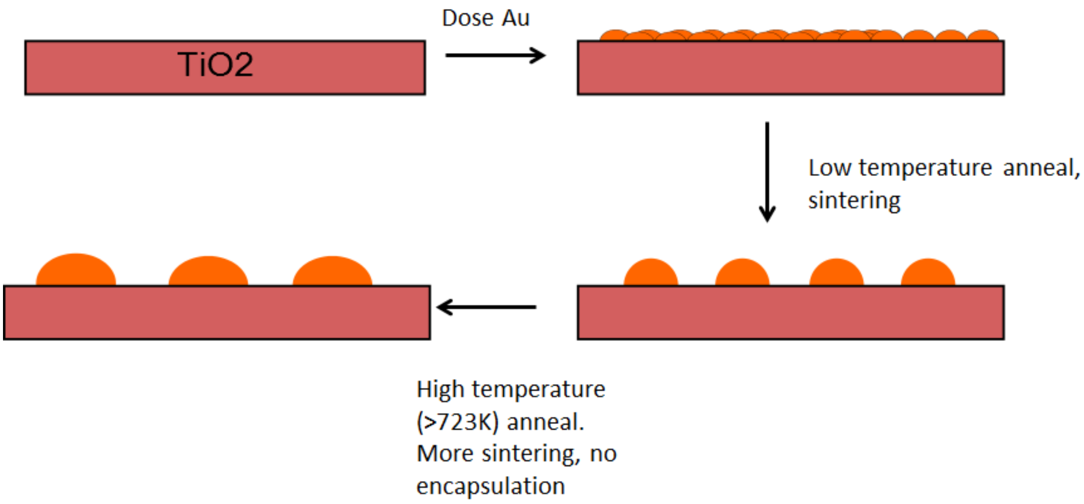

Figure 4-9 - Schematic of what occurs on annealing Au/TiO2(110)

4.3.2 Pd-Au bimetallics on $TiO_2(110)$

4.3.2.1 Growth of Au on $Pd/TiO_2(110)$

The growth of Au on Pd/TiO_2 was investigated. In two separate instances, a film of 0.4 nm and 1.4 nm of Pd was deposited on to $TiO_2(110)$ (determined using the thickness equation, described in chapter 2), and then Au was deposited and the growth was monitored with ISS and XPS. The ISS raw data for the deposition of Au on to 0.4 and 1.4 nm of Pd on $TiO_2(110)$ are shown in Figure 4-10 and Figure 4-11 respectively. In Figure 4-10, after depositing Pd, there is still a visible Ti signal in the ISS, which shows that the film is not uniform across the TiO_2 sample, and instead the Pd is most likely present as 3D islands across the surface. This is in contrast to Figure 4-11, where enough Pd was deposited to completely cover the Ti ISS signal at ~740 eV. In both instances, as gold is deposited on to the Pd-$TiO_2(110)$ surface, the Au signal increases whilst the Pd signal decreases. The Au/Pd, Au/Ti and Au/O ISS height ratios are shown in Figure 4-12 (the Au:Ti ratio is not shown for the 1.4 nm Pd, as the Ti signal was not visible on deposition of the Au). The Au:Pd ratio follows the same, approximately linear, trend, regardless of the starting amount of Pd. The Au:Ti ratio for growth on 0.4 nm of Pd, follows a similar trend.

Figure 4-13 shows the area ratios taken from the XPS. Each of the growth curves are linear, suggesting that the growth is Frank-van der Merwe in nature.

The change in Au:Ti ISS ratio in Figure 4-12 is greater than the Au:Pd ratio (the Au:Ti ratio increases to ~16, whereas the Au:Pd ratio increases to only ~4), indicating that the Au grew preferentially on the $TiO_2(110)$ substrate, rather than nucleating around and over the Pd particles on the surface. Davies and co-workers observed something similar when depositing Au and Pd on to $Fe_2O_3(0001)$[24]. In this study, Au was deposited first, followed by Pd. STM was carried out in between depositing the two metals, and it was noted that the Au and the Pd formed particles of differing sizes, suggesting that it is more favourable for the Pd and Au metal to bond with the substrate rather than with each other. ISS confirmed this, as both Pd and Au were visible after deposition.

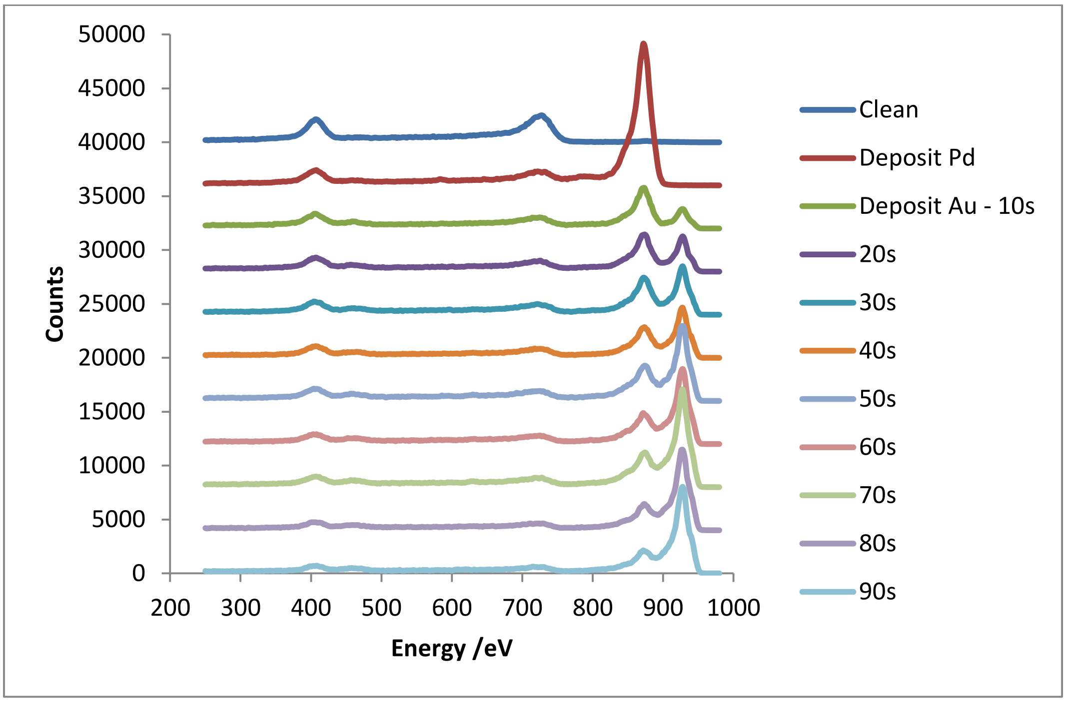

Figure 4-10 - ISS raw data showing the growth of Au on 0.4 nm of Pd on TiO_2

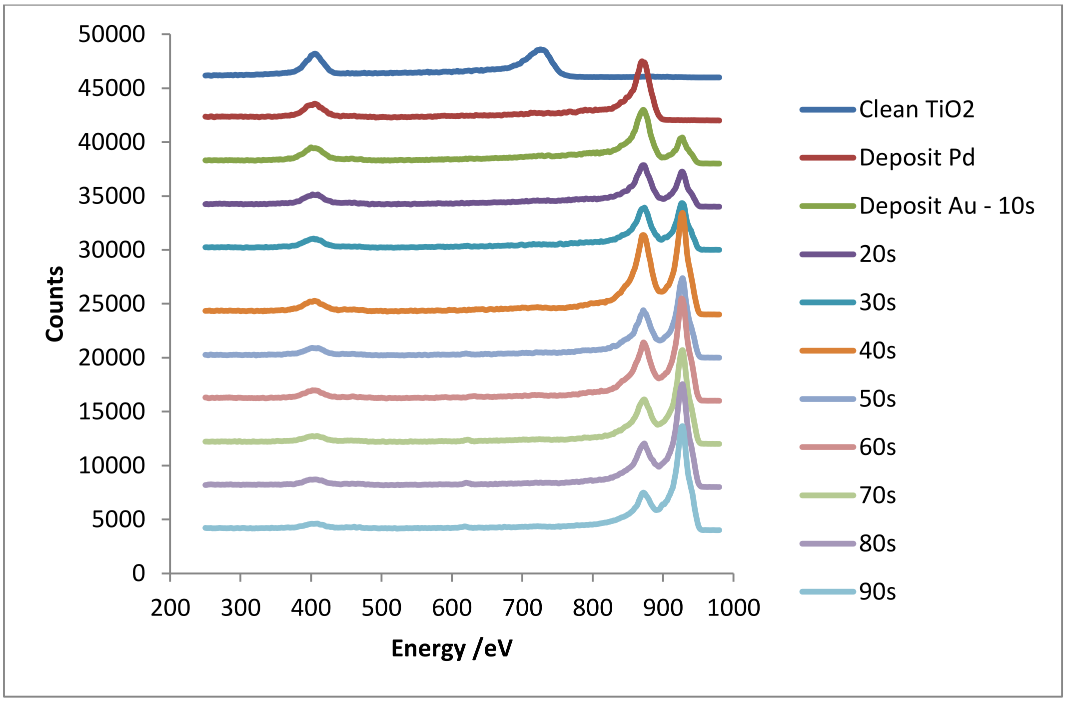

Figure 4-11 - ISS raw data showing the growth of Au on 1.4 nm of Pd on TiO_2(110)

An earlier ISS study by Steltenpohl on the co-deposition of Pd and Au thin films on Ru(001) found a similar result[26]. 0.5 ML of Pd was first deposited on to the Ru(001) substrate and characterised with ISS. After this, several small doses of Au were evaporated and the surface composition was analysed with ISS after each step. They found that Au initially adsorbed on to the clean Ru patches, until they were almost completely filled, giving an almost complete 2D monolayer consisting of Pd and Au patches. After completion of the first monolayer, the Au preferentially grew on the Pd patches. Steltenpohl also observed that the co-deposited Pd and Au grows (nearly) as a two-dimensional monolayer, independent of the deposition sequence[26], which again agrees with the ISS and XPS data presented here. The growth of Au on 1.4 nm of Pd also appears to be Franck-van der Merwe in nature, as shown by the XPS ratios in Figure 4-13 – a linear growth curve indicates layer-by-layer growth, whereas a non-linear growth curve indicates 3-dimensional island growth, as explained in chapter 3.

On depositing Au on to the Pd, no shifts were observed in either the Pd3d or Au4f XPS. This contrasts with work by Nemsak and Skala who found that the Pd and Au binding energies shift when depositing Au and Pd alternately on Al_2O_3[27]. The shift was very small, only ~0.4 eV, so it is possible that this shift was not observable with our XPS set up, whereas Nemsak was using synchrotron XPS, which is much more sensitive to small shifts in binding energy.

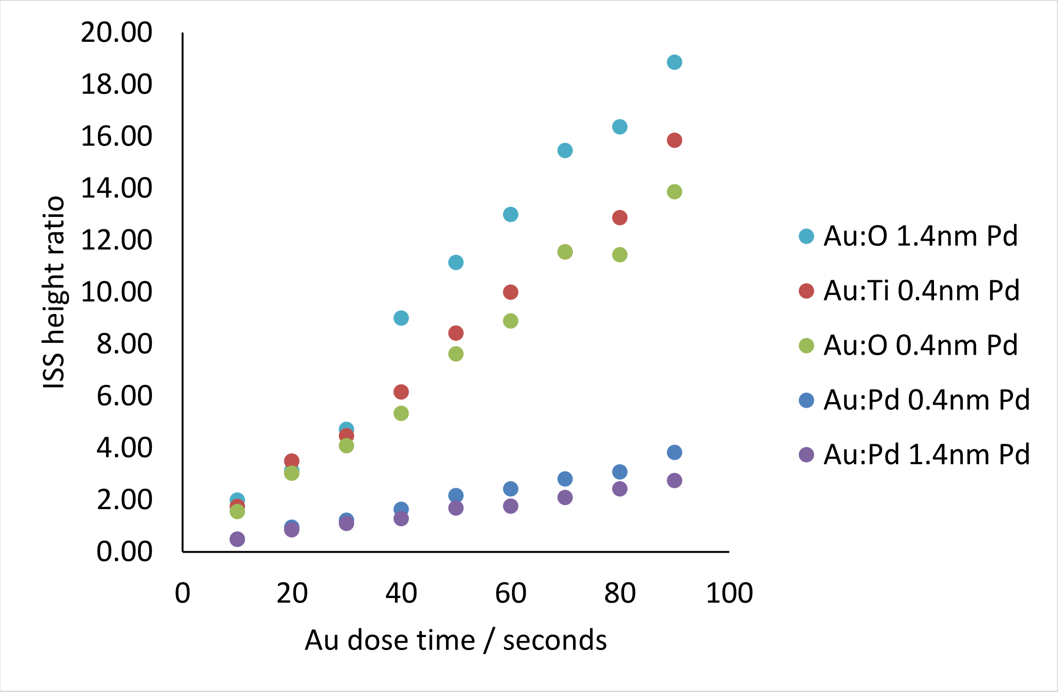

Figure 4-12 - ISS height ratios – not normalised

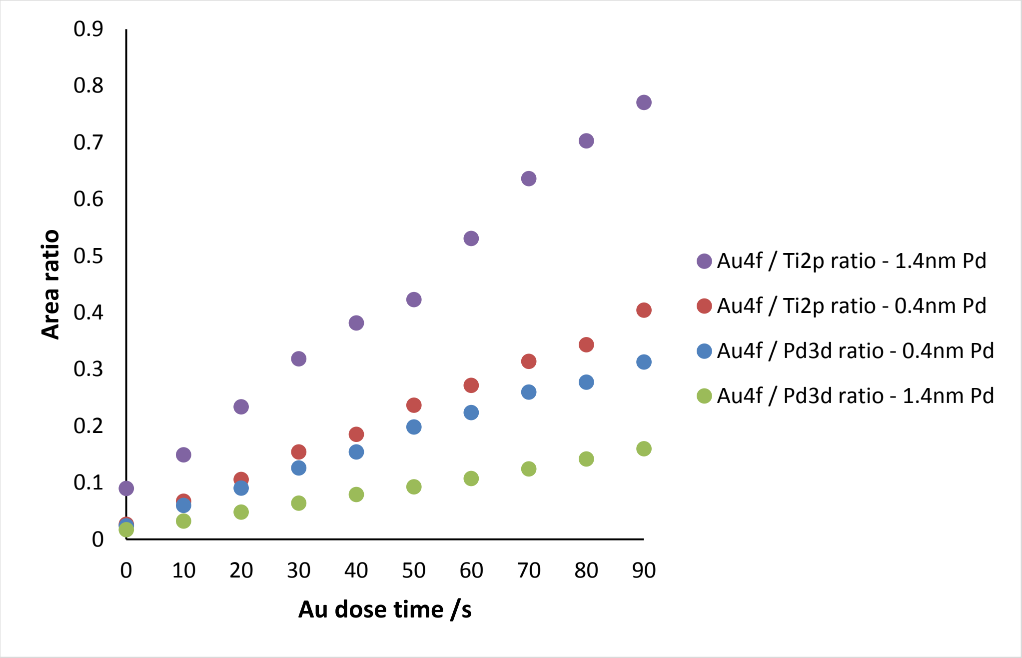

Figure 4-13 - XPS area ratios

4.3.2.2 Annealing Pd and Au on $TiO_2(110)$

After depositing both Pd and Au separately onto $TiO_2(110)$ and examining their behaviour under thermal treatment, both metals were deposited onto the surface in the same experiment, with the objective being to observe any interaction between them and any changes in their interaction with the surface in each other's presence. The experiment was initially carried out on a sputtered surface. Pd was deposited first on to the TiO_2 for 180 seconds (approximately 2.4 nm) and the surface was then characterised with XPS and ISS, before then depositing Au for 30 seconds and characterising the surface again. After this, the surface was annealed to 823 K and examined once more with ISS and XPS. Ion scattering spectroscopy of the entire experiment is shown in Figure 4-14. The peak assignments are as follows: oxygen is observed at ~410 eV, titanium at ~740 eV, palladium at ~880 eV and gold at ~930 eV. In Figure 4-14a, only a Ti and an O peak are visible, as the surface is freshly cleaned. On depositing Pd, in Figure 4-14b, the Pd signal dominates the spectrum. The Ti signal is no longer visible and the O signal is greatly reduced. The fact that the oxygen signal is not as reduced as the Ti signal once Pd has been deposited suggests that there is oxygen on the Pd surface. Diebold and Madey made a similar observation when investigating the growth of Hf on TiO_2 with ISS[28]. After depositing a monolayer of Hf onto TiO_2, the Ti signal had decreased and the Hf signal had increased as would be expected for complete wetting of the first monolayer, indicating that no mixing of the Hf and Ti had occurred on deposition. However, oxygen stayed visible up to much higher coverages, suggesting that the oxygen was incorporated into the reactive metal overlayer and that a relatively high coverage was required before metallic Hf could be seen. However, as described below, the XPS indicated that the Pd metal was not oxidised on deposition. On depositing the Au, the Pd/O signal ratio increases from ~3.6 to ~7.2. It is possible that there is a small amount of O on the Pd (either as CO or O) which is then displaced by the Au when it is deposited, as Au cannot adsorb CO from the background whereas Pd can, very easily. On depositing the Au, both Pd and Au are visible in the ISS. It is interesting to note that the Pd signal actually increases on deposition of Au (Figure 4-14c). This is unexpected –one would expect the Pd signal to decrease as the Au is surely covering at least some of the Pd metal. This same phenomenon was observed by Ovari and Kiss when depositing Rh on top of $Au/TiO_2(110)$[29]. They suggested that the enhancement of the Au LEIS peak due to Rh deposition was because the Rh atoms moved to subsurface sites of the Au particles immediately after being deposited on top of the Au clusters. The enhanced volume of the bimetallic clusters with the Au atoms outside led to the increase in LEIS intensity[29]. It is very likely that the same thing is happening here on depositing the Au on top of the Pd thin film – the Au atoms are moving to subsurface sites of the Pd particles, giving an enhanced volume of bimetallic clusters with Pd on the outside, leading to an increase in the Pd ISS signal. On annealing to 823 K, the ISS no longer shows any Au signal (Figure 4-14d). The Pd signal at 880 eV is still present, and the Ti signal at 740 eV has returned.

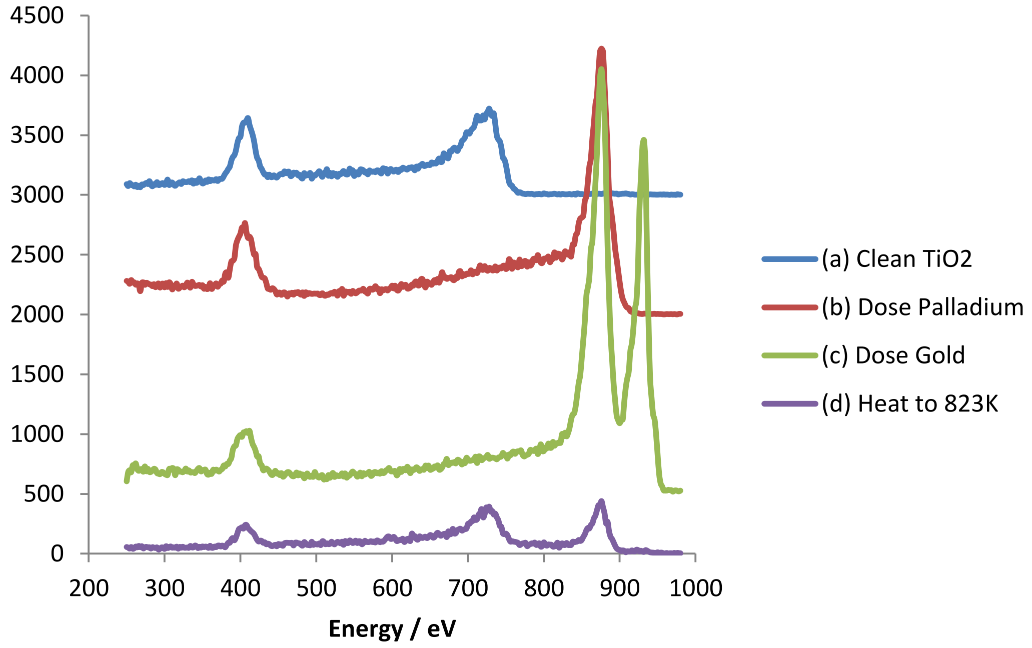

Figure 4-14 – Ion Scattering Spectra of the $TiO_2(110)$ surface after: (a) cleaning, (b) depositing ~2.4 nm Pd (c) depositing Au and (d) annealing to 823 K for 5 minutes

XPS of the Ti2p, Pd3d and Au4f regions taken during this experiment are shown in Figure 4-15, Figure 4-16 and Figure 4-17 respectively. Figure 4-15a shows the Ti2p region before depositing any metal. The $2p_{3/2}$ peak can be seen at 459 eV and the $Ti2p_{1/2}$ peak is at 464 eV. The TiO_2 surface was sputtered before taking this spectra, in order to get a reduced surface with a large concentration of Ti^{3+} and Ti^{2+}present, hence why the peaks are very broad (for a detailed discussion on the effect of sputtering on TiO_2, please see chapter 3 of this thesis). On depositing Pd and then Au, the Ti signal decreases. On annealing the sample, the Ti signal increases again and a shoulder peak emerges at 455 eV, as shown in Figure 4-15d. The Pd3d signal in Figure 4-16 is largely unaffected by depositing Au, and then decreases by 25% on annealing to 823 K. The peak at 335 eV is the $Pd3d_{5/2}$, and the peak at 340 eV is $Pd3d_{3/2}$. The Au4f region shows a peak at 88eV after depositing Pd, but before depositing any Au (Figure 4-17a). The single peak at 88 eV is the Pd1s peak. After depositing Au, the Au4f peak dominates the Pd1s peak. However, the Pd1s peak does contribute to the overall peak – the $Au4f_{7/2}$ peak at 84 eV should be 4/3 times bigger than the $4f_{5/2}$ peak due to spin orbit splitting, as described above in section 4.3.1.1. However, the $4f_{5/2}$ peak is 25% times bigger than the $4f_{7/2}$ peak, due to the contribution of the Pd1s peak.

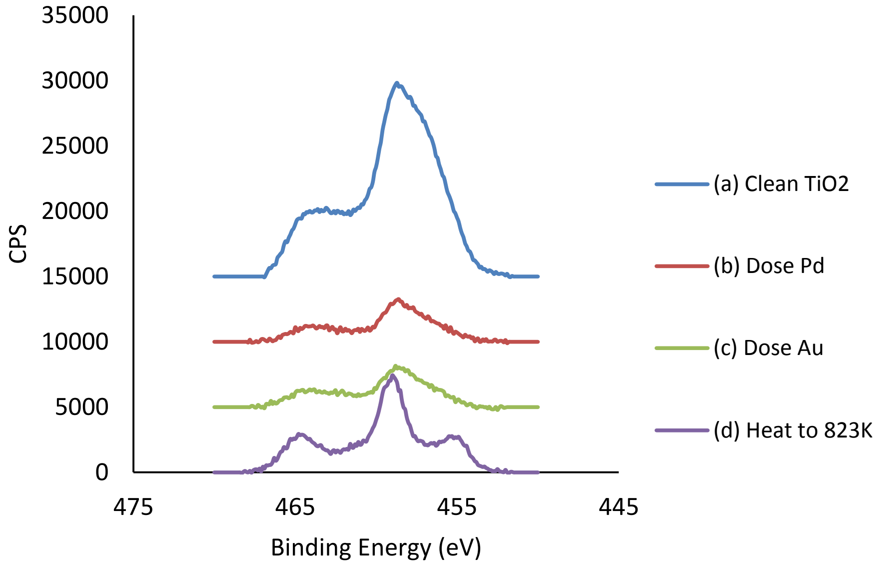

Figure 4-15 - XPS of the Ti2p region of TiO_2 after (a) cleaning, (b) depositing ~2.4 nm Pd (c) depositing Au and (d) annealing to 823 K for 5 minutes

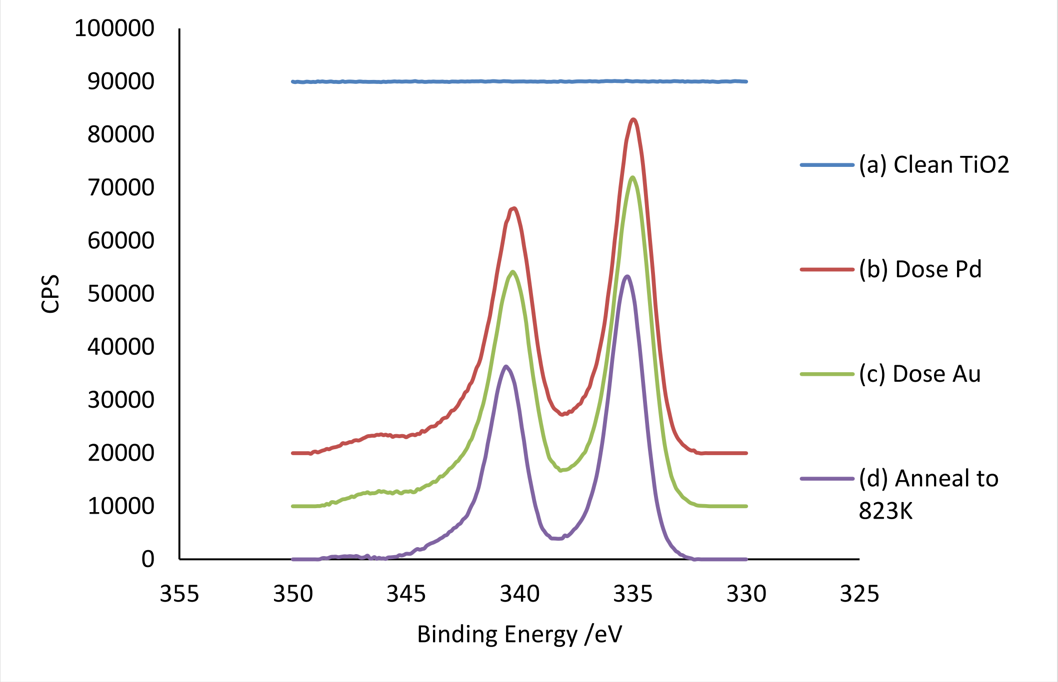

Figure 4-16 - XPS of the Pd3d region of TiO$_2$ after (a) cleaning, (b) depositing Pd at 3.0A for 180s, (c) depositing Au at 3.0A for 30s and (d) annealing to 823 K for 5 minutes

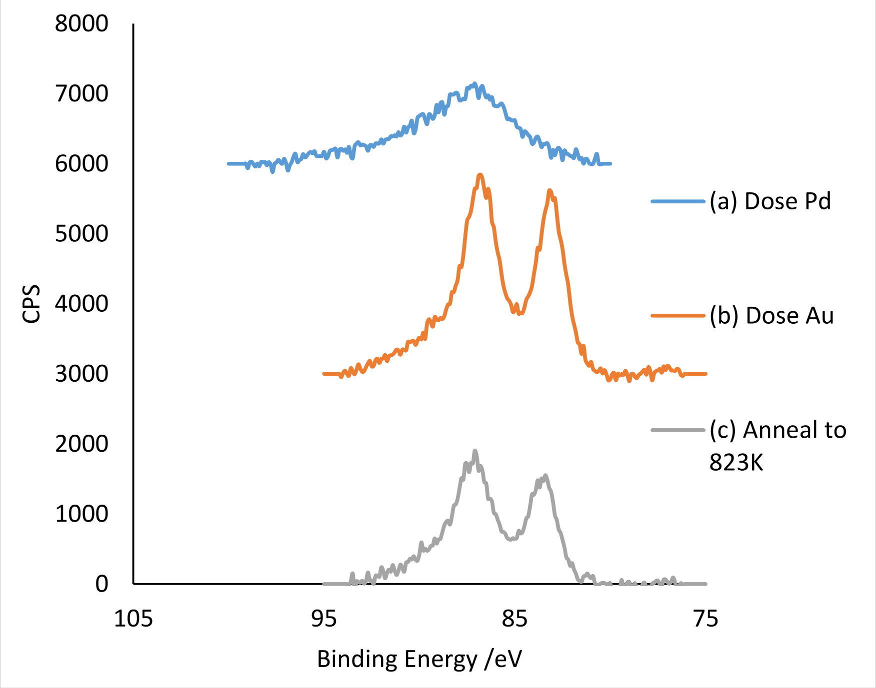

Figure 4-17 - XPS of the Au4f region of TiO$_2$ after (a) depositing Pd at 3.0A for 180s, (b) depositing Au at 3.0A for 30s and (c) annealing to 823 K for 5 minutes

The disappearance of the Au signal from the ISS after annealing suggests one of two things; either the Au has evaporated from the surface, or it is being covered by something, rendering it unobservable by ISS. There are two observations that suggest that the Au has not left the surface: (i) when Au is annealed in the absence of Pd (see section 4.3.1.2 above), the Au signal is not lost from the ISS, and (ii) the Au signal is still very much present in the XPS after annealing. Taking this into account, it seems most likely that on heating the Au and Pd form bimetallic particles, with an Au-core and a Pd-shell. At the same time, there appears to be an SMSI effect occurring (as seen with Pd and discussed in Chapter 3, but not seen with Au on its own), as evidenced by the reduced Pd signal in the ISS and the appearance of a shoulder peak at 455 eV (characteristic of Ti^{2+}) in the Ti2p spectra on annealing. In order to determine if the core-shell formation and the SMSI were related or not, the experiment was repeated, with intermittent annealing from 473-873 K after depositing both metals. The resulting ISS and XPS are shown in Figure 4-18 and Figure 4-19-Figure 4-23 respectively. The ISS shows that, even when annealing to only 473 K, the Au signal drops dramatically – the Au/Ti signal drops from ~18:1 (the Ti signal is essentially completely covered) to only ~0.5:1, whereas the Pd/Ti signal is ~2.3:1, as shown in

Table 4-2. The Au/Pd ratio drops from ~1.14:1 to ~0.2:1. The Au signal continues to decrease, until it disappears entirely from the ISS at 773 K. The Pd/Ti signal decreases from ~2.3 (on annealing to 473 K) to ~0.33 (on annealing to 873 K). The Ti2p XPS spectra shown in Figure 4-20 shows an increase in signal on increasing temperature. A Ti^{2+} shoulder emerges at 455.5 eV only on annealing to 773 K. This is further shown in Figure 4-21, a closer look at the normalised Ti2p spectra. The Pd3d (Figure 4-22) and Au4f (Figure 4-23) XPS spectra show that the metal signals decrease on annealing, as they do when annealed separately (i.e. in the absence of the other metal). Table 4-3 shows the XPS ratios – the Au4f:Pd3d ratios do not change drastically on annealing, suggesting that the Pd shell around the Au cannot be thicker than a few nanometres – if it was thicker, the Au signal would decrease relative to the Pd signal on annealing to higher temperatures, as the XPS would be unable to penetrate the Pd layer. The C1s spectra (Figure 4-19) shows a carbon peak is present after depositing the Pd.

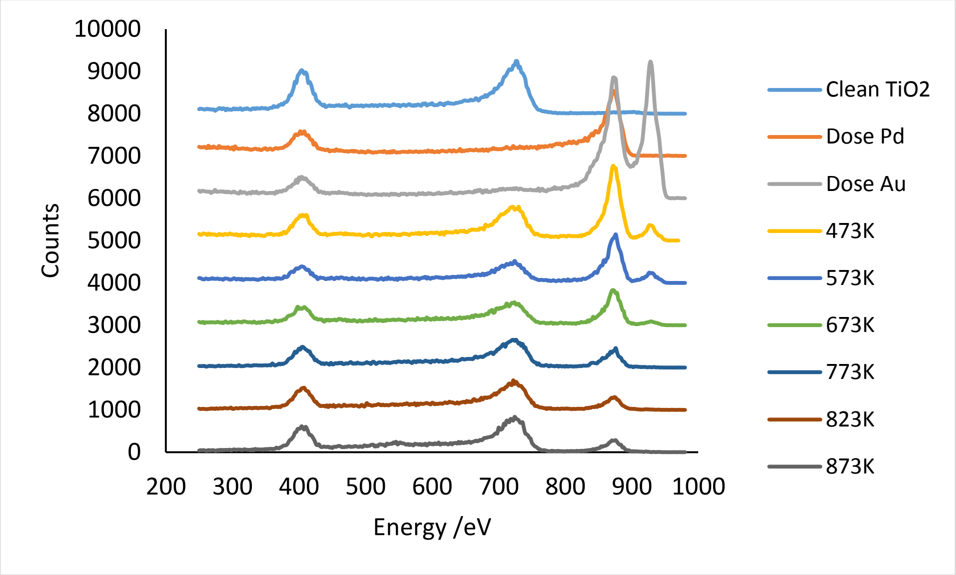

Figure 4-18 - ISS raw data of the TiO_2 surface taken after heating at increasing incremental temperatures

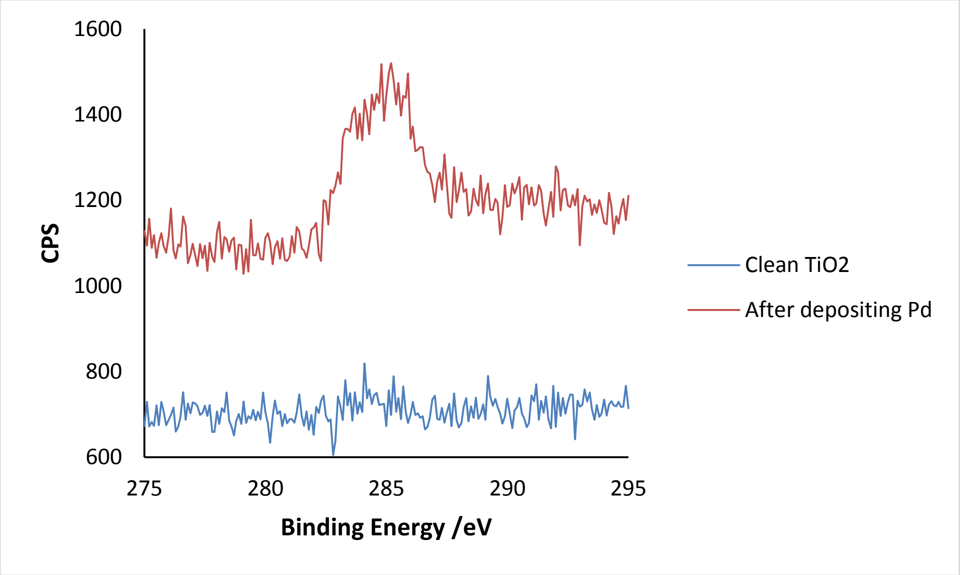

Figure 4-19 - C1s XPS spectra before and after depositing Pd on to $TiO_2(110)$

Table 4-1 – ISS area ratios taken from Figure 4-18

	Au/Pd	**Au/Ti**	**Pd/Ti**
Clean TiO_2	-	-	-
Dose Pd	0.00	-	-
Dose Au	1.02	-	-
Anneal to 473 K	0.14	0.21	1.48
573 K	0.15	0.28	1.89
673 K	5.67E-02	5.78E-02	1.02
773 K	0.00	0.00	0.37
823 K	0.00	0.00	0.23
873 K	0.00	0.00	0.20

Table 4-2 - ISS height ratios taken from Figure 4-18

	Au/Pd	**Au/Ti**	**Pd/Ti**	**Au/O**	**Pd/O**
Clean TiO_2	-	-	-	-	-
Dose Pd	-	-	10.17	-	3.21
Dose Au	1.14	18.29	16.00	8.00	7.00
Anneal to 473 K	0.21	0.48	2.26	0.72	3.39
573 K	0.23	0.50	2.22	0.82	3.64
673 K	0.10	0.17	1.61	0.21	2.07
773 K	0.00	0.00	0.70	0.00	0.95
823 K	0.00	0.00	0.42	0.00	0.58
873 K	0.00	0.00	0.33	0.00	0.46

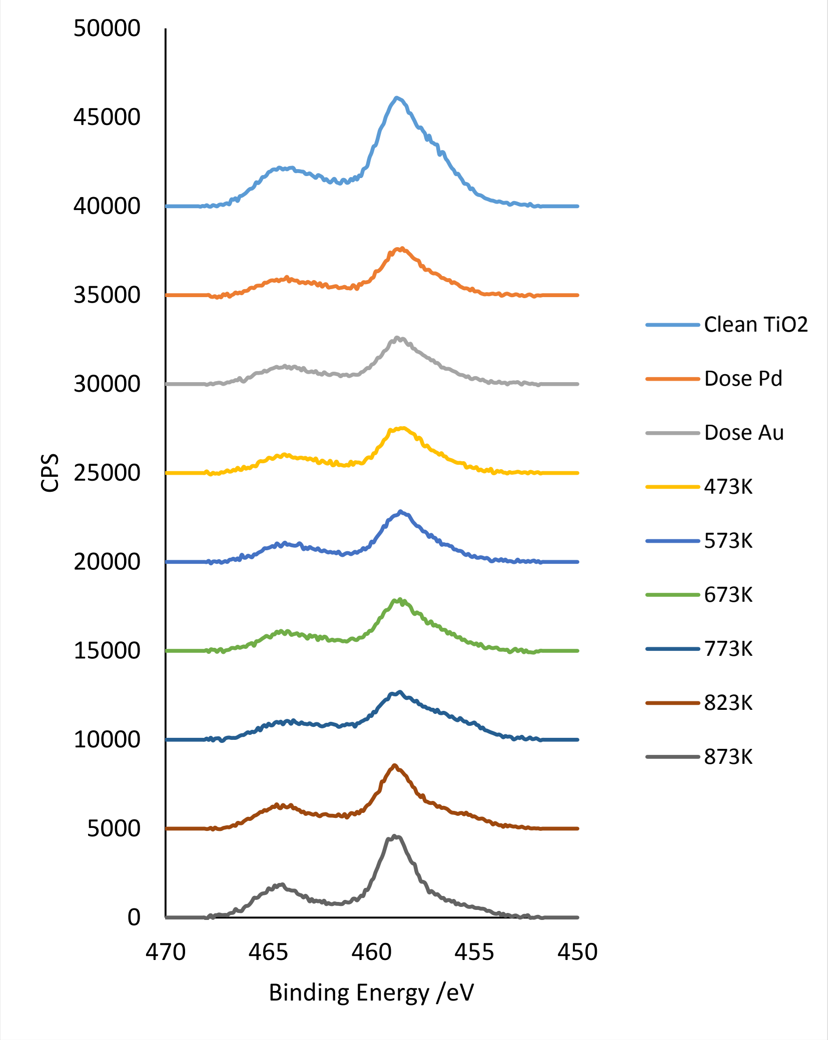

Figure 4-20 - Ti2p XPS raw data taken whilst annealing Pd and Au on TiO_2 at increasing incremental temperatures

Table 4-3 – XPS ratios taken from Figures 4-19, 21 & 22

	Au4f/Pd3d	**Au4f/Ti2p**	**Pd3d/Ti2p**
Clean TIO_2	0.00	0.00	0.00
Dose Pd	0.017	0.074	4.40
Dose Au	0.061	0.24	3.90
473 K	0.065	0.25	3.86
573 K	0.052	0.18	3.51
673 K	0.060	0.19	3.11
773 K	0.058	0.14	2.40
823 K	0.062	0.108	1.73
873 K	0.069	0.082	1.19

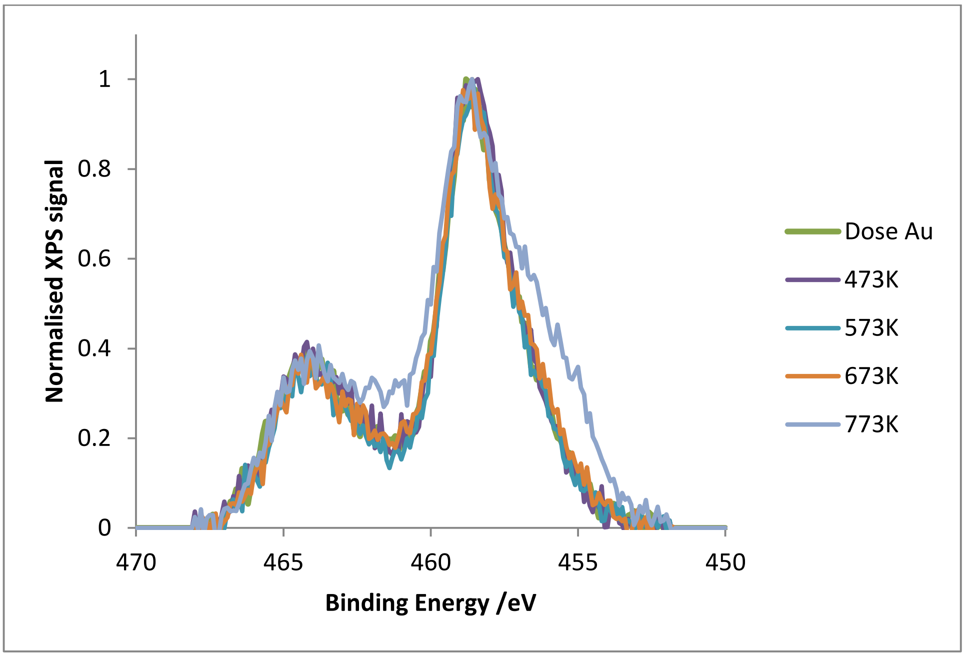

Figure 4-21 – Closer look at the Ti2p spectra shown in Figure 4-20

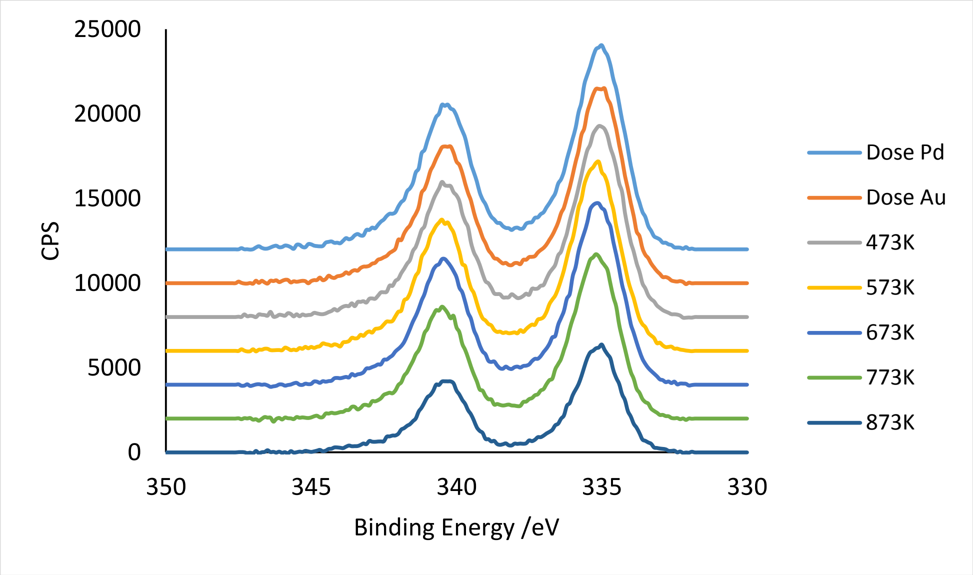

Figure 4-22 - Pd3d XPS data taken whilst annealing Pd and Au on TiO$_2$ at increasing incremental temperatures

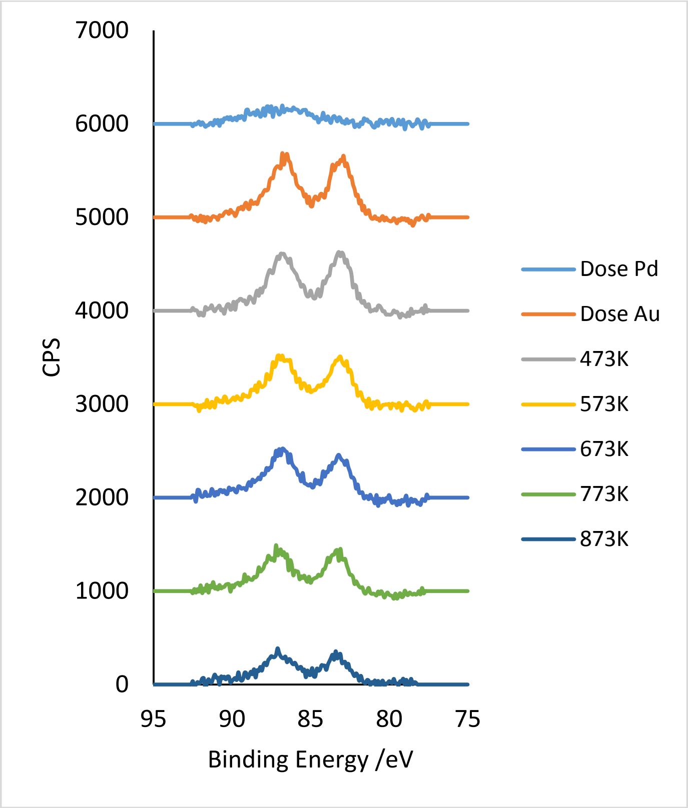

Figure 4-23 - Au4f XPS data taken whilst annealing Pd and Au on TiO_2 at increasing incremental temperatures

These results show that, not only do Pd and Au form an Au-core Pd-shell structure on TiO_2, but that it occurs separate from the SMSI effect seen when annealing Pd/TiO_2 to high temperatures, as the Au signal in the ISS begins to disappear at very low temperatures (below 773 K) whereas SMSI only begins to occur at temperatures above 773 K. The formation of this core-shell structure is surprising as, under ideal conditions, Au/Pd clusters are expected to form Au-shell Pd-core structures[31-33] as segregation of Au to the surface of a Pd-Au bimetallic particle has been found to be thermodynamically favourable[32]. The surface free energy for Au is 1.63 Jm^{-2}, whereas the corresponding value for Pd is 2.04 Jm^{-2} [34], which should favour enrichment of the surface with Au. Pd-core Au-shell particles were found to be the most stable when analysed using classic molecular dynamics simulation[31], and, according to these calculations, can even be formed when annealing other structures, e.g. Au-core Pd-shell particles.

However, Au-core Pd-shell structures have been observed when kinetics dominate over thermodynamic factors[35-37] or when the Pd has been oxidised[38]. Davies et al observed the formation of Au-core Pd-shell nanoparticles on γ-Fe_2O_3[24]. They found that the Au signal disappeared from the ISS after annealing to 573 K, and observed particles with STM. The formation of these particles was attributed to the oxidation of the Pd, however they could not be conclusive about this due to the lack of XPS or similar technique. This can't be a factor in my case, however, as the Pd3d XPS shows no signs of oxidation – PdO appears at 336-336.4 eV whereas the Pd metal signal appears at 335.1 eV[39] as shown in Figure 4-22. However, the ISS spectra do show an oxygen signal even when the Ti signal is covered by the Pd. Furthermore, there is a carbon signal present in the C1s XPS on deposition of the Pd. It's possible that the Pd has adsorbed CO from the chamber; CO has a very high sticking probability on Pd[40, 41], which will affect the surface free energy of the Pd once it is adsorbed. Guesmi and Zhu carried out a combined DFT and DRIFTS study, finding that Pd will enrich the surface of an Au-Pd nanocluster in the presence of CO[30]. Alternatively, as mentioned above, Madey et al observed oxygen in the ISS when depositing Hf on TiO_2 even at high coverages of Hf[28]. They proposed that oxygen from the titania was incorporated into the reactive metal overlayer, which may be occurring here as well.

It is interesting to note that Davies et al[24] saw the Au signal disappear from the ISS at 573 K, whereas the Au signal in Figure 4-18 (above) doesn't disappear until 773 K. This may be due to the amounts of Pd and Au deposited onto each surface. Davies evaporated only 10 seconds of Pd and Au onto the Fe_2O_3 surface forming only small nanoparticles between 5-10 nm in size, whereas I have evaporated a thin film onto the TiO_2 surface. A study by Freund found the opposite occurrence – after co-depositing Pd and Au onto various well-ordered oxide films [e.g. MgO(100), CeO_2(111), Fe_3O_4(111)] and annealing to 600 K with alternating O_2 and CO treatments, Au was found to segregate to the surface. The formation of unexpected core-shell structures has also been found with other elements - a combined XPS and ISS study of Pt & Au on TiO_2(110) was carried out by Chen et al[42]. LEIS showed that deposition of Au on Pt did not result in core-shell structures with Au on top, as predicted for the bulk phase. Instead, the clusters were 10-30% richer in Pt at the surface compared to the overall composition.

It was thought that the differing behaviour of these Au-Pd structures compared to that in the literature could be due to the differing amounts deposited – Goodman et al deposited 5 monolayers of Au and then Pd onto Mo(110) and, on annealing to 800 K, observed the segregation of Au to the surface in the ISS[34]. However, in my experiment, only 30 seconds of Au was deposited onto 180 seconds of Pd.

To investigate this further, this experiment was repeated twice with thicker films of Au deposited onto a film of Pd, to see if this encapsulation of Au by Pd still occurred. In the first instance, 150 seconds of Pd and 80s of Au was deposited onto an oxidised TiO_2 surface. In the second instance, 180s of Pd and then 180s of Au were deposited onto a sputtered TiO_2 surface. Both these were then annealed to 873 K.

The ISS results of the first instance are shown in Figure 4-24. On depositing Au on to the Pd/TiO_2, the Au/Pd ratio in the ISS is ~3:1 (see Table 4-4), substantially higher than the 1:1 ratio after depositing 30s of Au onto 180s of Pd. On annealing, the Au signal decreases and the Pd signal increases, as shown in Table 4-4. By 673 K, the Au signal has decreased to 1/3rd the area of the Pd signal, and the Ti and O signals are fully visible, having started to re-emerge at 473 K. At 723 K, both the Pd and Au signals drop dramatically – the Au:Ti ratio drops from 3 at 673 K to 0.4 at 723 K, and the Pd:Ti ratio drops from 8.7 to 0.7. At 773 K, the Au signal disappears from the spectra, just as with the previous experiment (where 30s of Au and 180s of Pd were deposited). The Ti and O signals continue to increase as the temperature rises, until 873 K where the Pd:Ti ratio is ~0.36. At 923 K, the Au signal returns in the ISS, and the Au:Ti and Pd:Ti ratios both increase. A closer look at the difference between heating to 873 and 923 K is shown in Figure 4-25. Bugyi et al[43] observed a similar phenomenon when annealing Rh nanostructures on TiO_2(110). On annealing to 750 K, there was a strong suppression of the Rh signal, indicating complete encapsulation of Rh. A further increase in the temperature led to a reappearance of the Rh LEIS signal. This behaviour was linked to an "intermediate" state of reduction of the TiO_2(110) crystal compared to former studies. Alternatively, it was mentioned earlier in this chapter that the observation of a Au-core-Pd-shell structure was thought to be due to kinetic effects dominating over thermodynamic effects[35-37]. It is possible that, on annealing to 923 K, thermodynamic effects start to dominate over kinetic effects, causing the de-encapsulation of the Au by the Pd. The Ti2p XPS results are shown in Figure 4-26. The Ti2p signal decreases on depositing the Pd, but does not change shape on deposition of either metal or on annealing to any temperature. Likewise, the Pd3d and Au4f XPS spectra, shown in Figure 4-27 and Figure 4-28 respectively, do not change shape or position on annealing, although they do decrease in size as the temperature increases. There is no noticeable change in any of the XPS on annealing to 923 K.

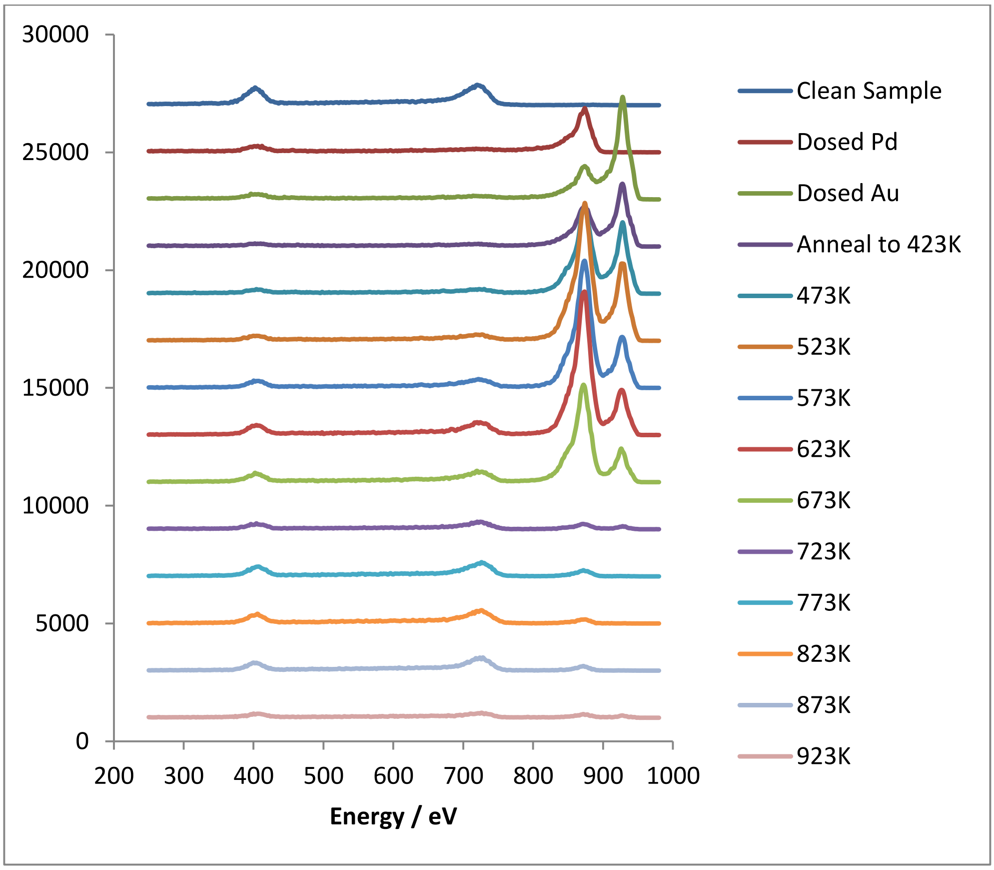

Figure 4-24 – ISS raw data taken after depositing 150s of Pd and 80s of Au and annealing

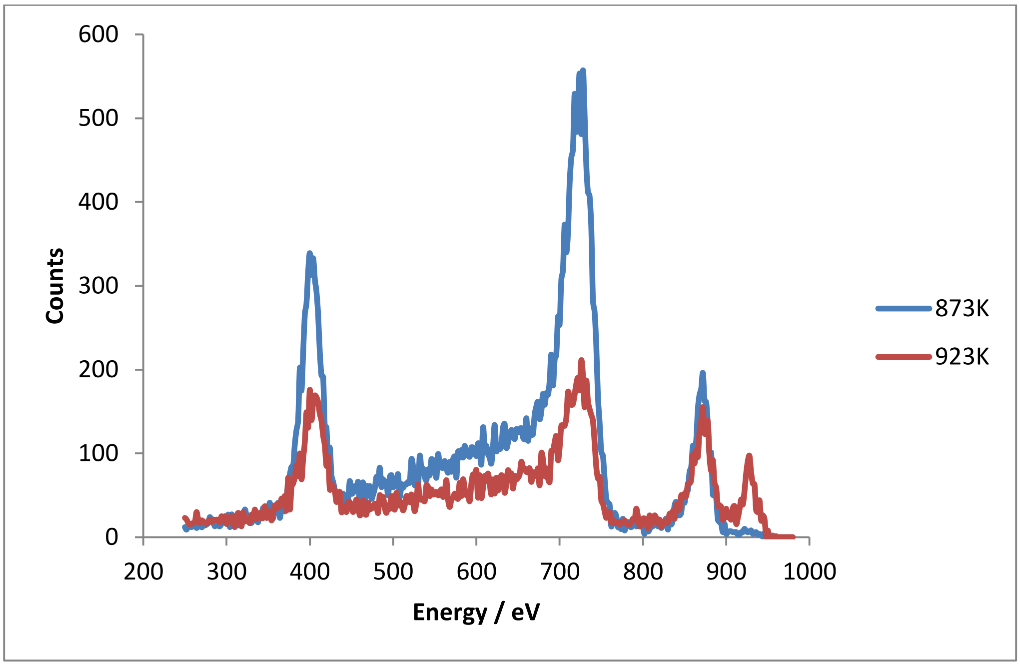

Figure 4-25 - A closer look at the differences in the ISS when heating to 873 and 923 K

Table 4-4 - ISS height ratios of Figure 4-24

	Au/Pd	Au/Ti	Pd/Ti
Clean	0.00	0.00	0.00
Dose Pd	0.00	0.00	14.00
Dose Au	3.07	32.25	10.50
Anneal 423 K	1.50	30.00	20.00
473 K	0.82	17.25	21.00
523 K	0.57	12.67	22.33
573 K	0.40	5.40	13.50
623 K	0.32	3.43	10.71
673 K	0.35	3.00	8.67
723 K	0.57	0.40	0.70
773 K	0.00	0.00	0.44
823 K	0.00	0.00	0.29
873 K	0.00	0.00	0.36
923 K	0.67	0.50	0.75

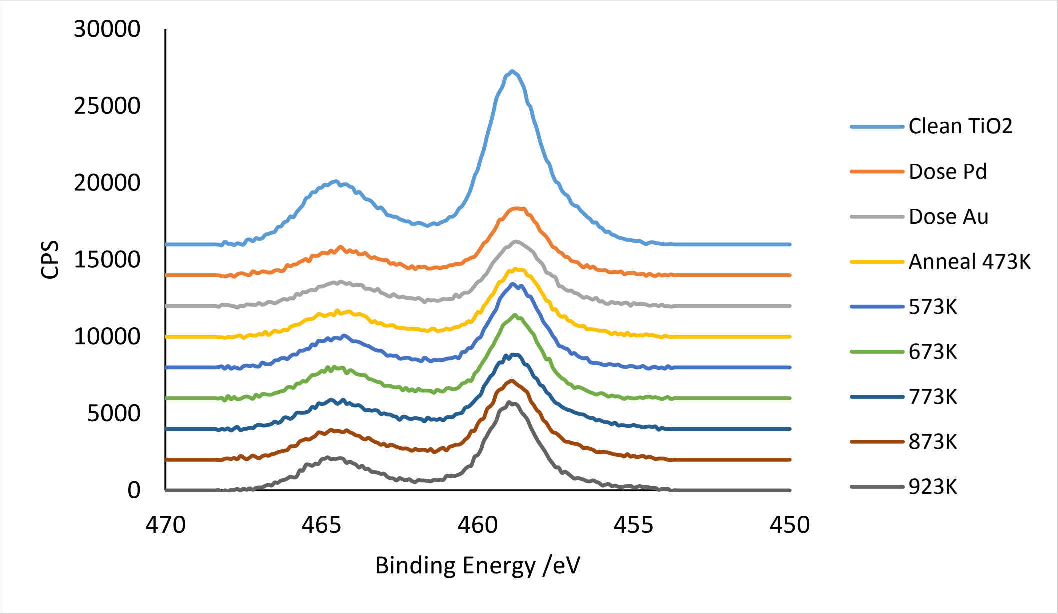

Figure 4-26 - Ti2p XPS after depositing 150s of Pd and 80s of Au and annealing

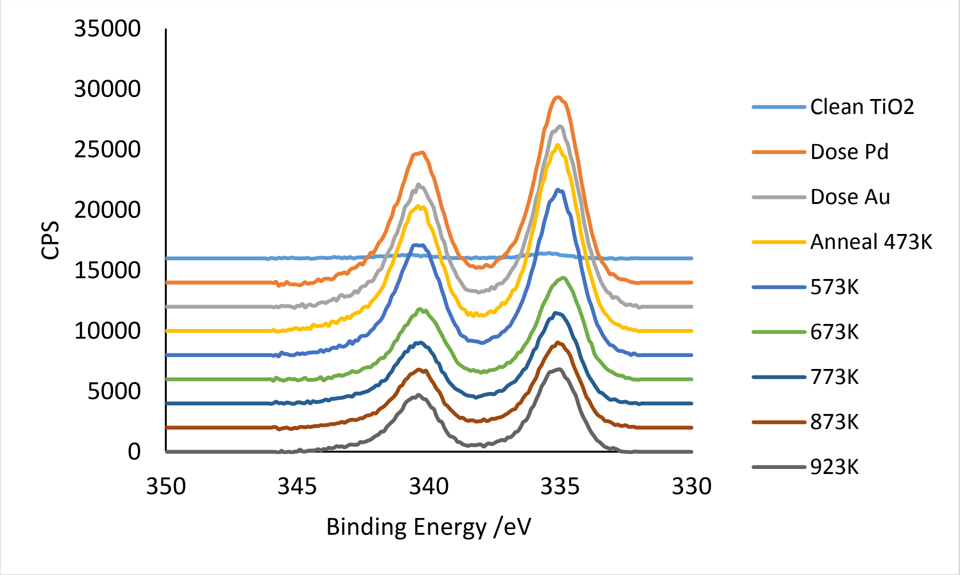

Figure 4-27 - Pd3d XPS after depositing 150s of Pd and 80s of Au and annealing

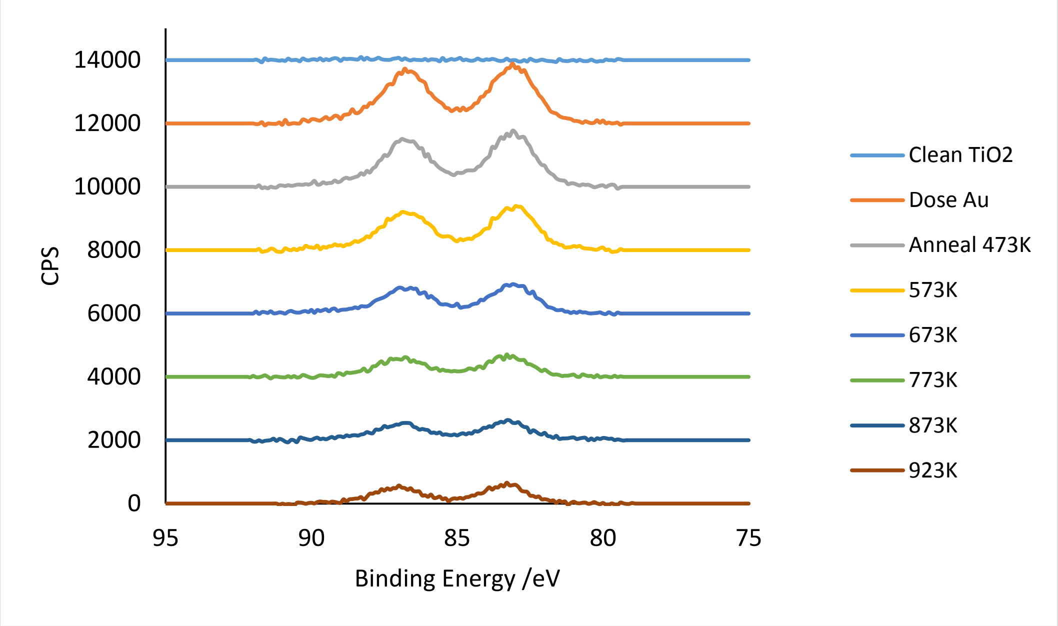

Figure 4-28 - Au4f XPS after depositing 150s of Pd and 80s of Au and annealing

Table 4-5 - XPS area ratios from Figure 4-26 -Figure 4-287

	Au/Pd	Au/Ti	Pd/Ti
Clean TiO2	N/A	N/A	N/A
Dose Pd	N/A	N/A	3.76
Dose Au	0.132	0.512	3.88
423	0.127	0.479	3.78
473	0.117	0.447	3.81
523	0.107	0.374	3.50
573	0.108	0.314	2.91
623	0.111	0.223	2.02
673	0.120	0.218	1.82
723	0.099	0.170	1.72
773	0.094	0.149	1.58
823	0.094	0.145	1.54
873	0.097	0.135	1.40
923	0.092	0.118	1.29

A second experiment was then carried out, with 180s of Pd and 180s of Au deposited onto a sputtered TiO_2 surface and then annealed to 873 K. The resulting ISS results are shown in Figure 4-29. On depositing Au onto the Pd/TiO_2(110), the Au signal can be seen to dwarf the Pd signal – the Au:Pd height ratio is ~8.5:1 (see Table 4-6). On annealing, the Au signal decreases and the Pd signal increases, just as with smaller amounts of Au on Pd/TiO_2. However, the Au signal does not disappear from the ISS, even on annealing to 873 K. It seems as though the amounts of Pd and Au present affect whether or not an Au-core-Pd-shell structure will be formed. It is possible that the Au film was too thick for the Pd to completely segregate to the surface and encapsulate the Au in this instance. This is despite the presence of a carbon signal in the C1s XPS region. However, some segregation has occurred, as evidenced by the increasing Pd signal and decreasing Au signal. The XPS raw data are shown in Figure 4-30 to Figure 4-32. The Au4f:Pd3d ratio in the XPS deceases very slightly during heating (Table 4-7), and can be seen to behave similarly to when a much smaller amount of Au was deposited. However, the Au:Pd ratio does appear to decrease by a greater amount when the starting amount of Au is smaller. When looking at Table 4-5 and Table 4-7, the Au:Pd area ratio drops by ~0.3 in Table 4-5 compared to only ~0.06 in Table 4-7. Bugyi et al[43] observed a similar phenomenon when investigating encapsulation of Rh on TiO_2(110). They found that SMSI (i.e. encapsulation of Rh by TiO_x) took place at a temperature at least 100 K higher when annealing a 50 monolayer thick Rh multilayer than when annealing a 1 monolayer Rh thin film. Taking this into account, it is possible that the Au would have been encapsulated by the Pd if it had been subjected to a longer anneal time or higher annealing temperature.

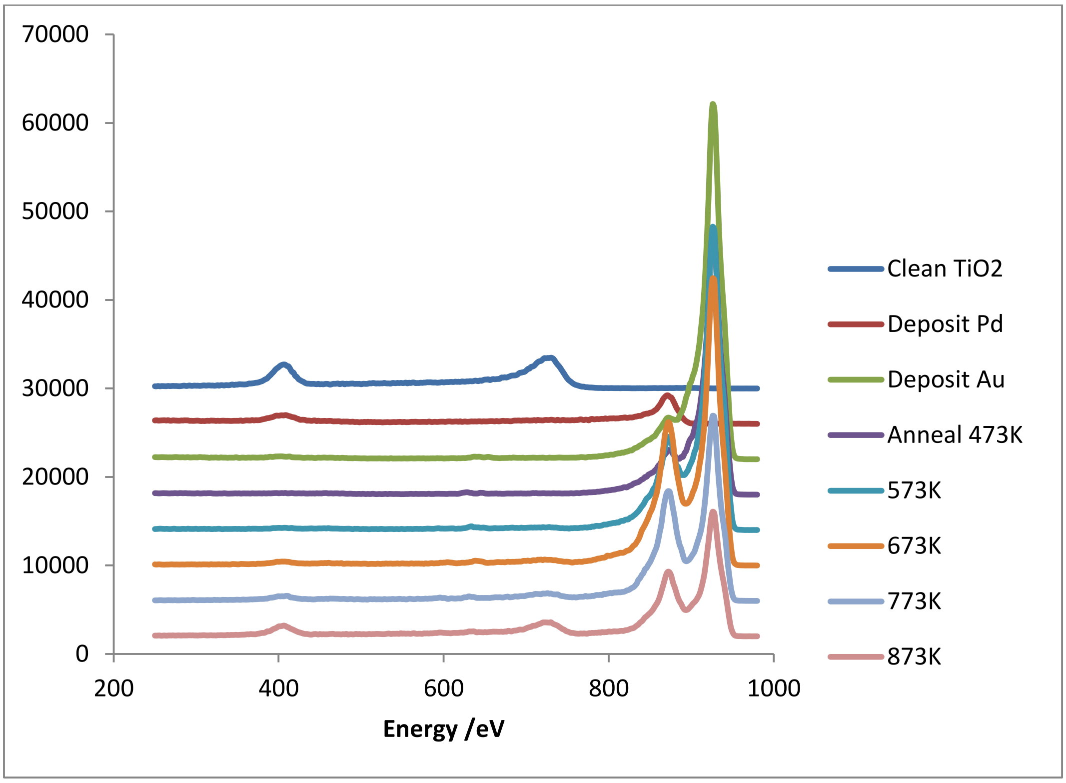

Figure 4-29 - ISS raw data taken after depositing 180s of Pd and 180sof Au and annealing

Table 4-6 – ISS height ratios taken from Figure 4-29

	Au/Pd	**Au/Ti**	**Pd/Ti**
Clean	0	0	0
Dose Pd	0	0	8.67
Dose Au	8.46	N/A	N/A
473	5.9	N/A	N/A
573	3.25	117	36
673	2	56	28
773	1.69	23	13.6
873	2.09	9.75	4.67

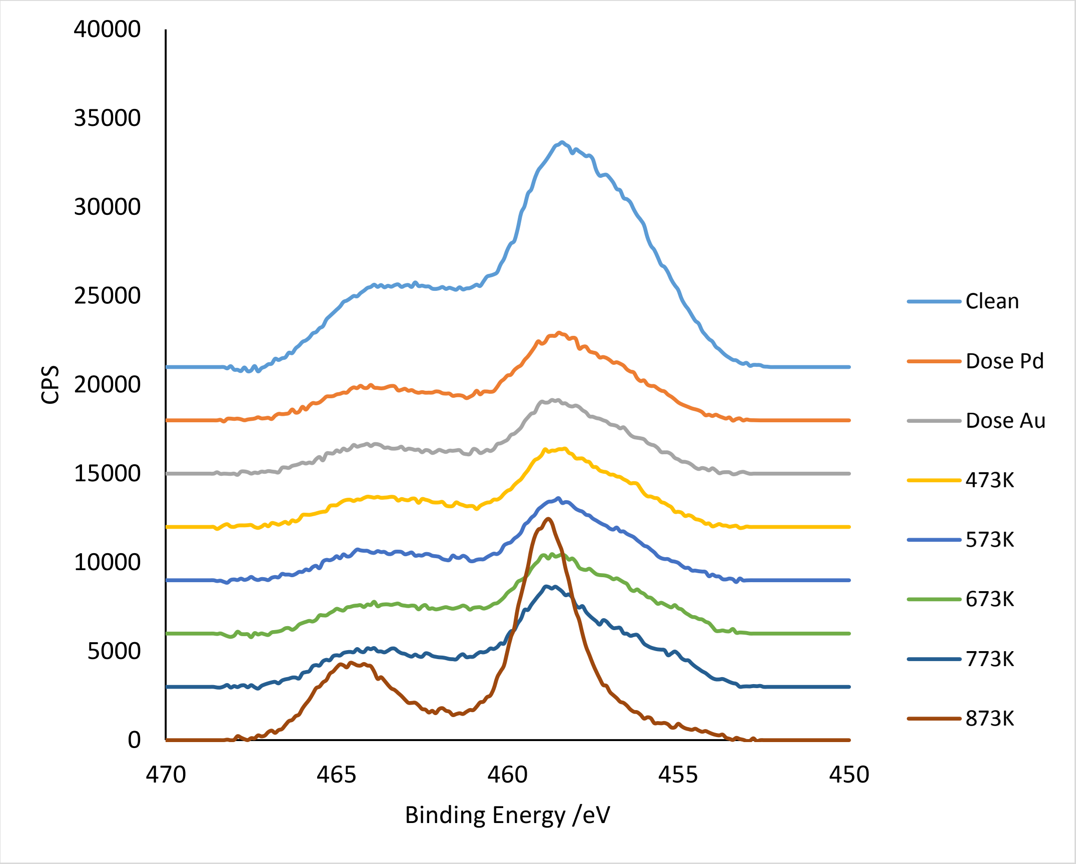

Figure 4-30 – Ti2p XPS taken after depositing 180s of Pd and 180sof Au and annealing

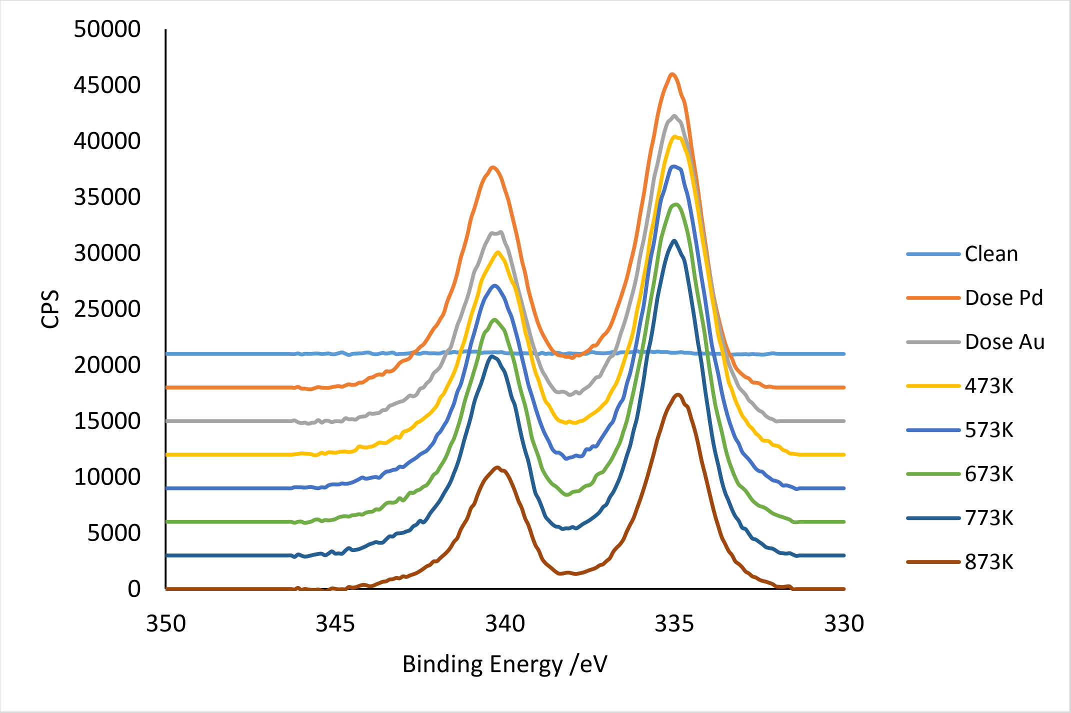

Figure 4-31 - Pd3d XPS taken after depositing 180s of Pd and 180sof Au and annealing

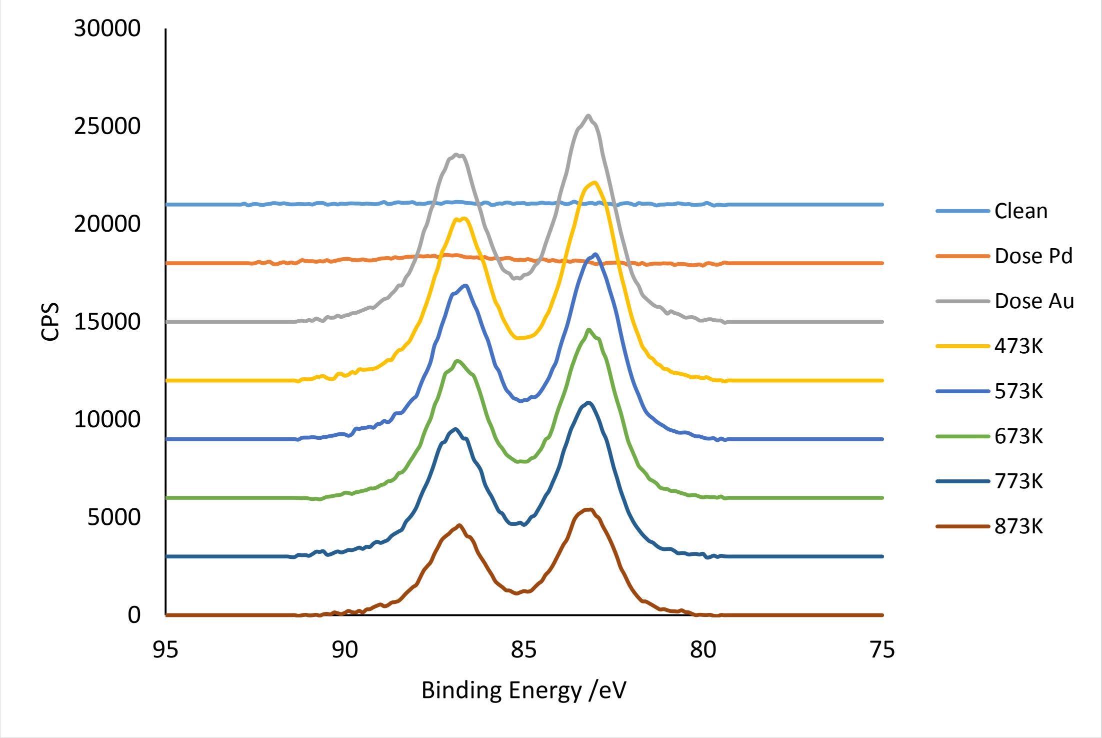

Figure 4-32 - Au4f XPS taken after depositing 180s of Pd and 180s of Au and annealing

Table 4-7 - XPS ratios taken from Figure 4-30 - Figure 4-32

	Au/Pd	Au/Ti	Pd/Ti
Clean	0	0	0
Dose Pd	0	0	4.07
Dose Au	0.37	1.75	4.69
473	0.34	1.61	4.80
573	0.31	1.49	4.78
673	0.29	1.26	4.39
773	0.28	0.95	3.40
873	0.31	0.44	1.43

A further observation is that the amount of SMSI observed on annealing to 773-873 K appears to be related to the amount of gold deposited on the surface before annealing, as shown in Table 4-8. The more Au that is deposited on the $TiO_2(110)$ surface before annealing and the greater the Au:Pd XPS area ratio on annealing, the less Ti^{2+} is observed on annealing to 823 K. This is also highlighted in Figure 4-33, showing the Ti2p XPS of each of the four surfaces after annealing to 823 K. The first Ti2p spectrum, corresponding to the lowest Au:Pd ratio in Table 4-8, clearly has a much larger amount of Ti^{2+} than the other Ti2p spectra, each corresponding to a lower Au:Pd ratio. Grazing angle XPS experiments carried out by Chen et al[42] showed that Au-Pt clusters annealed to 600 K are covered by reduced titania. The extent of this encapsulation from SMSI effects was thought to be controlled by the Pt composition – reduced TiOx covered the Pt regions at the surface of the bimetallic structure, but the presence of Au was thought to inhibit migration of TiOx onto the surface of the cluster. It's possible that this also applies to Pd-Au on $TiO_2(110)$. Likewise, Ovari and co-workers have found that Rh clusters on $TiO_2(110)$ are encapsulated at 750 K by the oxide. However, encapsulation is negligible up to 900 K when the Rh-Au bimetallic particles are almost completely covered by Au[29]. They investigated this further, depositing a thin layer of Au (~1 nm) on to a thick (~10 nm) layer of Rh on $TiO_2(110)$, and found that the Au layer kinetically hindered the diffusion of O up to 850 K and that the characteristic "pinwheel" $TiO_{1.2}$ layer that forms on monometallic Rh films did not form on the Au-Rh bimetallic film up to 950 K[44]. It seems to be the case with Pd as well, that the presence of Au reduces the extent of the SMSI effect and hinders encapsulation of the metal by the reduced oxide. However, further experiments would need to be carried out in order to take into account several different variables, including the starting amount of Pd and Au and the starting condition of the $TiO_2(110)$ single crystal (i.e. have a consistent starting amount of Ti^{4+}, $^{3+}$ and $^{2+}$ before depositing any metal). This is beyond the scope of this thesis, and is instead just an observation for future work in this area.

Table 4-8 - How the amount of Au present affects SMSI

	Corresponding XPS	Au XPS area on deposition	Au XPS area at 823 K	Au:Pd XPS area ratio at 823 K	Ti^{2+} present in the Ti2p XPS spectra at 823 K
1	Figures 4-15 - 17	13758	8821	0.045	23.81
2	Figures 19, 21-22	2679	1846	0.051	13.62
3	Figures 4-25 - 27	7529	7529	0.094	6.56
4	Figures 4-29 - 31	39604	29721	0.311	5.22

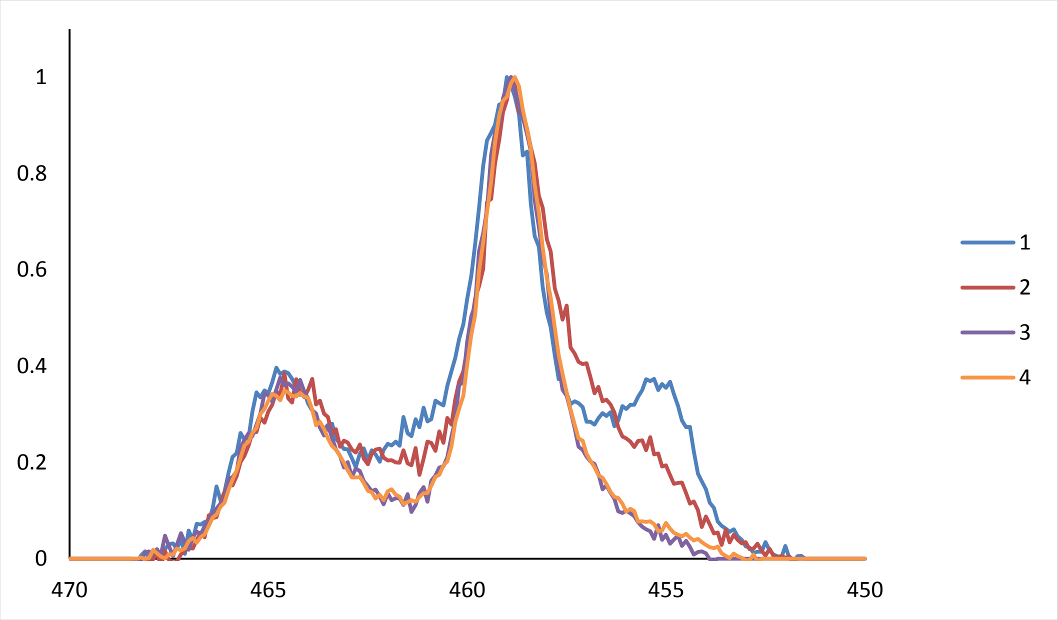

Figure 4-33 – the Ti2p XPS spectra referred to in Table 4-8, showing the differing amounts of Ti^{2+} present on annealing each of the 4 surfaces to 823 K

The effect of annealing Pd and Au on TiO_2(110) was also investigated using Auger electron spectroscopy in UHV2. The TiO_2(110) single crystal was subject to several sputter-anneal cycles, as described in the experimental above, until the Auger revealed no impurities. 240s of Pd was deposited on to the TiO_2(110), followed by 60s of Au. This was then annealed incrementally to 873 K, as described above. The resulting Auger are shown in Figure 4-34. The peak assignments are as follows: gold is observed at 73 eV, titanium at 384 and 421 eV, oxygen at 513 eV and palladium at 330, 280 and 250 eV. The Auger spectra follows a similar pattern to that seen in the XPS and ISS above. The Au signal initially dwarfs the Pd signal on deposition. On annealing, the Au signal rapidly decreases. The Pd signal also decreases, but by a much smaller amount. The Ti signal remerges at 673 K and continues to grow at higher temperatures, until it is larger than the Pd and Au signal at 873 K. The change in Pd and Au signal is further illustrated in Figure 4-35, which shows how the Pd:Au signal height ratio changes with increasing temperature. The Auger peak height ratios exhibit similar behaviour to that shown by the XPS – there is a slight increase in the Pd:Au ratio at low temperatures, up to 673 K. Then, at higher temperatures, the Pd:Au ratio rapidly increases, indicating that the Pd is encapsulating the Au. The emergence of the Ti signal at 673 K in Figure 4-34 corresponds to when these thin films coalesce and form nanoparticles. It is difficult to determine from the Auger whether or not any SMSI has occurred on annealing to 873 K. Figure 4-36 shows a detailed look at the Ti region of the Auger spectra (i) before depositing Pd, and (ii) after depositing Pd and annealing to 873 K. If there was a significant amount of Ti^{2+} present, one might expect a broadened Ti peak. However there is no noticeable broadening, making this inconclusive.

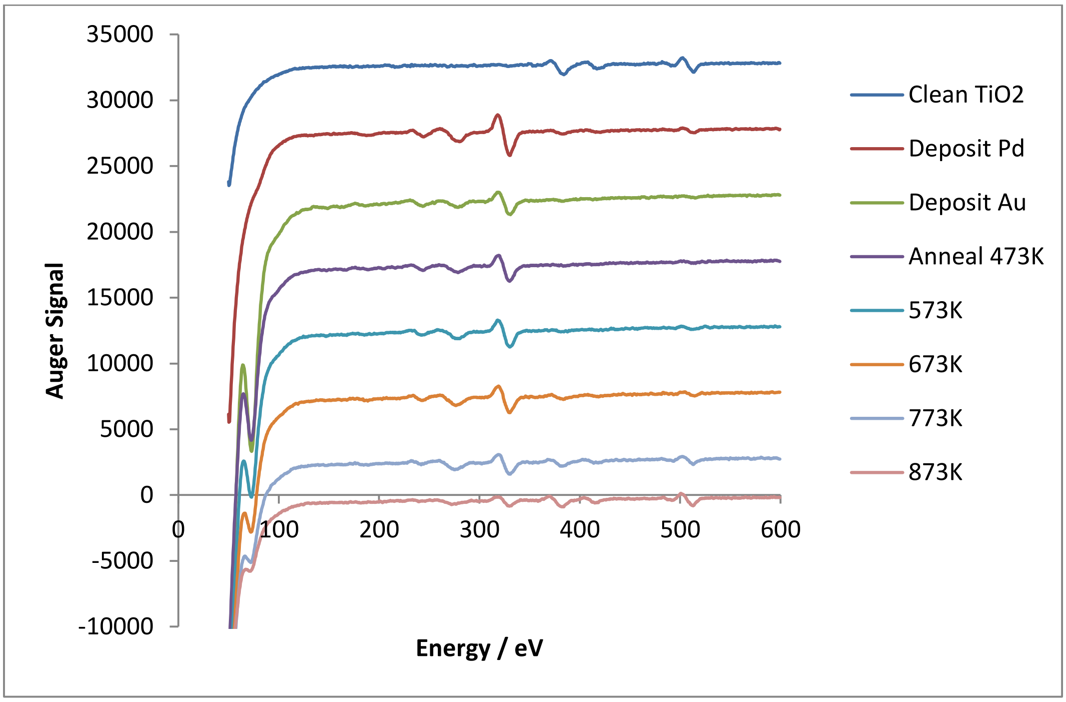

Figure 4-34 - Auger electron spectra showing the effect of depositing Pd and then Au onto $TiO_2(110)$ and then annealing to 873 K

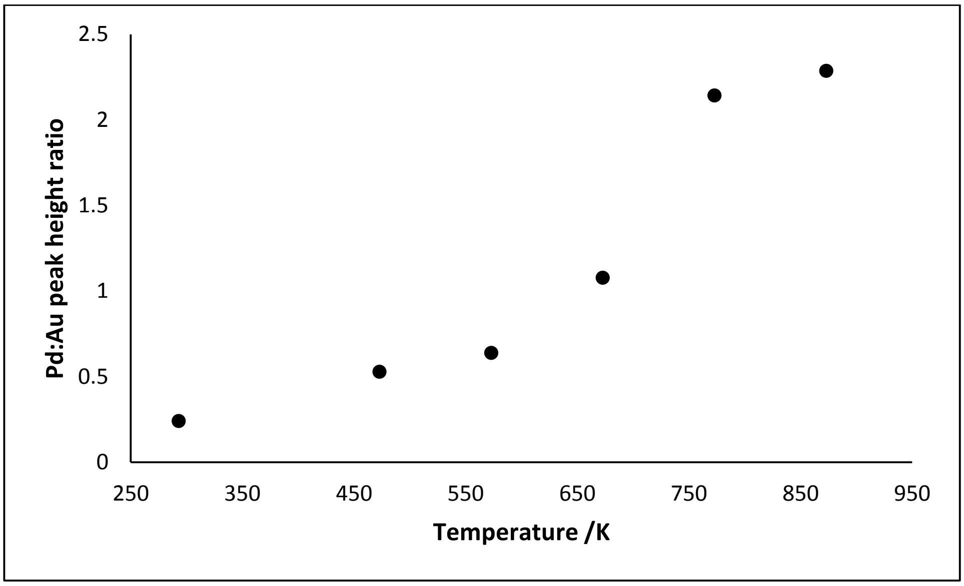

Figure 4-35 - Pd:Au Auger peak height ratios taken from Figure 4-34.

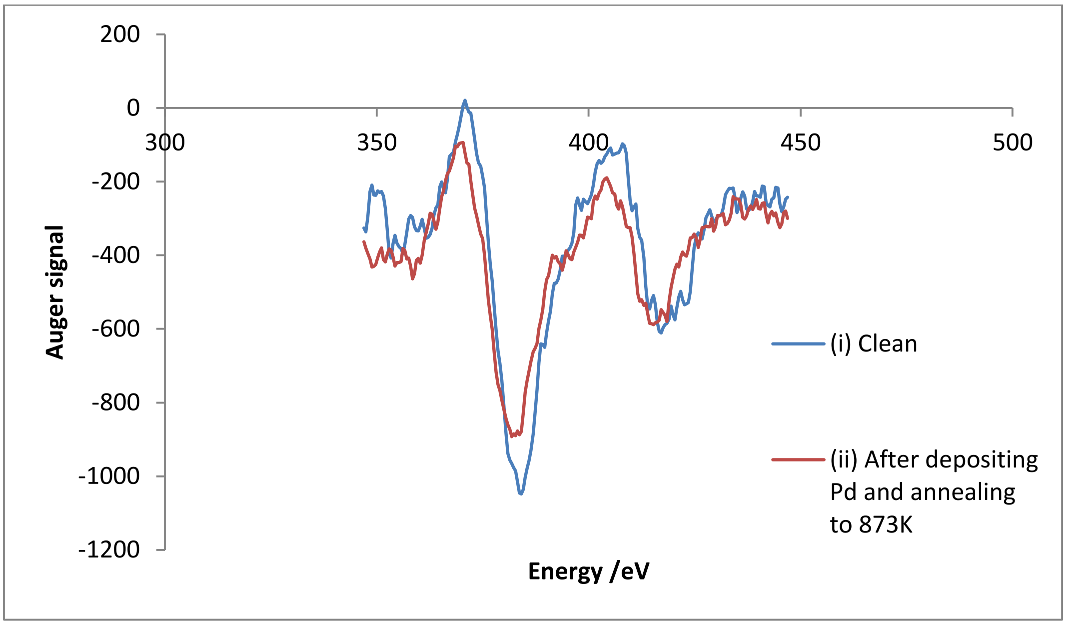

Figure 4-36 - Auger spectra of the Ti region (i) before depositing

The Auger experiment was then repeated, but rather than deposit Pd first, Au was deposited first, followed by Pd. The resulting Auger spectra are shown in Figure 4-37. Surprisingly, the results appear to be the opposite of that shown in Figure 4-34 – the Pd signal initially dwarfs the Au signal on deposition, as is expected. However, on annealing, the Pd signal decreases and the Au signal increases. This is further demonstrated in Figure 4-38, which shows the Au:Pd Auger signal height ratio increasing on annealing to 873 K. It is possible that this Auger spectra indicates that Pd and Au do not form entirely distinct Au-core Pd-shell nanoparticles on annealing to 873 K. Instead, the structure may be a Pd-shell Pd/Au-alloy-core. This would explain why the Au signal increases on annealing when it is already covered by a Pd film, and still corresponds with the ISS data shown above, where the Au signal is completely gone on annealing to 873 K.

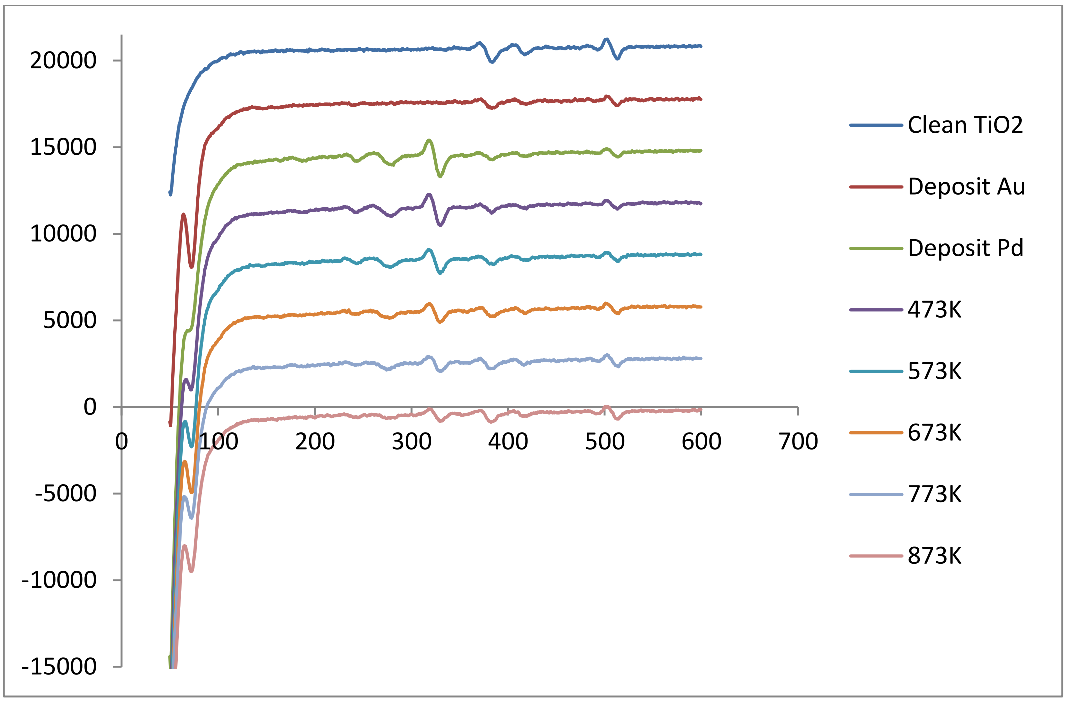

Figure 4-37 - Auger electron spectra showing the effect of depositing Au and then Pd onto $TiO_2(110)$ and then annealing to 873 K

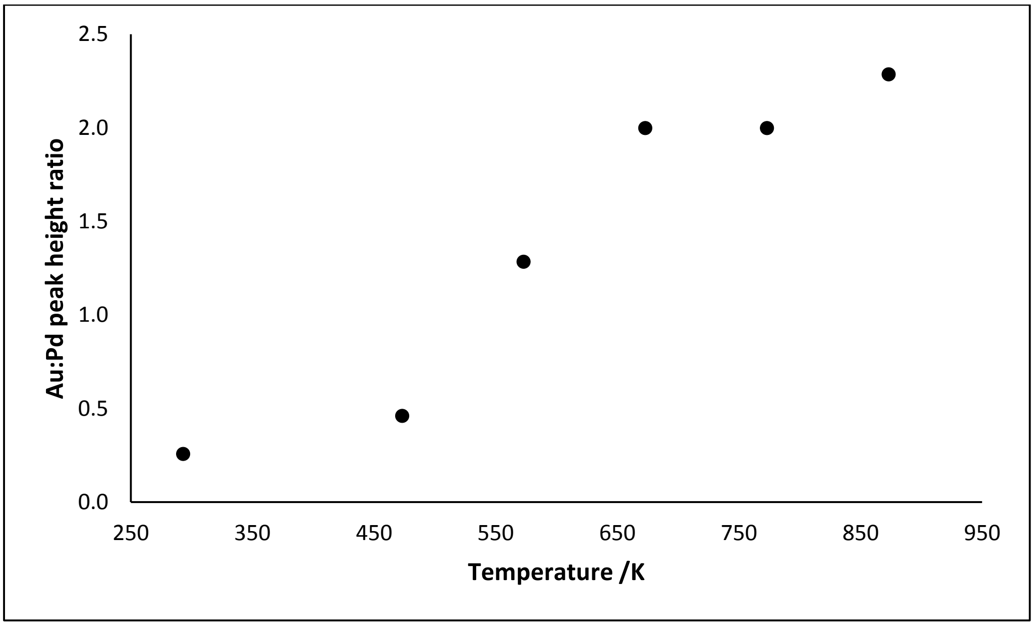

Figure 4-38 - Au:Pd Auger peak height ratios taken from Figure 4-37

4.4 Conclusions

In this chapter, the effect of annealing Au on TiO_2(110) has been studied. The formation of Au-Pd bimetallic structures on TiO_2(110) was then investigated.

It was found that Au doesn't undergo SMSI, as was evidenced by a lack of a shoulder in the Ti2p XPS at 455 eV on annealing to temperatures above 773 K. Au does, however, de-wet from the surface on annealing, as seen by the increasing Ti and O signals in the ISS and XPS on annealing, and the corresponding decrease in the Au signals.

Pd and Au form Au-core-Pd-shell structures on TiO_2(110) on annealing to 773 K. ISS showed that Au disappeared from the spectra on annealing to 773 K, whereas it was still visible in the XPS. In some instances, these core-shell structures undergo SMSI on annealing to 873 K, and are encapsulated by TiOx, where the Ti is likely in the Ti^{2+} state, as evidenced by the Ti2p XPS. Auger data indicates that the core may be a Pd-Au alloy, encapsulated by a Pd shell. The presence of O in the ISS even after enough Pd and Au has been deposited to cover the Ti ISS signal suggested that CO was adsorbed onto Pd, which would lower the surface free energy enough for the formation of the Au-Pd core-shell structure to be favourable, when it otherwise shouldn't be.

There appeared to be a correlation between the amount of Au in the Au-Pd core-shell structure and whether or not any SMSI was seen. However, this was not investigated thoroughly enough for any conclusive statements about this to be made, and further work would be required.

When a much thicker layer of Au was deposited on top of the Pd layer, the encapsulation of Au by Pd was no longer observed. It is likely that the Pd was unable to diffuse through the thicker layer – perhaps the drive for the Pd to adsorb with the CO could not in this instance overcome the thick Au overlayer over the Pd.

4.5 References

1. T. Kobayashi, M. Haruta, H. Sano and M. Nakane, *Sensors and Actuators*, 1988, **13**, 339.
2. S. D. Lin, M. Bollinger and M. A. Vannice, *Catalysis Letters*, 1993, **17**, 245.
3. S. Lin and M. A. Vannice, *Catalysis Letters*, 1991, **10**, 47.
4. H. Sakurai, A. Ueda, T. Kobayashi and M. Haruta, *Chemical Communications*, 1997, 271.
5. J. L. Gong, *Chemical Reviews*, 2012, **112**, 2987.
6. L. Zhang, R. Persaud and T. E. Madey, *Physical Review B*, 1997, **56**, 10549.
7. F. Cosandey and T. E. Madey, *Surface Review and Letters*, 2001, **8**, 73.
8. M. Valden, X. Lai and D. W. Goodman, *Science*, 1998, **281**, 1647.
9. E. Wahlstrom, N. Lopez, R. Schaub, P. Thostrup, A. Ronnau, C. Africh, E. Laegsgaard, J. K. Norskov and F. Besenbacher, *Physical Review Letters*, 2003, **90**.
10. A. K. Santra, A. Kolmakov, F. Yang and D. W. Goodman, *Japanese Journal of Applied Physics Part 1-Regular Papers Brief Communications & Review Papers*, 2003, **42**, 4795.
11. M. S. Chen and D. W. Goodman, *Accounts of Chemical Research*, 2006, **39**, 739.
12. S. C. Parker, A. W. Grant, V. A. Bondzie and C. T. Campbell, *Surface Science*, 1999, **441**, 10.
13. M. Eyrich, S. Kielbassa, T. Diemant, J. Biskupek, U. Kaiser, U. Wiedwald, P. Ziemann and J. Bansmann, *Chemphyschem*, 2010, **11**, 1430.
14. J. A. Rodriguez, G. Liu, T. Jirsak, J. Hrbek, Z. P. Chang, J. Dvorak and A. Maiti, *Journal of the American Chemical Society*, 2002, **124**, 5242.
15. L. Zhang, F. Cosandey, R. Persaud and T. E. Madey, *Surface Science*, 1999, **439**, 73.
16. A. Kolmakov and D. W. Goodman, *Chemical Record*, 2002, **2**, 446.
17. X. Lai, T. P. St Clair, M. Valden and D. W. Goodman, *Progress in Surface Science*, 1998, **59**, 25.
18. J. R. Kitchin, M. A. Barteau and J. G. G. Chen, *Surface Science*, 2003, **526**, 323.
19. C. E. J. Mitchell, A. Howard, M. Carney and R. G. Egdell, *Surface Science*, 2001, **490**, 196.

20. P. J. Schmilz, H. C. Kang, W. Y. Leung and P. A. Thiel, *Surface Science*, 1991, **248**, 287.
21. Y. Kuk, L. C. Feldman and P. J. Silverman, *Physical Review Letters*, 1983, **50**, 511.
22. M. Kralj, A. Bailly, M. C. Saint-Lager, S. Degen, A. Krupski, C. Becker, P. Dolle, M. De Santis and K. Wandelt, *Surface Science*, 2006, **600**, 2614.
23. V. Ponec, *Applied Catalysis a-General*, 2001, **222**, 31.
24. R. J. Davies, M. Bowker, P. R. Davies and D. J. Morgan, *Nanoscale*, 2013, **5**, 9018.
25. C. T. Campbell, *Surface Science Reports*, 1997, **27**, 1.
26. A. Steltenpohl, N. Memmel, E. Taglauer, T. Fauster and J. Onsgaard, *Surface Science*, 1997, **382**, 300.
27. S. Nemsak, T. Skala, J. Libra, P. Hanys, K. Masek, M. Yoshitake and V. Matolin, *Applied Surface Science*, 2007, **254**, 490.
28. U. Diebold, J. M. Pan and T. E. Madey, *Surface Science*, 1995, **331**, 845.
29. L. Ovari, L. Bugyi, Z. Majzik, A. Berko and J. Kiss, *Journal of Physical Chemistry C*, 2008, **112**, 18011.
30. B. Zhu, G. Thrimurthulu, L. Delannoy, C. Louis, C. Mottet, J. Creuze, B. Legrand and H. Guesmi, *Journal of Catalysis*, 2013, **308**, 272.
31. H. B. Liu, U. Pal, R. Perez and J. A. Ascencio, *Journal of Physical Chemistry B*, 2006, **110**, 5191.
32. I. V. Yudanov and K. M. Neyman, *Physical Chemistry Chemical Physics*, 2010, **12**, 5094.
33. O. A. Oviedo, L. Reinaudi, M. M. Mariscal and E. P. M. Leiva, *Electrochimica Acta*, 2012, **76**, 424.
34. M. S. Chen, K. Luo, T. Wei, Z. Yan, D. Kumar, C. W. Yi and D. W. Goodman, *Catalysis Today*, 2006, **117**, 37.
35. A. F. Lee, C. J. Baddeley, C. Hardacre, R. M. Ormerod, R. M. Lambert, G. Schmid and H. West, *Journal of Physical Chemistry*, 1995, **99**, 6096.
36. Y. Kobayashi, S. Kiao, M. Seto, H. Takatani, M. Nakanishi and R. Oshima, *Hyperfine Interactions*, 2004, **156**, 75.
37. Y. W. Lee, M. Kim, Z. H. Kim and S. W. Han, *Journal of the American Chemical Society*, 2009, **131**, 17036.
38. J. K. Edwards, B. E. Solsona, P. Landon, A. F. Carley, A. Herzing, C. J. Kiely and G. J. Hutchings, *Journal of Catalysis*, 2005, **236**, 69.

39. D. Briggs and M. Seah, *Practical Surface Analysis by Auger and X-ray Photoelectron Spectroscopy*, John Wiley & Sons, Chichester, 1983.
40. I. Z. Jones, R. A. Bennett and M. Bowker, *Surface Science*, 1998, **402**, 595.
41. M. Bowker, P. Stone, R. Bennett and N. Perkins, *Surface Science*, 2002, **497**, 155.
42. J. B. Park, S. F. Conner and D. A. Chen, *Journal of Physical Chemistry C*, 2008, **112**, 5490.
43. L. Bugyi, L. Ovari and Z. Konya, *Applied Surface Science*, 2013, **280**, 60.
44. L. Ovari, A. Berko, R. Gubo, A. Racz and Z. Konya, *Journal of Physical Chemistry C*, 2014, **118**, 12340.

Chapter 5 – Reactivity of TiO_2(110) and deposited metal nanoparticles

Chapter 5 Contents

5.1 Introduction

In this chapter the reactivity of both clean and precious-metal doped TiO_2(110) is examined using TPD.

The reactivity of the clean TiO_2(110) single crystal is initially investigated. This is then dosed separately with palladium and gold and changes in reactivity are noted. Finally, both Au and Pd are deposited on to the TiO_2(110) substrate and annealed to form the Au-core Pd-shell structures described in chapter 4. The reactivity of these structures are compared to the reactivity of the individual component metals. The aim of these experiments is to help increase understanding of the reactivity of industrially important bimetallic catalysts.

5.1.1 TiO_2 reactivity

Ethanol

Alcohol reactivity with TiO_2 has been frequently used to study photocatalytic oxidation of organic molecules, revealing the catalytically active sites on the metal oxide surfaces[1, 2]. An XPS and TPD study on the adsorption and reaction of ethanol and several other aliphatic alcohols on TiO_2(001)[3] with TPD and XPS observed that ethanol adsorbs at 200 K in a mixed layer of molecular C_2H_5OH and dissociated C_2H_5O. On annealing, this was seen to desorb as either ethanol, acetaldehyde or ethylene. Another XPS and TPD study by Gamble et al looked at the adsorption of ethanol on stoichiometric TiO_2(110) at 125 K and reported that half of the ethanol molecules adsorbed dissociatively on to the Ti^{4+} sites[4]. They observed broad peaks, and proposed that the adsorbed ethoxy species was combining with surface H atoms. An STM study at 78 K showed that the ethanol molecules adsorb above Ti^{4+} sites in rows in the [001] direction[5]. At room temperature ethanol desorbed from the surface, reducing the multilayer to a monolayer. Madix et al confirmed that the ethoxy groups recombined with H adatoms and desorbed as ethanol gas[6]. DFT calculations showed that dissociative adsorption on Ti^{4+} is slightly more favourable than molecular dissociation[7]. This difference was predicted to be even greater on oxygen-deficient $TiO_2(110)$. Besenbacher et al revealed that molecular oxygen is only weakly bonded to the Ti atoms via a lone oxygen pair, whereas the ethoxy groups are bonded via a much stronger covalent bond[8].

Formic acid

Formic acid adsorption and reactivity on $TiO_2(110)$ has been widely studied[1, 9]. It has been well established that it adsorbs dissociatively at room temperature on $TiO_2(110)$ as formate and hydrogen, due to cleavage of the acidic hydrogen[10, 11]. Onishi showed that two different decomposition pathways can occur at elevated temperature[10, 12]. These are dehydrogenation to CO_2 and H_2, or dehydration to CO and H_2O. A TPD study by Henderson identified the major products as CO and H_2O, but also identified a range of minor side-products, including formaldehyde, carbon dioxide and ethene[11]. FTIR studies showed that formic acid may adsorb on the (1x1) surface to produce two types of adsorbed formate; one bridging the 5-fold co-ordinated Ti^{4+} ions, and another orthogonal species in which one formate oxygen is inserted in at a vacancy in the bridging oxygen rows[13]. Bowker et al carried out a molecular beam study of the reaction of formic acid with $TiO_2(110)$-(1 x 1), observing only the dehydration reaction above 500 K, with no evidence for a dehydrogenation pathway[14]. STM studies by the same group showed that formic acid readily adsorbs on to the cross-linked (1 x 2) reconstructed surface, preferentially on the cross-links[15]. Temperature programmed STM was used to show the growth of extended islands at the expense of individual formate islands, formed by the reaction of oxygen from the decomposition of formate and Ti^{n+} interstitials from the crystal[15]. Formic acid was shown to have negligible activity on the (1 x 2) Ti_2O_3 surface due to a lack of Ti^{4+} ions. Recent DFT calculations further confirmed that the formic acid molecule quickly dissociates on the reduced surface to a formate ion and proton[16]. Thornton and Chang used HREELS to compare the reaction of formic acid with TiO_2 thin films and rutile TiO_2 and found that they exhibited very similar behaviour, with complete dissociation to formate at about 260 K[17].

Acetic acid

The adsorption of acetic acid has generally been found to follow the same trends as that found for formic acid[1]. However, there has been much less work carried out with this molecule. At room temperature, acetic acid adsorbs as acetate, H_3COO^-, in a (2x1) structure, with the two oxygen molecules bonded in a bridging configuration across the fivefold coordinated Ti atoms[18]. Kim and Barteau studied the decomposition of acetic acid on the TiO_2(001) surface with XPS and TPD and reported that the adsorbed acetate decomposed through dehydration to ketene[19]. Onishi observed the decomposition of acetic acid with STM. After a temperature jump to 580 K, the number of bright spots on the STM decreased exponentially with time. This was attributed to the unimolecular decomposition of acetate to ketene[20].

5.1.2 Pd/TiO_2 reactivity

Formic acid

Molecular beam studies were carried out on TiO_2(110) and Pd-loaded TiO_2(110) by Bowker et al. As described above, on the oxide surface only the dehydration reaction was seen:

$$HCOOH \rightarrow CO + H_2O$$

However, when the surface was loaded with Pd nanoparticles, the dehydrogenation reaction was also observed, beginning at ~350 K[14]. The formation of CO_2 and H_2 has been associated with the presence of a stable formate intermediate on the surface[21]. Pd particles were found to be less reactive than a single crystal, which is surprising considering that the surface energy should be higher, encouraging greater reactivity[14]. They proposed that this was due to the alloying of the Pd nanoparticles with Ti from the support. This alloying was seen with STM by Bowker et al[22] and similar structures were seen by Diebold for Pt nanoparticles on TiO_2[23]. The same group also studied the adsorption and decomposition of formic acid on clean and oxygen dosed Pd(110) using TPD and XPS[21]. The formic acid decomposed to give CO, CO_2, H_2 and H_2O during TPD. CO and H_2 were evolved in desorption limited peaks at 470 and 320 K respectively. Thornton et al used HREELS to investigate the effect of Pd on the interaction of formic acid with $TiO_2(110)$[24]. At low Pd coverage, with visible bare substrate, formate vibrational modes characteristic of that seen on clean TiO_2 were observed, consistent with a bidentate bonding configuration. As well as that, three other v(CO) modes were detected at 1900, 1915 and 1734cm^{-1}. The peak at 1900 cm^{-1} was attributed to CO bound to the Pd, whilst the other two modes were assigned to either CO or HCO bound to Pd cluster perimeter sites.

Ethanol

There have been several studies on the surface chemistry of ethanol on Pd(111)[25-28] and Pd(110)[29, 30]. Using TPD[26] and HREELS[27], Davis and Barteau proposed that ethanol decomposed on clean Pd(111) by O-H scission to form the ethoxide (CH_3CH_2O) followed by the sequential dehydrogenation to acetaldehyde and acetyl, until it is decarbonylated to form CO and CH_4 at ~410 K. They also carried out the reaction of ethanol on Pd(111) containing ¼ ML of adsorbed O atoms. The presence of O led to the oxidation of ethanol to the acetaldehyde at 220 K and the formation of surface acetate, which reacted via either decomposition at 410 K or hydrogenation to acetic acid at 280 K[25]. However, a DFT study of ethanol's adsorption and decomposition on Pd(111) by Li et al[31] calculated that a C^{α}-H bond was the first to break in this process. Pang et al carried out an investigation using TPD and HREELS using deuterated ethanol in to which occurred first – O-H or C-H bond scission[28]. They ultimately concluded, based on the sequence of desorption of D_2O and H_2O during TPD and the thermal evolution of the vibrational spectra, that the decomposition of adsorbed ethanol proceeded via the initial breaking of the O-H bond to form the ethoxide.

TPD studies of ethanol on Pd(110) concluded that alcohols appear to react on this clean surface via the same dehydrogenation and decarbonylation steps observed on the Pd(111) surface – ethanol was found to give H_2, CO and CH_4[29]. Bowker et al carried out molecular beam studies of ethanol on Pd(110), finding that the major pathway for ethanol decomposition occurs via a surface ethoxy to a methyl group, CO and H adatom[30]. These methyl groups then either combine with surface H to produce methane at 270-350 K or further decomposed to surface carbon. The presence of oxygen on the surface did not significantly alter the products observed, except that water was produced above 250 K. Additionally, CO_2 was observed if the adsorption occurred above 380 K, as the oxygen adatoms would react with the CO. Below 250 K, the adsorbed oxygen led to the formation of acetate which decomposed at ~400 K to produce CO_2 and H_2, leaving behind C on the surface.

The Bowker group has also carried out TPD studies with several alcohols, including ethanol, on Pd/TiO_2 catalysts[32]. Dehydration occurred in the absence of Pd, giving ethene. With 5% weight loading of Pd, no dehydration products were observed. Instead, H_2, CH_3CHO, CO and CH_4, characteristic of dehydrogenation and decarbonylation, were seen, suggesting that the adsorbed species was able to diffuse to the Pd before dehydration on titania occurred.

Acetic Acid

No literature on the reactivity of acetic acid on Pd/TiO_2(110) could be found. There has, however, been some work on the adsorption and reactivity of acetic acid on palladium single crystals. Davis and Barteau looked at acetic acid on clean[33] and oxygen-covered[34] Pd(111) and found that it adsorbed as acetate. It is known to form η^2-acetate species on heating to ~300 K, although the formation of a less stable η^1-species has also been identified with XPS and

HREELS[35]. Pre-dosed oxygen was found to stabilise the acetate, and acetate decarboxylation occurred at 305 K and 420 K on the O-dosed Pd(111) surface[34]. Two reaction pathways for the acetate were observed on the Pd(111) surface – either hydrogenation to acetic acid, or decarboxylation.

Several years later, Bowker et al used TPD[36] and a molecular beam reactor[37] to investigate the adsorption and decomposition of acetic acid on a clean and oxygen-dosed Pd(110) single crystal. On clean Pd(110), it dissociates to form a stable acetate and hydrogen is desorbed at 300 K. Some of the acetate was then seen to decompose at ~350 K to give CO_2(g) and H_2(g), leaving behind adsorbed C. This C stabilised the acetates, resulting in desorption temperatures increasing by as much as 100 K. Oxygen pre-dosing lead to stabilisation of the acetate[36], as with Pd(111)[33, 34], leading to an autocatalytic acetate decomposition, a phenomenon also known as "surface explosion" i.e. once the reaction starts, it is self-accelerating. Only one decomposition pathway was observed for acetate on Pd(110), to CO_2(g) and CH_3(a), as opposed to the two pathways seen on Pd(111) found by Barteau[33]. On clean Pd(110), CO_2 and H_2 were observed at 350 and 375 K. On the oxygen-treated surface, the same peaks were seen, although the CO_2 desorption signal has changed from a broad signal to a very narrow, tall peak, accompanied by H_2O desorption. Acetic acid sticking was found to be very efficient, resulting in hydrogen evolution and acetate formation at room temperature[37]. The acetate decomposed between 320 and 440 K, producing coincident CO_2 and H_2, leaving behind C on the surface. It was observed that, at high temperature, acetic acid sticking is not poisoned by build up of C on the crystal, as most of the C is lost from the surface into the bulk above ~450 K.

From the literature, it can be said that acetic acid generally reacts with Pd surfaces in the following manner, involving dehydrogenation and C deposition on the surface[37]:

$$CH_3COOH_{(g)} \rightarrow CH_3COO_{(a)} + H_{(a)}$$

$$CH_3COO_{(a)} \rightarrow C_{(a)} + 3H_{(a)} + CO_{2(g)}$$

$$2H_{(a)} \rightarrow H_2$$

Acetic acid is a weaker acid than formic acid, and so the conjugate base, the acetate, is a stronger base than the formate and is typically more stable on the surface. Hence, on Pd(110) surface acetate decomposes at ~350 K[36, 38] whilst the formate breaks down at ~250 K[21].

More recently, Gao and Tysoe investigated the surface chemistry of acetic acid on clean and oxygen-covered Pd(100) using XPS and TPD[39]. On clean Pd(100), molecular acetic acid desorbs at ~200 K and acetate species form at higher temperatures and decompose at ~300 K. On O-covered Pd(100), acetate species are predominantly formed and are stable to ~380 K, where acetic acid and its decomposition products (H_2, H_2O, CO and CO_2) form simultaneously[39].

5.1.3 Au/TiO_2 reactivity studies

Ethanol

Metallic Au has been found to oxidise many alcohols, including both primary[40-43] and secondary[40-42]. Studies have shown that there are strong parallels between the oxidation of alcohol on oxidised Au(111) at low pressure and over Au supported on TiO_2 under high-pressure, aqueous phase conditions[44, 45]. Using TPD and molecular beam studies, Mullins and Gong found that ethanol is selectively oxidised on Au(111) with a low pre-adsorbed O coverage to acetaldehyde and water[46]. Isotopic experiments showed that ethanol initially undergoes O-H bond cleavage, producing ethoxide, followed by selective β-C-H bond activation to form acetaldehyde and water. No other partial oxidation products or C_1-containing species were detected. At higher oxygen coverages, CO_2 was also formed due to the cleavage of the γ-C-H and the C-C bond[46]. Different products have been observed depending on the method of pre-adsorbing oxygen onto the Au(111) surface. Liu et al saw that, as well as molecular acetaldehyde, ethyl acetate at 230 K and acetic acid at 450 and 545 K were formed on Au(111) with 0.4 ML pre-adsorbed oxygen prepared by the decomposition of O_3 at 200 K[44]. At oxygen coverages below 0.1 ML, ethyl acetate was the only product. However, the source of oxygen may not be the only reason for this discrepancy. Mullins et al used m/z 29 to identify the acetaldehyde. However, Liu pointed out that the m/z 29 fragment is also due to ethanol and ethyl acetate. DFT by Gong et al examined different reaction pathways for selective oxidation of ethanol on Au(111) and found that surface oxygen is necessary in the O-H bind activation of ethanol, consistent with experimental observations[47]. Idriss et al used TPD and IR spectroscopy to look at the surface reactions of ethanol over TiO_2 and Au/TiO_2 nanoparticle catalysts[48].

Acetic acid

There has not been much work on the reactivity of acetic acid on either gold single crystals or on supported gold catalysts. Work by Green et al showed that localised Au-Ti perimeter sites (Au/TiO_2 catalysts which involve both Au and Ti^{4+} centres) can catalytically oxidise acetic acid to a novel gold ketenylidene surface intermediate (Au_2=C=C=O, also known as gold ketenide)[49]. They proposed that this species is produced by the activation of the C-H bonds in the methyl group of the chemisorbed CH_3COO/TiO_2 at the Au/TiO_2 perimeter, subsequently following the breaking of one C=O bond. This gold ketenylidene species was formed at around 400 K, and was further oxidised to CO_2 and H_2O at 473 K.

Formic acid

Kiss and co-workers looked at the reaction of formic acid on TiO_2(110) and TiO_2-supported noble metals, including Au[50-52]. The decomposition of formic acid on Au/TiO_2 was examined at 300-473 K with Fourier transform infrared (FTIR) spectroscopy and mass spectrometry[50]. Adsorbed HCOOH, formate and formaldehyde species were detected by FTIR. Some formaldehyde desorbed from the surface, whilst some decomposed into H and CO. They proposed that the CO was produced by the decomposition of the formaldehyde rather than by the direct dehydration of the formic acid. Madix and Outka investigated the adsorption of formic acid on clean and oxidised Au(110) surfaces with temperature programmed reaction spectroscopy[53]. Formic acid was found to react with oxygen adatoms below 210 K in a typical Bronsted acid-base reaction to form water and adsorbed formate (HCOO). The formate was seen to decompose at 340 K, giving water, CO_2 and formic acid. A DFT study by Gao and Jacob found that HCOOH oxidation under gas-phase conditions proceeds through a single formate as the active intermediate. The rate-limiting step was found to be formate formation on the Au, in good agreement with experimental findings[54]. A combined DFT and experimental study showed that HCOOH decomposition on Au follows the formate mediated path, with 100% selectivity to the dehydrogenation products (CO_2 and H_2), regardless of the reaction conditions[55]. A TPD study showed that the Au(111) surface is inactive for formic acid decomposition[56], consistent with observations that formic acid interacts weakly with the clean Au(111) surface using XPS and RAIRS[57]. On O/Au(111), it dissociates its acidic H to give adsorbed formate[57].

5.1.4 Au-Pd/TiO_2

There has been no work on the reactivity of Au-Pd bimetallic systems on TiO_2(110) single crystals.

Acetic Acid

Tysoe et al have carried out RAIRS and TPD studies on the adsorption and reactivity of acetic acid on Au/Pd(111)[58] and on clean and oxygen-covered Au/Pd(100) alloy surfaces[59]. They found that acetic acid adsorbs molecularly on an Au/Pd(111) alloy surface for gold concentrations greater than ~0.33 mol fraction. When the gold concentration is less than ~0.33, adsorption of acetic acid at 80 K and heating to 210 K forms η^1-acetate species on the surface. On further heating, these were found to either decompose to give H_2, H_2O, CO and CO_2, or to form η^2-acetate species. The coverage of η^2-acetate species increases with decreasing gold concentration. Acetic acid was found to have similar behaviour on Au/Pd(100)[59]. Acetic acid adsorbs molecularly on Au/Pd(100) for gold coverages greater than ~0.5 ML. This then forms some η^1-acetate species which decompose to form CO and H_2. η^1-acetate species also form on surfaces with lower gold coverages, which converts to a η^2-acetate species which then thermally decomposes to CO and H_2, with a small portion re-hydrogenating to acetic acid at 280-320 K. The presence of oxygen facilitates acetate dehydrogenation[59].

Formic acid

Pd-Au bimetallic catalysts have received a lot of attention for their ability to selectively hydrogenate HCOOH ($HCOOH \rightarrow H_2 + CO_2$)[60-62] and have been found to have a much higher catalytic activity and a higher tolerance to CO poisoning than their monometallic Pd and Au counterparts[63, 64]. Mullins et al used TPD and reactive molecular beam scattering (RMBS) to look at the decomposition of HCOOH on Pd/Au(111)[56]. They found that Pd atoms at Pd-Au interface sites favour dehydrogenation of formic acid, whereas Pd atoms without neighbouring Au atoms favour dehydration of HCOOH.

Ethanol

A study into the photoreforming of biofuels using Au-Pd/TiO_2 photocatalysts by Bowker et al found that ethanol produces CO_2, H_2 and methane[65]. Alloying Au and Pd was found to show a benefit in activity compared to just Pd or Au. However, they were unable to determine the extent of the alloying, and whether a core-shell structure had been formed, or if the surface of the catalysts were a mix of the two metals. Similar studies by Masahashi et al formed Au-core Pd-shell nanoparticles on TiO_2 and found that Au-Pd bimetallic nanoparticles had improved activity over their component metals[66].

5.2 Experimental

The experiments were carried out as described in Chapter 2, in the system referred to as "UHV2."

A $TiO_2(110)$ single crystal was placed into the machine and subject to cleaning cycles until the AES showed no contaminations. The cycles consisted of sputtering (1 keV, 20-40 minutes) at room temperature, followed by annealing to 873 K for 15 minutes. It was, however, difficult to be completely sure of the surface cleanliness of the sample after depositing palladium, as both palladium and carbon have a peak in the same region (275eV and 283eV for C and Pd respectively).

Palladium and gold were both deposited on to the crystal by MVD (metal vapour deposition). A current was passed through the metal filament and allowed to degas for 20 seconds. The crystal was then moved below the filament, approximately 1-2 cm below.

Ar and O_2 gases were supplied by Argo with purities of 99.999%. Ethanol, acetic acid and formic acid were supplied by Fisher with purities of 99.99%, 99.83% and 99.5+% respectively and were cleaned prior to use by repeated freeze-pump-thaw cycles. The organic molecules were dosed by exposing the TiO_2 substrate to a background pressure of the desired organic molecule for 5 minutes.

Prior to carrying out a TPD experiment, the sample was annealed to 573 K in order to remove any adsorbed contaminants. Heating to temperatures greater than 573 K was purposely avoided to minimise sintering and any SMSI effects.

5.3 Results – reactivity of organic molecules

5.3.1 TiO_2

Before investigating the effect of depositing gold and palladium on the reactivity of $TiO_2(110)$, $TiO_2(110)$ alone was examined. TPDs with three simple organic molecules were carried out – ethanol, formic acid and acetic acid.

5.3.1.1 Ethanol

Figure 5-1 shows an ethanol TPD on $TiO_2(110)$. There are coincident mass 28 and mass 44 peaks at ~350 K. There appears to be a double peak in the mass 28, the second of which is coincident with mass 27, at 393 K, indicating ethene desorption. There is a small mass 31 peak at ~325 K, indicative of ethanol desorption. There is no noticeable mass 43 peak. There is a sharp increase in the mass 2 (hydrogen) signal, but it has no discernible shape and may just be as a result of the increasing background pressure. Finally, there is a small, broad mass 29 peak at ~380 K, indicating acetaldehyde desorption. These results all broadly agree with an indepth TPD & XPS study by Kim and Barteau in 1990[3] into the adsorption and reactivity of ethanol and other higher aliphatic alcohols on $TiO_2(001)$. They observed that adsorption of ethanol at room temperature leads to an ethoxylated surface. Half of this ethoxy species recombined with a proton:

$$CH_3CH_2O_{(ads)} + H_{(ads)} \rightarrow CH_3CH_2OH_{(g)}$$

and desorbs as ethanol. The other half decomposes to produce either ethene:

$$CH_3CH_2O_{(ads)} \rightarrow H_2C{=}CH_{2(g)} + O_{(lattice)} + H_{(ads)}$$

or acetaldehyde:

$$CH_3CH_2O_{(ads)} \rightarrow CH_3CHO_{(g)} + H_{(ads)}$$

There is, however, a difference in the desorption temperatures between this work and Barteau's. Barteau found that ethanol desorption occurred at 365 K, rather than 325 K, and the remaining ethoxy species decomposed above 500 K, rather than 380-400 K. Barteau found that the selectivity between the dehydration pathway to ethene and the dehydrogenation pathway to produce acetaldehyde was largely in favour of producing the olefin. The dehydrogenation/dehydration selectivity ratios were less than 0.25. This agrees with Figure 5-1, as the mass 27 peak is greater than the mass 29 peak. A TPD study by Campbell and Gamble observed a broad peak between 250 and 400 K, ascribed to ethoxy desorption as ethanol. They proposed that the broadness of the peak resulted from protonation of the surface ethoxy species by surface H atoms[4].

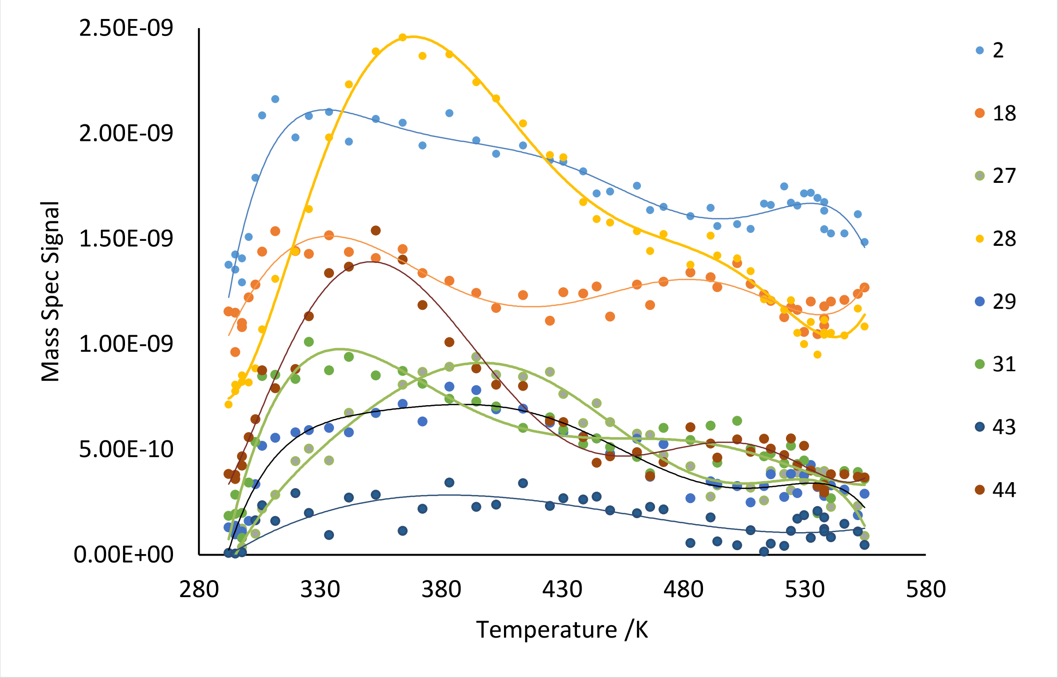

Figure 5-1 - Ethanol TPD on TiO_2(110)

5.3.1.2 Formic Acid

Figure 5-2 shows a formic acid TPD on TiO_2(110). Mass 28 appears to have two peaks, one at ~340 K and one which is coincident with mass 44 at ~360 K. There is a small increase in mass 18 at 310 K, although there is no discernible peak shape. Finally, there is a mass 2 peak at ~320 K.

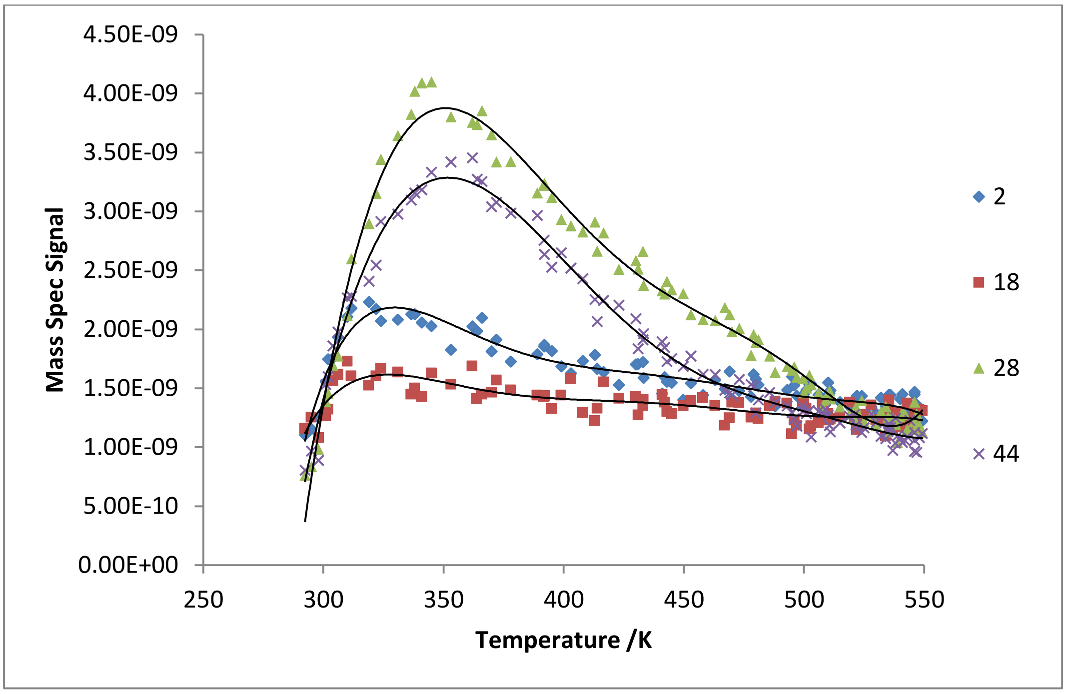

Figure 5-2 - Formic acid TPD on TiO_2(110)

Previous studies have shown that formic acid dissociates on rutile TiO_2(110) to give formate[67]:

$$HCOOH_{(g)} + O_{(lattice)} \rightarrow HCOO_{(ads)}^{-} + O_{(lattice)}H_{(ads)}$$

Two decomposition routes can then occur at elevated temperature. The first is a dehydration reaction producing carbon monoxide and water:

$$HCOOH_{(ads)} \rightarrow CO_{(g)} + H_2O_{(g)}$$

The second is a dehydrogenation reaction, which produces carbon dioxide and hydrogen:

$$HCOOH_{(ads)} \rightarrow CO_{2(g)} + H_{2(g)}$$

Both reaction pathways have been observed on TiO_2(110)[10, 12], although the dehydrogenation pathway was found to be preferred below 500 K. This may agree with Figure 5-2 – the hydrogen (mass 2) peak is approximately twice the size of the water (mass 18) peak, indicating that, although both pathways occurred, the dehydrogenation pathway was preferred.

5.3.1.3 Acetic Acid

Figure 5-3 shows an acetic acid TPD on TiO_2(110). There is a mass 28 peak at 355 K, coincident with a mass 44 peak. There are also coincident mass 14 and 42 peaks at ~390 K. Mass 2 and 18 peaks appear to be minimal or non-existent. This agrees with previous findings – acetic acid has been shown to adsorb as acetate on TiO_2(110). It then typically undergoes unimolecular decomposition to release ketene:

$$CH_3COO_{(ads)}^{-} \rightarrow H_2C{=}C{=}O_{(gas)} + {}^{-}OH_{(ads)}$$

A comprehensive TPD/XPS study by Barteau and Kim on differently treated TiO_2(001) surfaces found a difference in the desorption between the oxidised and sputtered surfaces[19]. On the sputtered, oxygen deficient surface the main decomposition product is atomic C which is then burned off as CO via reaction with surface oxygen. On a more oxidised surface, ketene was produced via a net dehydration reaction. The presence of both CO and ketene in Figure 5-3 may indicate that the TiO_2(110) surface was in an intermediate state of reduction.

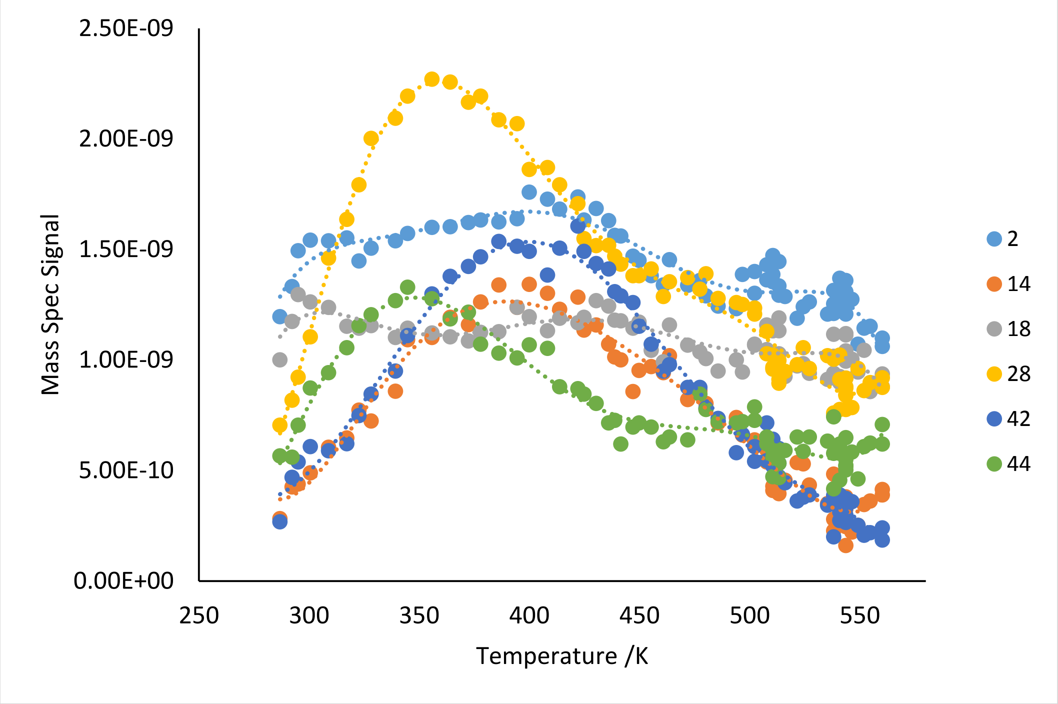

Figure 5-3 - Acetic acid TPD on $TiO_2(110)$

5.3.2 Pd/TiO_2

The TPDs were only carried out up to a temperature of ~550 K, in order to avoid the encapsulation of the Pd by the TiO_2 via an SMSI effect and sintering of the metal nanoparticles. The Pd:Ti peak height ratios from the AES before doing each of these TPDs is shown in Table 5-1 . An example Auger is shown in Figure 5-4. The peak assignments are as follows: titanium is observed at 384 and 421eV, oxygen at 513eV and palladium at 330, 280 and 250eV.

Table 5-1 - Auger Pd:Ti peak height ratios

Substrate condition	Pd:Ti height ratio
After dosing Pd	13.3
After annealing to 573 K	10.4
After carrying out the TPDs	7.3

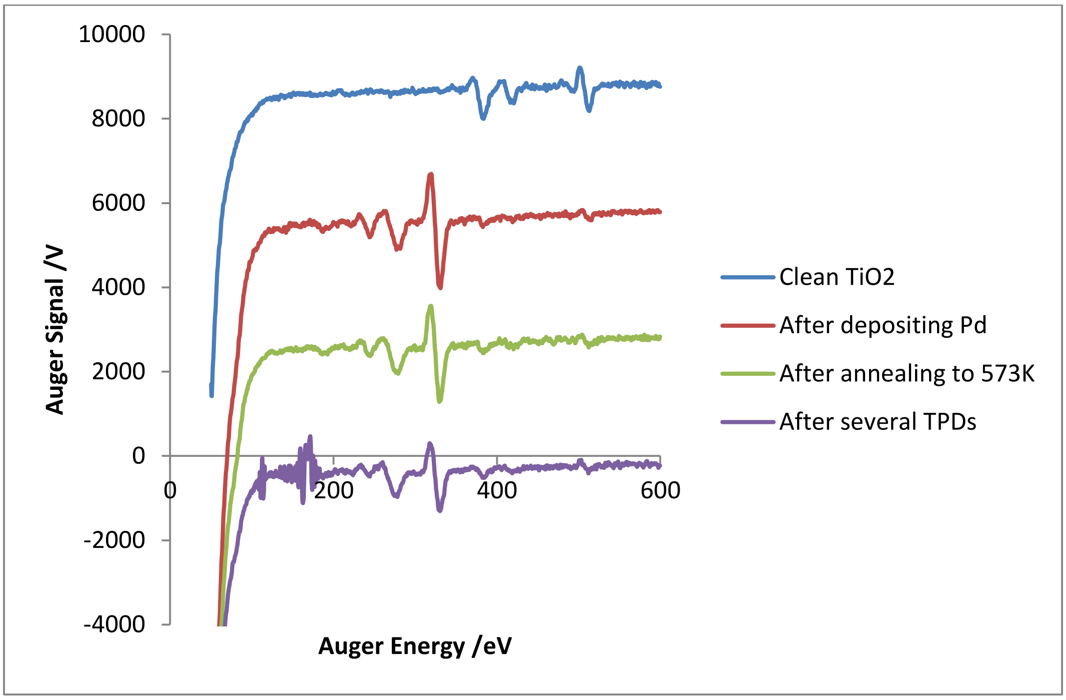

Figure 5-4 - Auger spectra of Pd-TiO_2 before TPD

5.3.2.1 Ethanol

Figure 5-5 shows an ethanol TPD on Pd/TiO_2(110). Due to a limitation with the mass spec software (on attempting to run the software with too many masses at once, it would either freeze and crash, or take a reading every 10-20 seconds, which is far too infrequent), two separate TPDs had to be run with fewer masses inspected each time (i.e. the first TPD looked at masses 2, 15, 18, 27, 28, 29, 31 and 44, whilst the second TPD looked at masses 2, 14, 28, 31, 42, 43 and 44. These two TPDs were combined into one, shown in Figure 5-5). There are coincident mass 2 and 18 peaks at 320 K and at 430 K and a mass 31 peak at 330 K. Mass 28 is a broad peak, stretching from 300 K to a maximum at 450 K, and there is a broad mass 44 peak with a maximum at 390 K.

The broad mass 28 peak is due to CO desorption and the mass 2 peak at 320 K is due to H_2. These are both common desorption products found in the literature[29, 30]. The broad, very shallow mass 44 peak at 390 K is CO_2, observed by Bowker et al when oxygen was pre-adsorbed onto Pd(110) at 380 K and then combined with the CO. The mass 31 and 29 peaks at ~330 K correspond to molecular ethanol desorption. There are no coincident mass 29, 43 and 44 peaks, indicating that there is no acetaldehyde desorption at the temperatures investigated, or that it is all decarbonylated to CO and CH_4, as proposed by Barteau et al[29]. The mass 27 peak at 320 K indicates a small amount of ethene desorption.

This TPD is similar to the corresponding TiO_2 TPD in some respects. There are, however, several large differences between the two TPDs. The first is the CO_2 peak present at 350 K on the TiO_2 TPD, but absent from the Pd/TiO_2 TPD. The second major difference is a lack of any obvious ethene evolution – mass 27 and 28 were observed at ~393 K on the TiO_2(110), but this is not seen from the Pd/TiO_2(110). The other difference is that the CO peak is very broad in the Pd/TiO_2 TPD, stretching from ~300 to ~500 K, with the maximum at ~450 K. The corresponding peak in the TiO_2 TPD is narrower, and occurs at ~365 K. Otherwise, the same peaks are seen in both TPDs, with the peaks occurring between 10-30 K lower in the TiO_2 TPD than in the Pd/TiO_2 TPD.

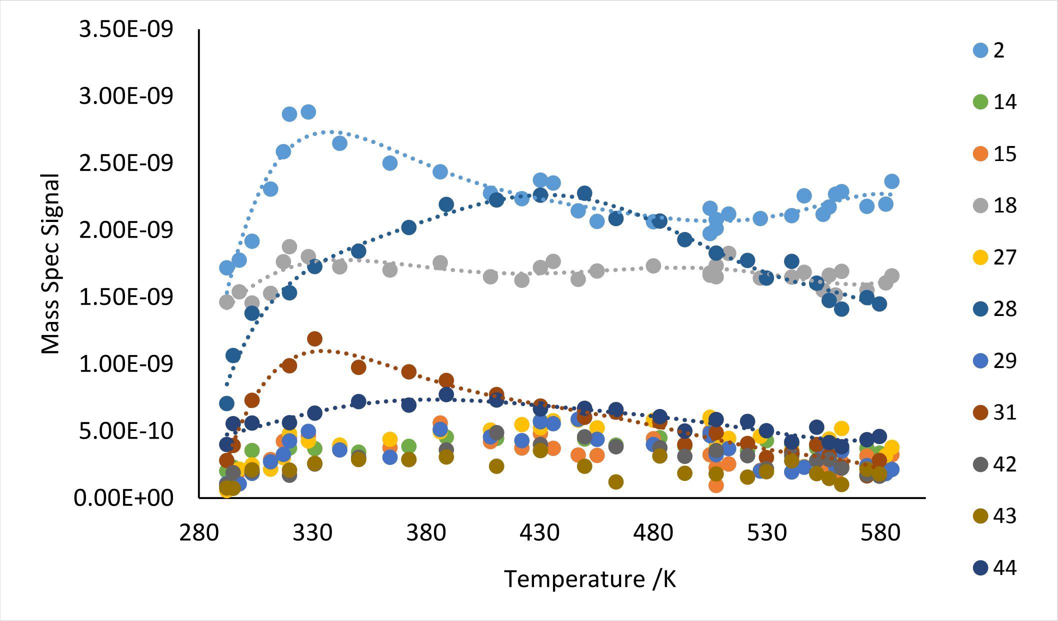

Figure 5-5 - Ethanol TPD on Pd/TiO_2(110)

5.3.2.2 Formic Acid

Figure 5-6 shows a formic acid TPD taken after depositing Pd on to TiO_2(110) and annealing to 573 K. A mass 2 desorption peak can be seen at 310 and 330 K. Mass 44 and 28 are coincident with mass 2 at 310 K, and then give a very broad, shallow peak at ~400 K. There is also a very broad, shallow mass 18 peak over the entirety of the TPD spectrum. Mass 14 and 42 give short, sharp peaks at ~310 K and then a second peak with a very gradual incline at ~430-470 K. Finally, there is no observable mass 30 peak, and only a short mass 29 peak at 310 K.

All of the coincident peaks at 310 K are likely to be due to the filament heating up and are not real peaks from the sample. It appears that both the dehydrogenation and dehydration pathways occur on Pd/TiO_2(110). The mass 44 peak at 400 K and the mass 2 peak at 330 K are due to CO_2 and H_2 respectively as a result of the dehydrogenation pathway, whereas the mass 28 peak at 400 K indicates CO desorption due to the dehydration pathway. When comparing the formic acid TPD on TiO_2 (Figure 5-2) and Pd/TiO_2 (Figure 5-6), the Pd/TiO_2 TPD appears much more complicated. The mass 28 and 44 peaks occur at a higher temperature (400 K, as opposed to 350 K for the pure TiO_2), as do the mass 2 and 18 peaks (330 K rather than 320 K). However, these peaks are much less well defined than the TiO_2 TPD. The mass 14 and 42 peaks in Figure 5-6 are ketene, which is possibly as a result of acetic acid still being present in the gas dosing line. Great care was taken to bake the gas lines each time after changing the adsorbate, although there still appears to be some residual acetic acid despite this. However, it is worth pointing out that these ketene peaks are not seen in the ethanol TPD (Figure 5-5), which was also taken after the acetic acid TPD. The mass 29 peak at ~360 K indicates formic acid desorption.

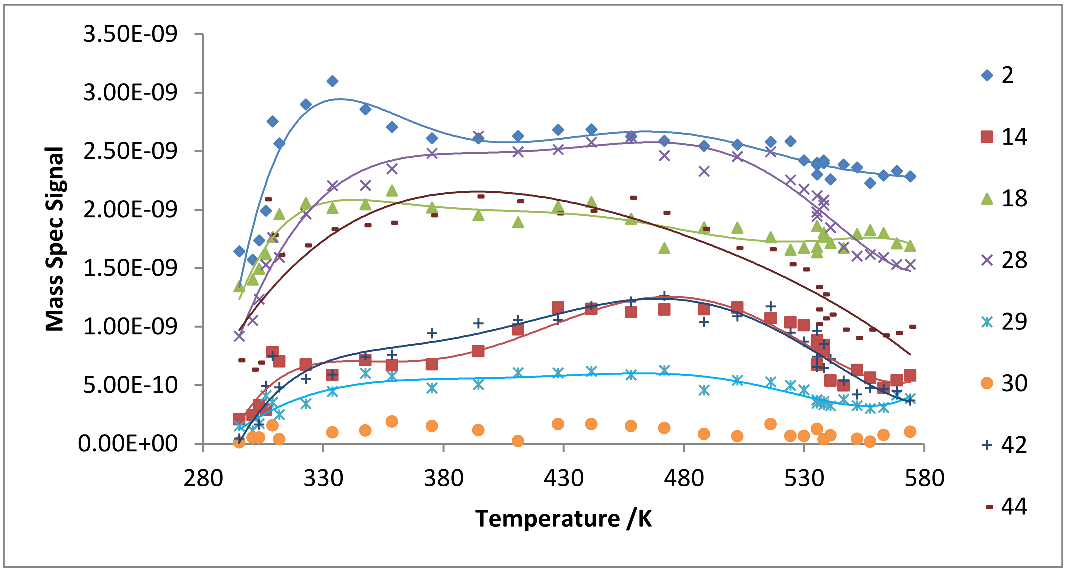

Figure 5-6 - Formic acid TPD on $Pd/TiO_2(110)$

Bowker et al carried out TPD on Pd(110) and also observed CO, CO_2, H_2 and H_2O[21]. The CO and H_2 were seen in desorption-limited peaks at 420 and 320 K respectively, which is similar to that seen here with $Pd/TiO_2(110)$. Molecular beam studies were also carried out on $Pd/TiO_2(110)$[14], where both dehydration and dehydrogenation pathways were seen. The rate of formic acid decomposition was found to be slower with Pd nanoparticles than with Pd(110) single crystal. It was suggested that the nanoparticles are much less reactive than the bulk metal, possibly due to the nanoparticles alloying with Ti. When these same experiments were carried out on a higher loading of Pd, the results were essentially the same, except now CO_2 was produced at 573 K. This is probably because the average diffusion length is now greater than the interparticle distance, so the formate decomposes on the Pd by dehydrogenations rather than by dehydration of the TiO_2.

5.3.2.3 Acetic Acid

Figure 5-7 shows an acetic acid TPD from $Pd/TiO_2(110)$. There are sharp coincident mass 14 and 42 peaks at 310 K and much broader coincident peaks at 410-480 K. Mass 2, 18 and 44 are also coincident at 310 K. There is a very broad, shallow mass 28 peak at ~390 K. There is no mass 45 peak present in the spectrum.

The lack of a mass 45 peak suggests that there is no acetic acid desorption. The CO_2 and H_2 peaks may be due to the decarboxylation of the adsorbed acetate on the Pd – this has been observed on the Pd(110)[36, 37] and (111)[33, 34] surface. Ketene (mass 14 and 42) has not been observed on Pd single crystals, but are characteristic of acetic acid on TiO_2[19]. However, the mass 14 and 42 peaks occur at a higher temperature than on the TiO_2 surface shown in Figure 5-3. Desorption from the TiO_2 occurred at 370-420 K, whereas desorption from Pd/TiO_2 was observed at 410-480 K. The peaks are also broader and shallower than seen on the TiO_2 surface.

The TPD spectrum on the whole appears to show less reactivity than the equivalent TiO_2 TPD shown in Figure 5-3. Each of the equivalent peaks on the Pd/TiO_2 spectrum occur at a higher temperature than the TiO_2 spectrum, and are generally broader and shallower. This appears to suggest that the Pd is decreasing the activity of the TiO_2.

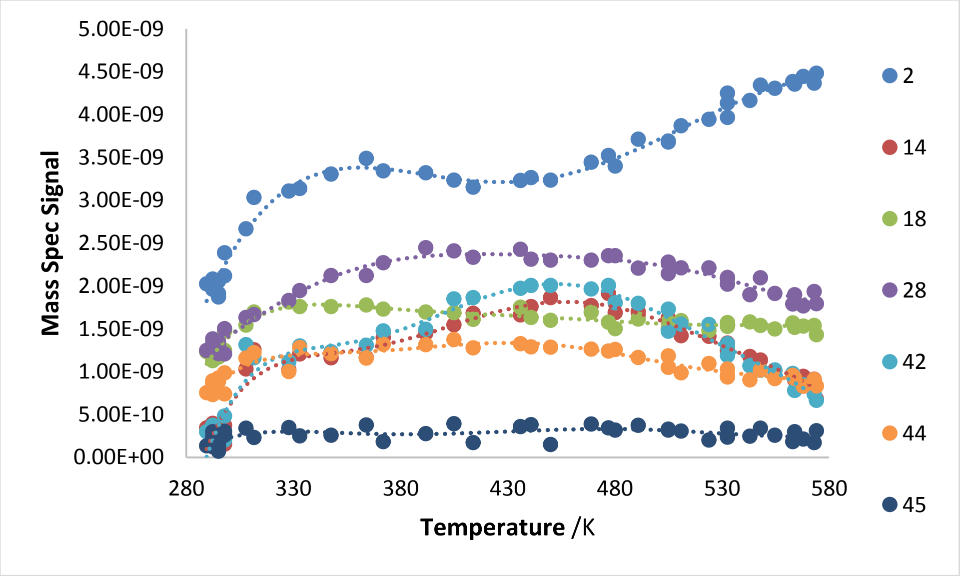

Figure 5-7 - Acetic acid TPD on Pd/TiO_2(110)

5.3.3 Au/TiO_2

The TPDs were only carried out up to a temperature of ~550 K, in order to avoid the encapsulation of the Au by the TiO_2 via an SMSI effect and to avoid an excess of sintering. The Au:Ti peak height ratios from the AES before doing each of these TPDs is shown in Table 5-2. An example Auger is shown in Figure 5-8. The peak assignments are as follows: gold is observed at 73 eV, titanium at 384 and 421 eV and oxygen at 513 eV.

Table 5-2 – Auger Au:Ti peak height ratio

Substrate Condition	Au:Ti height ratio
After depositing Au	3.7
After annealing to 573 K	3.4
After the TPDs	2.9

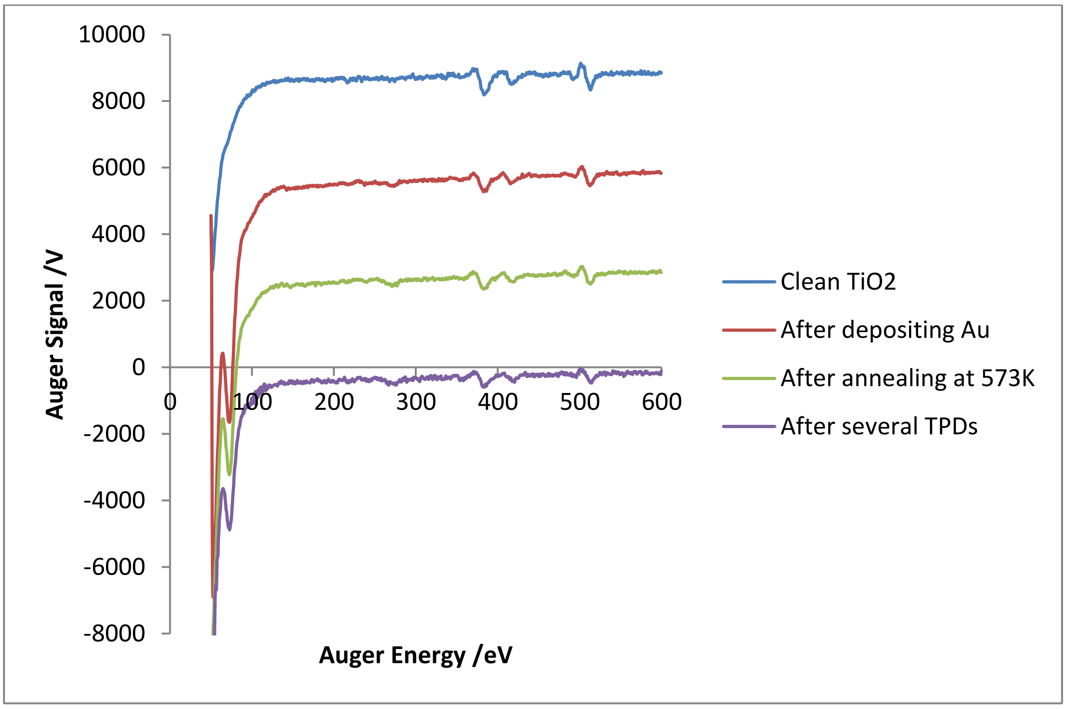

Figure 5-8 – Auger spectra before Au-TiO2 TPD

5.3.3.1 Ethanol

Figure 5-9 shows the resulting ethanol TPD from Au/TiO_2(110). There is a small mass 18 peak at ~315 K coincident with masses 27, 29 and 31. There is a second broad mass 27 peak from 370-400 K coincident with mass 28. Mass 29 and 43 are also coincident at ~380 K, but have a different shape to the mass 27 and 28 peaks. There is no evidence of any mass 2 or mass 44 peaks.

The coincident peaks at ~315 K are characteristic of molecular ethanol desorption. Masses 29 and 43 are characteristic of both acetaldehyde and ethyl acetate – both have been reported on oxidised Au(111)[44, 46]. However, in this instance the mass 29 signal is greater than the mass 43 peak, which is characteristic of acetaldehyde. The coincident mass 27 and 28 peaks are characteristic of ethene, which has not been reported for Au, but has been reported for TiO_2[3]. The absence of a mass 44 peak suggests that very little oxygen has migrated from the TiO_2 (110) substrate to the Au particles – at high oxygen coverages on Au(111), CO_2 has been observed due to the cleavage of the γ-C-H and the C-C bond[46]. Ethyl acetate has been reported for oxygen coverages on Au(111) of less than 0.1 ML – the absence of ethyl acetate suggests that the Au here is not very reactive. Likewise, the mass 28 and 29 ethene peaks at 370-400 K are much larger in size than the mass 29 and 43 acetaldehyde peaks. This also suggests that the Au is not being very reactive, and the bulk of the products observed are due to the titania substrate. However, there are some differences between this ethanol TPD on Au/TiO_2 and the ethanol TPD on clean TiO_2 shown in Figure 5-1 above. There is no evidence of H_2 in the Au/TiO_2 TPD, whereas there is a sharp increase in the H_2 signal at ~310 K in the ethanol TPD on TiO_2. Whilst there is no mass 44 CO_2 peak in this Au/TiO_2 TPD, there is a large mass 44 peak when carrying out the ethanol TPD on titania. Finally, the mass 28 and 27 ethene peaks are much larger (by a factor of >2) in the TiO_2 ethanol TPD. It appears as though addition of Au nanoparticles to the TiO_2 (110) surface has decreased the overall reactivity of the TiO_2 (110) substrate whilst not adding any benefit.

Perhaps the ethanol is just not adsorbing on to the Au, hence the reduction in reactivity.

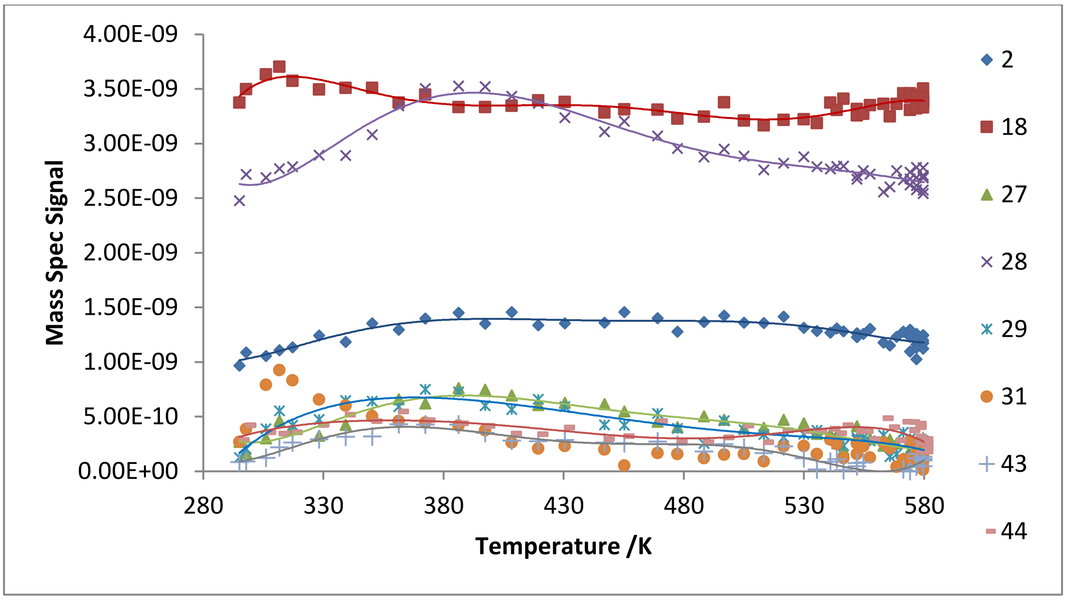

Figure 5-9 - Ethanol TPD on Au/TiO$_2$(110)

5.3.3.2 Formic acid

Figure 5-10 shows the formic acid TPD obtained on Au/TiO$_2$(110). There are large, broad coincident mass 28 and 44 peaks at 345-385 K and smaller mass 2 and mass 18 peaks at 310 and 300 K respectively. There is no observable mass 30 peak. There are very small mass 14 and 42 peaks at 386eV and a small, broad mass 29 peak at ~355 K.

This TPD looks very similar to the TiO$_2$ formic acid TPD shown in Figure 5-2. In both cases, the mass 2, 18, 28 and 44 peaks have similar peak shapes and heights. Again, much like the Au/TiO$_2$ ethanol TPD above, it seems as though the Au is not very reactive, despite covering a large amount of the surface (as seen in Figure 5-8). This is not entirely surprising – Mullins et al found that Au(111) is inactive for formic acid decomposition during TPD[56], and formic acid has been found to bond weakly to Au(111)[57]. The small mass 29 peak at ~355 K could be evidence of formaldehyde, which was seen by FTIR and mass spec studies on

Au/TiO_2[50]. However, it is small enough relative to the CO and CO_2 peaks that it seems that the Au has made no difference to the reactivity of the $TiO_2(110)$ single crystal. Alternatively, it could just be formic acid.

Reactivity studies and DFT calculations on Au/TiO_2 have found that these catalysts are 100% selective for the dehydrogenation pathway[55] ($HCOOH \rightarrow CO_2 + H_2$) at 340 K. Likewise, oxygen-covered Au(111)[57] and Au(110)[53] have been shown to be active, although that appears not to be the case here. It seems most likely that, in this instance, the formic acid is not adsorbing on to the Au, hence the TPD looks almost identical to the corresponding $TiO_2(110)$ TPD.

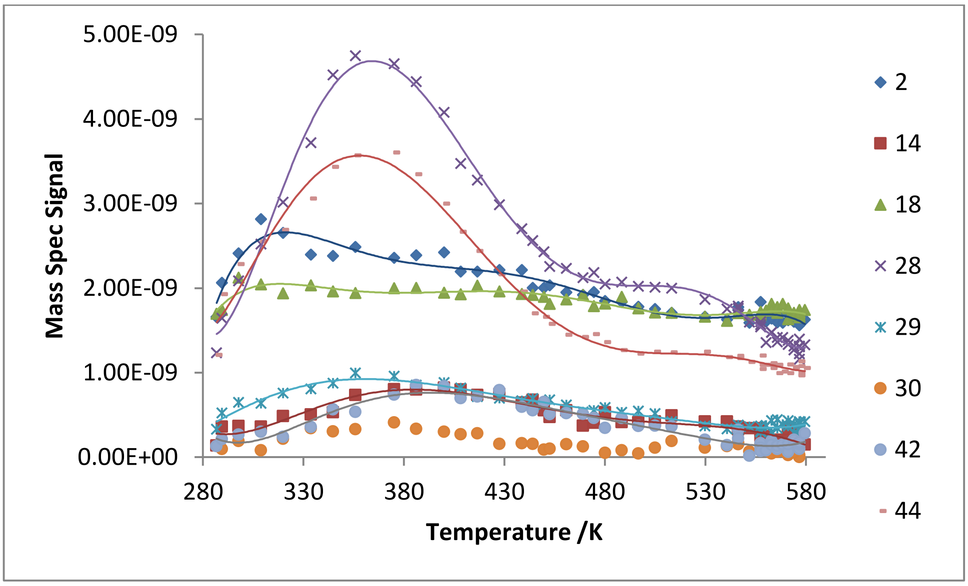

Figure 5-10 - Formic acid on $Au/TiO_2(110)$

5.3.3.3 Acetic acid

Figure 5-11 shows the acetic acid TPD recorded on $Au/TiO_2(110)$.There are sharp coincident mass 14 and 42 peaks at 370 K. Mass 28 is observed at 360-380 K. There is a much smaller, broader mass 44 peak at 360 K. Finally, there are no observable mass 45, mass 2 or mass 18 peaks above the noise.

Much like the ethanol and formic acid TPDs above, the addition of Au has not greatly impacted the observed TPD. The mass 14 and 42 peaks, characteristic of ketene ($H_2C=C=O$) occur at the same temperature, although they are slightly broader on the TiO_2 spectra. TPD carried out on Au/TiO_2 observed the formation of ketenylidene at 400 K, which decomposed to CO_2 and H_2O at 470 K[49]. However, this is not observed here – there are no peaks at 470 K, and no water peak at all. Again, it seems likely that the acetic acid is not adsorbing onto the Au.

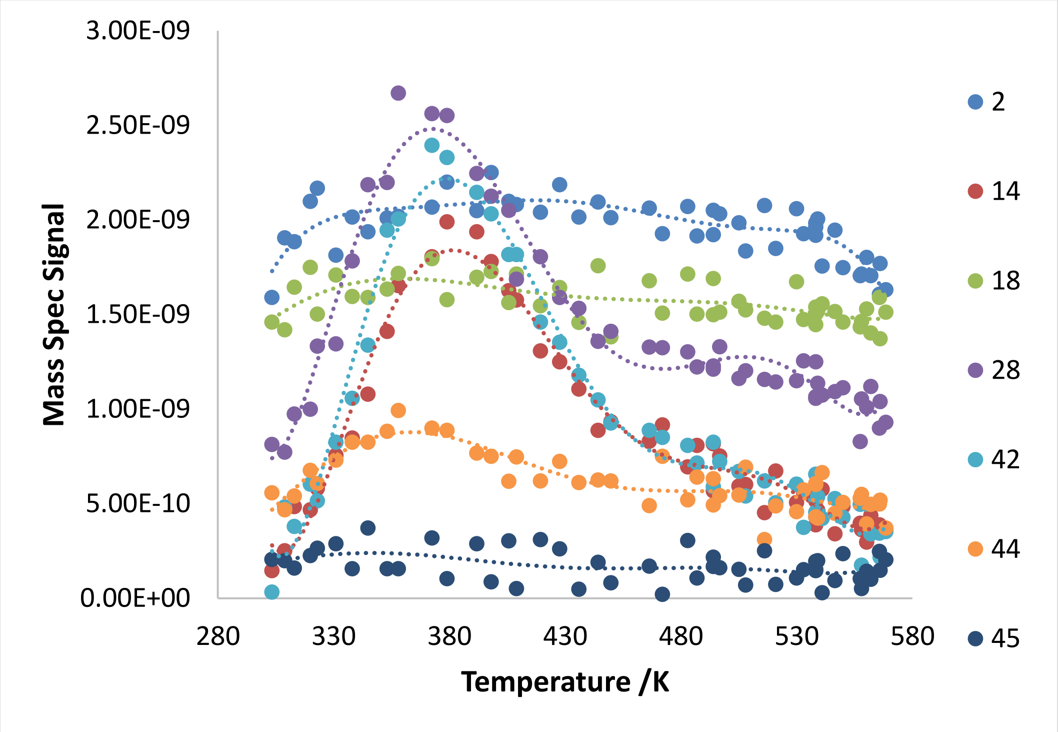

Figure 5-11 - Acetic Acid TPD on Au/$TiO_2(110)$

5.3.4 Au-Pd/TiO_2

Pd and Au were deposited at room temperature and then annealed to 723 K, to give an Au-core Pd-shell structure described in chapter 4. The resulting Pd/Au ratio was 2.71, see Table 5-3. Figure 5-12 shows Auger spectra taken after depositing each metal, after annealing and after several TPDs. The peak assignments are as follows: gold is observed at 73eV, titanium at 384 and 421eV, oxygen at 513eV and palladium at 330, 280 and 250eV. On depositing Au, the Pd:Au ratio was ~0.2. This increased to ~0.6 on annealing to 573 K and increased again to ~2.7 after annealing to 723 K. The Au signal itself decreases by ~80% after annealing at 723 K. This corresponds with the results presented in chapter 4 – on annealing to ~723 K the Pd and Au form Au-Pd core-shell structures, causing the Au signal to be greatly reduced whereas the Pd signal is not.

The TPDs were only carried out up to a temperature of ~550 K, in order to avoid the encapsulation of the Pd or Au by the TiO_2 via an SMSI effect and to avoid sintering.

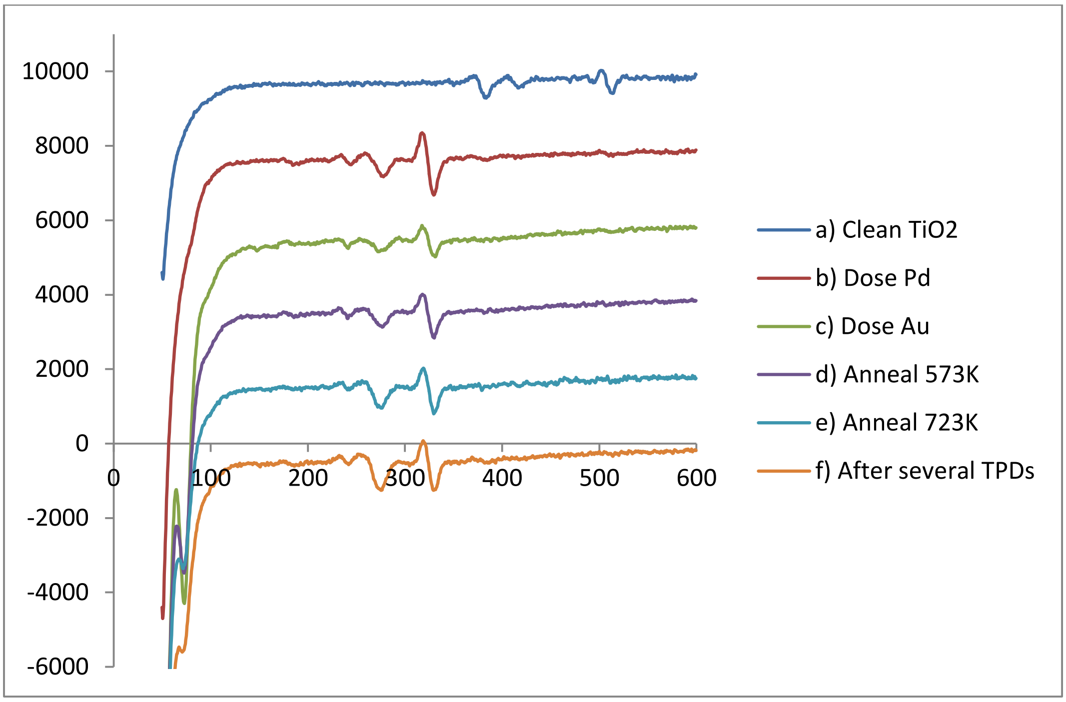

Figure 5-12 – Auger spectra of Pd-Au/TiO_2 before TPD

Table 5-3 – Auger Au:Pd and Pd:Au peak height ratios

Substrate Condition	Pd:Au ratio	Au:Pd ratio
After depositing Pd then Au	0.21	4.75
Annealing to 573 K	0.63	1.6
Annealing to 723 K	2.71	0.37
After several TPDs	3.57	0.28

5.3.4.1 Ethanol

Figure 5-13 shows an ethanol TPD on Pd-Au/TiO_2(110). The most obvious feature is the large mass 31 peak at ~340 K. This is coincident with the mass 29 peak, and the two combined are characteristic of ethanol desorption. Mass 29, 44 and 43 are also all coincident at ~320 K, indicative of acetaldehyde desorption. The mass 43 and 44 peaks then decrease whilst the mass 29 peak continues to increase, coincident with mass 31 as stated above. The mass 44 peak then rises again, separate from the mass 29 and 43 peaks, indicating desorption of a product other than acetaldehyde, possibly CO_2. This mass 44 peak is coincident with the mass 28 peak between temperatures of 390-410 K. Mass 28 is a fragment of CO_2, adding credibility to this possibility. At temperatures above ~420 K, the mass 44 peak decreases whilst the mass 28 peak continues to rise, up to ~460 K, indicating the desorption of CO as well. At ~345 K, mass 27 is coincident with mass 28; these are both the main cracking fragments of ethene. There is mass 18 (water) peak at ~345 K and two mass 2 peaks at 310 and 360 K, caused by H_2 desorption.

The ethanol TPD on Pd-Au/TiO_2 has some similarities and differences to the corresponding TPD carried out on Pd/TiO_2 and Au/TiO_2 separately. The most obvious difference is the much larger, broader mass 31 peak - much more ethanol is desorbed from the Pd-Au substrate. Much more mass 27 and 29 is seen as well, suggesting that the Pd-Au substrate is more effective at converting ethanol to acetaldehyde and ethene than the component metals. The Pd-Au TPD also shows greater mass 44 (CO_2) desorption at ~390-440 K. The Pd and Pd-Au TPDs share a mass 28 peak at ~430-480 K which is not present in the Au TPD – this peak instead appears at a lower temperature, at ~380 K. All 3 TPD spectra show very little mass 43. The Pd TPD actually produces more mass 2 (H_2) than either the Au or Pd-Au TPD and has a much more obvious, discernible peak shape. Finally, both the Pd and Pd-Au ethanol TPD share the same mass 18 (H_2O) peak shape. The Au TPD also produces mass 18, although it is difficult to distinguish it from the background noise. Overall, it seems as though the Pd-Au/TiO_2(110) substrate is more reactive than the individual component metals, with more ethene and acetaldehyde being produced.

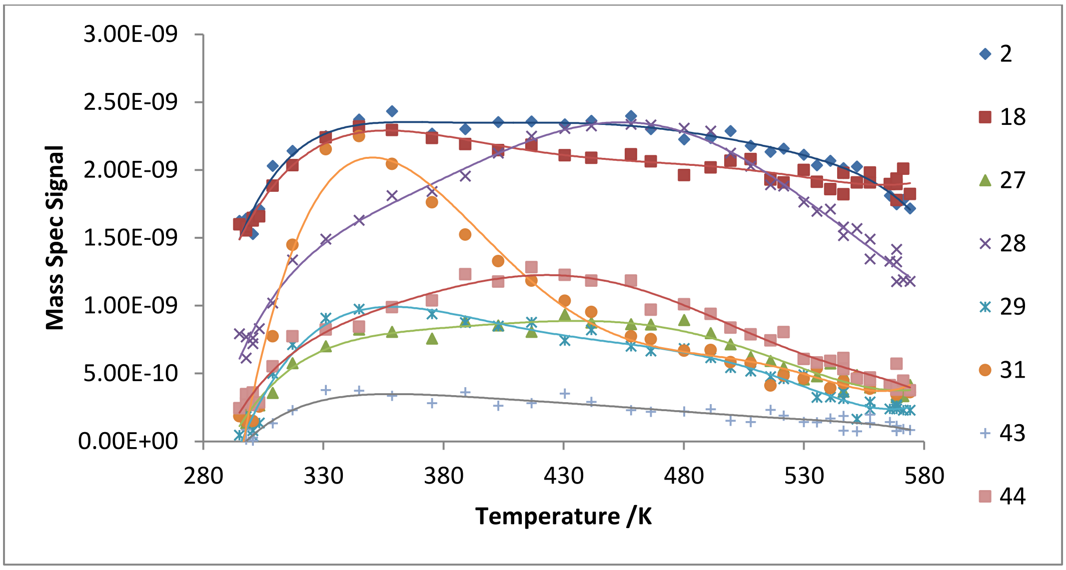

Figure 5-13 - Ethanol TPD on Pd-Au/TiO_2(110)

5.3.4.2 Formic acid

Figure 5-14 shows a formic acid TPD carried out on Pd-Au/TiO_2(110). There is a broad mass 2 peak at 355 K. Both mass 28 and 44 also show a broad peak at ~410-425 K. However, both masses have a different peak shape, suggesting that both CO and CO_2 is being desorbed. Mass 18, H_2O, has a broad peak at 345 K. There are no observable mass 29 peaks above the noise. There are also no noticeable peaks of mass 14, 30 and 42. The lack of mass 14 and 42 suggests that there is no ketene desorption, as would be expected for formic acid. However, this doesn't explain why ketene is seen in the Pd/TiO_2(110) formic acid TPD at ~300 and 430 K. It could just be because the issue with baking and degassing the lines had been sorted out by this point, or it could be something else.

There are several other differences between the Pd-Au TPD and the TPDs on the individual metals. The mass 44 CO_2 peak is much larger (approximately twice the height) and broader on the Pd-Au substrate than the Pd, and the peak maxima is at a higher temperature (430 K, rather than ~400 K). The mass 28 CO peak at 420 K is also much steeper in the Pd-Au TPD than the individual Pd TPD. The mass 28 and 44 peaks are much more defined and sharp in the Au spectra, appearing at ~355 K. The corresponding peaks in the Pd-Au spectra are much broader and the peak maxima is at ~420 K. The three TPD spectra all have similar mass 2, 18 and 29 peak shapes. The broader CO and CO_2 peaks in the Pd-Au/TiO_2(110) TPD suggest that the bimetallic particles are more reactive than the component metals, as seemingly more products are desorbed.

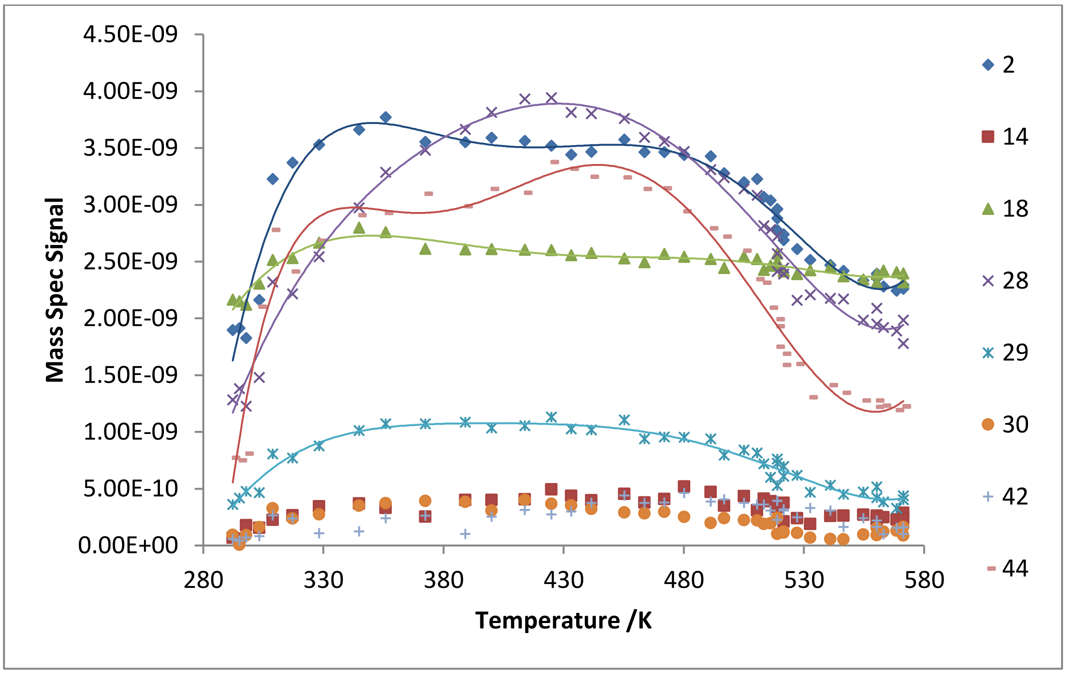

Figure 5-14 - Formic acid TPD on Pd-Au/TiO_2(110)

5.3.4.3 Acetic acid

Figure 5-15 shows an acetic acid TPD on Pd-Au/TiO_2(110). It is unfortunately a very poor TPD overall, and great difficulty was had in obtaining it. It is however possible to distinguish some features. It has coincident mass 2 and 18 peaks at 320-330 K, showing H_2 and H_2O desorption respectively. There are also coincident mass 14 and 42 peaks at 300-310 K and at ~420 K, indicating ketene desorption. Mass 28 shows a rise at ~300 K, coincident with mass 14 and 42. It also shows a separate increase at 350-400 K and then another rise at 420 K, coincident with mass 14 and 42 again. This shows that, as well as ketene, CO is also being produced. The lack of a coincident mass 44 peak at ~350-400 K further implies that it is caused by CO, and is not just a fragment of CO_2. There is however a mass 44 peak at ~310 K, probably caused by CO_2. Finally, there is a very small mass 45 peak at ~320 K, probably caused by some acetic acid desorption.

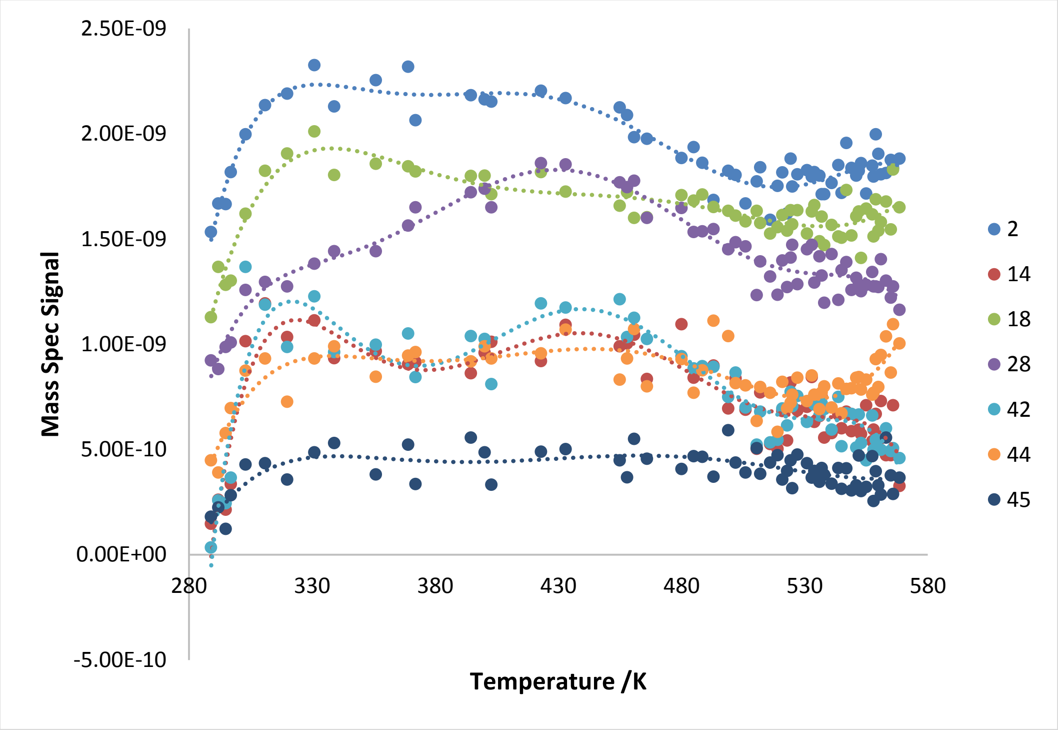

Figure 5-15 - Acetic acid TPD on Pd-Au/$TiO_2(110)$

This TPD looks very similar to the Pd/$TiO_2(110)$ TPD shown in Figure 5-7. The only slight differences are that the Pd-Au TPD has a larger mass 18 peak at 330 K (approximately twice the height), whereas the Pd TPD has much larger, broader and more distinguished mass 14 and 42 peaks at 400-480 K. Otherwise, the two TPDs look almost identical, with very similar peak heights and peak shapes for each of the products observed. There are more differences when comparing the Pd-Au/TiO_2(110) TPD to the Au/TiO_2(110) TPD. The Au TPD has much more distinguished mass 14, 28 and 42 peaks at ~380 K. The two TPD spectra have similar mass 2, 18 and 45 peaks. The mass 44 peak of Au/TiO_2 is more distinguished than the corresponding Pd-Au/TiO_2 peak, but the two peaks are nonetheless very similar. This all appears to suggest that Au/TiO_2(110) is more active for acetic acid reactivity than Pd/TiO_2(110) or Pd-Au/TiO_2(110).

5.4 Conclusions

In this chapter, the reactivity of the TiO_2(110) surface has been investigated with TPD when clean and when dosed with Pd and Au both separately and together. The aim was to investigate the interaction between Pd and Au and to see how the reactivity of the component metals is affected.

Unfortunately there were several problems encountered whilst acquiring this data, leading to some poor TPD spectra. The final TPD figure in this chapter (Figure 5-15), for example, is especially messy and does not give any particularly reliable information. One problem in particular was a lack of an electronic temperature control, which would have enabled a constant heating rate to be achieved between experiments. The mass spectra shown above are often quite messy and difficult to distinguish – one way of improving this could have been to use a differential pumped mass spectrometer, in order to reduce the background pressure in the spectra and obtain peaks with better resolution. Unfortunately these are very expensive and were beyond the scope of this PhD. A further problem is illustrated by the presence of ketene in some spectra of molecules that shouldn't produce it (formic acid, for example). This may have been caused by poor degassing of the gas lines – the molecules were dosed via a needle that protruded deep into the system, making it harder to heat and degas that area compared to the gas lines outside of the system. Despite these issues, some of the information obtained is still useful and further work could be developed to build on this. This section summarises the results of this chapter.

The TPD on TiO_2 showed similar reactivity to what has previously been shown in the literature. Ethanol was found to decompose primarily to ethene and acetaldehyde. Formic acid was shown to follow both reaction pathways, giving both CO and H_2O, and CO_2 and H_2. Acetic acid decomposed to give ketene, CO and CO_2.

The reactivity on adding Pd to TiO_2(110) was overall very similar to just TiO_2(110). The ethanol TPD showed a much broader CO peak at a higher temperature than the equivalent TiO_2 ethanol TPD, but did not possess the CO_2 peak at 350 K that was very prominent on the TiO_2 TPD. Otherwise, all of the other peaks found in the TiO_2 ethanol TPD were present after adding Pd, but were seen at a temperature ~10-20 K higher. Formic acid still followed both reaction pathways (from HCOOH to CO_2 & H_2, and CO & H_2O) on addition of Pd. These products desorbed at a higher temperature than on just TiO_2(110) and there appeared to be a smaller amount of each produced. Likewise, the acetic acid TPD showed the same products on both TiO_2 and Pd/TiO_2 (predominantly ketene and CO), but only at a higher temperature on adding the Pd (~50 K higher). Overall, it appears as though adding Pd to the TiO_2(110) decreased the reactivity of the substrate.

The addition of Au to TiO_2(110) generally did not positively impact the resulting TPD, which is unsurprising as Au has been shown to be unreactive towards the adsorbates investigated[56, 57]. It seems most likely that the molecules investigated did not adsorb onto the Au.

The addition of Au to Pd appeared to increase the reactivity towards formic acid and ethanol, but decrease the reactivity towards acetic acid. More products were seen from the ethanol and formic acid TPDs compared to the individual Au or Pd substrates. However, the acetic acid TPD on Pd-Au/TiO_2 showed very poor reactivity, suggesting that Au/TiO_2(110) is the better catalyst in this respect.

5.5 References

1. U. Diebold, *Surface Science Reports*, 2003, **48**, 53.
2. M. A. Henderson, *Surface Science Reports*, 2011, **66**, 185.
3. K. S. Kim and M. A. Barteau, *Journal of Molecular Catalysis*, 1990, **63**, 103.
4. L. Gamble, L. S. Jung and C. T. Campbell, *Surface Science*, 1996, **348**, 1.
5. C. P. Leon, K. Sagisaka, D. Fujita and L. Y. Han, *Rsc Advances*, 2014, **4**, 8550.
6. E. Farfan-Arribas and R. J. Madix, *Journal of Physical Chemistry B*, 2002, **106**, 10680.
7. J. N. Muir, Y. Choi and H. Idriss, *Physical Chemistry Chemical Physics*, 2012, **14**, 11910.
8. J. O. Hansen, P. Huo, U. Martinez, E. Lira, Y. Y. Wei, R. Streber, E. Laegsgaard, B. Hammer, S. Wendt and F. Besenbacher, *Physical Review Letters*, 2011, **107**, 4.
9. C. L. Pang, R. Lindsay and G. Thornton, *Chemical Reviews*, 2013, **113**, 3887.
10. H. Onishi, T. Aruga and Y. Iwasawa, *Journal of Catalysis*, 1994, **146**, 557.
11. M. A. Henderson, *Journal of Physical Chemistry B*, 1997, **101**, 221.
12. H. Onishi, T. Aruga and Y. Iwasawa, *Journal of the American Chemical Society*, 1993, **115**, 10460.
13. B. E. Hayden, A. King and M. A. Newton, *Journal of Physical Chemistry B*, 1999, **103**, 203.
14. M. Bowker, P. Stone, R. Bennett and N. Perkins, *Surface Science*, 2002, **511**, 435.
15. R. A. Bennett, P. Stone, R. D. Smith and M. Bowker, *Surface Science*, 2000, **454**, 390.
16. S. L. Hu, P. A. Bopp, L. Osterlund, P. Broqvist and K. Herrnansson, *Journal of Physical Chemistry C*, 2014, **118**, 14876.
17. Z. Chang and G. Thornton, *Surface Science*, 2000, **462**, 68.
18. Q. Guo, I. Cocks and E. M. Williams, *Journal of Chemical Physics*, 1997, **106**, 2924.
19. K. S. Kim and M. A. Barteau, *Journal of Catalysis*, 1990, **125**, 353.
20. H. Onishi, Y. Yamaguchi, K. Fukui and Y. Iwasawa, *Journal of Physical Chemistry*, 1996, **100**, 9582.

21. N. Aas, Y. X. Li and M. Bowker, *Journal of Physics-Condensed Matter*, 1991, **3**, S281.
22. M. Bowker, R. A. Bennett, A. Dickinson, D. James, R. D. Smith and P. Stone, *Studies on Surface Science and Catalysis*, 2001, **133**, 3.
23. O. Dulub, W. Hebenstreit and U. Diebold, *Physical Review Letters*, 2000, **84**, 3646.
24. Z. Chang and G. Thornton, *Surface Science*, 2000, **459**, 303.
25. J. L. Davis and M. A. Barteau, *Surface Science*, 1988, **197**, 123.
26. J. L. Davis and M. A. Barteau, *Surface Science*, 1987, **187**, 387.
27. J. L. Davis and M. A. Barteau, *Surface Science*, 1990, **235**, 235.
28. R. M. Williams, S. H. Pang and J. W. Medlin, *Surface Science*, 2014, **619**, 114.
29. R. Shekhar and M. A. Barteau, *Catalysis Letters*, 1995, **31**, 221.
30. M. Bowker, R. P. Holroyd, R. G. Sharpe, J. S. Corneille, S. M. Francis and D. W. Goodman, *Surface Science*, 1997, **370**, 113.
31. M. Li, W. Y. Guo, R. B. Jiang, L. M. Zhao and H. H. Shan, *Langmuir*, 2010, **26**, 1879.
32. H. Bahruji, M. Bowker, C. Brookes, P. R. Davies and I. Wawata, *Applied Catalysis a-General*, 2013, **454**, 66.
33. J. L. Davis and M. A. Barteau, *Langmuir*, 1989, **5**, 1299.
34. J. L. Davis and M. A. Barteau, *Surface Science*, 1991, **256**, 50.
35. R. D. Haley, M. S. Tikhov and R. M. Lambert, *Catalysis Letters*, 2001, **76**, 125.
36. N. Aas and M. Bowker, *Journal of the Chemical Society-Faraday Transactions*, 1993, **89**, 1249.
37. M. Bowker, C. Morgan and J. Couves, *Surface Science*, 2004, **555**, 145.
38. M. Bowker and Y. Li, *Catalysis and Surface Characterisation*, Royal Society of Chemistry, Cambridge, 1992.
39. Z. J. Li, F. Gao and W. T. Tysoe, *Surface Science*, 2008, **602**, 416.
40. S. Biella and M. Rossi, *Chemical Communications*, 2003, 378.
41. A. Abad, C. Almela, A. Corma and H. Garcia, *Tetrahedron*, 2006, **62**, 6666.
42. A. Abad, P. Concepcion, A. Corma and H. Garcia, *Angewandte Chemie-International Edition*, 2005, **44**, 4066.
43. D. I. Enache, D. W. Knight and G. J. Hutchings, *Catalysis Letters*, 2005, **103**, 43.

44. X. Y. Liu, B. J. Xu, J. Haubrich, R. J. Madix and C. M. Friend, *Journal of the American Chemical Society*, 2009, **131**, 5757.

45. R. J. Madix, C. M. Friend and X. Y. Liu, *Journal of Catalysis*, 2008, **258**, 410.

46. J. L. Gong and C. B. Mullins, *Journal of the American Chemical Society*, 2008, **130**, 16458.

47. Q. S. Meng, Y. L. Shen, J. Xu and J. L. Gong, *Chinese Journal of Catalysis*, 2012, **33**, 407.

48. A. M. Nadeem, G. I. N. Waterhouse and H. Idriss, *Catalysis Today*, 2012, **182**, 16.

49. .

50. T. Kecskes, J. Rasko and J. Kiss, *Applied Catalysis a-General*, 2004, **268**, 9.

51. T. Kecskes, J. Rasko and J. Kiss, *Applied Catalysis a-General*, 2004, **273**, 55.

52. T. Kecskes, R. Nemeth, J. Rasko and J. Kiss, *Vacuum*, 2005, **80**, 64.

53. D. A. Outka and R. J. Madix, *Surface Science*, 1987, **179**, 361.

54. P. Mars, J. J. F. Scholten and P. Zwietering, *Advances in Catalysis*, 1963, **14**, 35.

55. S. Singh, S. Li, R. Carrasquillo-Flores, A. C. Alba-Rubio, J. A. Dumesic and M. Mavrikakis, *Aiche Journal*, 2014, **60**, 1303.

56. W. Y. Yu, G. M. Mullen, D. W. Flaherty and C. B. Mullins, *Journal of the American Chemical Society*, 2014, **136**, 11070.

57. S. D. Senanayake, D. Stacchiola, P. Liu, C. B. Mullins, J. Hrbek and J. A. Rodriguez, *Journal of Physical Chemistry C*, 2009, **113**, 19536.

58. Z. Li, F. Calaza, F. Gao and W. T. Tysoe, *Surface Science*, 2007, **601**, 1351.

59. Z. J. Li and W. T. Tysoe, *Surface Science*, 2012, **606**, 1934.

60. Z. L. Wang, J. M. Yan, H. L. Wang, Y. Ping and Q. Jiang, *Journal of Materials Chemistry A*, 2013, **1**, 12721.

61. O. Metin, X. L. Sun and S. H. Sun, *Nanoscale*, 2013, **5**, 910.

62. X. C. Zhou, Y. J. Huang, C. P. Liu, J. H. Liao, T. H. Lu and W. Xing, *Chemsuschem*, 2010, **3**, 1379.

63. X. J. Gu, Z. H. Lu, H. L. Jiang, T. Akita and Q. Xu, *Journal of the American Chemical Society*, 2011, **133**, 11822.

64. Y. J. Huang, X. C. Zhou, M. Yin, C. P. Liu and W. Xing, *Chemistry of Materials*, 2010, **22**, 5122.

65. M. Bowker, C. Morton, J. Kennedy, H. Bahruji, J. Greves, W. Jones, P. R. Davies, C. Brookes, P. P. Wells and N. Dimitratos, *Journal of Catalysis*, 2014, **310**, 10.

66. Y. Mizukoshi, K. Sato, T. J. Konno and N. Masahashi, *Applied Catalysis B-Environmental*, 2010, **94**, 248.
67. M. A. Barteau, *The Chemical Physics of Solid Surfaces*, Elsevier, Amsterdam, 2001.

Chapter 6 – Conclusions

Chapter 6 Contents

6.1 Introduction

This chapter concludes the thesis and summarises the main findings of this work, together with recommendations for further work following on from that reported here.

The results in chapters 3-5 are consistent with the aims outlined in chapter 1. The growth of Pd and the effect of annealing Pd on $TiO_2(110)$ was investigated in chapter 3; the effect of heating Au on $TiO_2(110)$ and the formation of Au-Pd core-shell structures was investigated in chapter 4; and the reactivity of $TiO_2(110)$ deposited with Pd and Au, separately and combined with ethanol, formic acid and acetic acid was explored in chapter 5.

6.2 Summary

6.2.1 – $TiO_2(110)$ and Pd on $TiO_2(110)$

The $TiO_2(110)$ surface was characterised with ISS, XPS and LEED. Sputtering the clean titania single crystal resulted in reduction of the surface, with an increase in Ti^{2+} and Ti^{3+} in the Ti2p XPS. This was somewhat re-oxidised after annealing in UHV, especially converting Ti^{2+} to Ti^{3+}. However, annealing in oxygen was found to be much more effective, converting the Ti^{3+} to Ti^{4+}.

Pd was deposited on $TiO_2(110)$ after the titania had been subjected to a range of different treatments – sputtering, sputtering then annealing in UHV, and annealing in oxygen. The palladium was shown to grow in a Volmer-Weber mode, regardless of the reduction and condition of the crystal.

On annealing the Pd/$TiO_2(110)$ to temperatures above 723 K, an SMSI effect occurs between the Pd nanoparticles and the TiO_2 support. The Pd signal in the ISS decreases to almost zero, whilst there is an emergence of a shoulder at 355.5 eV in the Ti2p XPS spectra, characteristic of Ti^{2+}. This indicates that a layer of TiO begins to cover the Pd nanoparticles. This was found to be strongly affected by the oxidation state of the titania surface – SMSI occurred at a higher temperature for an oxidised surface than for a reduced surface.

6.2.2 – Au and Au-Pd on TiO_2(110)

The effect of annealing Au on TiO_2(110) was studied, finding that it sinters and forms nanoparticles, but does not undergo an SMSI effect. This was supported by an increase in the Ti and O signals in the ISS and XPS and the corresponding decrease in the Au signals (signifying sintering) and a lack of a Ti^{2+} shoulder in the Ti2p XPS (showing no SMSI encapsulation by the titania support).

Pd and Au were deposited sequentially on to TiO_2(110). On annealing to 773 K the Au signal disappeared from the ISS whilst remaining present in the XPS, indicating that they had formed an Au-Pd core-shell structure. On annealing to 773 K and above, a shoulder in the Ti2p XPS at 355.5 eV emerges, indicating an SMSI effect (i.e. encapsulation by the reduced titania support) much like with Pd on its own. There appeared to be a correspondence between the amount of Au deposited and whether or not an SMSI effect occurs. However, this is not conclusive and a more thorough inspection would be required before making this claim.

The presence of O in the ISS after depositing enough Pd and Au to cover the Ti ISS signal suggested that there was some CO adsorbed on the Pd. This would lower the surface free energy of the Pd, making the formation of the Au-Pd core-shell structure more favourable than a Pd-Au core-shell structure, which is otherwise expected from the literature.

The encapsulation of Au by Pd on annealing was hampered when the starting ratio of Au and Pd was closer to 1 (rather than there being much more Pd than Au) and the Pd was unable to diffuse through the thick Au layer and encapsulate the Au.

6.2.3 – Reactivity studies of Pd and Au on TiO_2(110)

The reactivity of TiO_2(110) towards ethanol, formic acid and acetic acid was investigated using TPD. It was found that TiO_2 showed similar reactivity to what has previously been shown in the literature. Ethanol decomposed primarily to ethene and acetaldehyde. Formic acid followed both dehydrogenation and dehydration reaction pathways, giving CO_2 and H_2, and CO and H_2O respectively. Acetic acid decomposed to give ketene, CO and CO_2. The reactivity of this substrate towards these same small organic molecules was then looked at after depositing Pd, Au, and Pd-Au.

The addition of Au generally did not positively impact the resulting TPD, which is unsurprising as Au has been shown to be unreactive to these adsorbates. It was ultimately thought that the molecules investigated did not even adsorb onto the Au.

The products observed after adding Pd to $TiO_2(110)$ were overall very similar to just the titania single crystal, although typically at a higher temperature than from the $TiO_2(110)$ substrate on its own, implying that the addition of Pd decreased the reactivity of the substrate. Formic acid still followed both reaction pathways, with both CO_2 and CO being seen at temperatures ~50 K higher than on $TiO_2(110)$. Likewise, the main desorption products seen from acetic acid (ketene and CO) were observed at ~50 K higher than on just the $TiO_2(110)$ single crystal, as were the main desorption peaks from ethanol (although these were only ~10-20 K higher).

The addition of both Au and Pd appeared to increase the reactivity of formic acid and ethanol, with more products seen from both metals combined than from either metal individually. However, the acetic acid showed very poor reactivity.

6.3 Concluding remarks

The first half of this thesis uses two powerful surface science techniques, low energy ion scattering (LEIS) and X-ray photoelectron spectroscopy (XPS), to look at the interaction of Pd and Au, separately and combined, with a $TiO_2(110)$ support. Pd was found to undergo a strong SMSI effect on annealing whereas Au does not, as previously reported in the literature. When the two were co-deposited on to $TiO_2(110)$ and annealed, a Au-Pd core-shell structure was first observed, followed by an intermediate amount of SMSI. The presence of Au with

Pd inhibited the SMSI effect – the more Au was present, the less SMSI encapsulation was observed.

The second half of this thesis concerned the study of Pd and Au on $TiO_2(110)$, specifically their interactions with each other, and how this affects the reactivity towards a number of small organic molecules. As described above, on deposition of Pd and Au on to the $TiO_2(110)$ single crystal and annealing a Au-Pd core-shell structure was observed. When the reactivity of this was examined with TPD, it was found that the Au-Pd/$TiO_2(110)$ was more reactive than the individual component metals on $TiO_2(110)$. This agrees with the general literature, which has discovered in recent years that bimetallic catalysts exhibit greater selectivity and activity in a wide number of reactions than the original individual component metals. The observation of the Au-Pd core-shell structure on $TiO_2(110)$ gives a greater understanding of why this is.

6.4 Outlook and further study

There is a lot of potential for further study in this area. It is unfortunate that for the duration of this study, the STM present in UHV1 did not work properly. It would have allowed me to see the effect of SMSI on the Pd nanoparticles described in chapter 3, and would have enabled the direct observation of the formation of the Au-Pd core-shell structures seen in chapter 4.

A more indepth study of the Au-Pd core-shell structures would be beneficial. A systematic study of how the amount of Pd and Au affects these structures could be carried out. It was observed that, with a small amount of Au present, an Au-Pd core-shell structure was formed. However, with a large amount of Au, this does not happen. It would interesting to find out at what point this occurs. Furthermore, computational work (i.e. DFT) could be carried out to aid and guide the experimental work.

The TPDs in chapter 5 suffered from several problems that could be improved upon in future work. An electronically controlled temperature ramp would ensure a consistent rise in temperature between experiments, making them easier to compare. A differentially pumped mass spectrometer would help eliminate background pressure and noise in the mass spectra, enabling the identification of smaller peaks in the TPD. Finally, improving the degassing of the gas lines when changing between different small organic molecules would help to avoid cross contamination. The reactivity work itself could be compared with real catalysts, to see if the results are consistent, and also with Au/Pd(110) and Pd/Au(111) model catalysts. Molecular beam studies could be carried out to obtain sticking probabilities on the core-shell structures.

Appendix

A.1 – referred to in Chapter 3, section 3.3.5, pg 120

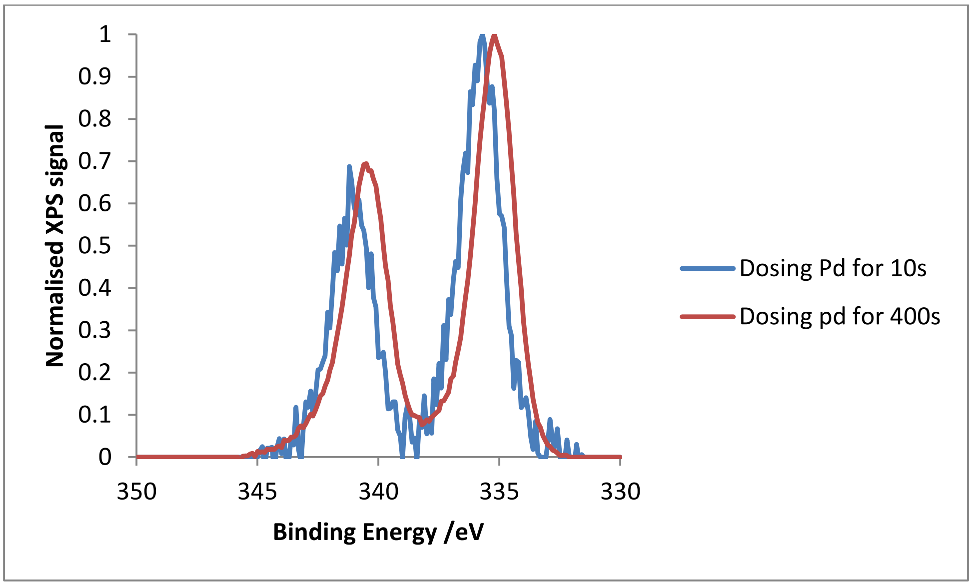

Figure 1 – Pd 3d XPS spectra after dosing 10s and 400s of Pd onto oxidised $TiO_2(110)$

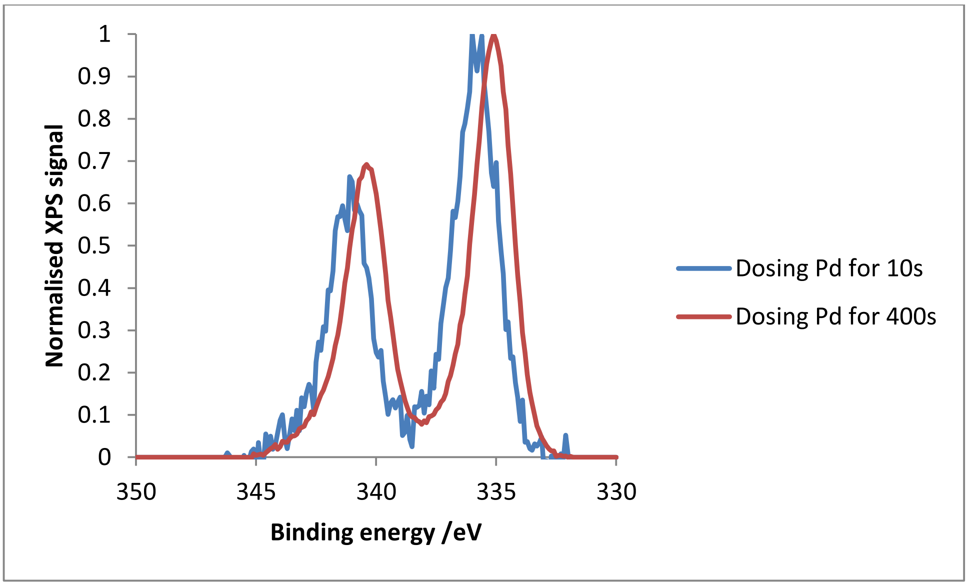

Figure 2 – Pd spectra after dosing 10s and 400s of Pd onto sputtered $TiO_2(110)$

A.2 – referred to in Chapter 3, section 3.3.6, pg 124

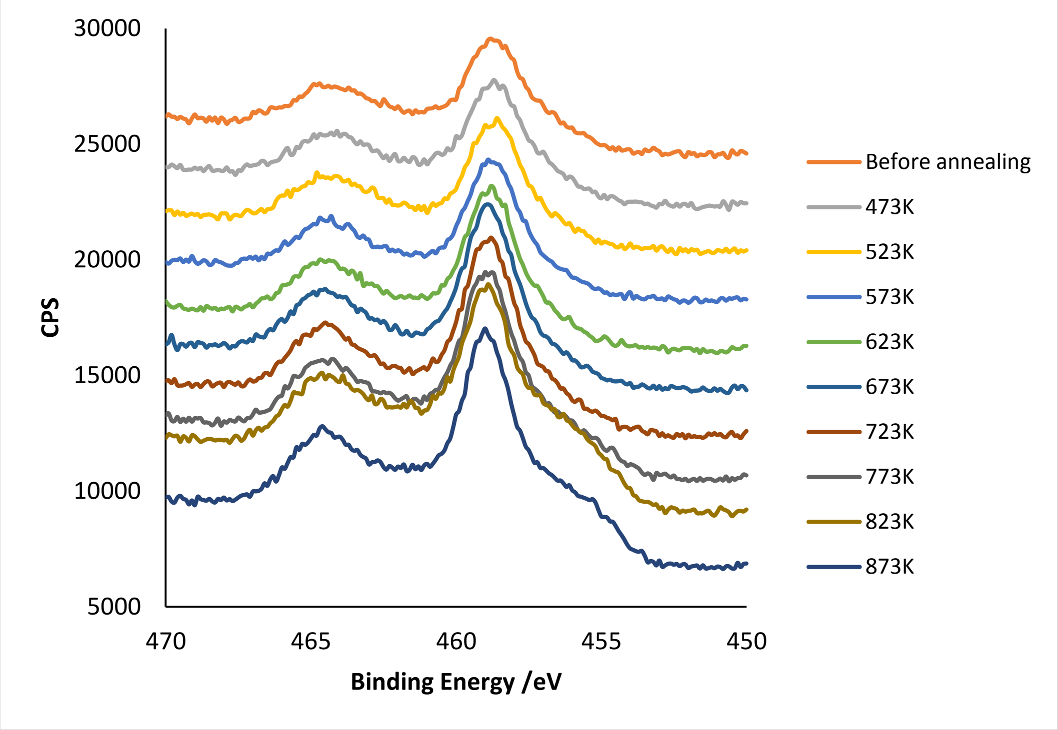

Figure 3 – The variation in the Ti 2p XPS signal with increasing temperature for the sputter-annealed surface dosed with Pd

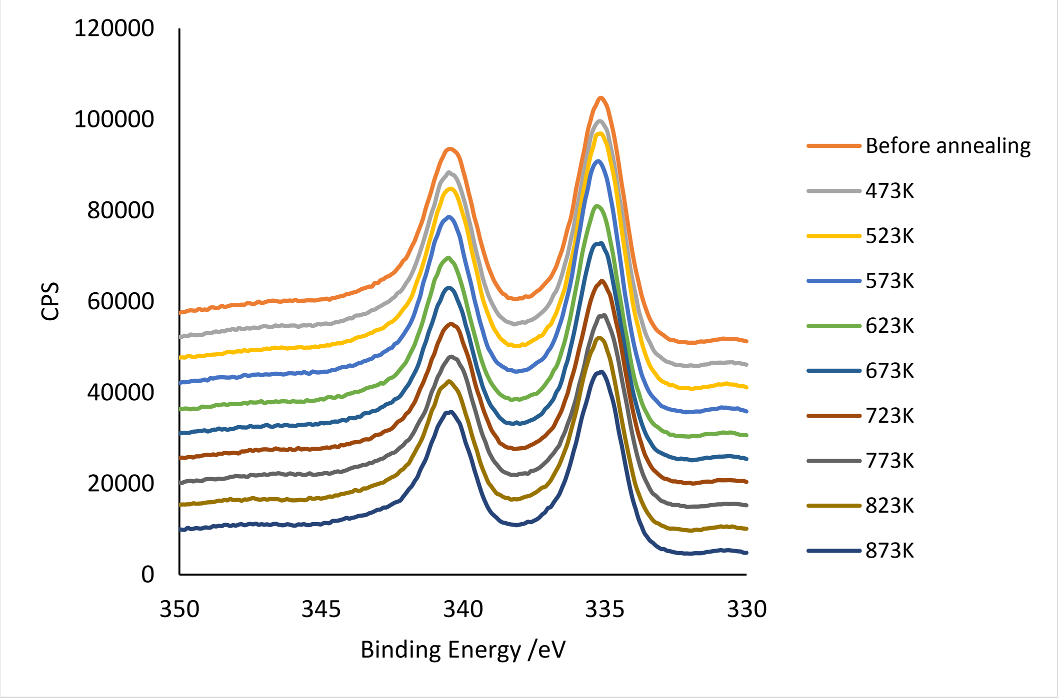

Figure 4 – The variation in the Pd 3d XPS spectra with increasing temperature for the sputter-annealed surface dosed with Pd

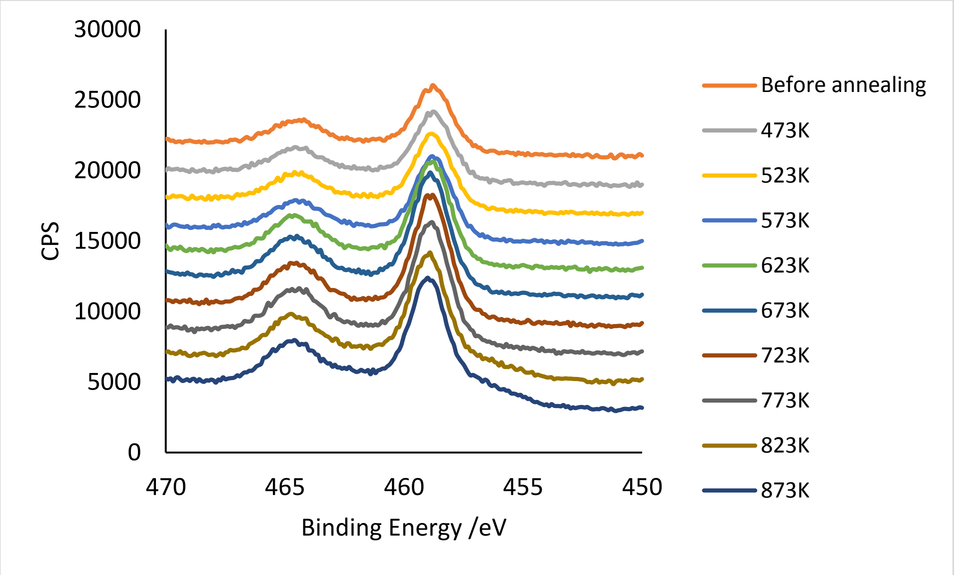

Figure 5 – The variation in the Ti 2p XPS spectra with increasing temperature for the oxidised surface dosed with Pd

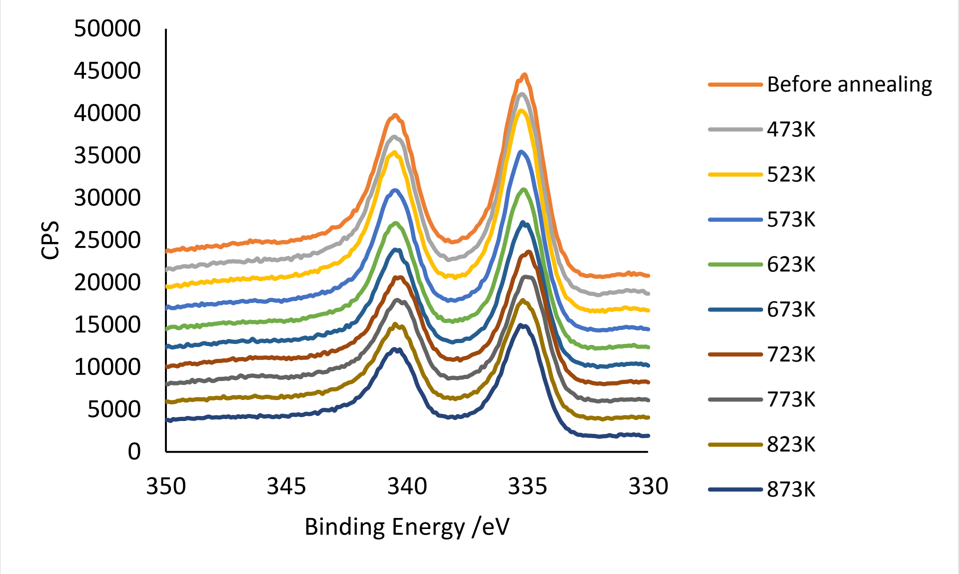

Figure 6 – The variation in the Pd 3d XPS spectra with increasing temperature for the oxidised $TiO_2(110)$ surface dosed with Pd

A.3 – referred to in Chapter 3, section 3.3.6, pg 126

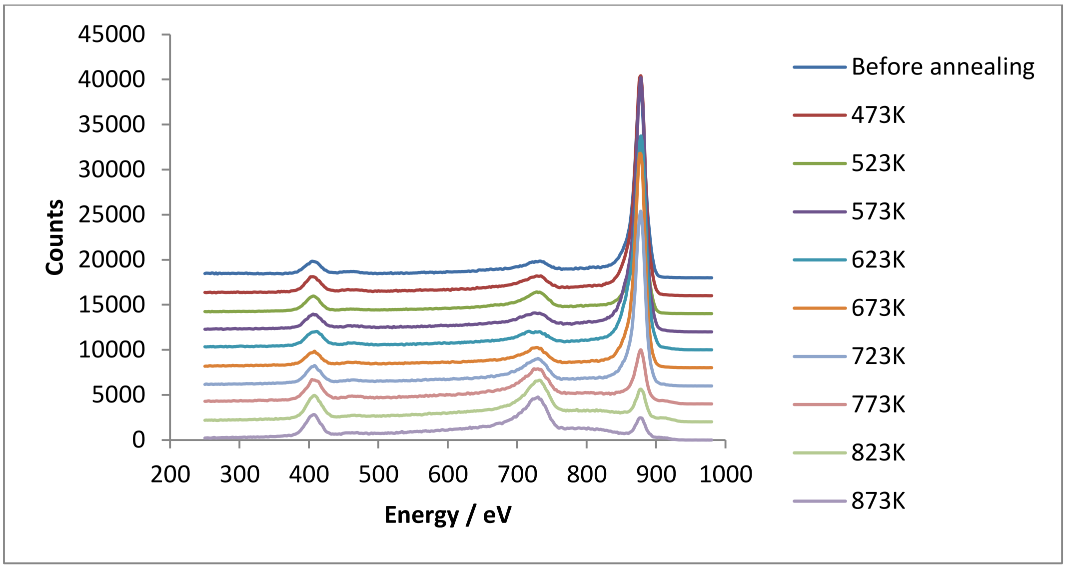

Figure 7 – ISS raw data of Pd on the sputter-annealed $TiO_2(110)$ surface after annealing to increasing temperatures

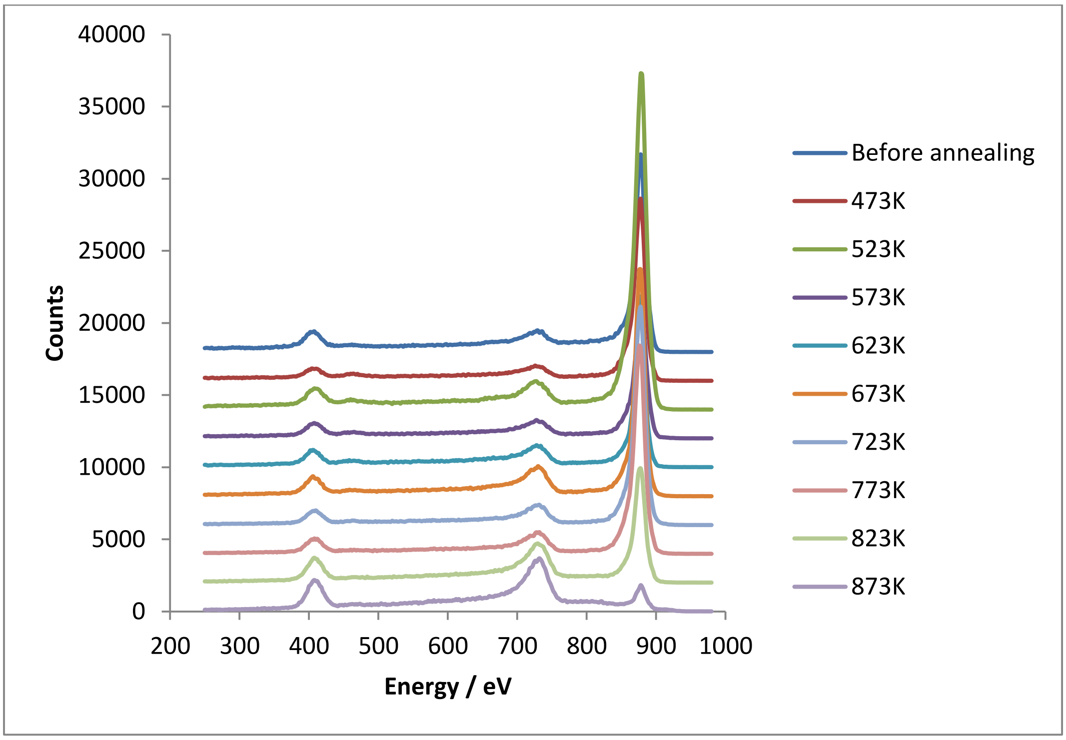

Figure 8 – ISS raw data of Pd on the oxidised $TiO_2(110)$ surface after annealing to increasing temperatures